Smoluchowski theory for concentrated colloidal dispersions far from equilibrium

by

Ehssan Nazockdast

A desertion submitted to Department of Chemical Engineering and committee of graduate studies of The City University of New York in partial fulfillment of the requirements for the degree of Doctor of Philosophy

2013

This manuscript has been read and accepted for the Graduate Faculty in Engineering in satisfaction of the dissertation requirement for the degree of Doctor of Philosophy.

Jeffrey F Morris

Date

Chair of Examining Committee

Ardie D. Walser

Date

Executive Officer

Morton M. Denn

Mark M. Shattuck

Raymond Tun

Heinrich Jaeger

Supervisory Committee

THE CITY UNIVERSITY OF NEW YORK

Abstract

Smoluchowski theory for concentrated colloidal dispersions far from equilibrium

by

Ehssan Nazockdast

ADVISOR:

Jeffrey F Morris

This thesis develops a theory for the analytical prediction of microstructure of concentrated Brownian suspensions of spheres in simple-shear flow. The computed microstructure is used in a prediction of the suspension rheology. Following an introduction in Chapter 1, the theoretical framework is given in Chapter 2; the remaining chapters involve different extensions of the theory and more detailed analysis of the variables included in it.

In Chapter 2, a near-hard-sphere suspension is studied for solid volume fractions $\phi \leq 0.55$ and Péclet number $Pe = 6\pi\eta\dot{\gamma}a^3/k_bT \leq 100$; a is the particle radius, η is the suspending Newtonian fluid viscosity, $\dot{\gamma}$ is the shear rate, k_b is the Boltzmann constant and T is absolute temperature. The method developed determines the steady pair distribution function $g(\mathbf{r})$, where $\mathbf{r}$ is the pair separation vector, from a solution of the Smoluchowski equation (SE) reduced to pair level. To account for the influence of the surrounding bath of particles on the interaction of a pair, an integro-differential form of the pair SE is developed; the integral portion represents the forces due to the bath which drive the pair interaction. Hydrodynamic interactions are accounted in a pairwise fashion, based on the dominant influence of pair lubrication interactions for concentrated suspensions. The pair SE is heuristically modified to include the influence of

shear-induced relative diffusion, and this is found to be crucial for success of the theory; a simple model based on understanding of the shear-induced self-diffusivity is used for this property. In Chapter 4 the properties of shear-induced diffusivity are considered in greater depth. The predictions are compared against Accelerated Stokesian Dynamics simulation (ASD) which takes into account both near-contact and far-field hydrodynamic interactions. Agreement of the predicted microstructure with observations from simulations is generally good and discrepancies are clearly noted. The predicted rheology captures shear thinning and shear thickening as well as normal stress differences in good agreement with simulation; quantitative agreement is best at large ϕ.

In Chapter 3, an extension of the theory for hard-sphere sheared suspensions is given to study structure and rheology of colloidal suspensions with soft repulsive interactions. ASD simulations are carried out to provide insight and to enable direct comparison with theoretical predictions. The effect of extended range repulsive interactions is studied by considering repulsive interactions with different steepness in the range of $0.1 \leq Pe \leq 100$. The predicted $g(\mathbf{r})$ and shear viscosity are in good agreement with simulations before the onset of a shear-induced ordering transition in simulations of the soft colloids.

In Chapter 4, an alternative formulation based on pair-wise summation of relative velocities for hydrodynamic interactions is developed. Also, based on ASD results, a modified form is proposed for modeling shear-induced relative diffusion. These modifications result in considerable improvement in the agreement of structure and rheology with simulations. The primary focus of this chapter is to consider the the pair relative velocity predicted by the theory in comparison to Stokesian Dynamics simulations, as well as to evaluate quantities related to the hydrodynamic dispersion needed in the theoretical approach. The pair dynamics for moderate particle volume fraction, $0.2 \leq \phi \leq 0.45$, are found to be remarkably different from the form for an isolated pair of spheres, and at $\phi > 0.45$ a qualitative change is again seen in this problem. Agreement of the theory and simulation on the gross features of the particle motion and structure is good, and

discrepancies are clearly delineated.

In Chapter 5, the theoretical framework constructed for sheared colloidal suspensions is extended to study the active microrheology, wherein the motion of a spherical probe driven through a bath of colloidal suspension by application of a fixed external force or velocity is studied. The theory gives predictions of microstructure in form of $g(\mathbf{r})$, which here is the normalized likelihood of observing the colloidal bath particles at a relative distance $\mathbf{r}$ with respect to the probe. This distribution is then used to compute the resistance to motion and hence the micro-viscosity of the suspension using the Stokes drag law at $0.01 \leq Pe \leq 400$. The differences between the two scenarios of pulling the probe with constant force and fixing the velocity are elucidated. The results indicate a noticeable difference between the two methods both for microstructure and rheology. In general, although active microrheology gives a similar qualitative picture of variations of viscosity with ϕ and Pe, quantitative agreement of the computed micro-viscosity with shear flow viscosity is not achieved in all conditions.

The last chapter presents preliminary results related to two other extensions of the theory: 1- non-Newtonian rheology of suspensions when $Pe \to \infty$ and 2- microstructure and rheology for general linear flow kinematics. The predictions of rheology at $Pe \to \infty$ are in reasonable agreement with ASD results at $Pe = 1000$. The results suggest that the theory can be applied to non-Brownian suspensions with different types of interparticle interactions. Predictions of $g(\mathbf{r})$ and rheology are presented for linear flows ranging from pure straining motion with no vorticity to motions dominated by vorticity. This is pursued by fixing the magnitude of straining motion and changing the strength of the rotational component of the linear flow. These results show a steep reduction in the magnitude of normal stress differences with increase of the rotational component of the flow.

Contents

List of Figures

1 Introduction

1.1 Motivation

Suspension flows are two-phase flows of materials composed of a fluid (matrix) and a dispersed solid phase. They occur in nature and technological applications [1] and exist over a wide range of length scales from mudflows which can expand for kilometers [2] to motion of particles at nanometer scales [3]. Macroscopic properties of suspensions including their flow behavior is determined by their microstructure, i.e. the arrangements of solid particles with respect to each other. Microstructure is set by microscopic interactions between the suspended particles, as well as their interactions with the fluid medium and any external forces.

Suspension flows are normally further categorized based on the type of forces governing their microstructure. This is determined by parameters such as the size and shape of the particles, strength of the flow, and properties of the fluid. Typical categories are colloidal suspensions [4, 5], non-Brownian suspensions [6, 7], suspensions at finite inertia [8, 9] and wet granular suspensions [10]. This work focuses on colloidal suspensions which roughly means suspensions with the particle size ranging from nanometers to micrometers, a range where thermal forces, hydrodynamics, and interparticle forces of conservative form generally all may play a role in the microscopic dynamics. The aim of this work is to develop a theoretical framework to relate microscopic interactions in a flowing colloidal suspension to its macroscopic behavior, namely the rheology, and in particular to develop an approach applicable to concentrated suspensions.

Theoretical study of microstructure and rheology of colloidal suspensions is of significant practical relevance. Colloidal suspensions are encountered in many consumer products such as cosmetics, pharmaceutical products and foodstuffs [11]. Colloidal particles are now synthesized with a high degree of control over shape and interparticle interactions [3]. This has led to a burst in use of these materials in advanced technologies particularly as building blocks for fabricating new types of materials [12, 13]. Other applications include 3D ink-jet technology [14], advanced ceramic processing [15] and microfluidics [16]. A predictive theory for structure and rheology enables one to explore the parameter space and potentially engineer the shape, interactions and external forces to obtain the desired microstructure and macroscopic behavior based on design rules. Alternatively an undesired behavior may be prevented by regulating the microscopic interactions and external forces.

Microstructural theories are also important in gaining a clearer understanding of rheology of complex fluids, as colloidal suspensions are one of the simplest of complex fluids. In simple liquids (small molecule liquids such as water) the typical external shear rates applied to flow the fluid are negligible compared to the interactions at the rate caused by the thermal velocity, and the structure remains essentially in equilibrium. As a consequence, the theoretical understanding of microstructure and macroscopic properties for simple liquids is well-developed using equilibrium statistical mechanics [17]. In complex fluids the constituent elements of the fluid (polymer chains, or particles in suspension) are large enough that thermal forces are not sufficient to fully relax their rearrangement due to external forces or flow; as a result microstructure is driven away from equilibrium and the structure and rheology become coupled. Hence theoretical progress is more challenging and most of the success has been limited to polymeric liquids and colloidal suspensions. First-principles theories for these model systems form the basic understanding of more complicated fluids such as suspensions in viscoelastic media [18], and deformable and anisotropic particles [19].

We consider flow-induced microstructure in colloidal suspension flows by means of applying a constant stress or deformation rate (linear flows). Also we minimize the complexity related to particle shape and consider monodisperse spherical particles with the same density as the fluid, hence eliminating the influence of gravitational force. Changing the particle shape expands the parameter space [3]. The majority of the analysis presented in this thesis is carried out for "hard-sphere" suspensions where particles are assumed rigid with only excluded volume interactions which are mediated by the fluid. This allows us to systematically investigate fundamental questions about the interplay between the packing (geometry) and fluid-particle hydrodynamic interactions in setting the microstructure and rheology in concentrated suspensions. The formulation provided in this study is, however, not limited to hard-sphere suspensions and can be extended to suspensions with long-range interparticle interactions. This is carried out in Chapter 3 where microstructure and rheology of suspensions interacting through soft repulsive potentials are studied.

The forces in a sheared spherical suspension are

$$\mathbf{F}^B \sim k_b T/a, \quad \mathbf{F}^P, \quad \mathbf{F}^H \sim 6\pi\eta\dot{\gamma}a^2, \quad \mathbf{F}^I \sim \rho\dot{\gamma}^2 a^4,$$

where $\mathbf{F}^B$, $\mathbf{F}^P$, $\mathbf{F}^H$ and $\mathbf{F}^I$ are Brownian, interparticle, viscous (hydrodynamic) and inertial forces, k_b is the Botzmann constant, T is the absolute temperature, η is the fluid viscosity and a is the particle radius. The microstructure is therefore controlled by volume fraction of the dispersed phase, ϕ, and three other dimensionless quantities:

$$F^\star = \frac{F^P}{F^B}, \quad Pe = \frac{F^H}{F^B} = \frac{6\pi\eta\dot{\gamma}a^3}{k_b T}, \quad Re_p = \frac{F^I}{F^H} = \frac{\rho\dot{\gamma}a^2}{\eta}.$$

The relative strength of inertial to viscous forces is given by particle scale Reynolds number, Re_p. Inertial forces typically become important when the size of suspended particles is of the order of 100 μm or larger, particularly when dispersed in a low viscosity

fluid such as water. Inertial forces introduce interesting variations to microstructure and rheology of suspensions [9]. In a colloidal suspension, however, due to the size of the dispersed particles, $Re_p \ll 1$. In this work, inertia is neglected, meaning we take $Re_p \equiv 0$, and the hydrodynamic interactions are governed by Stokes flow. The reader interested in suspensions with finite inertia is referred to the relevant articles and references in [8, 9].

The ratio of hydrodynamic to Brownian forces is determined by the Péclet number, Pe, which can also be regarded as the dimensionless shear rate. Depending on the flow rate, fluid viscosity and the size of the particles, a wide range of Pe is accessible in typical applications involving colloidal dispersions; the Péclet number can vary from zero or nearly so in colloidal suspensions in quiescent conditions to $Pe = O(1)$ in weak shear and to $Pe \gg 1$ at strong shear rates. The primary focus of this work is to study microstructural changes and the resulting non-Newtonian rheological behavior with ϕ and deformation rate, i.e. as a function of Péclet number, with results of $Pe \gg 1$ and large ϕ being a key novel contribution.

The relative importance of interparticle to Brownian forces is determined by $F^\star$. In quiescent conditions ($Pe = 0$), the structure is set by volume fraction and interparticle and thermal forces. Changing the interparticle interactions can change the structure from disordered in case of weak interparticle interactions to gel-like structure in suspensions with strong attractive interaction [20] and colloidal crystals for colloidal particles with strong long-ranged repulsive interactions [21]. These microstructures evolve differently under flow conditions and show a diverse range of non-Newtonian rheology [22]. In hard-sphere suspensions, particles are assumed rigid (non-deformable) with only excluded volume interactions for which $F^P \sim k_bT/a$ and $F^\star \sim O(1)$; as a result both Brownian and interparticle forces scale as k_bT/a and the microstructure is set only by volume fraction, ϕ, and Pe.

Studies on microstructural theories for rheology of colloidal suspensions goes back to

the pioneering work of Einstein who showed $\hat{\eta} = 1 + 2.5\phi$ for very dilute dispersions where $\hat{\eta}$ is the shear viscosity normalized by fluid viscosity. There has been remarkable advancement in this field over the past century; Chapter 2 gives a review of the works on the topic. Despite this progress, prior to the work described in this thesis, the theories were applicable in two limits of Pe and ϕ. The first group of theories consider very near equilibrium dispersions, $Pe \ll 1$ [23, 24, 25, 26]. These theories generally use perturbation techniques to extend the equilibrium theory constructed for simple liquids to systems slightly perturbed away from equilibrium. They are successful in predicting the bulk properties at $Pe \ll 1$ over a wide range of volume fractions but no attempt has been made to extend them to $Pe \geq 1$. The second group of theories consider dilute dispersions where interactions of particles up to pair level are considered. The evolution of microstructure in this limit is described by the pair Smoluchowski equation (see §1.2.2) and microstructure can be computed for the entire range of Pe [27, 28]. These theories are very useful in providing an understanding of microstructure and non-Newtonian rheology at $Pe \gg 1$, and are able to qualitatively predict important simulational and experimental observations in this limit; these include as shear thinning at low Pe and shear thickening at large Pe, and also the correct sign and trend for normal stress differences. However they are restricted to dilute suspensions; attempts have been made to extend the dilute theories to more concentrated suspensions through scaling arguments, but important features including the behavior of normal stress differences cannot be predicted within these scaling theories. The theory presented in this thesis borrows certain elements of each of these two groups of theories and adds new features to give predictions of microstructure and rheology for dilute to concentrated suspensions, $\phi \leq 0.50$, over the entire range of Pe. This work breaks new ground in microstructural theories of colloidal dispersion and it is the first theory of its kind which gives reasonably accurate predictions of microstructure and rheology of strongly sheared concentrated colloidal dispersions.

1.2 Background and goals

In this section, we give a brief description of the essential ideas and the framework of Smoluchowski theory.

1.2.1 Langevin equation

The evolution of position and velocity of colloidal particles can be described using the Langevin equation, which is the conservation of momentum on each particle:

$$\frac{d\mathbf{p}}{dt} = m\frac{d\mathbf{U}}{dt} = \mathbf{F}^B + \mathbf{F}^H + \mathbf{F}^P, \tag{1.1}$$

where for an N-particle system $\mathbf{p}$ is the linear and angular momentum vector of size $6N$, m is the mass and moment of inertia, and $\mathbf{U}$ the linear and angular velocity vector of all particles. Recall $\mathbf{F}^B$, $\mathbf{F}^H$, and $\mathbf{F}^P$ are Brownian, hydrodynamic and interparticle forces. As long as the forces are defined based on the position and velocity of the particles, (1.1) can be integrated twice in time to give the evolution of velocity and position of each particle. The interparticle force on particle α is obtained from a pairwise summation: $\mathbf{F}^P_\alpha = \Sigma_{\beta=1}^{\beta=N}\mathbf{F}^P_{\alpha\beta}$ where $\mathbf{F}^P_{\alpha\beta} = \nabla_\beta\Phi$, ∇_β is the gradient operator with respect to the position of particle β, and Φ is a two particle potential field.

Brownian forces are induced by collisions of fluid molecules with the particles. The typical relaxation time of liquid molecules is in the order of 10^{-14} s; thus for any time interval of interest the collisions of fluid molecules can be assumed to be completely decorrelated and the net Brownian force on each particle to be zero:

$$\langle\mathbf{F}^B\rangle = 0, \qquad \langle\mathbf{F}^B(t)\mathbf{F}^B(t')\rangle = \Theta\delta(t-t') \tag{1.2}$$

where δ is Dirac Delta function, $\langle\rangle$ denotes averaging over time for each individual particle and Θ is the strength of Brownian fluctuations. Assuming the liquid molecules are in equilibrium and the collisions to be decorrelated, the strength of the fluctuation field can

be formulated exactly as $\Theta = 2k_bT\mathbf{R}^{FU}$ where k_b is the Boltzmann constant constant and T is the absolute temperature and $\mathbf{R}^{FU}$ is the hydrodynamic resistance tensor relating force to velocity. This relationship is one version of the fluctuation-dissipation theorem.

When a fluctuating force (such as Brownian kicks) is applied on a particle it induces a change in the momentum of that particle. The characteristic time for the momentum to relax and reach the steady state is $\tau_I = m/6\pi\eta a$ where subscript I refers to inertia [5]. The Brownian forces cause the particles to go through a random walk diffusive motion. The characteristic time for a particle to travel a distance of its radius, a, by Brownian diffusion is $\tau_D \approx \dfrac{6\pi\eta a^3}{k_bT}$. For the majority of colloidal suspensions (and the case considered here), $\tau_I \ll \tau_D$ i.e. the momentum of the particles has relaxed before the particles change their configurations significantly. The appropriate time scale to study the microstructural evolution is therefore $\tau_I \ll \tau \ll \tau_D$. We may safely neglect the variations of momentum and take the total force to be zero on each particle while considering times small enough to allow a detailed study of the change of configuration of the particles on their own length scale.

As a particle moves, as a result of bulk flow or Brownian and interparticle forces, it creates a disturbance in the fluid flow around it. This flow disturbance propagates and encounters other particles and changes their dynamics. The interactions of colloidal particles through the mediating fluid are referred to as hydrodynamic interactions. As an example, consider the case of having a chain of nearly touching particles with a force being applied to the particle in front of the chain to draw it away from the rest of the particles. Due to hydrodynamic interactions between the particles, the entire chain of particles would move with nearly the same velocity in the force direction and "stick together" as a solid object. If there was no fluid between the particles, however, only the lead particle would have moved away from the particles.

In case of $Re_p = 0$, the inertial terms in the Navier-Stokes equations are neglected and the hydrodynamic interactions are described by Stokes equations. The characteristic

time for the flow disturbance to diffuse a length l in Stokes flow is $\tau_\nu = l^2/\nu$. For a typical fluid and $l \sim 10a$, $\tau_\nu \ll \tau_D$ and we assume that the disturbance field is set instantly. Consequently, in linear flows (constant velocity gradient), the hydrodynamic force is linearly related to the velocity of the particle and the strain rate imposed:

$$\mathbf{F}^H = -\mathbf{R}^{FU} \cdot \left(\mathbf{U}^H - \mathbf{U}^\infty\right) + \mathbf{R}^{FE} : \mathbf{E}^\infty, \tag{1.3}$$

where $\mathbf{U}^\infty$ and $\mathbf{E}^\infty$ are the velocity and strain rate tensor due to the imposed linear flow; $\mathbf{R}^{FU}(\mathbf{X})$ and $\mathbf{R}^{FE}(\mathbf{X})$ are resistance tensors and give hydrodynamic drag force induced by relative motion of the particles with respect to the fluid ($\mathbf{R}^{FU}$) and the force caused by the imposed strain rate ($\mathbf{R}^{FE}$). The resistance tensors are functions of the configuration of the particles, $\mathbf{X} = (\mathbf{x}_1, \mathbf{x}_2, ..., \mathbf{x}_N)$, but have no dependence on their velocities.

The velocity of particles can be computed by setting the force equal to zero on all particles as

$$\frac{d\mathbf{X}}{dt} = \mathbf{U}^G = \mathbf{U}^\infty + \left(\mathbf{R}^{FU}\right)^{-1} \cdot \left[\mathbf{R}^{FE} : \mathbf{E}^\infty + \mathbf{F}^P\right] + \mathbf{U}^B, \tag{1.4}$$

where G refers to "grand" velocity vector of all particles. $\mathbf{U}_c = \mathbf{U}^\infty + \left(\mathbf{R}^{FU}\right)^{-1} \cdot \left[\mathbf{R}^{FE} : \mathbf{E}^\infty + \mathbf{F}^P\right]$ is the velocity vector by which the particles are convected while $\mathbf{U}^B = \dfrac{d\mathbf{X}^B}{dt}$ is the Brownian velocity which results in zero net average motion but induces a diffusive motion, $\langle \mathbf{X}^B \mathbf{X}^B \rangle = \mathbf{D}t$ with $\mathbf{D} = 2k_bT\mathbf{M}^{UF}$ so that it satisfies the fluctuation-dissipation theorem; here $\mathbf{M}^{UF} = \left(\mathbf{R}^{FU}\right)^{-1}$ is the mobility tensor. The essential point is that the velocities of particles can be computed in any given configuration based on the position of the particles. The evolution of microstructure is obtained by integrating (1.4) forward in time as is done in Stokesian Dynamics simulations [29].

1.2.2 Smoluchowski equation

The macroscopic behavior of a system, including its rheology, is an ensemble average over many (infinitely many, in principle) microscopic states. One useful method for microscopic realization of suspensions is using the concept of phase space which, for the case of relaxed momentum coordinates, is a $3N$ dimensional space formed by spatial coordinates of the N particles. Thus any snapshot of the system in time (which presents a microstate of the system) is a point in phase space. Figure 1.1(a) shows a schematic presentation of microstates of a system in phase space. Note that density (probability) of points is not uniform and varies throughout the phase space. Suppose the density or probability of observing a particular microstate at time t, is given by $P_N(\mathbf{X}, t)$. The ensemble average of a macroscopic quantity such as total stress, $\mathbf{\Sigma}(\mathbf{X})$, is obtained by integrating over all possible configurations:

$$\langle \mathbf{\Sigma} \rangle(t) = \int \mathbf{\Sigma}(\mathbf{X}, t) P_N(\mathbf{X}, t) d\mathbf{X}. \tag{1.5}$$

In the Langevin dynamics the probability density function, $P_N(\mathbf{X}, t)$, may be obtained by solving (1.4), a stochastic differential equation. However, for interacting particles (1.4) becomes nonlinear in terms of $\mathbf{X}$ due to interaction terms, making theoretical progress very difficult.

The alternative approach to study the dynamics of colloids is by equations of motion for probability density functions in phase space, which is given below (some parts of the descriptions presented in this section closely follow the text by Dhont [5]). Consider an arbitrary volume painted in phase space, $\mathcal{W}$, and let $\partial\mathcal{W}$ be the closed boundary of $\mathcal{W}$ as shown in figure 1.1(b). The conservation equation for the number of points within $\mathcal{W}$ is written as

$$-\oint_{\partial\mathcal{W}} \mathbf{U}^G(\mathbf{X}) \cdot d\mathbf{S} = \frac{\partial}{\partial t} \int_{\mathcal{W}} P_N(\mathbf{X}, t) d\mathbf{X}. \tag{1.6}$$

where $d\mathbf{S}$ is the surface vector element with the dimension $3N - 1$ pointing outward

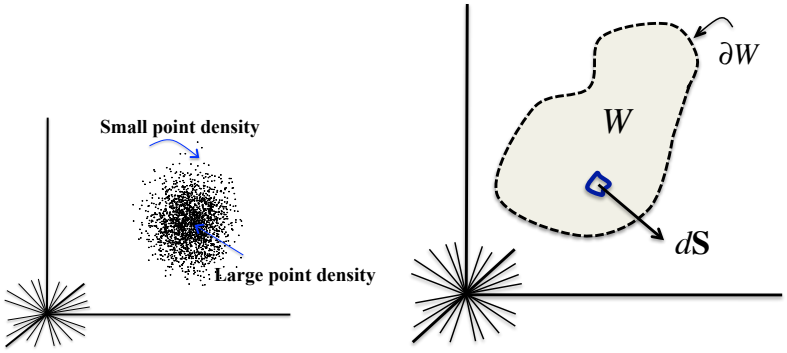

(a) (b)

Figure 1.1: (a) Different microscopic states of a suspension in $3N$ dimensional phase space, schematically shown by multiple axes; each point presents a microstate and, (b) the arbitrary control volume, $\mathcal{W}$, the bounded volume surface, $\partial\mathcal{W}$, and the related surface element $d\mathbf{S}$ in (1.6).

and normal to $\partial\mathcal{W}$. The surface integral on the right hand side of (1.6) presents the flux through the boundaries and the volume integral is the accumulation/consumption of points in the volume. Using the divergence theorem (1.6) simplifies to

$$\frac{\partial P_N(\mathbf{X},t)}{\partial t} = \nabla_{\mathbf{X}} \cdot \big(\mathbf{U}^G(\mathbf{X}) P_N(\mathbf{X},t)\big). \tag{1.7}$$

Recall that $\mathbf{U}^G = \mathbf{U}_c + \mathbf{U}^B$ where $\mathbf{U}_c$ is the average velocity by which the particles are convected and $\mathbf{U}^B$ is the fluctuating velocity induced by Brownian forces. Assuming that the probability distribution function obeys Boltzmann distribution at equilibrium, $P_N(\mathbf{X}) \propto \exp(-\nabla_{\mathbf{X}}\Phi(\mathbf{X})/k_bT)$, it is straightforward to show that $\mathbf{U}^B = k_bT\mathbf{M}^{UF}\nabla P_N/P_N$ which modifies (1.7) to Smoluchowski probability density balance equation:

$$\frac{\partial P_N}{\partial t} = \nabla_{\mathbf{X}} \cdot \Big[\mathbf{U}_c P_N - k_bT\mathbf{M}^{UF} \cdot \nabla P_N\Big]. \tag{1.8}$$

The first term on the right hand side of (1.8) is the probability flux associated with the average motion of the particles and the second term describes the diffusive flux

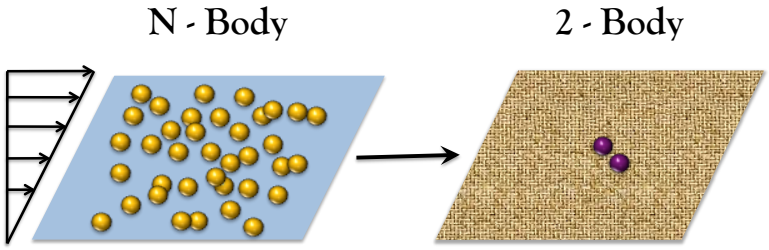

Figure 1.2: A physical illustration of reducing the N-particle suspension, described by the N-particle SE (1.8), to a pair dispersed in a mean-field, described by pair SE, (1.9).

induced by Brownian fluctuations. A similar balance is commonly observed in problems involved in transport phenomena including heat and mass transfer which directs us to this observation: The evolution of shear-induced microstructure can be viewed as the transport of probability where the structure in set by interplay between the convective and the dispersive flux.

Pair Smoluchowski equation

The Smoluchowski equation given in (1.8) is in $3N$-dimensional space and must be reduced for analytical progress. In almost all theories based on Smoluchowski equation, two particles in the suspension are "fixed" (i.e., of known positions, but still moving) and (1.8) is integrated over all possible configurations of the remaining $N-2$ particles. Physically, a dispersion of N particles in a fluid is replaced with a pair dispersed in a mean-field that contains the dynamical effect of the $N-2$ "*bath*" particles. A schematic illustration of this reduction is given in figure 1.2. After appropriate manipulations and assumptions (described in detail in Chapter 2), (1.8) reduces to pair Smoluchowski equation

$$\frac{\partial g(\mathbf{r},t)}{\partial t} = \nabla_{\mathbf{r}} \cdot \Big[\mathbf{U} g(\mathbf{r},t) - \mathbf{D} \cdot \nabla g(\mathbf{r},t)\Big], \tag{1.9}$$

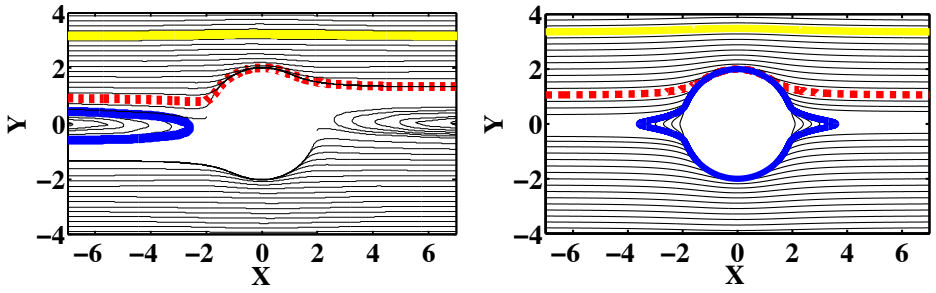

(a) $\phi = 0.2$, $Pe = 1000$, ASD (b) Isolated pair

Figure 1.3: Average pair trajectories in shear plane, (a) ASD simulation for $\phi = 0.20$ and $Pe = 1000$ and (b) isolated pair.

where $\mathbf{r}$ is the relative separation vector between the selected pair, and $\mathbf{U}(\mathbf{r})$ and $\mathbf{D}(\mathbf{r})$ are the relative velocity and diffusivity of the pair. These quantities describe the average relative motion and dispersion around this average motion respectively. Here $g(\mathbf{r})$, the pair distribution function, is the normalized likelihood of observing a pair at $\mathbf{r}$ which is the microstructural quantity eventually computed from the theory by solving (1.9).

The effect of interactions of bath particles on the dynamics of pair motion is embedded in $\mathbf{U}$ and $\mathbf{D}$. In the dilute theories, interactions only to two particle level are considered and interactions of the pair with bath particles are neglected. In this limit the relative velocity and diffusivity are well-known for all pair separations [30] and $g(\mathbf{r})$ can be computed by solving the convection-diffusion equation in (1.9) with the proper boundary conditions [28]. Note that for dilute suspensions, the dispersion around the pair motion is induced only by Brownian fluctuations and thus the ratio of convection to diffusion flux scales as Pe. The key question is how do the bath particle interactions with the pair modify the dynamics, specifically $\mathbf{U}$ and $\mathbf{D}$?

To display the effect of bath particle interactions on $\mathbf{U}$, in figure 1.3 the well-known relative trajectory of an isolated pair (no bath particle interactions) is compared against the pair trajectory lines obtained from sampling Accelerated Stokesian Dynamics (ASD) [31] simulation results at $\phi = 0.20$ and $Pe = 1000$ (thermal fluctuations have negligible

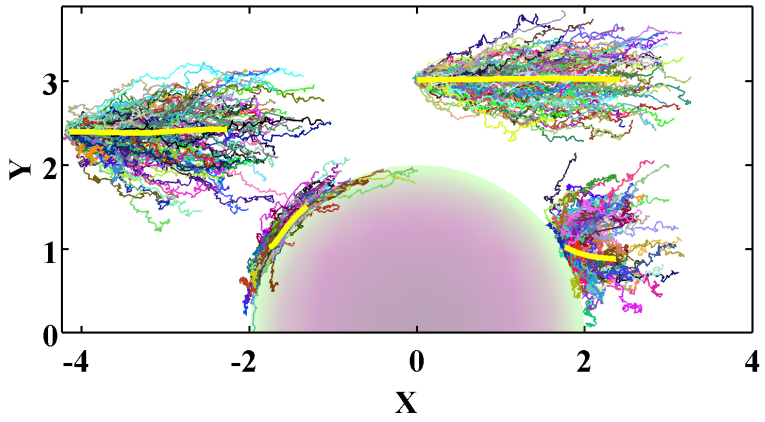

Figure 1.4: Dispersion of pair trajectories for different starting points in shear plane obtained by sampling the configuration from ASD simulation for $\phi = 0.40$ and $Pe = 10$. The thick lines are the average trajectories and the average motion is from left to right along these trajectories.

effect on trajectories) in the shear plane. An explanation of the simulation method and the background literature is given in §2.5. The separation vector is normalized by the particle radius and the circle in the figures is the excluded volume region for two particles. Note that the trajectory lines for $\phi = 0.20$ are dramatically different from the isolated pair, indicating that bath particles interactions have a determining role on the average pair dynamics even at volume fractions as low as $\phi = 0.20$.

Many-body interactions in sheared suspensions also change the characteristics of the dispersion around the average relative motion. This is visualized in figure 1.4, where different pair trajectories all starting at the same relative separations in the shear plane are presented from ASD samplings of a sheared hard-sphere suspension with $\phi = 0.40$ and $Pe = 10$. We can see that the dispersion is of the same order of magnitude as the average motion (illustrated by thick lines) even though the Brownian motion is an order of magnitude smaller than the shear flow ($Pe = 10$). This is a clear indication that the dispersion is proportional to the strength of the imposed flow, $\mathbf{D}^{\dot{\gamma}} \sim \dot{\gamma} a^2$, and significantly larger than the Brownian diffusion at $Pe \gg 1$.

In dilute theories, the volume fraction is arbitrarily small, allowing a pair of particles to

be assumed isolated. Thus the pair of interest does not interact with any other particles: hence $\mathbf{D}^{\dot{\gamma}}$ is neglected. In near-equilibrium theories, since $Pe \ll 1$ and the shear-induced motion is thus small relative to thermal motion, the shear-induced dispersive effects can be neglected. However, in semi-dilute to concentrated suspensions, the dispersion at $Pe \gg 1$ is dominated by hydrodynamic interactions of the pair with bath particles. Thus it is essential to include shear-induced diffusion in the theory to be able to give predictions of microstructure at $Pe \gg 1$ and $\phi \geq 0.15$. The success of the theory in the predictions of microstructure and non-Newtonian rheology is determined by how accurately the many-body interactions are captured in the formulation of $\mathbf{U}$ and $\mathbf{D}$, and this will be the primary topic in the following chapters.

1.3 Outline

The detailed formulation of the theory and the essential ideas and assumptions are outlined in Chapter 2. The remaining Chapters discuss problems related to different extensions of this theory (Chapters 3, 5 and 6) and give a more detailed analysis of it (Chapter 4). We compute the pair distribution function, $g(\mathbf{r})$, over a range of Pe and $0.20 \leq \phi \leq 0.55$ by numerically solving the pair Smoluchowski equation (SE) in the form of an integro-differential convection-diffusion equation. The integral aspect models the many-body interactions enabling the theory to be extended to concentrated dispersions. Hydrodynamic interactions are assumed to be pairwise additive due to the dominant role of lubrication interactions in sheared suspensions. One novel feature of the theory is modeling the shear-induced dispersion using a diffusion flux. Including this dispersion is essential for the success of the theory at $Pe > 1$ and large ϕ. A simple model is considered for the shear-induced relative diffusivity in pair SE based on the understanding of dynamics of two particles very near contact and when they are well-separated. The formulation is derived for suspensions with any type of conservative potential but the results are only presented for "nearly hard-sphere" suspensions.

The predicted $g(\mathbf{r})$ is then used to compute the rheology. To evaluate the predictions, they are compared against discrete particle simulations by ASD. The predictions of microstructure and rheology are in generally good agreement with simulation results. Systematic discrepancies between simulation and theory are also observed and the possibilities resulting in these deviations from simulation are discussed. In Chapter 4, we revisit these limitations and make modifications to the basic theory.

In Chapter 3, we describe the structure and rheology of colloidal suspensions of particles interacting by an extended range repulsive potential, as a model for colloidal particles with surface charges. The predictions are compared against ASD simulations with different pair potential steepness over a wide range of Pe. The primary goal of this chapter is to evaluate the general validity of the theory for suspensions with interparticle interactions other than hard-sphere. Through both simulation and theory we also seek to gain further understanding on the evolution of microstructure and non-Newtonian rheology in soft repulsive colloidal dispersions under shear. In particular we discuss the shear-induced ordering transition observed for these suspensions and how that is reflected in the theory.

The fourth chapter takes a closer look at the theoretical framework developed in Chapter 2. We investigate the dynamics of the motion of a pair in a sheared suspension through studying the variables in the pair SE, i.e. average relative velocity and relative diffusivity. This chapter starts with a brief review of the theory and a new formulation is proposed for relative hydrodynamic velocity based on the pairwise summation of velocities instead of forces. Also using ASD simulation results, a slightly modified formulation is proposed for shear-induced relative diffusivity. These modifications result in a notable improvement in the agreement between theory and simulation for both pair microstructure and rheology.

The remainder of Chapter 4 focuses on average pair relative motion and dispersion around this average motion. The average pair trajectories obtained from sampling ASD

simulation results are compared against the predictions of the theory for a range of ϕ and large Péclet numbers. The most important observation is that, for both theory and simulation, at volume fractions as low as $\phi = 0.20$ the many-body interactions of the pair with bath particles induce a remarkably different trajectory field than the isolated pair trajectory field (no interactions with bath particles). To gain further insight about shear-induced diffusion, we analyze the variations of dispersion around average trajectory and relative velocity fluctuation fields obtained from sampling ASD over the pair space for varying ϕ at large Pe.

In Chapter 5, we use the theoretical framework for sheared suspensions to develop a microstructural theory for active microrheology. Specifically, we study the motion of a spherical probe pulled through the suspension with a constant force or constant velocity. The apparent viscosity of the suspension is then determined by use of Stokes drag law: $\mathbf{F} = 6\pi\eta_{micro}\mathbf{U}a$ with $\eta_{micro}/\eta = \mathbf{R}^{FU}/R_0$ where $R_0 = 6\pi\eta a$ is the resistance to motion of a single particle in a fluid and $\mathbf{R}^{FU}$ is the resistance tensor of the probe which is set by the distribution of suspension particles around it. This is determined in the theory through solving the pair Smoluchowski equation in terms of $g(\mathbf{r})$, defined in this cases as the likelihood of having a particle around the probe at the relative distance of $\mathbf{r}$. We focus on two scenarios of pulling the probe: constant force (allowing the probe to change path) and constant velocity (fixing the probe trajectory). We limit our analysis to hard-sphere suspensions and study microstructure and rheology over a wide range of Pe and ϕ.

The last chapter presents preliminary results related to two problems. First we study the structure and rheology of non-Brownian suspensions ($Pe \to \infty$), opening the possibility of applying this theory to non-Brownian suspension with different types of interparticle interactions such as contact or friction models. The predictions of rheology for hard-sphere suspensions at $Pe \to \infty$ are compared against ASD results at $Pe = 1000$ for $0.20 \leq \phi \leq 0.50$. We then investigate the rheology for general linear kinematics. This

is the essential step in moving towards a constitutive equation and opens an avenue to predicting suspension flows in complex geometries.

2 Smoluchowski theory for sheared colloidal dispersions [1]

2.1 Introduction

Colloidal suspensions can be found in a wide range of applications and natural flows including processing of cement and foodstuffs or flow of mud [4, 33]. Colloidal suspensions, also called dispersions, are complex fluids. These materials are distinct from simple fluids because the relative arrangement of the constituents, commonly referred to as microstructure, is determined by the interplay of particle scale forces with the motion imposed by macroscopic flow. A consequence of this coupling is that the properties become flow-rate dependent. Of these properties, we will be particularly interested in the rheology. Examples of complex fluids include well-known non-Newtonian materials such as polymeric liquids and gels, in addition to colloidal suspensions.

We have a substantial theoretical understanding of the transport properties of simple liquids because these are determined primarily by equilibrium microstructure, for which experimental and theoretical understanding is well-developed [17]. By contrast, the theoretical foundations for complex fluid rheology are incomplete, and the task is substantially more demanding than in the case of simple fluids. For complex fluids, the *nonequilibrium* microstructure must be determined for any condition (rate and composition), and then related through structure-property relations to the rheological properties.

[1] The contents of this chapter are published as a paper in *Journal of Fluid Mechanics* [32].

This work describes a theoretical framework to determine the microstructure of colloidal suspensions, and demonstrates its application to prediction of the bulk rheological properties of the mixture. We consider here the hard-sphere colloidal suspension, arguably the simplest complex fluid and thus a material for which a theory of some completeness is possible. The simplicity arises from the small number of parameters necessary to characterize the conditions. Because the size of the dispersed particles, a, is typically 10 nm to 1 μm, the particle scale Reynolds number satisfies $Re_p = \rho\dot{\gamma}a^2/\eta \ll 1$, which implies that inertial effects at the particle scale can typically be neglected in colloidal dispersions. Thus the dynamics may be assumed to take place at $Re_p = 0$; here we specify a as the particle radius, η is the fluid viscosity, and $\dot{\gamma}$ is the shear rate of the flow. Restricting attention to monodisperse spherical particles, the microstructure and properties of the hard-sphere dispersion in simple-shear flow can be expressed as functions of only two dimensionless parameters, one being the volume fraction of the solid phase, $\phi = 4\pi na^3/3$ where n is the particle number density, and the other the Péclet number, $Pe = \dfrac{6\pi\eta\dot{\gamma}a^3}{k_bT}$, which is the ratio of hydrodynamic (viscous) forces to Brownian forces where k_b is the Boltzmann constant and T is the absolute temperature. At $Pe = 0$, the dispersion is at equilibrium, while $Pe \to \infty$ refers to the limit where the structure and rheology are governed by hydrodynamics. For computational ease, we find it necessary to include a short-ranged repulsive force and it is more appropriate to describe the system studied here as a "nearly hard-sphere" dispersion. Such forces have been shown to be critical to overcome jamming in concentrated noncolloidal suspensions of smooth spherical particles [34], while the breaking of symmetry of the Stokes-flow interactions was shown to overcome the singular limit of purely hydrodynamic interactions of smooth particles by Brady & Morris [27], giving rise to self-diffusion and normal stresses as observed in experiment.

Despite their simplicity, nearly hard-sphere dispersions show rich non-Newtonian rheological behaviors including shear thinning at low shear rates, shear thickening at high

shear rates, and normal stress differences. These behaviors are seen in both experiments [35, 36] and simulations [37]. The microstructure and resulting rheology of colloidal dispersions is of importance in describing such flow behaviors as shear-induced migration [38, 39] and abrupt shear thickening [40] and flow-induced jamming.

Simulation techniques such as Stokesian Dynamics (SD), which accurately capture the near-field lubrication interactions and far-field hydrodynamic interactions in sheared colloidal suspensions, allow investigation of the microstructure and rheology with valuable insight to the role of Brownian, hydrodynamic and interparticle forces on the dynamics of the dispersed phase and its impact on rheology [29, 41]. While the level of detail is not yet comparable to simulation, microscopy [42] and scattering studies [43] provide experimental measures of the relative distribution of particles. Theoretical study of the microstructure in sheared suspensions has made significant progress since the pioneering work of Batchelor & Green [44, 45], but any theoretical formulation to date has been severely limited in its range of validity. The existing theories tend to explore either near-equilibrium conditions, i.e. $Pe \ll 1$, for which concentrated conditions have been studied [26, 24, 46], or dilute conditions, $\phi \ll 1$ where both $Pe \ll 1$ and $Pe \gg 1$ have been considered [47, 27, 28]. This work utilizes certain elements of each of these groups of studies, in combination with essential novel features motivated by theory for the equilibrium liquid state, to provide a formulation describing the nonequilibrium response of colloidal dispersions over a wide range of ϕ and Pe.

Near-equilibrium structure developed in weak shear flow remains predominately controlled by thermal forces and excluded volume. Therefore, theories in this limit are often based in liquid-state theory. In these works, the many-body thermodynamic coupling is modeled through the well-known integral equation formulations in liquid-state theory while the role of hydrodynamics has been either neglected [25] or approximated through simple mean-field arguments and near contact lubrication interactions [24]. Comparison with the available experimental data shows that the predictions are primarily controlled

by the method used to account for thermodynamic coupling, while different approximations of hydrodynamic functions are found to have a minor influence. These results are limited to $Pe \ll 1$, and have not been extended to $Pe \geq 1$ where hydrodynamics becomes a controlling factor. The integral equation approaches, so successful for the equilibrium liquid state, are not readily extended to far-from-equilibrium conditions, but an underlying concept of these methods – namely that of coupling direct and indirect interactions – is utilized in our integro-differential formulation of the Smoluchowski equation (SE) for the pair structure. The essential feature which makes the pair SE appropriate for general flow conditions is that it represents a balance of the different and competing fluxes of pair probability, and thus flow is naturally captured. This is quite different from the relation of direct and indirect interactions appearing in such closures as the Percus-Yevick and hypernetted chain approximations [17] for equilibrium structure.

The primary challenges in describing concentrated suspension microstructure at the pair level are to handle the many-body interaction, and to couple appropriately to the 'bath' representing the influence of the other particles under flow conditions. This intrinsically raises two basic issues, one being the need to relate the pair distribution function to the triplet distribution, say $g_3(\mathbf{r}, \mathbf{r}_{13})$, and higher particle-number distributions. The second is how to handle hydrodynamic interactions. We address both of these essential difficulties in the present work. The closure of the hierarchy involving g_3 is made using a modification of the Kirkwood superposition approximation, and more is detailed regarding the hydrodynamic interactions just below.

The problems associated with many-body hydrodynamics can be eliminated in dilute colloidal suspensions where interactions of more than two particles are assumed negligible. This allows one to use isolated pair hydrodynamic functions, and shear-induced diffusion is negligible. These dilute theories provide an understanding of the nature of anisotropic pair structure and the consequent nonlinear rheology observed at $Pe \gg 1$. Brady & Morris [27] showed analytically that at $Pe \gg 1$ there is a singular influence

of short-ranged interparticle forces, as these break the pair microstructural symmetry associated with Stokes flow, leading to normal stress differences which do not vanish as $Pe \to \infty$. The pair structure becomes highly anisotropic, and develops a boundary layer in $g(\mathbf{r})$ near contact where convection balances diffusion. Bergenholtz et. al. [28] solved the dilute pair SE for simple-shear flow numerically over a wide range of Pe, and showed the development of the wake corresponding to the noted boundary layer. They were able to predict shear thinning at low Pe and shear thickening at large Pe, as well as a change in sign of the first normal stress difference with increase of Pe, as also seen in simulations at elevated ϕ.

Thus certain behavior in more concentrated suspensions is captured by dilute theories, but much is not properly captured. Attempts to extend the dilute theories to higher ϕ through scaling analysis [27, 37] assume that the effective mean-field outside the boundary layer can be represented by a uniform fluid with modified viscosity scaling as high frequency viscosity, $\eta_\infty(\phi)$ at the desired ϕ. However, detailed study of $g(\mathbf{r})$ from SD simulations at $Pe = 1$ – 1000 by Morris & Katyal [48] shows that the microstructural anisotropy changes qualitatively as ϕ increases at fixed Pe. Specifically, at large Pe, the maximum value of $g(\mathbf{r})$ shifts from being near the compressional axis for $\phi \leq 0.3$ to along the flow direction for $\phi \geq 0.35$; this is reflected in rheology significantly differing from what one would predict using the scaling arguments. These rheological changes are most pronounced in the highly structurally dependent normal stress differences. This shows the need for a detailed treatment of the structure at large ϕ in sheared dispersions.

The present formulation provides a self-consistent method for modeling many-body hydrodynamic interactions in concentrated suspensions at $Pe \gg 1$ and the resulting rheology. The theory is motivated by the observation that particles near contact control the properties and dynamics in concentrated sheared suspensions. This point was used by Lionberger & Russel [24], who proposed different approximations of hydrodynamic functions based on mean-field arguments and near contact lubrication interactions. The

present theory of the microstructure is built on the assumption that short-range lubrication interactions determine the dynamics of particles, and on the recognition that shear-induced diffusion plays an important role in setting the microstructure. The formulation developed here can, in principle, be applied over the entire range of Pe and ϕ, although here we limit the investigation to $Pe \leq 100$ and $0.1 \leq \phi \leq 0.55$. The resolution of current experimental techniques is not high enough to probe the details of microstructure, and as an alternative we compare predictions of the theory with results of our own Accelerated Stokesian Dynamics [41, 31] simulations.

The paper begins in §2.2 with the formulation of the problem, and elaborates the steps taken to arrive at a closed integro-differential Smoluchowski equation for the pair distribution function, $g(\mathbf{r})$. This is followed, in §2.3, by the description of the particle stress contributions in terms of the pair microstructure. The solution technique for the microstructure equation is presented in §2.4. As the methods are well-known, we give only a brief outline of the simulation technique used, with this appearing in §2.5. Predictions of microstructure and rheology at various Pe and ϕ, and their comparison with simulations, are given in §2.6.1 and §2.6.2, respectively.

2.2 Microstructure

2.2.1 Smoluchowski equation of motion

We consider suspensions at very small particle-scale Reynolds number, so that inertia is negligible and the motion can be described by Stokes equations. The microstructure is assumed to be governed by the Smoluchowski equation, which for the N-particle configuration space is written

$$\frac{\partial P_N}{\partial t} + \sum_{\alpha=1}^{N} \nabla_\alpha \cdot \mathbf{j}_\alpha = 0, \tag{2.1}$$

where $P_N(\mathbf{x}_1, \mathbf{x}_2, ..., \mathbf{x}_N)$ is the N-particle configurational probability distribution, and $\mathbf{j}_\alpha$ is the probability flux associated with particle α. The flux is expressed as

$$\mathbf{j}_\alpha = \left(\mathbf{U}_\alpha^H + \sum_{\beta=1}^{\beta=N} \mathbf{M}_{\alpha\beta}^{FU} \cdot \mathbf{F}_\beta \right) P_N - \sum_{\beta=1}^{\beta=N} \mathbf{D}_{\alpha\beta} \cdot \nabla_\beta P_N, \tag{2.2}$$

where $\mathbf{U}_\alpha^H$ is the velocity of particle α induced both by bulk flow and by hydrodynamic interactions with other particles, $\mathbf{M}_{\alpha\beta}$ is the mobility of particle α to a force on particle β, and $\mathbf{D}_{\alpha\beta} = k_b T \mathbf{M}_{\alpha\beta}^{UF}$ is the diffusion tensor. The force exerted on particle β may be expressed in terms of the gradient of an interparticle potential energy as $\mathbf{F}_\beta = -\nabla_\beta V$.

To reduce to an equation for the pair microstructure, (2.1) is integrated over all possible configurations of $N-2$ particles keeping two particles fixed, which yields for the steady state of interest

$$\nabla_1 \cdot \langle\, \mathbf{j}_1 \,\rangle_2 + \nabla_2 \cdot \langle\, \mathbf{j}_2 \,\rangle_2 = 0, \tag{2.3}$$

where $\langle \quad \rangle_2$ is defined by

$$P_2 \langle\, A \,\rangle_2 (\mathbf{x}_1, \mathbf{x}_2) = N(N-1) \int A(\mathbf{x}_1, \mathbf{x}_2, ..., \mathbf{x}_N) P_N d\mathbf{x}_3 d\mathbf{x}_4 ... d\mathbf{x}_N, \tag{2.4}$$

where $P_2(\mathbf{x}_1, \mathbf{x}_2) d\mathbf{x}_1 d\mathbf{x}_2$ is the likelihood of having a particle between $\mathbf{x}_1$ and $\mathbf{x}_1 + d\mathbf{x}_1$ and a second particle between $\mathbf{x}_2$ and $\mathbf{x}_2 + d\mathbf{x}_2$. Expressed in terms of the relative position vector, $\mathbf{r} = \mathbf{x}_2 - \mathbf{x}_1$, (2.3) simplifies to

$$\nabla_{\mathbf{r}} \cdot \langle \mathbf{j}_2 - \mathbf{j}_1 \rangle_2 = 0, \tag{2.5}$$

where $\nabla_{\mathbf{r}}$ is the gradient with respect to $\mathbf{r}$. Applying (2.2) to (2.5) yields

$$\nabla_{\mathbf{r}} \cdot \Bigg[\langle\, \mathbf{U}^H \,\rangle_2 P_2 \;+\; \langle \mathbf{M} \cdot \mathbf{F} \rangle_2 P_2 - \langle \mathbf{D} \rangle_2 \cdot \nabla_{\mathbf{r}} P_2 \;+\; \int \Big(\big\langle \big(\mathbf{M}_{23} - \mathbf{M}_{13} \big) \cdot \mathbf{F}_3 \big\rangle_3 P_3 - \langle \mathbf{D}_{23} - \mathbf{D}_{13} \rangle_3 \cdot \nabla_3 P_3 \Big) d\mathbf{x}_3 \Bigg] = 0, \tag{2.6}$$

with

$$\mathbf{U}^H = \mathbf{U}_2^H - \mathbf{U}_1^H, \tag{2.7a}$$

$$\mathbf{D} = 2\big(\mathbf{D}_{11} - \mathbf{D}_{12} \big), \tag{2.7b}$$

$$\mathbf{M} = 2\big(\mathbf{M}_{11}^{UF} - \mathbf{M}_{12}^{UF} \big) = 2\big(\mathbf{R}_{11}^{FU} - \mathbf{R}_{12}^{FU} \big)^{-1}, \tag{2.7c}$$

and

$$\mathbf{F} = \frac{\mathbf{F}_2 - \mathbf{F}_1}{2}. \tag{2.7d}$$

Here, $\mathbf{R}^{FU}$ is the resistance tensor coupling velocity to force, with the subscript 12 indicating this is the coupling of the force on particle 1 due to motion of particle 2. The integral term in (2.6) is the additional flux induced by the forces on the other $N-2$ particles. The probability of finding a third particle between $\mathbf{x}_3$ and $\mathbf{x}_3 + d\mathbf{x}_3$ when particles 1 and 2 lie between $\mathbf{x}_1$ and $\mathbf{x}_1 + d\mathbf{x}_1$ and $\mathbf{x}_2$ and $\mathbf{x}_2 + d\mathbf{x}_2$, respectively, is given by $P_3 d\mathbf{x}_1 d\mathbf{x}_2 d\mathbf{x}_3$. The mean relative velocity $\langle\, \mathbf{U} \,\rangle_2$ is obtained by averaging the relative velocity of the pair at each $\mathbf{r}$, over all configurations of the remaining $N-2$ particles.

The relative velocity in each configuration fluctuates around the average value and the velocity fluctuations result in a dispersion process. In a quiescent state, associated with an equilibrium structure, Brownian velocity fluctuations drive the dispersion captured as a diffusion represented by the well-known Stokes-Einstein relationship: $\mathbf{D}_{\alpha\beta} = k_b T \mathbf{M}_{\alpha\beta}^{UF}$. Shear flow also drives a random walk which may be described as a diffusion; this phenomenon is known as shear-induced diffusion [49, 50]. While Brownian diffusion is pro-

portional to the thermal energy of the system, k_bT, shear-induced diffusion scales with the shear rate, and is thus the dominant diffusion mechanism at elevated shear rates, i.e. at large Pe. To formulate a predictive theory for the microstructure and rheology of a concentrated dispersion at $Pe > 1$, it is found to be essential to include the shear-induced diffusion, as we will illustrate in the results section. However, as seen in (2.6), systematic integration of the Smoluchowski equation does not take into account the time correlation of shear induced velocity fluctuations and the resulting *shear-induced relative diffusion* between a pair of particles. We note that there is no prior published work addressing the shear-induced relative diffusion, which we incorporate as

$$\langle \mathbf{D} \rangle_2 = k_bT \langle \mathbf{M} \rangle_2 + \langle \mathbf{D}^{\dot{\gamma}} \rangle_2, \tag{2.8}$$

where $k_bT \langle \mathbf{M} \rangle_2$ is the Brownian diffusion and $\langle \mathbf{D}^{\dot{\gamma}} \rangle_2$ is the shear-induced diffusion, whose functional form will be discussed below.

The combined force and torque balance for non-Brownian particles interacting only through hydrodynamics can be formulated as

$$\mathbf{R}^{FE} : \mathbf{E}^{\infty} - \mathbf{R}^{FU} \cdot \left(\mathbf{U}^H - \mathbf{U}^{\infty} \right) = 0. \tag{2.9}$$

Here $\mathbf{E}^{\infty} = (\nabla \mathbf{U}^{\infty} + \nabla \mathbf{U}^{\infty T})/2$ is the strain rate tensor with $\mathbf{U}^{\infty}$ being the imposed flow, here simple shear. The resistance functions, $\mathbf{R}^{FE}$ (coupling force and torque to a bulk straining motion) and $\mathbf{R}^{FU}$ (coupling force and torque to velocity), are functions of the N-particle configuration. For an isolated pair of spheres, the resistance tensors are well-known [30], and are only a function of the pair separation vector, $\mathbf{r}$. Following (2.9), the relative pair velocity can be written

$$\mathbf{U}^H_{\alpha} = \mathbf{U}^{\infty}_{\alpha} + (\mathbf{R}^{FU})^{-1} \cdot \left(\mathbf{R}^{FE} : \mathbf{E}^{\infty} \right)_{\alpha}, \tag{2.10}$$

where α labels the particle of interest. By contrast, with no hydrodynamic interactions,

the relative translational/angular pair velocity in a suspension with an external flow and interparticle forces is

$$\mathbf{U}_\alpha^H = \mathbf{U}_\alpha^\infty + (\mathbf{R}^{FU})^{-1} \cdot \mathbf{F}_\alpha, \tag{2.11}$$

where $\mathbf{R}^{FU} = 6\pi\eta a\mathbf{I}$ is simply a Stokes drag coefficient for this case, and here $\mathbf{F}^\alpha$ includes both force and torque.

Comparing (2.10) and (2.11) reveals a similarity. The force, $\mathbf{F}_\alpha$, is replaced by $(\mathbf{R}^{FE} : \mathbf{E}^\infty)_\alpha$ in (2.10). Hydrodynamic interactions may thus be thought of as a composition of two generally opposing forces: (1) the external force that drives the suspension flow and gives rise to velocity $\mathbf{U}_\alpha^\infty$, and (2) the resisting force that imposes the effect of excluded volume through fluid/particle interaction, $\mathbf{R}^{FE} : \mathbf{E}^\infty$. When no other forces are present, these forces must be equal and opposite to yield a force-free (and torque-free) motion. We call the second of these forces the *lubrication force*, $\mathbf{F}^{lub} = \mathbf{R}^{FE} : \mathbf{E}^\infty$, to indicate the dominant influence of lubrication interactions for the conditions we will study. Including the known pair resistance functions, the lubrication force that particle 2 applies on particle 1 for an isolated pair is

$$\mathbf{F}_{21}^{lub} = 6\pi\eta a\Big[X(r)(\hat{\mathbf{r}} \cdot \mathbf{E} \cdot \hat{\mathbf{r}})\hat{\mathbf{r}} + Y(r)\big(\mathbf{E} \cdot \hat{\mathbf{r}} - (\hat{\mathbf{r}} \cdot \mathbf{E} \cdot \hat{\mathbf{r}})\hat{\mathbf{r}}\big)\Big]. \tag{2.12}$$

Limiting values of the radially-dependent functions are [30]

$$X(r) = \epsilon^{-1} \quad r \to 2, \quad X(r) = \frac{5}{r^2} \quad r \gg 1,$$

$$Y(r) = 0.271\ln(\epsilon^{-1}) \quad r \to 2, \quad Y(r) = \frac{16}{3r^4} \quad r \gg 1,$$

where $r = |\mathbf{r}|/a$, $\hat{\mathbf{r}} = \mathbf{r}/r$ and $\epsilon = r/a - 2$. The first term on the right hand side of (2.12) is the lubrication force along the line of centers, and the second term is the force in the plane normal to the line of centers, i.e. the local $\hat{\theta} - \hat{\varphi}$ plane. The definitions of angles and directions in relation to the shear flow are shown in figure 2.1.

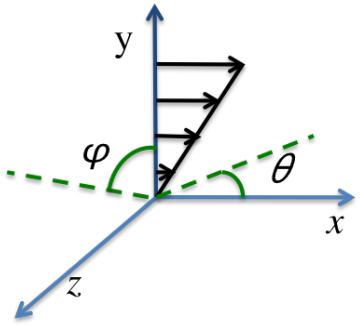

Figure 2.1: Angle definitions defined in a simple-shear flow $u_x(y)$: $0 \leq \theta \leq 2\pi$ is the azimuthal angle measured clockwise from the positive x axis, and $-\pi/2 \leq \varphi \leq \pi/2$ is the polar angle measured from $x - y$ plane.

Recall that the lubrication force is repulsive in case of particles approaching, and is attractive while they are being separated. Integrating (2.10) to the pair level yields

$$\left\langle \mathbf{U}^H \right\rangle_2 = \mathbf{U}^\infty + \left\langle \mathbf{M} \cdot \mathbf{F}^{lub} \right\rangle_2 . \tag{2.13}$$

We may write

$$\langle \mathbf{M} \cdot \mathbf{F} \rangle_2 = \langle \mathbf{M} \rangle_2 \cdot \langle \mathbf{F} \rangle_2 + \langle \mathbf{M}' \cdot \mathbf{F}' \rangle_2, \tag{2.14}$$

where $\mathbf{M}'$ and $\mathbf{F}'$ are fluctuations of mobility and forces around their average value. We now make a mean-field approximation by assuming that the pair is immersed in a field that contains the average effect of the bath of the other particles. We assume that the convective flux is determined only by the average values of force, $\langle \mathbf{F} \rangle_2$, and mobility, $\langle \mathbf{M} \rangle_2$, and the fluctuations, $\langle \mathbf{M}' \cdot \mathbf{F}' \rangle_2$, do not result in a net convective flux. However these fluctuations result in a dispersive flux which is modeled here through shear-induced relative diffusion, $\langle \mathbf{D}^{\dot{\gamma}} \rangle_2$ in (2.8), so that we replace (2.14) by

$$\langle \mathbf{M} \cdot \mathbf{F} \rangle_2 \, g \; = \; \langle \mathbf{M} \rangle_2 \cdot \langle \mathbf{F} \rangle_2 \, g \; - \; \langle \mathbf{D}^{\dot{\gamma}} \rangle_2 \cdot \nabla_{\mathbf{r}} g. \tag{2.15}$$

Note that a general dispersion process may not always be formulated using a diffu-

sion model. The form chosen here, as judged by the results presented later in this work, provides a reasonable representation of the influence of trajectory dispersion on microstructure.

The mean-field approach applied here, which is expected to be valid if the suspension is not near maximum packing, allows the integral term in (2.6) to be modified as follows:

$$\int \Big(\big\langle \left(\mathbf{M}_{23} - \mathbf{M}_{13}\right) \cdot \mathbf{F}_3 \big\rangle_3 P_3 - \big\langle \mathbf{D}_{23} - \mathbf{D}_{13} \big\rangle_3 \cdot \nabla_3 P_3 \Big) d\mathbf{x}_3 \approx \tag{2.16}$$
$$\Big(\int \big\langle \mathbf{M}_{23} - \mathbf{M}_{13} \big\rangle_3 P_3 d\mathbf{x}_3 \Big) \Big(\int \langle \mathbf{F}_3 \rangle_3 P_3 d\mathbf{x}_3 \Big) - \Big(\int \big\langle \mathbf{D}_{23} - \mathbf{D}_{13} \big\rangle_3 P_3 d\mathbf{x}_3 \Big) \Big(\big\langle \nabla_3 \ln(P_3) \big\rangle_3 P_3 d\mathbf{x}_3 \Big) = 0,$$

where the integrals one the second line are identically zero, based on pair-particle symmetry. After including lubrication forces, and applying the mean-field assumption, (2.6) is modified to

$$\nabla_{\mathbf{r}} \cdot \left(\mathbf{U}^{\infty} g + \langle \mathbf{M} \rangle_2 \cdot \left(\langle \mathbf{F}^{HS} \rangle_2 + \langle \mathbf{F}^{lub} \rangle_2 \right) g - \langle \mathbf{D} \rangle_2 \cdot \nabla_{\mathbf{r}} g \right) = 0, \tag{2.17}$$

where $\mathbf{F}^{HS}$ represents forces due to potential interaction, and $g = P_2/n^2$ is the pair distribution function. Quantities are made dimensionless by scaling as follows:

$$\begin{aligned} \mathbf{r} \sim a, \quad \mathbf{D} \sim D_0, \quad \mathbf{M} \sim D_0/k_b T, \\ \mathbf{F}^{HS} \sim k_b T/a, \quad \mathbf{F}^{lub} \sim 6\pi\eta\dot{\gamma}a^2, \quad \mathbf{U}^{\infty} \sim \dot{\gamma} a, \end{aligned} \tag{2.18}$$

where $D_0 = k_b T/6\pi\eta a$. Note that lubrication force scales with $\dot{\gamma}$ while thermal forces scale with $k_b T$; hence to have $O(1)$ forces they were made dimensionless with $6\pi\eta\dot{\gamma}a^2$ and $k_b T/a$ respectively. In dimensionless form, (2.17) becomes

$$\nabla \cdot \left[\mathbf{U}^{\infty} g + \langle \mathbf{M} \rangle_2 \cdot \left(\langle \mathbf{F}^{lub} \rangle_2 + Pe^{-1} \langle \mathbf{F}^{HS} \rangle_2 \right) g - Pe^{-1} \langle \mathbf{D} \rangle_2 \cdot \nabla g \right] = 0, \tag{2.19}$$

where $\nabla = a\nabla_{\mathbf{r}}$ is the dimensionless gradient operator, and we have defined the Péclet number,

$$Pe = \frac{\dot{\gamma} a^2}{D_0} = \frac{6\pi\eta\dot{\gamma} a^3}{k_b T}. \tag{2.20}$$

The boundary conditions on (2.19) are

$$\mathbf{j_r} = 0 \quad \text{at} \quad r = 2, \tag{2.21a}$$

$$g \sim 1 \quad \text{as} \quad r \to \infty. \tag{2.21b}$$

The first boundary condition implies zero radial flux at contact.

2.2.2 Conditional Averages

In the convection-diffusion equation for the pair microstructure (2.19), the conditionally-averaged quantities $\langle \mathbf{F}^{lub} \rangle_2$, $\langle \mathbf{F}^{HS} \rangle_2$, $\langle \mathbf{M} \rangle_2$ and $\langle \mathbf{D} \rangle_2$ should be self-consistently expressed in terms of $\mathbf{r}$ and g. To determine the conditional averages requires, in principle, including many-body hydrodynamic interactions. This is intractable, and we make simplifications based on the observation from experiments and simulation that the controlling configuration in concentrated sheared colloidal suspensions is particles near contact, where lubrication interactions control the dynamics. As lubrication is intrinsically a two-body interaction, these interactions can then be assumed to be summations of individual pair lubrication interactions.

Mean forces, $\langle \mathbf{F}^{HS} \rangle_2$ and $\langle \mathbf{F}^{lub} \rangle_2$:

We begin by considering $\mathbf{F}^{HS}$ and $\mathbf{F}^{lub}$. Due to the symmetry of the pair geometry, $\langle \mathbf{F}_1 \rangle_2 = -\langle \mathbf{F}_2 \rangle_2$ for either of the HS or lub forces. Applying the assumption of pairwise additivity, $\langle \mathbf{F}_1 \rangle_2$ is formulated as

$$\langle \mathbf{F}_1 \rangle_2 g(\mathbf{r}) = \mathbf{F}_{21}(\mathbf{r}) g(\mathbf{r}) + n \int \mathbf{F}_{31}(\mathbf{r}_{31})\, g_3(\mathbf{r}, \mathbf{r}_{31}) d\mathbf{r}_{31}, \tag{2.22}$$

where $\mathbf{F}_{21}$ and $\mathbf{F}_{31}$ are forces particles 2 and 3 exert on particle 1, respectively, and $\mathbf{r}_{31} = \mathbf{x}_3 - \mathbf{x}_1$. A steep repulsion was used to model hard-sphere forces:

$$\mathbf{F}_{21}^{HS} = -F_0 \frac{\tau \exp(-\tau\epsilon)}{1 - \exp(-\tau\epsilon)} \hat{\mathbf{r}}, \quad F_0 = k_b T/a, \tag{2.23}$$

where we recall that $\epsilon = r - 2$. Larger τ results in a steeper decay of the repulsion, and we have used $\tau = 200$ for all calculations reported here. The hydrodynamic force, $\mathbf{F}^{lub}$, is defined according to (2.12).

We express the triplet distribution, g_3, in terms of the pair distribution function, g, through the superposition approximation proposed by Rice & Lekner [51], given by

$$g_3(\mathbf{x}_1, \mathbf{x}_2, \mathbf{x}_3) = g(\mathbf{r}_{21}) g(\mathbf{r}_{31}) g(\mathbf{r}_{32}) \exp\left[\tau^\star(\mathbf{r}, \mathbf{r}_{31}, \phi)\right]. \tag{2.24}$$

This closure modifies the standard Kirkwood superposition through the final exponential term which models interactions of particles 1, 2 and 3 with other particles through numerical evaluation of "irreducible cluster integrals"; Rice & Lekner[51] extended this cluster expansion to 5 particles level using a Padé expansion. We do not reproduce the full details here, but the interested reader may find these in Table 1 and equations 13 and 14 in the paper by Rice & Lekner [51]. This modified Kirkwood superposition gives very good agreement at equilibrium, $Pe = 0$, up to $\phi = 0.40$, the upper limit on ϕ for the Kirkwood superposition for the equilibrium triplet structure in hard-sphere liquids. Yurkovetzky & Morris [52] showed in their study of triplet correlation that the standard Kirkwood superposition gives a reasonable measure of triplet distribution at $Pe \gg 1$. The modified Kirkwood superposition is simple in format and gives reasonable accuracy at $Pe \ll 1$ as well; there is no obvious candidate to replace this closure for nonequilibrium conditions. Applying (2.24) in (2.22) gives

$$\langle \mathbf{F}_1 \rangle_2 = \mathbf{F}_{21}(\mathbf{r}) + n \int \mathbf{F}_{31}(\mathbf{r}_{31})\, g(\mathbf{r}_{32}) g(\mathbf{r}_{31}) \exp\left[\tau^\star(\mathbf{r}_{31}, \mathbf{r}, \phi)\right] d\mathbf{r}_{31}. \tag{2.25}$$

Mean relative mobility, $\langle \mathbf{M} \rangle_2$:

The effect of "bath" particles on the relative mobility is modeled through third particle integrals involving the probability distribution. When the third particle is near contact to either of the pair of interest, a resistance formulation is used to compute the added resistance due to near-contact interactions:

$$\langle \mathbf{R} \rangle_2(\mathbf{r})g = \mathbf{R}_{pair}(\mathbf{r})g + n \int \Big(\mathbf{R}(\mathbf{r}, \mathbf{r}_{31}, \mathbf{r}_{32}) - \mathbf{R}_{pair}(\mathbf{r}) \Big) g_3 d\mathbf{r}_{31}, \tag{2.26}$$

where $\mathbf{R}(\mathbf{r}, \mathbf{r}_{31}, \mathbf{r}_{32})$ is the resistance for particles 1 and 2 in the presence of a third particle and $\mathbf{R}_{pair}(\mathbf{r})$ is the resistance of the isolated pair 1 and 2. Note that these are the resistances associated with relative motion of the pair. The term $\Delta\mathbf{R} = \mathbf{R}(\mathbf{r}, \mathbf{r}_{31}, \mathbf{r}_{32}) - \mathbf{R}_{pair}(\mathbf{r})$ is therefore the increase of the resistance to pair relative motion with respect to the isolated pair, due to the influence of another particle. To calculate the resistance components in triplet configurations for particles near contact, the resistance is assumed to be pair-wise additive. The average resistance is then inverted to obtain the average mobility.

For configurations of three particles well outside the lubrication region, the third particle effect is modeled using a mobility formulation:

$$\langle \mathbf{M} \rangle_2(\mathbf{r})g = \mathbf{M}_{pair}(\mathbf{r})g + n \int \Big(\mathbf{M}(\mathbf{r}, \mathbf{r}_{31}, \mathbf{r}_{32}) - \mathbf{M}_{pair}(\mathbf{r}) \Big) g_3 d\mathbf{r}_{31}, \tag{2.27}$$

where $\mathbf{M}(\mathbf{r}, \mathbf{r}_{31}, \mathbf{r}_{32})$ is the mobility for particles 1 and 2 in the presence of 3 and it is obtained using the method of reflections [53]. The summation of near-contact and far-field contributions gives the final form of average pair mobility. We give a detailed description on computation of $\langle \mathbf{M} \rangle_2$ in the Appendix.

This formulation imposes the effect of excluded volume in a probabilistic fashion. For example, consider three closely-spaced particles along one line with particle 3 between particles 1 and 2. In this case, particle 3 effectively stops approach of particles 1 and

2 along their line of centers, and obviously causes a significant increase in resistance in this direction. If the third particle is far from both particles 1 and 2, it has a small effect on the relative resistance/mobility. Note that, after applying the superposition closure, $\langle \mathbf{R} \rangle_2$ and $\langle \mathbf{M} \rangle_2$ in (2.26) and (2.27) are only functions of $g(\mathbf{r})$.

Mean relative diffusivity, $\langle \mathbf{D} \rangle_2$:

As noted previously, Brownian diffusion and shear-induced diffusion are captured here by summing separate contributions for each mechanism. Note that after scaling by $k_b T$ as shown in (2.18), the dimensionless Brownian diffusion is equal to the mobility, $\langle \mathbf{M} \rangle_2$. The shear-induced relative diffusion is the result of velocity fluctuations directly related to the microstructure [54, 27], which makes formulation of shear-induced diffusion a difficult task even for the self-diffusion. While the relative diffusivity due to shearing has not been well-studied, a representation is obtained by considering particles near contact and widely separated. When $r \gg 1$, the motions of the two particles become uncorrelated, and the shear-induced relative diffusivity is twice the shear induced self-diffusivity, i.e. $2\mathbf{D}_s^{\dot{\gamma}}$. The self-diffusivity has been well-studied and thus is assumed known from simulations or experiments for each concentration [55]. For a pair near contact, $r - 2 \to 0$, the relative velocity along the line of centers goes to zero, and thus both radial velocity fluctuations and the radial relative diffusivity vanish. The pair may, however, rotate around the center of mass, and thus velocity fluctuations remain in the angular ($\hat{\theta}$ and $\hat{\varphi}$) directions. These considerations lead to a simple form for $\left\langle \mathbf{D}^{\dot{\gamma}} \right\rangle_2$, given in dimensionless form by

$$\left\langle \mathbf{D}^{\dot{\gamma}} \right\rangle_2 = \frac{D^*}{D_0} \Big(\mathcal{G}(r) \hat{\mathbf{r}}\hat{\mathbf{r}} + \mathcal{H}(r)(\mathbf{I} - \hat{\mathbf{r}}\hat{\mathbf{r}}) \Big), \tag{2.28}$$

where D^* is the magnitude of the shear-induced self-diffusivity. Simulation and experimental results show that shear-induced self diffusion is mildly anisotropic and slightly

stronger in the flow direction. We neglect this anisotropy and take the far-field relative diffusion to have the strongest shear-induced self-diffusion component, $D^* = 2D_s^{xx}$. The self-diffusivity is calculated as

$$D_s^{xx}(\phi, Pe) = D_s^{xx}(\phi = 0.45, Pe)\frac{D_s^{xx}(\phi, Pe = 1000)}{D_s^{xx}(\phi = 0.45, Pe = 1000)}$$

where the data for $D_s^{xx}(0.45, Pe)$ and $D_s^{xx}(\phi, 1000)$ are extracted from figures 6 and 13 in Foss & Brady [55] . The function $\mathcal{G}(r)$ determines the variation of the radial diffusivity with r, while $\mathcal{H}(r)$ determines the variation for the $\hat{\theta}$ and $\hat{\varphi}$ directions. While relative motion of a pair of particles along the line of centers may be highly restricted by other particles, relative motion in the angular directions is less influenced. Lacking a clearly better choice, we assume that the shear-induced relative diffusivity takes on the far-field value at all separations for directions other than $\hat{\mathbf{r}}$, and thus $\mathcal{H}(r) = 1$. The function $\mathcal{G}(r)$ is approximated as

$$\mathcal{G}(r) = \begin{cases} 1 & r \geqslant 4. \\ \exp\left[-\tilde{n}(\dfrac{4-r}{r-2})\right] & r < 4, \end{cases} \tag{2.29}$$

so that it decays from unity at $r = 4$ to 0 at $r = 2$. For larger values of $\tilde{n}$, the decay is more rapid, but we note that for any $\tilde{n}$, $\mathcal{G}(r) \ll r - 2$ as $r \to 2$ so that relative radial diffusion is dominated by the Brownian contribution sufficiently close to contact. The value of $\tilde{n}$ is a controlling parameter for the microstructure, and it is the primary adjustable parameter in the theory; although the choice of $r = 4$ as the separation at which far-field diffusion is active is also adjustable we have somewhat arbitrarily fixed this value. For each ϕ at $Pe > 1$, there is a critical $\tilde{n}$ value beyond which a convergent solution for $g(\mathbf{r})$ cannot be obtained. This limiting largest value of $\tilde{n}$ was determined for each ϕ and Pe studied. Values of $\tilde{n}$ slightly below this critical value, $\tilde{n} = 0.95\tilde{n}_c$, resulted in good agreement between the predictions and simulation results and were

chosen for the entire range of Pe and ϕ studied here. Physically, this retains just enough shear-induced diffusion near contact to maintain a stable disordered state.

This completes the formulation of a closed problem for the microstructure. All averaged values in (2.19) are expressed in terms of g and $\mathbf{r}$, and g will be determined by solving the integro-differential equation (2.19) with boundary conditions expressed by (2.21a) and (2.21b).

Summary of approximations

In this section, approximations made in §2.2 to reduce the N-body Smoluchowski equation to a closed equation, of convection-diffusion form, in terms of $g(\mathbf{r})$ are provided. Note that the assumptions listed below are independent of one other.

1- *Mean-field approximation:* We assume that the convective flux associated with interparticle and lubrication forces is determined by their conditional average values. The role of fluctuations around the average values is captured through a dispersion flux, which is approximated by shear-induced diffusion; see (2.15).

2- *Assumptions of pair-wise additivity:* This assumption enables us to write $\langle \mathbf{M} \rangle_2$, $\langle \mathbf{R} \rangle_2$ and $\langle \mathbf{F} \rangle_2$ as third-particle integrals, with the integrand an inner product of the relevant function with g_3. For computation of the average mobility, if the third particle was in near contact with particles 1 and 2 the resistance tensor was assumed to be pair-wise additive (see (2.26)), while for well-separated configurations a pair-wise additive mobility assumption was considered (see (2.27)).

3- *Triplet closure approximation*: In order to compute the third-particle integrals, a closure approximation is needed to express g_3 in terms of g. A modified Kirkwood superposition approximation [51] was used for this purpose.

4- *Shear-induced relative diffusion*: We write the flux associated with dispersion of pair motion around the average motion as a diffusive flux, $-\langle \mathbf{D}^{\dot{\gamma}} \rangle_2(\mathbf{r}) \cdot \nabla g(\mathbf{r})$. The variations of shear-induced diffusion were projected along the line of centers of the pair,

$\hat{\mathbf{r}}$ and in the orthogonal plane $\hat{\theta} - \hat{\varphi}$ in the form given in (2.28). The variations along $\hat{\mathbf{r}}$ are approximated by interpolating between the expected values of the shear-induced relative diffusion at the limits of two particles being well-separated, $r/a \gg 1$, and when they are near contact, $r \to 2$. In case of $r/a \gg 1$, the particles become uncorrelated and shear-induced relative diffusivity becomes twice the value of shear-induced self-diffusivity. When two particles are near contact the fluctuations of relative velocity and the resulting dispersive flux drop to zero. These two limits are interpolated with relation (2.29).

We assumed the shear-induced relative diffusion takes its far-field value for all separations in directions $\hat{\theta}$ and $\hat{\varphi}$. Note that two particles at contact can still move in $\hat{\theta}$ and $\hat{\varphi}$ directions and presence of bath particles in different configurations around the pair would results in $O(1)$ fluctuations in the relative angular velocity. Thus we expect a finite angular dispersive flux in this configuration. However there is no particular reason why there should be no spatial variation and the assumption of uniform diffusivity in $\hat{\theta}$ and $\hat{\varphi}$ directions is due to the lack of a better understanding and to keep the model as simple as possible.

2.2.3 Near-equilibrium formulation

The formulation outlined above is not convenient for obtaining structural changes of $O(Pe^2)$ near equilibrium ($Pe \ll 1$). To address this weak perturbation limit, we expand $g(\mathbf{r})$ in terms of Pe, similar to regular perturbation techniques used previously for dilute suspensions [56, 47]:

$$g\left(\mathbf{r}\right) = g^{eq}\left(r\right) + Pe\, g^{(1)}\left(\mathbf{r}\right) + Pe^2\, g^{(2)}\left(\mathbf{r}\right) + O(Pe^{5/2}), \tag{2.30}$$

where the superscript eq implies the equilibrium structure and the terms with superscripts (1) and (2) are first and second order perturbation structure from equilibrium

due to shear. The rheology is Newtonian to $O(Pe)$ and for obtaining non-Newtonian rheology the expansion should be pursued to Pe^2 [47]. Incorporating the expansion to (2.19), equations are obtained for g^{eq}, $g^{(1)}$ and $g^{(2)}$. The equation governing $g^{eq}(r)$ is

$$\nabla \cdot \left(\left\langle \mathbf{U}^{eq} \right\rangle_2 (r)\, g^{eq}(r) - \left\langle \mathbf{M}^{eq} \right\rangle_2 (r) \cdot \nabla g^{eq}(r) \right) = 0, \tag{2.31}$$

where $\mathbf{U}^{eq}$ is defined by

$$\left\langle \mathbf{U}^{eq} \right\rangle_2 (r) = \left\langle \mathbf{M}^{eq} \right\rangle_2 (r) \cdot \left(\mathbf{F}^{HS}(\mathbf{r}) + n \int \mathbf{F}^{HS}(\mathbf{r}_{31})\, g^{eq}(r_{31})\, g^{eq}(r_{32}) \exp(\tau^\star)\, \mathbf{dr}_{31} \right). \tag{2.32}$$

The quantities are rendered dimensionless using the scalings given by (2.18). For $Pe \ll 1$, shear-induced diffusion can be neglected in comparison with Brownian diffusion, and therefore we have $\left\langle \mathbf{M}^{eq} \right\rangle_2 (r) = \left\langle \mathbf{D}^{eq} \right\rangle_2 (r)$ in the dimensionless form. Due to the noted limitation of the Kirkwood superposition closure at high concentrations, rather than solving (2.32), $g^{eq}(r)$ was obtained using the Percus-Yevick approach [57].

The equation governing $g^{(1)}(\mathbf{r})$ is

$$\nabla \cdot \left(\left\langle \mathbf{U}^{1} \right\rangle_2 g^{eq}(r) + \left\langle \mathbf{U}^{eq} \right\rangle_2 (r)\, g^{(1)}(\mathbf{r}) - \left\langle \mathbf{M}^{eq} \right\rangle_2 (r) \cdot \nabla g^{(1)}(\mathbf{r}) \right) = 0, \tag{2.33}$$

where $\left\langle \mathbf{U}^{eq} \right\rangle_2 (r) = \left\langle \mathbf{M}^{eq} \right\rangle_2 (r) \cdot \nabla \ln g^{eq}(r)$, from (2.31). The velocity $\left\langle \mathbf{U}^{1} \right\rangle_2$ is given by

$$\begin{aligned} \left\langle \mathbf{U}^{1} \right\rangle_2 (\mathbf{r}) \;=\; & \left\langle \mathbf{M}^{eq} \right\rangle_2 (r) \cdot \left(\mathbf{F}^{lub}(\mathbf{r}) + n \int \mathbf{F}^{lub}(\mathbf{r}_{31})\, g^{eq}(r_{31})\, g^{eq}(r_{32}) \exp(\tau^\star)\, d\mathbf{r}_{31} \right. \\ & \left. + n \int \mathbf{F}^{HS}(\mathbf{r}_{31}) \left(g^{(1)}(\mathbf{r}_{31})\, g^{eq}(r_{32}) + g^{1}(\mathbf{r}_{32})\, g^{eq}(r_{31}) \right) \exp(\tau^\star)\, d\mathbf{r}_{31} \right). \end{aligned} \tag{2.34}$$

The boundary conditions are zero radial flux at the contact surface ($r = 2$) and $g^{(1)} \to 0$ as $r \to \infty$. Substituting (2.34) in (2.33) yields an equation with only $g^{(1)}$ unknown.

The equation governing $g^{(2)}(\mathbf{r})$ is

$$\nabla \cdot \Big(\left\langle \mathbf{U}^2 \right\rangle_2 g^{eq}(r) \quad + \left\langle \mathbf{U}^1 \right\rangle_2 (\mathbf{r})\, g^{(1)}(\mathbf{r}) \quad + \langle \mathbf{U}^{eq} \rangle_2 (r)\, g^{(2)}(\mathbf{r}) - \langle \mathbf{M}^{eq} \rangle_2 (r) \cdot \nabla g^{(2)}(\mathbf{r}) \Big) = 0, \tag{2.35}$$

where $\left\langle \mathbf{U}^1 \right\rangle_2 (\mathbf{r})\, g^{(1)}(\mathbf{r})$ is known from the previous step and $\left\langle \mathbf{U}^2 \right\rangle_2$ is given by

$$\begin{aligned} \left\langle \mathbf{U}^2 \right\rangle_2 (\mathbf{r}) \;=\; & \langle \mathbf{M}^{eq} \rangle_2 (r) \cdot \Bigg(n \int \mathbf{F}^{HS}(\mathbf{r}_{31})\, g^{(1)}(\mathbf{r}_{31})\, g^{(1)}(\mathbf{r}_{32}) \exp(\tau^\star)\, d\mathbf{r}_{31} \\ & + n \int \mathbf{F}^{lub}(\mathbf{r}_{31}) \Big(g^{(1)}(\mathbf{r}_{31})\, g^{eq}(r_{32}) + g^{eq}(r_{31}) g^{(1)}(\mathbf{r}_{32}) \Big) \exp(\tau^\star)\, d\mathbf{r}_{31} \\ & + n \int \mathbf{F}^{HS}(\mathbf{r}_{31}) \Big(g^{(2)}(\mathbf{r}_{31})\, g^{eq}(r_{32}) + g^{(2)}(\mathbf{r}_{32})\, g^{eq}(r_{31}) \Big) \exp(\tau^\star)\, d\mathbf{r}_{31} \Bigg). \end{aligned} \tag{2.36}$$

The boundary conditions are again no flux at contact and $g^{(2)} \to 0$ as $r \to \infty$. Substituting (2.36) in (2.35) and using $g^{(1)}(\mathbf{r})$ determined in the previous step, the only unknown is $g^{(2)}(\mathbf{r})$. The solution technique used for solving these integro-differential equations is similar to the method used for general Pe, to be described in §2.4.

2.3 Rheology

We start with the formal expressions for suspension stress. The bulk stress in the suspension is given by

$$\langle\, \boldsymbol{\Sigma} \,\rangle = -P\mathbf{I} + 2\eta \mathbf{E}^\infty + n \left(\langle\, \mathbf{S}^P \,\rangle + \langle\, \mathbf{S}^H \,\rangle + \langle\, \mathbf{S}^B \,\rangle \right), \tag{2.37}$$

where $-P\mathbf{I} + 2\eta\mathbf{E}^\infty$ is the pure fluid stress contribution, and the other terms are stresses contributed by the particle phase. The stresslets $\langle\, \mathbf{S}^B \,\rangle$, $\langle\, \mathbf{S}^H \,\rangle$, and $\langle\, \mathbf{S}^P \,\rangle$ give the average single-particle Brownian, hydrodynamic, and interparticle stress contributions, respec-

tively. Here, $\langle\ \rangle$ denotes an ensemble average taken over all particles and configurations. These stress contributions can be expressed in terms of resistance tensors as [46, 27]

$$\left\langle \mathbf{S}^{B} \right\rangle = -k_b T \left\langle \nabla \cdot \left(\mathbf{R}^{SU} \cdot (\mathbf{R}^{FU})^{-1} \right) \right\rangle, \tag{2.38a}$$

$$\left\langle \mathbf{S}^{H} \right\rangle = \left\langle \mathbf{R}^{SU} \cdot (\mathbf{R}^{FU})^{-1} \cdot \mathbf{R}^{FE} - \mathbf{R}^{SE} \right\rangle : \mathbf{E}^{\infty}, \tag{2.38b}$$

$$\left\langle \mathbf{S}^{P} \right\rangle = -\left\langle \left(\mathbf{x}\mathbf{I} + \mathbf{R}^{SU} \cdot (\mathbf{R}^{FU})^{-1} \right) \cdot \mathbf{F} \right\rangle, \tag{2.38c}$$

where $\mathbf{R}^{SU}$ is the resistance tensor that relates the particle stresslet to particle motion relative to the bulk flow, and $\mathbf{R}^{SE}$ relates the stresslet to the bulk rate of strain. To correctly couple microstructure to rheology, the general stresslet $\langle\, \mathbf{S} \,\rangle$ (with superscripts indicating the mechanism suppressed here) is formulated in terms of $g(\mathbf{r})$ as

$$\langle\, \mathbf{S} \,\rangle = n \int \langle\, \mathbf{S} \,\rangle_2 (\mathbf{r})\, g\,(\mathbf{r})\, d\mathbf{r}, \tag{2.39}$$

where $\langle\, \mathbf{S} \,\rangle_2(\mathbf{r})$ is the average stress on each particle in a pair configuration. This stress is a result of interactions of the individual pair and their interaction with the rest of particles at each pair separation $\mathbf{r}$. $\langle\, \mathbf{S} \,\rangle_2$ is formulated as indicated by (2.38), replacing $\langle\ \rangle$ with $\langle\ \rangle_2$. We define the conditional pair averages appearing in the formulation of the stress as outlined below.

2.3.1 Brownian stress, $\left\langle \mathbf{S}^{B} \right\rangle$

Following (2.38a) and (2.39), Brady [46] divided the Brownian stress contribution to two parts:

$$n \left\langle \mathbf{S}^{B} \right\rangle = \mathbf{\Sigma}^{B1} + \mathbf{\Sigma}^{B2}, \tag{2.40a}$$

$$\frac{\left\langle \mathbf{\Sigma}^{B1} \right\rangle}{\eta \dot{\gamma}} = -Pe^{-1} \frac{27}{8\pi} \phi^2 \int \mathbf{nn} g ds, \tag{2.40b}$$

$$\frac{\langle \mathbf{\Sigma}^{B2} \rangle}{\eta \dot{\gamma}} = Pe^{-1} \frac{27}{8\pi} \phi^2 \int \langle \mathbf{R}^{SU} \cdot (\mathbf{R}^{FU})^{-1} \rangle_2 \cdot \nabla g d\mathbf{r}, \tag{2.40c}$$

where $\mathbf{n}$ is the unit vector along the line of centers, from particle 1 to 2. The advantage of this division to two parts is that $\mathbf{\Sigma}^{B1}$, which is evaluated through a straightforward surface integration, becomes the dominant Brownian contribution for large ϕ [46]. To compute $\langle \mathbf{\Sigma}^{B2} \rangle$, $\left\langle \mathbf{R}^{SU} \cdot (\mathbf{R}^{FU})^{-1} \right\rangle_2$ is needed. Very near contact, pairwise lubrication interactions dominate and $\left\langle \mathbf{R}^{SU} \cdot (\mathbf{R}^{FU})^{-1} \right\rangle_2 \rightarrow \left(\mathbf{R}^{SU} \cdot (\mathbf{R}^{FU})^{-1} \right)_{pair}$ as $r \rightarrow 2$, where subscript *pair* refers to the isolated pair; this quantity goes to zero as r^{-2} for $r \gg 2$. The gradient of the pair distribution function, ∇g, is maximum at contact. Hence the main contribution to the stress comes from the boundary layer volume [27] near contact, and $\mathbf{\Sigma}^{B2}$ is taken to be

$$\frac{\langle \mathbf{\Sigma}^{B2} \rangle}{\eta \dot{\gamma}} \sim Pe^{-1} \frac{27}{8\pi} \phi^2 \int_{bl} \left(\mathbf{R}^{SU} \cdot (\mathbf{R}^{FU})^{-1} \right)_{pair} \cdot \nabla g d\mathbf{r}, \tag{2.41}$$

where the subscript *bl* refers to integration being carried out inside the boundary layer. We define the boundary layer as the volume adjacent to the contact surface where the angularly averaged pair distribution function is larger than unity: $\tilde{g}(r) \geqslant 1$. This formulation converges to the exact form for dilute suspensions when only pair interactions are considered, and provides a reasonable approximation for concentrated suspensions.

2.3.2 Interparticle force stress, $\langle \mathbf{S}^P \rangle$

We consider the influence of the hard-sphere force, $\mathbf{F}^{HS}$, and lubrication force, $\mathbf{F}^{lub}$. Recall that $\mathbf{F}^{lub}$ is introduced to mimic hydrodynamic interactions, so the role of this force on the stress will be considered hydrodynamic for the stress calculation. We model $\mathbf{F}^{HS}$ using a steep short-range repulsion negligible at any r except very small distances from the hydrodynamic contact surface. Since $\left\langle \mathbf{R}^{SU} \cdot \mathbf{R}^{FU^{-1}} \right\rangle_2 \rightarrow r\hat{\mathbf{r}}\hat{\mathbf{r}}$, the term $\mathbf{xI} + \mathbf{R}^{SU} \cdot (\mathbf{R}^{FU})^{-1}$ in (2.38c) goes as $r - 2$ for individual pairs near contact; the use of relative coordinates results in a -$\mathbf{r}$ from $\mathbf{x}$ in the expression. On the other hand,

from (2.23), $\mathbf{F}^{HS} \to (r-2)^{-1}$ only at contact. In fact, $\langle \mathbf{S}^P \rangle_2$ is zero except at contact in a true hard-sphere suspension, which makes $\langle \mathbf{S}^P \rangle$ identically zero. Because a steep repulsive force is used to model the hard-sphere interactions, $\langle \mathbf{S}^P \rangle_2$ will be non-zero in a thin layer at the contact surface. This layer becomes thinner as the repulsive force becomes steeper with increase of τ in (2.23). A scaling analysis shows $\left\langle \mathbf{S}^P \right\rangle \sim g(\mathbf{r} = 2\hat{\mathbf{r}})\Delta r$ where $\Delta r \sim \tau^{-1}$ is the thickness of the layer over which the repulsive force decays to zero which makes $\langle \mathbf{S}^P \rangle \sim O(\tau^{-1})\langle \mathbf{S}^B \rangle$. Therefore the contribution from interparticle forces on the bulk stress is negligible compared to Brownian and hydrodynamic contributions, and will not be further considered here.

2.3.3 Hydrodynamic stress, $\left\langle \mathbf{S}^H \right\rangle$

The hydrodynamic stress term requires evaluation of the conditionally averaged hydrodynamic resistances, $\langle \mathbf{R}^{SE} \rangle$ and $\langle \mathbf{R}^{SU} \rangle$, whose average form is less clear than that of $\mathbf{R}^{FU}$. The singular nature of resistance functions at contact and the need for a renormalization quantity to make the integrals converge adds to the difficulties even in case of an isolated pair [44]. We assume that the stress contribution is maximized near contact due to lubrication interactions, so that the hydrodynamic stress is dominated by the boundary layer lubrication stresses. The main contribution to the hydrodynamic stress comes from the constraint of relative pair movement along the line of centers (driven by the extensional portion of the bulk flow). We therefore focus on the stress induced by relative motion of the pair along the line of centers ($\hat{\mathbf{r}}\hat{\mathbf{r}}$ component) and ignore the stress generated by pair angular and rotational motion ($\mathbf{I} - \hat{\mathbf{r}}\hat{\mathbf{r}}$ component). For the case of particles nearly touching, the lubrication theory gives $\mathbf{R}^{SE} \sim \mathbf{R}^{FE}\hat{\mathbf{r}}a$ and $\mathbf{R}^{FE} \sim \mathbf{R}^{FU}\hat{\mathbf{r}}a$. Also, from the reciprocal theorem $\mathbf{R}^{SU} = \left(\mathbf{R}^{FE}\right)^T$ (the T here implies transpose). Thus, using (2.9), the average $\hat{\mathbf{r}}\hat{\mathbf{r}}$ component of the stress on each particle near contact can be written

$$\frac{n\langle \mathbf{S}^H \rangle}{\eta\dot{\gamma}} \approx \frac{n\mathbf{S}^H_{pair}}{\eta\dot{\gamma}} + \frac{27}{16\pi}\phi^2 \int_{bl} \langle R^{FU}_{rr} \rangle_2 \left(\langle U^{lub}_r \rangle_2 - U^r_{pair} \right) \hat{\mathbf{r}}\hat{\mathbf{r}} g \, d\mathbf{r}, \tag{2.42}$$

where U^r_{pair} and $\mathbf{S}^H_{pair}$ are the well-known relative radial velocity and hydrodynamic stress tensor for dilute suspensions [44, 45] and $\langle U_r^{lub}\rangle_2 = \langle M_{rr}\rangle_2\langle F_r^{lub}\rangle_2$ is the hydrodynamic relative radial velocity, with $\langle U_r^{lub}\rangle_2 \propto r-2$ as $r \to 2$. The quantity $\langle R_{rr}^{FU}\rangle_2 \sim (2(r-2))^{-1}$ yielding $\langle R_{rr}^{FU}\rangle_2\langle U_r^{lub}\rangle_2 = O(1)$ at contact. The stress is controlled by the force with which a pair is pushed together (or pulled apart) along the line of centers near contact. Note that $\hat{\mathbf{r}}\hat{\mathbf{r}}$ in (2.42) and $\mathbf{nn}$ in (2.40b) are different representations of the same quantity; this is done to differentiate volume integrals (using $\hat{\mathbf{r}}\hat{\mathbf{r}}$) from surface integrals (using $\mathbf{nn}$). Brady & Bossis [29] showed in early Stokesian Dynamics (SD) results that the added force due to large concentration surrounding a pair near contact (where resistance is strictly by the intervening fluid) causes pairs to approach more rapidly near contact as the concentration is increased: two particles nearly touching find themselves in an increased "effective" shear stress. This concept is seen in the boundary layer scaling analysis by Brady & Morris [27] for hydrodynamic stress in concentrated suspensions, where the high frequency dynamic viscosity, $\eta_\infty(\phi)$, is used in a modified Péclet number, or dimensionless effective shear stress. Foss & Brady [37] and Sierou & Brady [7] showed that this scaling agrees well with SD results for shear stress; however, the scaling was not applicable to particle pressure [58] and normal stress differences. The advantage of our approach is that the radial velocity of a pair comes naturally out of the forces predicted by the theory bypassing the need for a scaling theory. This enables us to study in detail how the relative motion and probability distribution impact on particle pressure and normal stress differences.

2.4 Solution technique

Equation (2.19) is nonlinear due to the product of pair distribution functions resulting from the Kirkwood superposition closure. We solve this equation by using an iterative technique. An initial value for $g(\mathbf{r})$ is obtained by ignoring the many-body integral terms. We thus first solve the dilute-limit equation for g, with conditional averages equal

to the well-known isolated pair hydrodynamic functions. Note that this first iteration solution corresponds to Bergenholtz et. al. [28] results. The resulting convection-diffusion equation is solved numerically by a finite element technique to obtain $g_{dilute}(\mathbf{r})$, which in turn is used to evaluate the integrals of the conditional averages appearing in (2.22) and (2.26). The calculated average values then replace the isolated pair values in (2.19), and the modified differential equation is solved to obtain $g(\mathbf{r})$. The process is repeated until the iterations yield a converged $g(\mathbf{r})$. The convergence criterion used here is $\frac{g^i_{max} - g^{i-1}_{max}}{g^i_{max}} < 10^{-3}$ where g^i_{max} is the maximum value of g at i^{th} iteration.

The mesh generation for the finite element method (FEM) calculation was carried out by discretizing the $\mathbf{r}$ space in spherical coordinates, $\mathbf{r} = (r, \theta, \varphi)$. The pair microstructure satisfies the symmetry $g(\mathbf{r}) = g(-\mathbf{r})$. Also, for simple-shear flow we must have $g(r, \theta, \varphi) = g(r, \theta, -\varphi)$. These symmetry properties reduce the calculation to a quarter of the full domain, i.e. $2 \leqslant r < \infty$, $0 \leqslant \theta \leqslant \pi$ and $0 \leqslant \varphi \leqslant \frac{\pi}{2}$. Equally spaced nodes were used in the θ and φ directions, with $\Delta\theta = \pi/24$ and $\Delta\varphi = \pi/24$. For accurate calculation of $g(\mathbf{r})$ at $Pe \gg 1$, several radial nodes should be inside the boundary layer, as seen also in sampling of microstructure [48]. Hence, a structured mesh was generated in the radial direction with node spacing increasing from Δr_0 at the contact surface as follows: $\Delta r_j = \Delta r_0 q^{j-1}$ where j is the number of the element and $q > 1$ controls the increase of radial spacing between elements. Here $\Delta r_0 = 0.001$ and $q = 1.1$ were chosen for all ϕ and Pe (recall $Pe \leq 100$ in this study). The outer radius of the computational domain was chosen as $r = 10$, which is found to be sufficiently large to capture long range correlations for the conditions studied. The results were shown to be independent of the mesh density. For instance with $\Delta r_0 = 0.0002$, $\Delta\theta = \pi/48$, and $\Delta\varphi = \pi/48$ the results were within 0.05 relative error of the regular meshing. Integrals involved in calculating conditional average quantities were carried out numerically by discretizing the integration domain for each pair separation $\mathbf{r}$ in the same fashion as described for the FEM calculation. Finally we note that although the solution to the theory is based on

the time-consuming iterative solution to a partial differential equation, the time required to compute the convergent $g(\mathbf{r})$ from theory is about an order of magnitude less than Accelerated Stokesian Dynamics (ASD) simulations of the size in this work. There are ways to increase the efficiency of the current computation scheme which we have yet to pursue.

2.5 Numerical simulation: Stokesian Dynamics

We use sampling of configurations generated by discrete-particle simulations of sheared Brownian dispersions for comparison with the developed theory. Stokesian Dynamics (SD) is a technique for simulating particles dispersed in an incompressible Newtonian fluid when inertial effects are negligible, i.e. at vanishing Reynolds number $Re_p = 0$. The fluid motion is governed by Stokes equation and the dynamics of particles is determined through the Langevin equation,

$$\mathbf{m} \cdot \frac{d\mathbf{U}}{dt} = \mathbf{F}^H + \mathbf{F}^B + \mathbf{F}^P, \tag{2.43}$$

where in a system composed of N particles, $\mathbf{m}$ is the generalized mass/moment-of inertia $6N \times 6N$ matrix, $\mathbf{U}$ is the generalized translational/rotational velocity vector of particles of size $6N$, and $\mathbf{F}^H, \mathbf{F}^B$ and $\mathbf{F}^P$ are generalized hydrodynamic, Brownian and interparticle force/torque vectors of size $6N$, respectively. The hydrodynamic force/torque is calculated as $\mathbf{F}^H = \mathbf{R}^{FE} : \mathbf{E} - \mathbf{R}^{FU} \cdot (\mathbf{U} - \mathbf{U}^\infty)$ with the resistance tensors defined in §2.2. At small pair separations, where lubrication interactions dominate the dynamics, a resistance formulation is used to compute the hydrodynamic functions while outside the lubrication zone, a mobility formulation is chosen. As a result SD is able to give an accurate presentation of the dynamics of the system in the limits of particles near contact and well-separated [29]. Brownian forces are fluctuating forces with zero average value and the variance is given by the fluctuation dissipation theorem:

$\langle \mathbf{F}^B(0)\mathbf{F}^B(t)\rangle = 2k_bT\mathbf{R}^{FU}\delta(t)$. Finally, interparticle forces are determined by taking the gradient of a pair interaction potential.

After computing all the forces, (2.43) is integrated twice in time to obtain the evolution of positions of particles. The integration time step, Δt, considered is large compared to inertial relaxation time, $t = m/6\pi\eta a$, and small compared to the time required to change the configuration of particles. The knowledge of the position of particles with time allows us to compute the average stress tensor using relations (2.38a) to (2.38c).

The computational speed in regular SD is controlled by the inversion of resistance matrix which is an $O(N^3)$ operation. In Accelerated Stokesian Dynamics (ASD), fast Fourier transform and particle-mesh-Ewald techniques are used to reduce the computational cost to $O(N \ln N)$ which enables study of much larger systems. The details of the ASD method for non-Brownian and Brownian suspensions are given in [41] and [31]. Periodic boundary conditions were considered in all three directions and Lees-Edwards boundary conditions were used for a sheared simulation box [59]. All simulations reported here were performed with $N = 512$ particles in a cubic box.

2.6 Results

Results are provided separately, first the microstructure, and then the rheology. We begin by describing results from the perturbation formulation for $Pe \ll 1$ at a range of ϕ. This is followed by a description of the predicted pair distribution function, $g(\mathbf{r})$, for a range of Pe and ϕ, with comparison to the results from Accelerated Stokesian Dynamics simulation at the same conditions. To investigate the variation with concentration at conditions far from equilibrium, predictions of $g(\mathbf{r})$ at $Pe = 10$ over a range of ϕ are also provided and compared with simulations. We note that the bulk of results presented are for $g(\mathbf{r})$ in the shear plane where the effect of external flow on microstructure is maximized, but for purposes of determining the rheology it is important to note that all calculations are fully three-dimensional.

2.6.1 Microstructure

We begin by considering the form of $g(\mathbf{r})$ computed by regular perturbation expansion at $Pe \ll 1$. Brady & Vicic [47] showed that for $Pe \ll 1$, the solution to $g^{(1)}(\mathbf{r})$ and $g^{(2)}(\mathbf{r})$ are of the form

$$g^{(1)}(\mathbf{r}) = f(r)(\hat{\mathbf{r}} \cdot \hat{\mathbf{E}} \cdot \hat{\mathbf{r}}), \tag{2.44a}$$

$$g^{(2)}(\mathbf{r}) = -h_2(r)(\hat{\mathbf{r}} \cdot \hat{\mathbf{E}} \cdot \hat{\mathbf{r}})^2 - h_3(r)(\hat{\mathbf{r}} \cdot \hat{\mathbf{E}} \cdot \hat{\mathbf{\Omega}} \cdot \hat{\mathbf{r}}) - h_4(r)(\hat{\mathbf{r}} \cdot \hat{\mathbf{E}} \cdot \hat{\mathbf{E}} \cdot \hat{\mathbf{r}}) - h_5(r)(\hat{\mathbf{E}} : \hat{\mathbf{E}}), \tag{2.44b}$$

where $\hat{\mathbf{E}}$ and $\hat{\mathbf{\Omega}}$ are the rate-of-strain and rate-of-rotation tensors, made dimensionless by the shear rate, $\dot{\gamma}$, of the imposed shear flow. In earlier work, Wagner & Ackerson [60] showed that (2.44a –2.44b) can be presented in terms of a finite number of spherical harmonics:

$$g^{(1)}(\mathbf{r}) = g_{2,-2}(r) Y_{2,-2} \tag{2.45a}$$

$$g^{(2)}(\mathbf{r}) = g_{00}(r) Y_{00} + g_{20}(r) Y_{20} + g_{22}(r) Y_{22} + g_{40}(r) Y_{40} + g_{44}(r) Y_{44}. \tag{2.45b}$$

Solutions for $g^{(1)}$ and $g^{(2)}$ were obtained here by three-dimensional FEM calculations, with no presumed functional form for the solution. However, the computed $g^{(1)}$ and $g^{(2)}$ were decomposable to (2.45a – 2.45b) with very good accuracy. Figure 2.2 shows $g^{(2)}(\mathbf{r})$ as a function of θ at $r = 2$ and different angles away from the shear plane for a suspension of volume fraction $\phi = 0.40$. The results are given for $0 \leq \theta \leq \pi$ since $g(r, \theta, \varphi) = g(r, \pi + \theta, \varphi)$. The variation is similar for other concentrations, but the magnitude of $g^{(2)}$ is a strong function of ϕ. This is evident from figure 2.3 which presents the values of the harmonic coefficients at contact as a function of ϕ when the solutions are decomposed onto (2.45a) and (2.45b). The data at $\phi = 0$ are predictions of the dilute theory of Brady & Vicic [47]. The results are given for $\phi \leq 0.50$; no convergent solution could be obtained for $g^{(1)}(\mathbf{r})$ at higher ϕ.

Hereafter, structural results are from the full theory, as opposed to the perturbation results above. Figures 2.4(a) and 2.4(b) show the pair distribution function at contact in

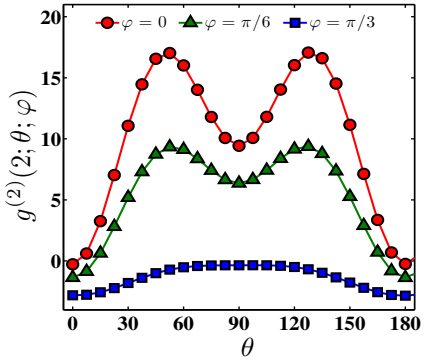

Figure 2.2: The angular variations of the perturbation solution $g^{(2)}(\mathbf{r})$ at the contact surface and azimuthal angles $\varphi = 0,\ \pi/6,\ \pi/3$ for $\phi = 0.40$ suspension.

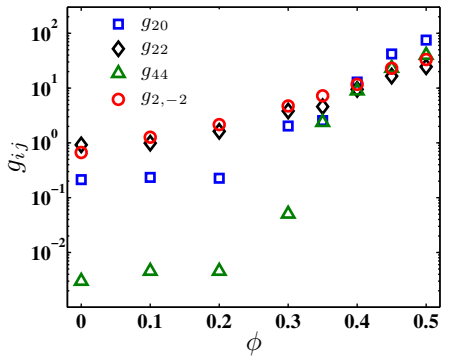

Figure 2.3: The values of spherical harmonic coefficients at $r = 2$ obtained by decomposing the perturbation solutions based on the the forms given by (2.45a – 2.45b).

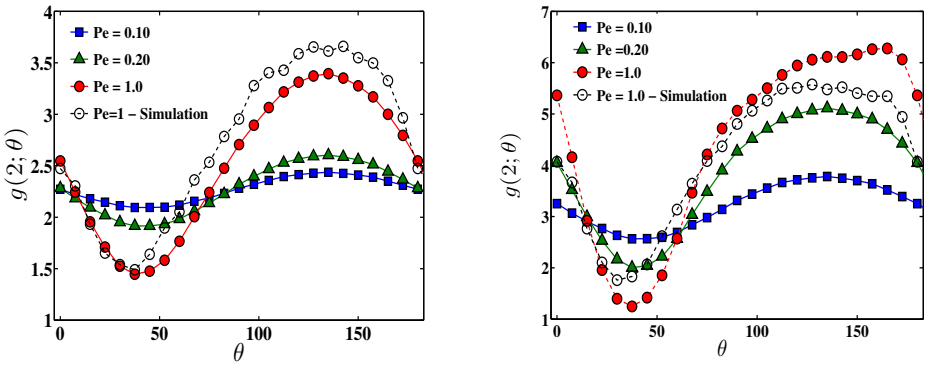

(a) (b)

Figure 2.4: Pair distribution function at contact in the shear plane from the solution of the full pair equation for $Pe = 0.10,\ 0.20$, and 1: (a) $\phi = 0.30$ and (b) $\phi = 0.40$.

the shear plane (x - y) at $Pe = 0.10$, 0.20 and 1 for $\phi = 0.30$ and 0.40 respectively. The simulation results for $Pe = 0.10$ and 0.20 are noisy, and as a result only the simulations at $Pe = 1$ are presented for comparison. The angular variations of $g(2;\theta)$ for both concentrations have a sinusoidal form at $Pe = 0.10$, as expected for $Pe \ll 1$. For $\phi = 0.30$ the angular variation remains similar as Pe is increased. By contrast, the changes in angular variation are significant for $\phi = 0.40$; for example, consider the appearance of a shoulder in $g(2;\theta)$ for $Pe = 1$ in both simulation and theory.

Figure 2.5 compares the predicted $g(\mathbf{r})$ for $\phi = 0.40$ and $Pe = 1$ with simulation results restricted to the shear plane. The results are given for the upper-half plane, recalling that $g(\mathbf{r}) = g(-\mathbf{r})$. The half circle in the center is the excluded volume region, $r < 2$. The theory captures the near contact anisotropy and the main features of the pair microstructure away from contact, including the next nearest neighbor peak in the compressional quadrant (near $r = 4$) and the zones depleted of pair correlation. A discrepancy is seen as the distortion of pair microstructure is predicted to be stronger than observed in simulation.

The pair distribution function at contact, $g(2)$ for brevity, is presented in figure 2.6 for $Pe = 10$ and different volume fractions, again restricting attention to the shear plane.

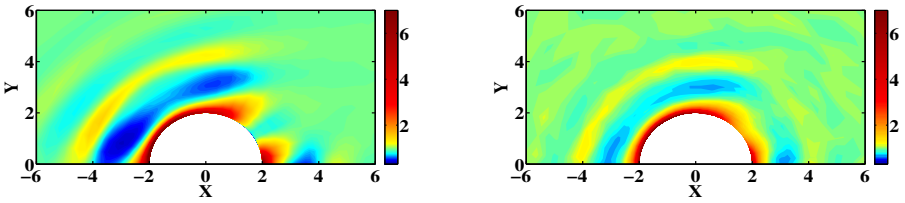

(a) Theory (b) Simulation

Figure 2.5: The pair distribution function, g, in the shear plane for $Pe = 1$ and $\phi = 0.40$ suspensions: (a) Theory prediction (b) results of simulation samplings. The colorbar is the same for the two figures and the flow direction is from left to right.

For $\phi = 0.20$, $g(2)$ shows a maximum in the compressional quadrant for both simulation and theory, while at higher ϕ a secondary peak appears in both cases. The largest value of g moves to angles closer to the flow direction with increase of ϕ, and at $\phi = 0.55$ the maximum is in the flow direction for both simulation and theory. The single peak which is present at lower ϕ remains; this peak appears at $\theta \approx 100^o$ for $\phi = 0.30$ and moves to $\theta \approx 120^o$ for $\phi = 0.55$, while for the theoretical prediction the angle is largely unchanged at $\theta \approx 120^o$. We see that an increase of volume fraction not only increases the magnitude of $g(\mathbf{r})$ near contact but also changes the form of the microstructural anisotropy; this is important for its rheological consequences, as it renders certain predictions of simple scaling analysis invalid, in particular for the nonlinear rheology found in the normal stress response of the material.

The theory captures much of the observed anisotropy correctly, but there are systematic deviations from simulation results. For example, theory over-predicts the value of the pair distribution function along the flow direction for all volume fractions. Also, the peaks in $g(2)$ appear at larger angles (measured from the flow direction) with respect to simulations. It is interesting to note that the agreement with simulation of the theoretical prediction improves with increasing volume fraction from $\phi = 0.30$ to $\phi = 0.55$, suggesting the simplifications made in formulating the theory become more accurate for

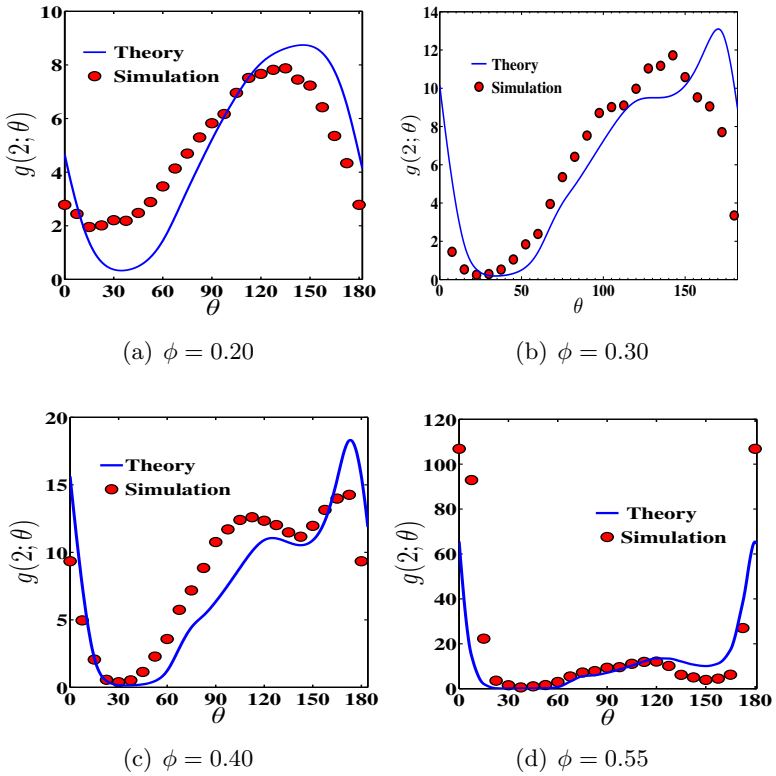

(a) $\phi = 0.20$ (b) $\phi = 0.30$

(c) $\phi = 0.40$ (d) $\phi = 0.55$

Figure 2.6: The pair distribution function at contact in the shear plane for $Pe = 10$: (a) $\phi = 0.20$, (b) $\phi = 0.30$, (c) $\phi = 0.40$, and (d) $\phi = 0.55$.

more concentrated suspensions.

Figure 2.7 compares $g(\mathbf{r})$ from simulation with theoretical predictions at $Pe = 50$ for $\phi = 0.40$, showing values in the shear plane. The maximum value of g is truncated to 10 to facilitate visualization and comparison of specific features of microstructure (colorbars are identical). At this elevated Pe, a clear boundary-layer structure is seen as found in theory [27] and simulation [48] studies. In the simulation results presented here, the boundary layer dissipates in a considerably shorter distance from the pair contact surface than seen in the predicted results. In the theoretically predicted structure, the high probability region extends downstream to $r \approx 4$ in the extensional quadrant. The spatial distribution of high and low probability regions is similar for theory and simula-

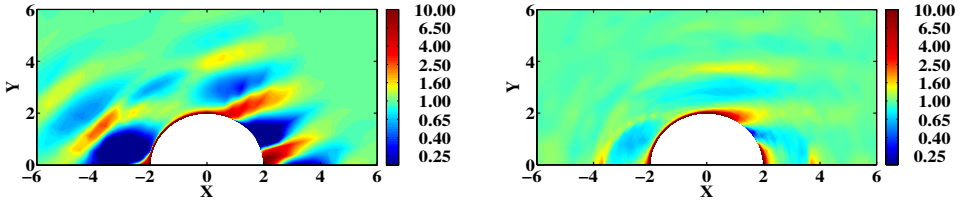

(a) Theory (b) Simulation

Figure 2.7: The pair distribution function at contact in the shear plane for $Pe = 50$ and $\phi = 0.40$: (a) theoretical prediction and (b) results of simulational sampling. The colorbar is the same for both figures.

tion, but the variations are intensified in the theory predictions. The high probability zone convected downstream is a point of clear discrepancy: for simulation, this region continues in the flow direction, while in the predictions it separates from the boundary at an angle with respect to the flow direction.

Figure 2.8 shows $g(\mathbf{r})$ at contact in the shear plane, for $\phi = 0.40$ with $Pe = 25$ and 50. From figures 2.6(c) and 2.8, we see that the main features of the angular variations at contact do not change significantly as Pe increases from 10 to 50; for example, the angles at which the peaks in g are observed remain similar for both simulation and the theory developed here. Increase of shear rate (i.e., Pe) simply amplifies the observed features. The same behavior is observed for other concentrations studied.

The variation of $g(\mathbf{r})$ with the angle φ about the flow axis, with $\varphi = 0$ on the shear plane, is similar for all Pe and ϕ studied. Figure 2.9(a) presents contact values of the theoretically determined g as a function of θ for different φ at $Pe = 10$ and volume fraction $\phi = 0.40$. To facilitate visualization, the results of simulational samplings for the same conditions are presented separately in figure 2.9(b). Microstructural distortion decreases with increase of the angle φ for both theory and simulation.

Finally we discuss the role of the parameter $\tilde{n}$ and its variations with Pe and ϕ. Recall that the iterations converge to a solution only for values of $\tilde{n} < \tilde{n}_c$. For $\tilde{n} \geq \tilde{n}_c$

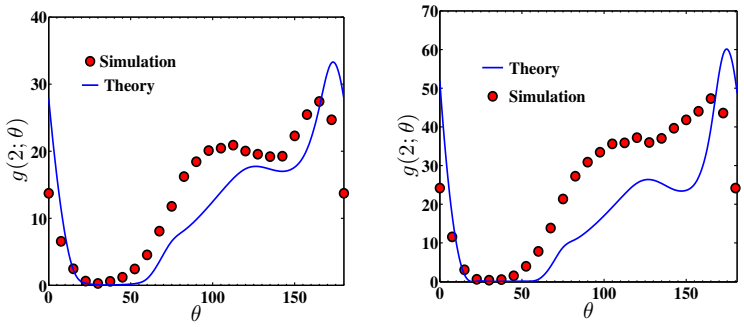

(a) Pe = 25 (b) Pe = 50

Figure 2.8: Angular variations of pair distribution function at contact in the shear plane for $\phi = 0.40$: (a) $Pe = 25$ and (b) $Pe = 50$.

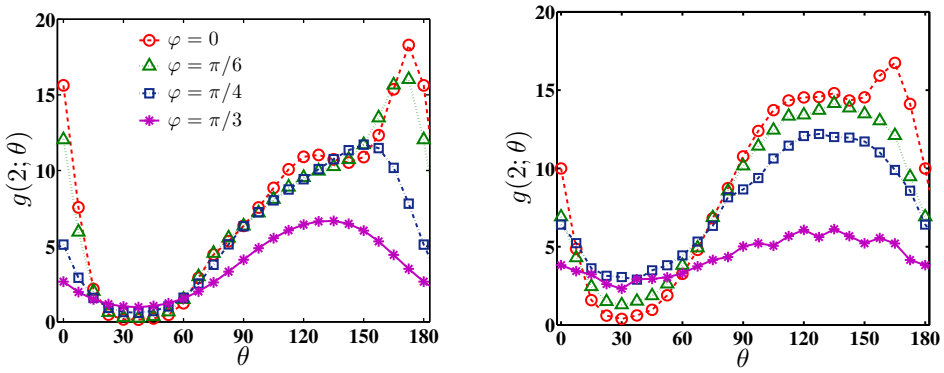

(a) Theory (b) Simulation

Figure 2.9: Pair distribution function at contact on different planes characterized by the angle φ measured from the shear plane, for $\phi = 0.40$ and $Pe = 10$: (a) theoretical predictions, (b) results of simulation samplings.

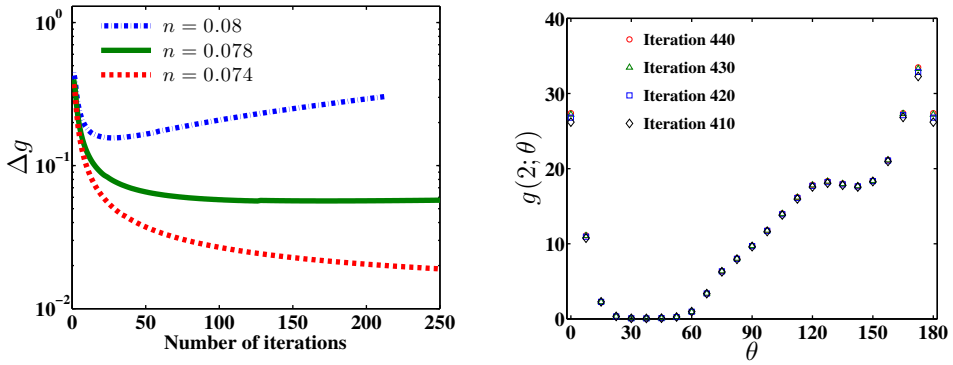

(a) (b)

Figure 2.10: (a) The change in pair distribution function per-iteration at contact along the flow direction, $\Delta g = g^i(2;0;0) - g^{i-1}(2;0;0)$, for $\phi = 0.40$ and $Pe = 25$ in three values of $\tilde{n} = 0.08$, 0.078 and 0.074. (b) Variations of $g(2;\theta)$ with numbers of iterations at $Pe = 25$, ϕ and $\tilde{n} = 0.95n_c = 0.074$.

(faster decay of relative diffusion), the pair distribution function at contact along the flow direction, $g(r = 2, \theta = 0, \varphi = 0)$, diverges. Figure 2.10(a) shows the increase of pair distribution function per-iteration at contact and in flow direction, $\Delta g = g^i(2;0;0) - g^{i-1}(2;0;0)$, for $Pe = 25$ and $\phi = 0.40$ for $\tilde{n} = 0.08, 0.078$ and 0.074.

In case of $\tilde{n} = 0.08$, the increase in $g(2;0;0)$ becomes larger with iterations resulting in a clearly divergent solution. We define $\tilde{n}_c$, as the value where Δg goes to a constant, so that g does not converge according to the convergence criterion: $\dfrac{g^i_{max} - g^{i-1}_{max}}{g^i_{max}} < 10^{-3}$ (see §2.4). From figure 2.10(a), $\tilde{n}_c = 0.078$ for $Pe = 25$ and $\phi = 0.40$. In order to obtain convergence, Δg must monotonically decrease with number of iterations and thus $\tilde{n} < \tilde{n}_c$. We have set $\tilde{n} \approx 0.95\tilde{n}_c$ for the entire set of results presented. Figure 2.10(b) shows variations of pair distribution function at contact in shear plane for $\phi = 0.40$, $Pe = 25$ at different iteration numbers for $\tilde{n} = 0.074$ (the value used for these conditions). The structure remains almost unchanged in the last 10 iterations and satisfies the criterion set for convergence of $g(\mathbf{r})$. Although the solution converges for smaller values of $\tilde{n}$ chosen here, further decrease of $\tilde{n}$ eventually results in disappearance of the boundary

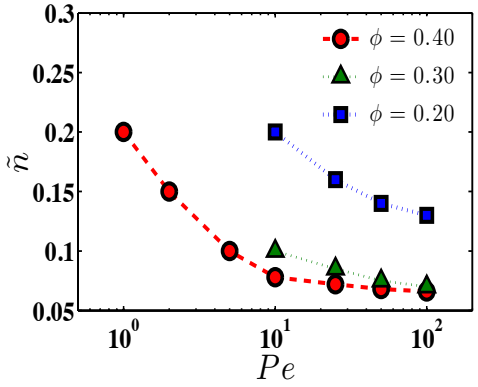

Figure 2.11: The critical $\tilde{n}$ in the shear-induced relative diffusion model (2.29), determined as a function of Pe for $\phi = 0.20$, 0.30, and 0.40.

layer structure at $Pe \gg 1$.

Finally figure 2.11 presents the $\tilde{n}$ used i.e. $\tilde{n} = 0.95\tilde{n}_c$, as a function of Pe for $\phi = 0.20$, 0.30, and 0.40. Recall $\tilde{n}$ is defined by (2.29). We notice that values of critical $\tilde{n}$ for obtaining a convergent solution decrease as Pe increases, appearing to approach a plateau for each volume fraction. Recall that according to (2.29), larger $\tilde{n}$ results in faster decay of relative radial shear-induced diffusion from its far-field value as the position of interest nears contact (the radial diffusivity is zero at contact). Figure 2.11 also shows that the $\tilde{n}$ values decrease with ϕ, e.g. shear-induced diffusion starts to decay to zero at a larger separation for lower volume fractions. This is consistent with the physical phenomenon modeled, noting that when $r < 4$ and no particle can be placed between, pair relative velocity fluctuations are induced through the particles surrounding the pair. As the suspension becomes more dilute, the behavior is dominated by the pair interactions alone, as these externally-induced fluctuations are weaker and the decay toward the zero value at contact begins at larger separation.

2.6.2 Rheology

We present the steady-shear rheology of suspensions in simple-shear flows predicted based on the computed structure. The rheology is characterized by the shear viscosity, $\hat{\eta} = \dfrac{\Sigma_{xy}}{\eta\dot{\gamma}}$, and the first and second normal stress differences, $\hat{N}_1 = \dfrac{\Sigma_{xx} - \Sigma_{yy}}{\eta\dot{\gamma}}$ and $\hat{N}_2 = \dfrac{\Sigma_{yy} - \Sigma_{zz}}{\eta\dot{\gamma}}$, respectively, with all in dimensionless form. As discussed in §2.3, the stress associated with the solid phase is divided into hydrodynamic and Brownian stress contributions, with negligible interparticle force contribution, and thus we write

$$\hat{\eta}^T = 1 + \hat{\eta}^B + \hat{\eta}^H, \quad \hat{N}_1^T = \hat{N}_1^B + \hat{N}_1^H, \quad \text{and} \quad \hat{N}_2^T = \hat{N}_2^B + \hat{N}_2^H,$$

where superscripts T, B, and H correspond to the total, Brownian, and hydrodynamic stress, respectively. The pair distribution function computed theoretically is used to deduce the Brownian contribution to the particle stress through the relations (2.40b) and (2.41); the hydrodynamic contribution is calculated as shown by (2.42).

Figure 2.12 shows the hydrodynamic and Brownian contributions for the zero-shear rate viscosity based on the perturbation solution for $g^{(1)}(\mathbf{r})$ alongside the Stokesian Dynamics simulation results of Foss & Brady[37] (these are computed for $Pe = 0$, using a Green-Kubo formulation) as a function of volume fraction. We see excellent agreement between the simulation results and predictions, indicating that the theory predicts the structure accurately near equilibrium. The results are presented for $\phi \leq 0.50$, the largest ϕ for which a convergent solution for $g^{(1)}(\mathbf{r})$ can be obtained.

While the zero-shear viscosity is well-understood for hard-sphere dispersions, examination of normal stress differences near equilibrium has been limited [47]. The magnitude of normal stress differences becomes very small near equilibrium, and this makes their experimental measurement difficult. Simulations by Stokesian Dynamics (in standard and accelerated versions) for $Pe \ll 1$ find the fluctuations comparable to the average value as shown by Foss & Brady [37] and also in the simulations of the current work. This

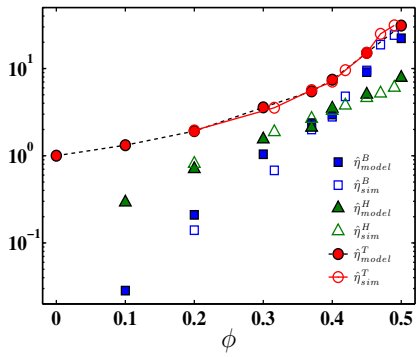

Figure 2.12: Brownian (■, □) and hydrodynamic (▲, △) contributions and total value (○, ●) of zero-shear rate viscosity as a function of volume fraction. Filled symbols present theoretical predictions based on the perturbation solution at $Pe \ll 1$, and the open symbols are the Stokesian Dynamics simulation results of Foss & Brady [37] at $Pe = 0$.

makes comparison with theoretical findings difficult. Considering the functional form of the perturbed microstructure, (2.44a - 2.44b), and the stress formulations (2.40b, 2.41, and 2.42), one can show that $g^{eq}(r)$ and $g^{(1)}(\mathbf{r})$ have no contribution to $\hat{N}_1$ and $\hat{N}_2$. Therefore, the normal stress differences scale as Pe^2 for $Pe \to 0$, and $\chi_1 = \dfrac{\hat{N}_1}{Pe}$ and $\chi_2 = \dfrac{\hat{N}_2}{Pe}$ should be constants in this limit. To see this point, it is important to note that $\hat{N}_1$ and $\hat{N}_2$ are first and second normal stress differences made dimensionless by $\eta\dot{\gamma}$. In figure 2.13 we present χ_1 and χ_2 as a function of volume fraction. Zero-shear viscosity values are given for comparison of the volume fraction dependencies. We see that χ_1 and χ_2 are stronger functions of ϕ than the zero-shear viscosity. This is in agreement with the scaling analysis made by Brady & Vicic [47], where they proposed $\hat{\eta} \sim (1 - \phi/\phi_m)^{-2}$ and $\chi_i \sim (1 - \phi/\phi_m)^{-3}$ as $\phi \to \phi_m$, a form also used in constitutive modeling by Frank et. al. [61]. Note also that the magnitudes of $\hat{N}_1$ and $\hat{N}_2$ are similar up to $\phi = 0.37$, above which ϕ the value of $\hat{N}_2$ grows more rapidly than $\hat{N}_1$.

We now consider the rheology determined from the structure deduced based on the full theory. We focus on strongly perturbed microstructures over a range of Pe and ϕ and compare the predicted rheology with simulation results.

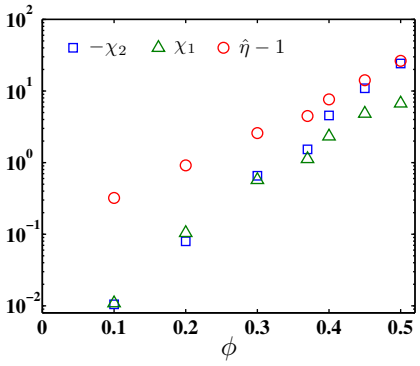

Figure 2.13: Near-equilibrium predictions based on the perturbation analysis of the microstructure, for $\chi_1 = \hat{N}_1/Pe$ and $-\chi_2 = -\hat{N}_2/Pe$ at different volume fractions. The zero-shear viscosity values are also presented.

Figures 2.14(a) and 2.14(b) compare the theoretically predicted values for Brownian and hydrodynamic contributions to shear viscosity to the simulation results for $\phi = 0.30$ and 0.40, respectively, considering a range of Pe. The error bars are the standard deviation of the shear viscosity from its average value, as determined by simulation. The relative magnitude of the error bar with respect to the average value for each Pe is similar for both $\phi = 0.30$ and 0.40, and the error bars are only presented for a few data points at $\phi = 0.40$ to aid visualization. However, we note that the error bars become smaller as Pe increases. For both ϕ, the decrease in Brownian viscosity with increasing Pe in the lower range of Pe and increase of hydrodynamic viscosity at high Pe are more pronounced in the predicted results than seen in simulation. This results in stronger shear thinning and shear thickening of the total viscosity for the theory than is observed in simulation. In essence, the theory over-predicts the apparent shear stress, and we find that the agreement is improved if the theoretically predicted results are shifted to higher values of Pe.

Figures 2.15(a) and 2.15(b) compare the predicted Pe-dependence of the first and second normal stress differences with simulation results for $\phi = 0.40$. The dotted lines for $0.01 \leq Pe \leq 0.2$ are the near-equilibrium perturbation results for $\hat{N}_1 = \chi_1 Pe$ and

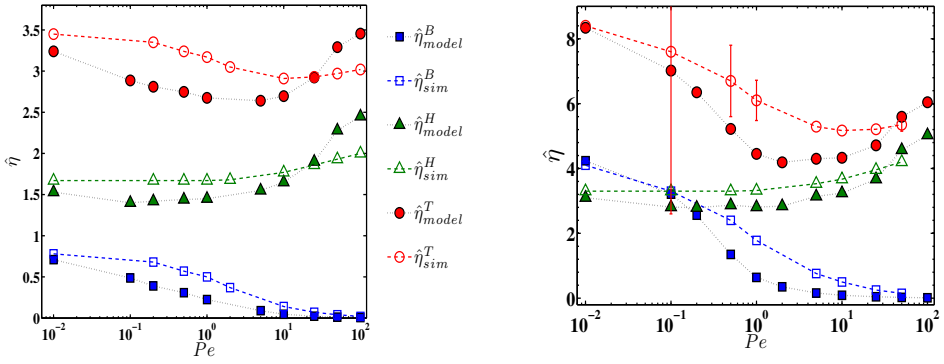

(a) $\phi = 0.30$ (b) $\phi = 0.40$

Figure 2.14: Brownian (■, □) and hydrodynamic (▲, △) contributions and total value (○, ●) of relative viscosity as a function of Pe for (a) $\phi = 0.30$ and (b) $\phi = 0.40$ from theory and ASD simulation. The predictions at $Pe = 0.01$ are from the perturbation solutions for the microstructure.

$\hat{N}_2 = \chi_2 Pe$ (see figure 2.13). The Brownian contributions are given in the inset figures. The predicted (normalized) normal stress differences tend linearly to zero for $Pe \ll 1$. As a result, a maximum is predicted in $\hat{N}_1$, which changes sign from positive to negative at intermediate Pe. The comparison shows that the signs and general trends for the normal stress difference are predicted correctly. Quantitative agreement is not obtained. Similar to the shear viscosity, the magnitude of the Brownian contribution decreases with Pe more rapidly in predictions than is found in simulation. The absolute value of $\hat{N}_1$ for $Pe \gg 1$ is also significantly over-predicted. The error bars for simulation results are not presented to aid visualization. The values of error bars increase from 0.3 at $Pe = 100$ to about 8 at $Pe = 0.01$ with the values being similar for $\hat{N}_1$ and $\hat{N}_2$. We note that simulations have yet to recover the approach to zero normal stress differences very near equilibrium and the results become increasingly uncertain at smaller Pe.

Figure 2.16 presents the variations of shear viscosity and normal stress differences with volume fraction at $Pe = 10$. Error bars for the simulation data are of the same order of magnitude for $\hat{N}_1$ and $\hat{N}_2$, and are presented only for $\hat{N}_2$. Error bars for shear

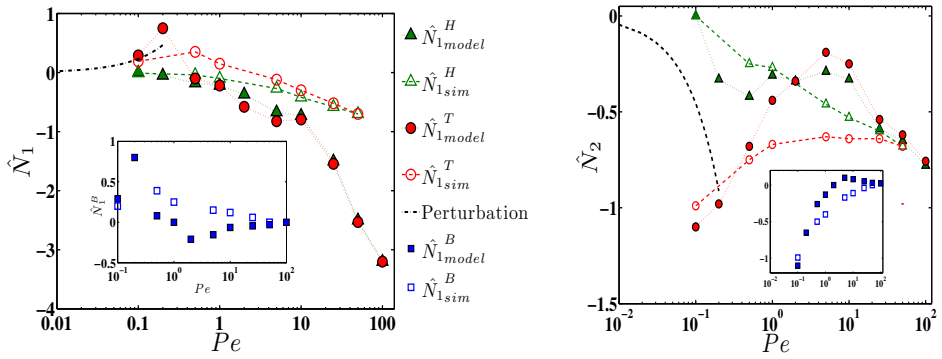

(a) (b)

Figure 2.15: Dimensionless (a) first and (b) second normal stress differences for $\phi = 0.40$ as a function of Pe. The inset figures present the Brownian contributions and the dotted lines at $Pe < 0.20$ are the perturbation results. Filled symbols present the predictions and the open symbols are the results of ASD simulation.

viscosity are the size of the symbols and are not presented. The results are presented for $\phi < 0.50$ where the system is in the disordered state for all Pe; we avoid consideration of the ordered phase formed at $Pe \geq 10$ and $\phi \geq 0.50$ in simulations [62]. The predictions and simulation results for shear viscosity are in good agreement while for normal stresses, the predictions have the correct sign and are within the range of error bars. However, the magnitude of first and second normal stress differences are over- and under-predicted, respectively (except at the lowest volume fraction, $\phi = 0.20$). The same trend is observed for higher Pe. This suggests that the anisotropy of the predicted structure has a systematic deviation from the observed structure in simulation, but the precise basis has not been determined.

2.6.3 Discrepancies between theory and simulation

The theory developed here breaks significant new ground in describing the microstructure of concentrated nonequilibrium dispersions. In order to facilitate further progress in theoretical rheology of dispersions using this theory, its shortcomings as seen in com-

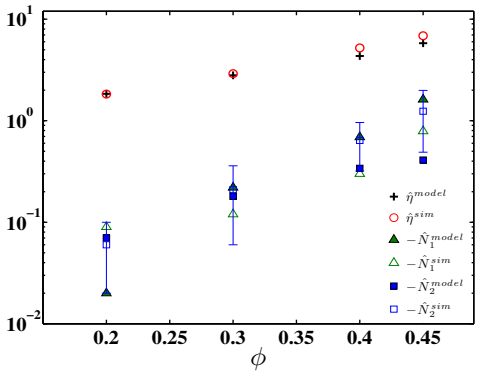

Figure 2.16: The predictions and simulation results for normalized shear viscosity and normal stress differences at $Pe = 10$ and different ϕ.

parisons against Stokesian Dynamics simulations are outlined briefly.

As shown in figures 2.4 and 2.5, the distortion of microstructure from the equilibrium distribution is stronger in theoretical predictions. Direct consequences for the rheology are seen in the stronger predicted shear thinning and shear thickening; in addition, this leads to the decrease in Brownian normal stress differences at lower Pe relative to those seen in simulation, as shown in figure 2.14 and the insets of figures 2.15(a) and 2.15(b). Although the average value of pair distribution function near contact is accurately predicted, the predicted microstructural anisotropies are generally systematically over-predicted: the predictions generally correspond to simulation results seen for either higher ϕ at the same Pe, or at a higher Pe for the same ϕ. This is clearly seen in figure 2.6 where the locations of the peaks at each ϕ resemble simulation data for a denser suspension at the same Pe. Hence, as shown in figures 2.6 and 2.8, the theory over-predicts the peak in $g(2)$ in the flow direction. This impacts upon the rheology as expected: $\hat{\Sigma}_{xx}$ has a stronger compressional (negative) component than the simulations while $\hat{\Sigma}_{yy}$ is less compressive which causes larger negative $\hat{N}_1$ and smaller negative $\hat{N}_2$, as seen in figures 2.15 and 2.16.

2.7 Concluding remarks

A microstructural theory for concentrated colloidal dispersions of near-hard spheres has been developed based on the Smoluchowski equation. The theory results in an integro-differential equation for the pair distribution function, which for steady simple-shear flow is studied here for Péclet numbers ranging from near equilibrium to strongly sheared conditions. The resulting structure is applied to predict the steady shear rheology of the suspension, and both structure and rheology are compared against our own simulations by the Accelerated Stokesian Dynamics algorithm. Agreement between simulation and the predictions of the theory are qualitatively very good, with some systematic quantitative discrepancies which have been described.

In formulation of both the microstructural theory and the rheology, simplifications based on the central role played by near-contact interactions are employed. The resulting approximations allow a reduction of the many-body hydrodynamic interactions to pairwise lubrication interactions. The success of the approach reveals an important aspect of how correlation is transferred in suspensions under shear flow. This theory is motivated in part by the integral equation techniques for equilibrium structure in liquids [17]. The similarity lies in the coupling of the interaction between the pair of interest to the influence of the bath through probabilistic methods. However, the earlier integral equation techniques are formulated as equilibrium methods and thus their extension to nonequilibrium conditions is unclear. By contrast, the Smoluchowski equation is intrinsically a transport equation for the probability distribution for configurations, and it thus introduces rate dependence naturally. When reduced to a description of the pair distribution function as we have done here, the coupling to the other particles is directly seen in the average forces these particles apply to drive the pair together or apart. This is physically appealing and leads naturally to approximations allowing analytical progress.

A feature in the theory which is novel is the introduction of a shear-induced component to the relative diffusion of a pair of particles. This diffusivity is closely related to the

shear-induced self-diffusivity [54, 50], but in prior treatments of the structure of sheared suspensions has not been implemented. For theories considering dilute dispersions [27], this is justified, but at ϕ not near zero there is clearly a dispersion around the mean pair relative velocity. From a Fokker-Planck perspective on the microstructure, this dispersion — which will be dominated by shear effects at elevated Pe for moderately to highly concentrated dispersions — must be included to obtain a proper description. In fact, we find that neglecting this dispersion while including the mean forces (due to the surrounding particles) driving a pair interaction leads to divergence in the pair correlation at contact. Hence, we see that the source of the large microstructural correlation seen in the pair distribution function self-consistently contains fluctuations which allow sufficient relaxation to achieve a steady microstructure. The shear-induced relative diffusion in the radial direction contains the only truly tuned fitting parameter in the theory, and this illustrates its centrality to the description of the microscopic dynamics. The shear-induced diffusivity has been simply modeled here, owing to lack of concrete information. Simulational evaluation of the pair relative diffusivity appears to be a valuable avenue of study.

The rheological predictions of the theory are qualitatively in agreement with all major observations from simulation and experiment, or predictions of other theory where applicable. We predict shear thinning and thickening. The normal stress differences determined are in agreement with theoretical expectations from Brady & Vicic [47] for $Pe \ll 1$, with this theory extended in the present work. At elevated Pe, the predicted structure deviates from the simulationally determined structure, but predicts the tendency for particles to align along the flow direction for $\phi \geq 0.35$, as noted previously by Morris & Katyal [48]. The predictions of the rheology thus deviate from the simulation results. We find that the theory agrees progressively better with simulation results of structure, and hence of rheology, as ϕ increases. This suggests that the simplifications made based on the dominance of near-contact lubrication interactions are sound but

must be modified to obtain quantitative agreement at lower ϕ. One possible explanation for the observed discrepancy is the inaccuracy of pair-wise additivity assumption of lubrication forces along directions other than $\hat{\mathbf{r}}$. Note that the lubrication interactions are primarily imposed along the line of centers and the interactions are considerably weaker in other directions. The pair-wise summation of forces in $\hat{\theta}$ and $\hat{\varphi}$ directions results in over-prediction of correlation of the pair of interest with bath particles in these directions. As a result the predicted boundary layer features are stronger than simulation and predicted structures resemble simulation results at larger ϕ and Pe. We are currently working on this issue but results are not conclusive enough to report here.

Increasing solid fraction at fixed Pe is found to cause an increase in the pair distribution function variations, with the contact values especially amplified. This effect may in part be captured in scaling arguments which seek to rescale the "driving force" — this amounts to a rescaling of the effective Péclet number. However, the structure is found to differ in a more complex fashion than this with change in ϕ in a sheared dispersion. The anisotropy at contact develops additional features, with development of additional peaks (local maxima) for larger ϕ, and as noted there is a shift to a maximum in pair correlation along the streamlines seen in both the theory developed here and in simulations. This makes a simple scaling of the volume-fraction dependence of the rheology of dispersions suspect.

Although only a very steep repulsive potential (as a model for hard sphere potential) was considered here, the theory can be used to study systems with different forms of interparticle interactions. This was shown in Nazockdast & Morris[63] where sheared suspensions with soft repulsive potentials were studied using the same theoretical framework and compared with ASD simulations. The predictions for structure and rheology were in reasonable agreement with simulated results over a range of steepness of the repulsive potential.

A final point to note is that while the theory was developed here for simple-shear

flow, the approach is applicable to general linear-flow kinematics, i.e. for bulk flows which can be written $\mathbf{U}^{\infty} = \mathbf{G}\cdot\mathbf{x}$ where $\mathbf{G}$ is a constant velocity gradient tensor. For other kinematics than simple shear, abundant simulation results are unfortunately not generally available.

2.8 Appendix

We describe the process of computation of $\langle \mathbf{M} \rangle_2$. The effect of "bath" particles on relative mobility is divided to near-contact and far-field effects. Bath particles are modeled through a probabilistic third particle labeled as particle 3 in relations (2.26) and (2.27). Near-contact configurations are defined here where $r_{31} < 2.3$ or $r_{32} < 2.3$ and far-field is defined as the region where both r_{31} and r_{32} are greater than 2.3. For "near-contact" configurations the symmetric resistance tensor for the triplet configuration is built based on pair-wise summation of individual pair resistance tensors and the triplet mobility tensor is computed by inversion:

$$\begin{bmatrix} \begin{bmatrix} \mathbf{M}^{11} & \mathbf{M}^{12} \\ . & \mathbf{M}^{22} \end{bmatrix} & \mathbf{M}^{13} \\ \mathbf{M}^{23} \\ . \quad . & \mathbf{M}^{33} \end{bmatrix} = \begin{bmatrix} \mathbf{R}^{11,2} + \mathbf{R}^{11,3} & \mathbf{R}^{12} & \mathbf{R}^{13} \\ . & \mathbf{R}^{22,1} + \mathbf{R}^{22,3} & \mathbf{R}^{23} \\ . & . & \mathbf{R}^{33,1} + \mathbf{R}^{33,2} \end{bmatrix}^{-1} . \quad (2.46)$$

Terms below the diagonal may be obtained from the matrix symmetry.

We consider the configuration of particles 1, 2 and 3 in the near-contact configuration forming a line with particle 3 in the central position. The effect of bath particles on pair dynamics is maximized in this configuration and thus it is an ideal example to illustrate the formulation. In this case $R_{rr}^{12} \approx O(1)$ and the connectivity of particles 1 and 2 through particle 3 is not apparent in this initial form of $\mathbf{R}^{12}$. Inverting the resistance matrix allows for coupling of motion of the three particles through the mobility matrix,

resulting in $M_{rr}^{11} \approx M_{rr}^{12}$. Subsequently, $\mathbf{R}$ in (2.26) is obtained by inverting the matrix within the mobility matrix between the interior square brackets on the left hand side:

$$\begin{bmatrix} \mathbf{R}^{11} & \mathbf{R}^{12} \\ . & \mathbf{R}^{22} \end{bmatrix} = \begin{bmatrix} \mathbf{M}^{11} & \mathbf{M}^{12} \\ . & \mathbf{M}^{22} \end{bmatrix}^{-1}, \tag{2.47}$$

with

$$\mathbf{R} = \mathbf{R}^{11} - \mathbf{R}^{12}.$$

This formulation allows for a proper accounting for configurations of two particles being connected through intermediate bath particles. As an example, $R_{rr}^{11} \to \infty$ and $R_{rr}^{12} \to \infty$ along the line of centers for the configuration of having three particles in a line with particle 3 in between. Having $\mathbf{R}$ at each triplet configuration, $\langle \mathbf{R} \rangle_2$ can be computed using (2.26) repeated here:

$$\langle \mathbf{R} \rangle_2(\mathbf{r}) g = \mathbf{R}_{pair}(\mathbf{r}) g + n \int \Big(\mathbf{R}(\mathbf{r}, \mathbf{r}_{31}, \mathbf{r}_{32}) - \mathbf{R}_{pair}(\mathbf{r}) \Big) g_3 d\mathbf{r}_{31}.$$

The change in pair mobility due to near-contact interactions of pair with bath particles is obtained by $\langle \Delta \mathbf{M} \rangle_2^{lub} = \langle \mathbf{R} \rangle_2^{-1} - \mathbf{M}_{pair}$ where superscript *lub* refers to near-contact or lubrication configurations.

When the third particle is not in near contact with particles 1 and 2, the effect of bath particles on pair mobility is computed using pair-wise summation of third particle effect on mobility using (2.27), repeated here:

$$\langle \mathbf{M} \rangle_2(\mathbf{r}) g = \mathbf{M}_{pair}(\mathbf{r}) g + n \int \Big(\mathbf{M}(\mathbf{r}, \mathbf{r}_{31}, \mathbf{r}_{32}) - \mathbf{M}_{pair}(\mathbf{r}) \Big) g_3 d\mathbf{r}_{31}.$$

The effect of bath particles far from the pair when particles 1 and 2 are near contact requires special treatment. Although the far-field effect may be studied within a mobility formulation, the method of reflections cannot be readily applied since in practice a large number of reflections would be required to give a reasonable answer. To address this

issue, the far-field calculation is divided to two parts , $r \geq 2.3$ and $r < 2.3$. We compute the far-field three-body hydrodynamic effects explicitly for all far-field triplet configurations with $r \geq 2.3$. We compute $\mathbf{M}(\mathbf{r}, \mathbf{r}_{31}, \mathbf{r}_{32})$ using the expressions derived in [53] and use (2.27) to compute $\langle \mathbf{M} \rangle_2(\mathbf{r})$ for $r \geq 2.3$. Finally we use a matching process to approximate the form of far-field mobility when $r < 2.3$ as follows.

1) For $r < 2.3$ we make the assumption that contributions to 11 and 22 components of mobility remain similar to their values at $r = 2.3$ which gives $\langle \Delta\mathbf{M}^{11} \rangle_2^{far}(r, \theta, \varphi) = \langle \Delta\mathbf{M}^{11} \rangle_2^{far}(2.3, \theta, \varphi)$, and by pair symmetry $\langle \Delta\mathbf{M}^{11} \rangle_2^{far}(r, \theta, \varphi) = \langle \Delta\mathbf{M}^{22} \rangle_2^{far}(r, \theta, \varphi)$.

2) To ensure a zero radial velocity at contact, $\langle \Delta M_{rr}^{12} \rangle_2^{far} \rightarrow \langle \Delta M_{rr}^{11} \rangle_2$ as $r \rightarrow 2$. To satisfy this condition and also match the far-field solution at $r = 2.3$, we linearly interpolate $\langle \Delta M_{rr}^{12} \rangle_2^{far}$ between $\langle \Delta M_{rr}^{12} \rangle_2^{far}$ at $r = 2.3$ to $\langle \Delta M_{rr}^{11} \rangle_2^{far}$ at $r = 2$ when $r < 2.3$:

$$\langle \Delta M_{rr}^{12} \rangle_2^{far}(r, \theta, \varphi) = \frac{(r-2)}{0.3} \langle \Delta M_{rr}^{12} \rangle_2^{far}(2.3, \theta, \varphi) + \frac{(2.3-r)}{0.3} \langle \Delta M_{rr}^{11} \rangle_2^{far}(2, \theta, \varphi). \quad (2.48)$$

Also we assume $\langle \Delta\mathbf{M}^{12} \rangle_2(r, \theta, \varphi) = \langle \Delta\mathbf{M}^{12} \rangle_2(2.3, \theta, \varphi)$ in directions other than radial direction at $r < 2.3$.

3) Finally the average pair mobility is computed by summation of the near-field and far-field effects with the isolated pair mobility:

$$\langle \mathbf{M} \rangle_2 = \mathbf{M}_{pair} + \langle \Delta\mathbf{M} \rangle_2^{far} + \langle \Delta\mathbf{M} \rangle_2^{lub}. \quad (2.49)$$

3 Extension to colloidal suspensions with soft repulsive interactions [2]

3.1 Introduction

Suspensions of Brownian particles in a viscous fluid, typically termed colloidal suspensions, can be found in a wide range of natural and industrial applications [4]. Colloidal particles generally interact through Brownian and interparticle forces, as well as through hydrodynamic interactions arising from the flow induced in the suspending fluid by the presence of the particles. These interactions determine the spatial distribution of particles relative to one another. This distribution in an average sense is commonly referred to as microstructure. The bulk properties, in particular the suspension rheology, are strongly influenced by the microstructure. In equilibrium the behavior is governed by the balance between Brownian (thermal) and interparticle forces. When the dispersion is subjected to flow, the structure is driven out of equilibrium. Under such conditions, flow-induced forces and hydrodynamic interactions may become comparable to (or dominate) thermal and interparticle forces. As a result, the microstructure and flow behavior of suspensions are coupled.

The relationship between microstructure and rheology of colloidal dispersions has been the subject of extensive theoretical [64, 65] and experimental [33] work. In addition, development of reliable dynamic simulation techniques has significantly improved our

[2] The contents of this chapter are published as a paper in *Soft Matter* [63].

understanding on colloidal (as well as noncolloidal) suspensions [29, 31, 66]. The simplest form of colloidal suspensions – and arguably the simplest of complex fluids – are hard-sphere (HS) colloids, where particles are subject only to hydrodynamic and thermal forces. The structure in shear flows of HS colloids is only a function of two dimensionless quantities, namely the particle volume fraction, ϕ, and the ratio of hydrodynamic to thermal forces given by the Péclet number, $Pe = \dfrac{6\pi\eta\dot{\gamma}a^3}{k_bT}$. Here η is the fluid viscosity, $\dot{\gamma}$ is the shear rate, a is the particle radius and k_bT is the thermal energy. Experiments and simulations have provided a detailed picture of HS colloidal dispersion structure and rheology. However, most prior theoretical studies have been limited to near-equilibrium, $Pe \ll 1$, [46, 24, 67] and dilute ($\phi \to 0$) hard-sphere suspensions [47, 27, 28]. The main difficulty in extending the theories to high Pe and ϕ is formulating the many-body interactions, and in particular the hydrodynamic interactions, which play a key role in determining the behavior under these conditions. In recent work [32], we have developed a theory for concentrated hard-sphere suspensions under shear; the approach is based upon solving the Smoluchowski equation for the pair distribution function $g(\mathbf{r})$, accounting for the many-body effects through an integro-differential formulation of the problem. The theory has been demonstrated to capture the main features of the near hard-sphere (employing an extremely short-range repulsion) structure and nonlinear rheology over a wide range of volume fraction ($\phi \leq 0.55$) for $0 < Pe \leq 100$.

The current work extends this theory to the case of particles interacting through extended range repulsive potentials of conservative form, representative of colloidal particles carrying a surface charge. The general purpose of this work is to study a more complex class of colloidal suspensions in order to establish the general validity of the noted theoretical approach [32], and its ability to predict the rheology of soft-sphere dispersions. In addition, we perform Accelerated Stokesian Dynamics (ASD) simulations [31] for further insight and to allow direct comparison with the theoretical predictions. The description of the simulation method is given in §2.5 and the original papers [41, 31].

The effect of the range of interparticle interactions is investigated, by considering equivalent soft repulsive potentials in both simulations and theory, with varying steepness of the interparticle potential. Predicted and simulated microstructure and rheology are presented and compared over a wide range of Péclet numbers ($0.1 \leq Pe \leq 100$).

As background, we note that the microstructure of soft colloids under shear has been widely studied using dynamic simulation techniques such as non-equilibrium Brownian dynamics [68, 69]. In these computational studies the hydrodynamic interactions are neglected and the structure is determined by the balance of interparticle and Brownian forces, as well as a simple constant viscous drag owing to particle motion relative to the fluid. In contrast to this, both the ASD simulations and our theoretical formulation capture hydrodynamic interactions. This allows for systematic study of behavior of colloidal suspensions ranging from hard spheres to soft repulsive colloids, and in particular investigation of the role of hydrodynamic interactions on flow-induced structures and the resulting flow behavior. Studying soft colloidal suspensions thus allows us to probe the applicability of assumptions made in the theory for formulating the hydrodynamic interactions. In soft colloids, the extended range repulsive interactions limit the approach of particles to contact, so that lubrication interactions are significantly reduced and the conservative forces are dominant, although the results are modulated by hydrodynamic interactions. The roles of the various forces are probed by comparing the predictions with ASD simulation results for varying range of the repulsive interaction, as well as for the near hard-sphere dispersion, over a range of shear rate (in dimensionless form, Pe).

In the following section, the theory is outlined. In §3.3, the formulation of the rheology and its coupling to the microstructure is provided. Results of the theory for the hard- and soft-sphere dispersions are given in §3.4.

3.2 Formulation

We consider suspensions in shear flow at very small particle-scale Reynolds number, $Re = \rho\dot{\gamma}a^2/\eta \ll 1$ where ρ is the common density of the particles and fluid, a is the particle radius, $\dot{\gamma}$ is the shear rate, and η is the viscosity of the suspending fluid. Thus inertia is negligible and Stokes equations govern the motion. The microstructural arrangement of the particles is governed by the Smoluchowski equation, which for the N-particle configuration space is written [5]

$$\frac{\partial P_N}{\partial t} + \sum_{\alpha=1}^{N} \nabla_\alpha \cdot \mathbf{j}_\alpha = 0, \tag{3.1}$$

where $P_N(\mathbf{x}_1, \mathbf{x}_2, ..., \mathbf{x}_N)$ is the N-particle configurational probability distribution, and $\mathbf{j}_\alpha$ is the probability flux associated with particle α. The flux is expressed as

$$\mathbf{j}_\alpha = \left(\mathbf{U}_\alpha^H + \sum_{\beta=1}^{\beta=N} \mathbf{M}_{\alpha\beta}^{FU} \cdot \mathbf{F}_\beta \right) P_N - \sum_{\beta=1}^{\beta=N} \mathbf{D}_{\alpha\beta} \cdot \nabla_\beta P_N, \tag{3.2}$$

where $\mathbf{U}_\alpha^H$ is the velocity of particle α induced by bulk flow and hydrodynamic interactions with other particles, $\mathbf{M}_{\alpha\beta}^{UF}$ is the mobility of particle α to a force on particle β, and $\mathbf{D}_{\alpha\beta} = k_b T \mathbf{M}_{\alpha\beta}^{UF}$ is the diffusion tensor. The force exerted on particle β is expressed in terms of an interparticle potential V as $\mathbf{F}_\beta = -\nabla_\beta V$, where ∇_β is the gradient with respect to the position of particle β. For the near hard-sphere suspension, we approximate $\mathbf{U}_\alpha^H$ by assuming that hydrodynamic interactions are primarily lubrication interactions near contact, with $\mathbf{U}_\alpha^H$ formulated as

$$\mathbf{U}_\alpha^H = \mathbf{U}_\alpha^\infty + \mathbf{M}_{\alpha\beta}^{UF} \cdot \mathbf{F}_\alpha^{lub}, \tag{3.3}$$

where ${\mathbf{U}_\alpha}^\infty$ is the average velocity at the center of particle α. We define $\mathbf{F}_\alpha^{lub}$ as the lubrication force applied by particle β on particle α to impose the excluded volume, with

this force given by

$$\mathbf{F}_{\alpha}^{lub} = \mathbf{R}_{\alpha\beta}^{FE} : \mathbf{E} = -6\pi\eta a\Big(X(r)(\hat{\mathbf{r}}\cdot\mathbf{E}\cdot\hat{\mathbf{r}})\hat{\mathbf{r}} + Y(r)\big(\mathbf{E}\cdot\hat{\mathbf{r}} - (\hat{\mathbf{r}}\cdot\mathbf{E}\cdot\hat{\mathbf{r}})\hat{\mathbf{r}}\big)\Big),$$

where $\mathbf{E} = (\nabla\mathbf{U}^{\infty} + \nabla\mathbf{U}^{\infty T})/2$ is the average bulk strain rate tensor, $\mathbf{R}_{\alpha\beta}^{FE}$ is the resistance function coupling force and torque to strain rate and $X(r)$ and $Y(r)$ are well-known functions of the pair separation distance[30], $r = |\mathbf{r}|$, with $\mathbf{r} = \mathbf{x}_2 - \mathbf{x}_1$ for particles labeled 1 and 2. To reduce to an equation for the pair microstructure, (3.1) is integrated over all possible configurations of $N-2$ particles keeping two particles fixed, yielding

$$\nabla_{\mathbf{r}}\cdot\left(\mathbf{U}^{\infty}g + \langle\mathbf{M}\rangle_2\cdot\left(\langle\mathbf{F}^{P}\rangle_2 + \langle\mathbf{F}^{lub}\rangle_2\right)g - \langle\,\mathbf{D}\rangle_2\cdot\nabla_{\mathbf{r}}g\right) = 0, \tag{3.4}$$

where $\mathbf{F}^{P}$ are forces due to the interparticle potential. We have defined the pair distribution function as $g(\mathbf{r}) = P_2(\mathbf{r})/n^2$ where $P_2(\mathbf{r})$ is the conditional pair probability for finding a second particle at a separation $\mathbf{r}$ given a particle at the origin, and n is the average number density of particles. The average of a function $A(\mathbf{r})$ at a fixed separation is denoted $\langle\,A\,\rangle_2(\mathbf{r})$, with the averaging performed over all possible configurations of the other $N-2$ "bath" particles. We define relative forms of the velocity, diffusion, and mobility, respectively, as

$$\mathbf{U} = \mathbf{U}_2 - \mathbf{U}_1, \tag{3.5a}$$

$$\mathbf{D} = 2\big(\,\mathbf{D}_{11} - \mathbf{D}_{12}\,\big), \tag{3.5b}$$

$$\mathbf{M} = 2\big(\mathbf{M}_{11}^{UF} - \mathbf{M}_{12}^{UF}\big) = 2\big(\mathbf{R}_{11}^{FU} - \mathbf{R}_{12}^{FU}\big)^{-1}, \tag{3.5c}$$

and the force between the particles is expressed in a relative form as

$$\mathbf{F} = \mathbf{F}_2 = -\mathbf{F}_1 \tag{3.5d}$$

In developing (3.4), we have made a mean-field approximation, assuming that the

particle pair of interest is immersed in a field that contains the average effect of the bath of other particles. As a consequence, fluctuations in force and mobility are neglected, which leads to

$$\langle \mathbf{M} \cdot \mathbf{F} \rangle_2 = \langle \mathbf{M} \rangle_2 \cdot \langle \mathbf{F} \rangle_2. \tag{3.6}$$

However, flow-induced fluctuations of force and mobility generally cause particles to execute a random walk in addition to the mean motion, which may be captured by modifying $\langle \mathbf{D} \rangle_2$ to the form

$$\langle \mathbf{D} \rangle_2 = k_b T \langle \mathbf{M} \rangle_2 + \langle \mathbf{D}^{\dot{\gamma}} \rangle_2, \tag{3.7}$$

where $k_b T \langle \mathbf{M} \rangle_2$ is the well-known Brownian diffusion and $\langle \mathbf{D}^{\dot{\gamma}} \rangle_2$ is the shear-induced relative diffusion. Including $\langle \mathbf{D}^{\dot{\gamma}} \rangle_2$ is crucial to the success of the theory for near hard-spheres, as neglect of this term while including the forces induced by bath particles causes a divergence in $g(r = 2a)$, i.e. in pair probability at contact. However, for soft colloidal particles, it is not essential to include the shear-induced relative diffusion, a point to be discussed later.

To develop their dimensionless counterparts, quantities in (3.4) are scaled as

$$\begin{gathered} \mathbf{r} \sim a; \quad \mathbf{D} \sim D_0; \quad \mathbf{M} \sim D_0/k_b T. \\ \mathbf{F}^P \sim k_b T/a; \quad \mathbf{F}^{lub} \sim 6\pi\eta\dot{\gamma}a^2; \quad \mathbf{U}^\infty \sim \dot{\gamma}a, \end{gathered} \tag{3.8}$$

where $D_0 = k_b T/6\pi\eta a$. In dimensionless form, (3.4) becomes

$$\nabla \cdot \left[\mathbf{U}^\infty g + \langle \mathbf{M} \rangle_2 \cdot \Big(Pe \langle \mathbf{F}^{lub} \rangle_2 + \langle \mathbf{F}^P \rangle_2 \Big) g - Pe^{-1} \langle \mathbf{D} \rangle_2 \cdot \nabla g \right] = 0, \tag{3.9a}$$

$$\mathbf{j}_\mathbf{r} = 0 \quad \text{at} \quad r = 2, \tag{3.9b}$$

$$g \to 1 \quad \text{as} \quad r \to \infty, \tag{3.9c}$$

where the first boundary condition implies zero radial flux at contact. We have used $\nabla = a\nabla_{\mathbf{r}}$ as the dimensionless gradient operator in relative coordinates, and we define the Péclet number,

$$Pe = \frac{\dot{\gamma}a^2}{D_0} = \frac{6\pi\eta\dot{\gamma}a^3}{k_bT}. \tag{3.10}$$

In the convection-diffusion equation for the pair microstructure, the conditionally-averaged quantities $\langle \mathbf{F}^{lub} \rangle_2$, $\langle \mathbf{F}^P \rangle_2$, $\langle \mathbf{M} \rangle_2$ and $\langle \mathbf{D} \rangle_2$ should be expressed in terms of $\mathbf{r}$ and g, as we now discuss.

Lubrication and interparticle forces are assumed to be pair-wise additive. Hence, the conditional average forces are formulated as

$$\langle \mathbf{F}_1 \rangle_2 g(\mathbf{r}) = \mathbf{F}_{21}(\mathbf{r})g(\mathbf{r}) + n \int \mathbf{F}_{31}(\mathbf{r}_{31})\, g_3(\mathbf{r}, \mathbf{r}_{31}) d\mathbf{r}_{31}. \tag{3.11}$$

Here, $g_3(\mathbf{r}, \mathbf{r}_{31})$ is the triplet distribution expressing the relative likelihood (this quantity is normalized to have value of unity for all particles widely deparated) of having particle 1 simultaneously at separations of $\mathbf{r}$ and $\mathbf{r}_{31}$ with respect to particle 2 and 3. The forces $\mathbf{F}_{21}$ and $\mathbf{F}_{31}$ are exerted on particle 1 by particles 2 and 3, respectively. It is necessary to express the triplet distribution, g_3, in terms of pair distribution function, g, through a closure approximation. A modification of the well-known Kirkwood superposition approximation proposed by Rice and Lekner[51], given by

$$g_3(\mathbf{x}_1, \mathbf{x}_2, \mathbf{x}_3) = g(\mathbf{r}_{21})g(\mathbf{r}_{31})g(\mathbf{r}_{32}) \exp(\tau^\star(\mathbf{r}, \mathbf{r}_{31}, \phi)), \tag{3.12}$$

was used in this work. This approximation modifies the standard Kirkwood superposition approximation through the exponential term, which evaluates correlations between particles 1,2 and 3 and other particles using "simple 123-irreducible cluster" defined by Salpeter [70]. Rice and Lekner carried out the extension to 5 particles using a Padé expansion. The details of the formulae and tabulated function are best obtained from the

original work[51]. This closure gives very good agreement at equilibrium, $Pe = 0$, up to $\phi = 0.40$, the upper limit on ϕ for the Kirkwood approximation for the equilibrium triplet structure in hard-sphere liquids. Previous work[52] by Stokesian Dynamics simulation on the triplet distribution under shear flow in a colloidal dispersion also showed that Kirkwood approximation gives reasonable accuracy at $Pe \gg 1$ which makes this closure a suitable one in the absence any obviously more appropriate alternative. We study the role of particle interactions by considering two types of Brownian suspensions, namely near hard-sphere dispersions and colloidal suspensions interacting through a long-range repulsive potential. The interparticle forces are described by

$$\mathbf{F}^{HS} = -(k_bT/a)\frac{\tau \exp[-\tau(r-2)]}{1-\exp[-\tau(r-2)]}\hat{\mathbf{r}}, \tag{3.13}$$

in the near hard-sphere case, and by a Yukawa potential,

$$\mathbf{F}^{P} = -(k_bT/a)\xi\frac{\exp[-\kappa(r-2)]}{r}(\kappa + 1/r)\hat{\mathbf{r}}, \tag{3.14}$$

in the case of the extended range repulsion. The parameter values of $\tau = 200$ and $\xi = 25$ were chosen for hard-sphere and soft repulsion potentials, respectively. Note that (3.14) goes to a finite value at $r = 2$. To study the effect of the range of interactions on structure and rheology, values of $\kappa = 3.8$, 6, and 12 were chosen, with the volume fraction fixed at $\phi = 0.20$. The corresponding radial forces between particles are shown in figure 3.1. The soft repulsion between the colloidal particles causes the particles to occupy a larger effective volume compared to the hard-spheres at equal true volume fractions. The effective volume fraction at equilibrium is approximated by $\phi_{\text{eff}} = (r_{\text{eff}}/2)^3\phi$, where r_{eff} is the radius at which the interparticle potential equals k_bT. For the Yukawa potential with the noted coefficients, $\phi_{\text{eff}} = 0.47$, 0.34, and 0.27 for $\kappa = 3.8$, 6, and 12, respectively.

Calculation of the conditional average mobility depends on the pair separation. For particles near contact, the influence of the bath particles is determined through a resis-

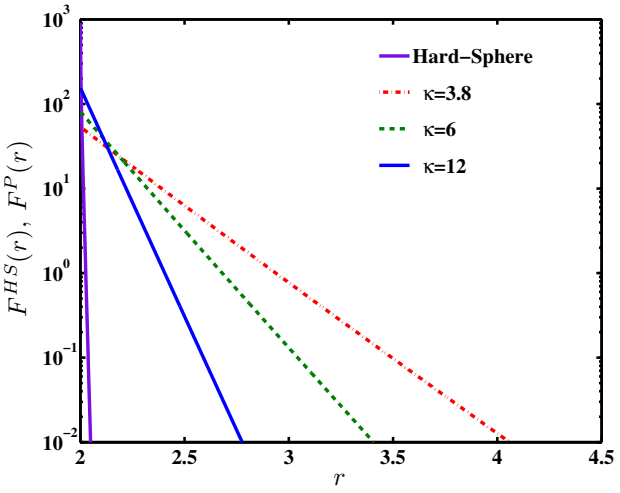

Figure 3.1: The interparticle forces for hard-sphere and Yukawa potential with $\kappa = 3.8$, 6, and 12, scaled by k_bT/a.

tance formulation, whereas for well-separated pairs, a mobility formulation is used. For nearly-touching configurations, $\langle \mathbf{R} \rangle_2$ is formulated as

$$\langle \mathbf{R} \rangle_2(\mathbf{r})g = \mathbf{R}_{pair}(\mathbf{r})g + n \int \Big(\mathbf{R}(\mathbf{r}, \mathbf{r}_{31}, \mathbf{r}_{32}) - \mathbf{R}_{pair}(\mathbf{r}) \Big)\, g_3 d\mathbf{r}_{31}, \tag{3.15}$$

where $\mathbf{R}(\mathbf{r}, \mathbf{r}_{31}, \mathbf{r}_{32})$ is the resistance to relative motion for particles 1 and 2 in the presence of a third particle and $\mathbf{R}_{pair}(\mathbf{r})$ is the equivalent resistance of the isolated pair 1 and 2. The term in parentheses in the integrand of (3.15) is thus the change (increase quite generally) of the pair resistance with respect to the isolated pair due to the other particles, as captured through the third-particle integral. To calculate the resistance components in triplet configurations for particles near contact, the resistance is assumed to be pair-wise additive. The resistance determined in this way is then inverted to obtain the modified mobility due to lubrication interactions. When the particles are well-separated the bath particle effect is formulated as

$$\langle \mathbf{M} \rangle_2(\mathbf{r})g = \mathbf{M}_{pair}(\mathbf{r})g + n \int \Big(\mathbf{M}(\mathbf{r}, \mathbf{r}_{31}, \mathbf{r}_{32}) - \mathbf{M}_{pair}(\mathbf{r}) \Big) g_3 d\mathbf{r}_{31}, \tag{3.16}$$

where $\mathbf{M}(\mathbf{r}, \mathbf{r}_{31}, \mathbf{r}_{32})$ is the mobility for particles 1 and 2 in the presence of a third particle and is obtained using the method of reflections [53]. The far-field and near-contact contributions are matched by smooth interpolation for intermediate separations.

We approximate the shear-induced relative diffusion, $\left\langle \mathbf{D}^{\dot{\gamma}} \right\rangle_2$ in (3.7), by considering particles near contact and in widely-separated configurations; this quantity is only used for the near-hard spheres, and not for soft repulsive colloids. When $r \gg 2$, the motions of the two particles become uncorrelated, and $\left\langle \mathbf{D}^{\dot{\gamma}} \right\rangle_2 \approx 2\mathbf{D}_s^{\dot{\gamma}}(\phi, Pe)$. Near contact, $r - 2 \to 0$, the relative velocity along the line of centers goes to zero, and thus both radial velocity fluctuations and the radial relative diffusivity vanish. However the pair rotation around the center of mass is not limited and thus velocity fluctuations remain in the angular ($\hat{\theta}$ and $\hat{\varphi}$) directions. These considerations lead to a simple form for $\left\langle \mathbf{D}^{\dot{\gamma}} \right\rangle_2$, given in dimensionless form by

$$\left\langle \mathbf{D}^{\dot{\gamma}} \right\rangle_2 = \frac{2D_s^{\dot{\gamma}}(\phi, Pe)}{D_0} \Big(\mathcal{A}(r)\hat{\mathbf{r}}\hat{\mathbf{r}} + \mathcal{B}(r)(\mathbf{I} - \hat{\mathbf{r}}\hat{\mathbf{r}}) \Big), \tag{3.17}$$

where $D_s^{\dot{\gamma}}(\phi, Pe)$ is taken as the strongest shear induced self-diffusion component, $D_s^{\dot{\gamma}}(\phi, Pe) = D_s^{xx}(\phi, Pe)$ which is assumed to be known for hard-sphere suspensions from prior work [37]. The function $\mathcal{A}(r)$ determines the radial variation of the diffusion coefficient in the r direction, while $\mathcal{B}(r)$ determines this radial variation for the $\hat{\theta}$ and $\hat{\varphi}$ directions. We assume the shear-induced relative diffusion for directions other than r is equal to the far field value at all separations, and thus $\mathcal{B}(r) = 1$. The function $\mathcal{A}(r)$ is approximated as

$$\mathcal{A}(r) = \begin{cases} 1 & r \geqslant 4. \\ \exp\left[-\tilde{n}\dfrac{4-r}{r-2}\right] & r < 4, \end{cases} \tag{3.18}$$

which decays uniformly from unity at $r = 4$ to 0 at $r = 2$. The value of $\tilde{n}$ is effectively the only adjustable parameter in the theory when the shear-induced relative diffusion must be considered, i.e., in the case of near hard-spheres. For each ϕ at $Pe > 1$,

there is a critical $\tilde{n}$ denoted $\tilde{n}_c$ for each condition (Pe and ϕ): for larger values, i.e. $\tilde{n} > \tilde{n}_c$, a convergent solution cannot be obtained and results are reported only for this critical value. Physically, this retains just enough shear-induced diffusion near contact to maintain a stable disordered state. All averaged values in (3.9a) have now been expressed in terms of g and $\mathbf{r}$, and g will be determined by solving the integro-differential equation (3.9a) with boundary conditions expressed by (3.9b) and (3.9c).

The structure of the equation for the microstructure under concentrated (large-ϕ) conditions is seen from (3.9a) to be a nonlinear integro-differential equation, by contrast with the linear form considered in dilute theories of the structure [27, 28]; the nonlinearity is due to the product of $g(\mathbf{r})$ used in the closure approximation. This multiparticle correlation is sufficient, as shown by the results, to capture the extended range structure driven by excluded volume in hard-sphere systems and well-known from equilibrium theories of integral-equation form. A finite element iterative technique, detailed elsewhere [32] is used to solve this equation with the B.C. given in (3.9b) and (3.9c).

3.3 Rheology

The bulk stress in the suspension is given by

$$\langle \boldsymbol{\Sigma} \rangle = -P\mathbf{I} + 2\eta\mathbf{E}^{\infty} + n\left(\langle \mathbf{S}^{P} \rangle + \langle \mathbf{S}^{H} \rangle + \langle \mathbf{S}^{B} \rangle\right), \tag{3.19}$$

where $-P\mathbf{I} + 2\eta\mathbf{E}^{\infty}$ is the pure fluid stress, and the remaining terms are the particle phase stresses. The stresslets $\langle \mathbf{S}^{B} \rangle$, $\langle \mathbf{S}^{H} \rangle$ and $\langle \mathbf{S}^{P} \rangle$, give the Brownian, hydrodynamic, and interparticle stress contributions, respectively, with $\langle\ \rangle$ denoting an ensemble average carried out over all particles in all possible configurations. These stress contributions can be expressed as [46, 27]

$$\left\langle \mathbf{S}^{B} \right\rangle = -k_b T \left\langle \nabla \cdot \left(\mathbf{R}^{SU} \cdot (\mathbf{R}^{FU})^{-1} \right) \right\rangle, \tag{3.20a}$$

$$\left\langle \mathbf{S}^{H} \right\rangle = \left\langle \mathbf{R}^{SU} \cdot (\mathbf{R}^{FU})^{-1} \cdot \mathbf{R}^{FE} - \mathbf{R}^{SE} \right\rangle : \mathbf{E}^{\infty}, \tag{3.20b}$$

$$\left\langle \mathbf{S}^{P} \right\rangle = -\left\langle \left(\mathbf{xI} + \mathbf{R}^{SU} \cdot (\mathbf{R}^{FU})^{-1} \right) \cdot \mathbf{F} \right\rangle, \tag{3.20c}$$

where $\mathbf{R}^{SU}$ is the resistance tensor that couples the particle stresslet to particle motion relative to the bulk flow, and $\mathbf{R}^{SE}$ relates the stresslet to the bulk rate of strain; $\mathbf{R}^{FU}$ is the tensor relating force to relative motion, i.e. the generalized Stokes drag coefficient. Microstructure is coupled to rheology by relating $\langle\, \mathbf{S} \,\rangle$ to $g(\mathbf{r})$ as follows:

$$\langle\, \mathbf{S} \,\rangle = n \int \langle\, \mathbf{S} \,\rangle_2 (\mathbf{r})\, g\,(\mathbf{r})\, d\mathbf{r}, \tag{3.21}$$

where $\langle\, \mathbf{S} \,\rangle_2(\mathbf{r})$ is the average stress on each particle in a pair configuration which is determined by interactions between the members of the pair and their interaction with the bath particles, at each separation $\mathbf{r}$. The quantity $\langle\, \mathbf{S} \,\rangle_2$ is formulated replacing $\langle\,\rangle$ with $\langle\,\rangle_2$ in the relations of (3.20). We approximate the conditional pair averages appearing in the formulation for hard-sphere and soft colloids, as described below.

3.3.1 Hard-spheres

Following (3.20a) and (3.21), the Brownian stress contribution can be separated to two parts [46]:

$$n \left\langle \mathbf{S}^{B} \right\rangle = \mathbf{\Sigma}^{B1} + \mathbf{\Sigma}^{B2}, \tag{3.22a}$$

$$\frac{\left\langle \mathbf{\Sigma}^{B1} \right\rangle}{\eta\dot{\gamma}} = -Pe^{-1} \frac{27}{4\pi} \phi^2 \int \mathbf{nn} g ds, \tag{3.22b}$$

$$\frac{\left\langle \mathbf{\Sigma}^{B2} \right\rangle}{\eta\dot{\gamma}} = Pe^{-1} \frac{27}{4\pi} \phi^2 \int \left\langle \mathbf{R}^{SU} \cdot (\mathbf{R}^{FU})^{-1} \right\rangle_2 \cdot \nabla g d\mathbf{r}, \tag{3.22c}$$

where $\mathbf{n}$ is the unit vector along the line of centers, from particle 1 to 2. The first term, $\mathbf{\Sigma}^{B1}$, which becomes the dominant contribution at concentrated ϕ, can be evaluated through a straightforward surface integration [46]. For the second term, we make the assumption that the integral is dominated by the volume near the contact surface

where ∇g is largest. Very near contact, pairwise lubrication interactions dominate and $\left\langle \mathbf{R}^{SU} \cdot (\mathbf{R}^{FU})^{-1} \right\rangle_2 \rightarrow \left(\mathbf{R}^{SU} \cdot (\mathbf{R}^{FU})^{-1} \right)_{pair}$ as $r \rightarrow 2$, where subscript *pair* refers to the isolated pair; hence $\mathbf{\Sigma}^{B2}$ is approximated as

$$\frac{\left\langle \mathbf{\Sigma}^{B2} \right\rangle}{\eta \dot{\gamma}} \sim Pe^{-1} \frac{27}{4\pi} \phi^2 \int_{bl} \left(\mathbf{R}^{SU} \cdot (\mathbf{R}^{FU})^{-1} \right)_{pair} \cdot \nabla g d\mathbf{r}, \tag{3.23}$$

where the subscript *bl* refers to integration being carried out inside the boundary layer. The boundary layer is defined as the volume adjacent to the contact surface where the angularly averaged pair distribution function, denoted $\tilde{g}(r)$, is larger than unity: $\tilde{g}(r) \geqslant 1$.

Hard-sphere suspensions are modeled through a very steep repulsive potential here (see Figure 3.1). Thus $\left\langle \mathbf{S}^P \right\rangle_2$ is only non-zero in a vanishingly small volume next to the contact surface (note (3.20c)). This makes $\left\langle \mathbf{S}^P \right\rangle$ identically zero for a true hard-sphere system and negligible for the potential used here to model hard-spheres $\left\langle \mathbf{S}^P \right\rangle \approx 0$.

To compute $\left\langle \mathbf{S}^H \right\rangle$ we assume that the hydrodynamic stress contribution is controlled by lubrication interactions, so that the hydrodynamic stress can be approximated by the boundary-layer lubrication stresses. Thus $\left\langle \mathbf{S}^H \right\rangle_2$ is approximated as

$$\frac{n \langle \mathbf{S}^H \rangle}{\eta \dot{\gamma}} \approx \frac{n \mathbf{S}^H_{pair}}{\eta \dot{\gamma}} + \frac{27}{16\pi} \phi^2 \int_{bl} R^{FU}_{rr} \left(U^r - U^r_{pair} \right) \hat{\mathbf{r}} \hat{\mathbf{r}} g(\mathbf{r}) \, d\mathbf{r}, \tag{3.24}$$

where U^r_{pair} and $\mathbf{S}^H_{pair}$ are the well-known relative radial velocity and average particle hydrodynamic stress for very dilute systems [44, 45]. The integral represents the effect of particle interactions beyond pair level on hydrodynamic stress. U^r is the relative radial velocity due to external flow and lubrication interactions, and R^{FU}_{rr} is the relative resistance in radial direction. Both quantities are computed as part of the theory.

3.3.2 Soft Colloids

In the case of long-range repulsive potentials, it is useful to first have an estimate of the relative importance of the contribution of each term in (3.20). To make the comparison more tractable first we take the conditionally averaged hydrodynamic functions to be equal to their isolated pair values. After incorporating this assumption, the stress contributions are simplified to

$$\frac{n\mathbf{S}^{B}_{pair}}{\eta\dot{\gamma}} = -Pe^{-1}\frac{27\phi^2}{16\pi}\int W(r)g\left(\mathbf{r}\right)\hat{\mathbf{r}}\hat{\mathbf{r}}d\mathbf{r}, \tag{3.25}$$

$$\frac{n\mathbf{S}^{P}_{pair}}{\eta\dot{\gamma}} = -Pe^{-1}\frac{27\phi^2}{16\pi}\int \left(1-A(r)\right)rF^{P}(r)g\left(\mathbf{r}\right)\hat{\mathbf{r}}\hat{\mathbf{r}}d\mathbf{r}, \tag{3.26}$$

$$\begin{aligned}\frac{n\,\mathbf{S}^{H}_{pair}}{\eta\dot{\gamma}} &= 2.5\phi + 2.5\phi^2 + \frac{15}{4\pi}\phi^2\int\Bigg[M(r)\left(\hat{\mathbf{r}}\cdot\hat{\mathbf{E}}\cdot\hat{\mathbf{r}}\right)\left(\hat{\mathbf{r}}\hat{\mathbf{r}}-\frac{\mathbf{I}}{3}\right) \\ &+ L(r)\Big(\hat{\mathbf{r}}\hat{\mathbf{E}}\cdot\hat{\mathbf{r}}+\hat{\mathbf{r}}\hat{\mathbf{r}}:\hat{\mathbf{E}}-\frac{2}{3}\mathbf{I}\left(\hat{\mathbf{r}}\cdot\hat{\mathbf{E}}\cdot\hat{\mathbf{r}}\right)\Big)+K(r)\hat{\mathbf{E}}\Bigg]g(\mathbf{r})d\mathbf{r}.\end{aligned} \tag{3.27}$$

Here $W(r) = -3A+3B-r\dfrac{dA}{dr}$ [24] and A, B, M, L and K are tabulated functions [30] of pair separation distance r. The scaling as Pe^{-1} of the interparticle stress arises because we have used k_bT to describe the strength of the interparticle potential. Figure 3.2 compares the hydrodynamic factors in (3.25) and (3.26) for the system with $\kappa = 3.8$. It is evident that the interparticle force piece is by far the dominating piece at $r > 2.1$. Also due to the long-ranged repulsive interactions the likelihood of having near contact configurations is significantly reduced. This makes Brownian stresses negligible compared with the interparticle stress contribution for the soft-sphere dispersions studied, a key difference from the hard-sphere case. This trend is also seen for $\kappa = 6$ and 12. Our ASD stress calculations discussed in §3.4 agree with this argument; hence Brownian stress is neglected for soft colloids hereafter.

As previously discussed, the main contribution to the hydrodynamic stress comes

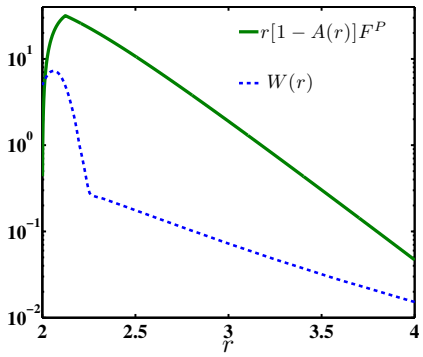

Figure 3.2: The hydrodynamic functions determining isolated pair interparticle and Brownian stress in (3.25) and 3.26 using $\kappa = 3.8$. The dotted and solid lines present the functions contributing to Brownian and interparticle stresses respectively.

from near-contact lubrication stresses. For soft colloids particle surfaces are separated by distances comparable to their radius, so that lubrication is not the controlling factor in setting the structure and stresses. The many-body contributions to hydrodynamic stress in (3.24) and (3.27) are substantially reduced and $\dfrac{n\left\langle \mathbf{S}^H \right\rangle}{\eta\dot{\gamma}} \approx 2.5\phi + 2.5\phi^2$; as a result all non-Newtonian rheology arises from $\left\langle \mathbf{S}^P \right\rangle$.

3.4 Results

We briefly outline the microstructure and rheology results for the near hard-sphere system, previously examined in detail [32], and then provide results for the soft repulsive potentials.

3.4.1 Near hard-spheres

The majority of the results of microstructure are presented in the $x-y$ plane where x and y are the flow and velocity gradient directions, respectively. The definitions of angles and directions are given in figure 3.3. Note that the polar angle is defined slightly different from its common definition in spherical coordinate (for which it is measured

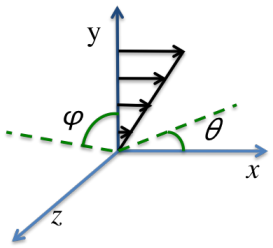

Figure 3.3: A schematic of the angle definitions and flow direction. $0 \leq \theta \leq 2\pi$ is the azimuthal angle measured counter-clockwise from the positive x axis and $-\pi/2 \leq \varphi \leq \pi/2$ is the polar angle measured from $x - y$ plane.

from **z** axis). In our definition, $\varphi = 0$ corresponds to the plane of shear. Figure 3.4 shows the predicted $g(\mathbf{r})$ for a hard-sphere dispersion in the plane of shear at $Pe = 1$, alongside the simulation results. The theory is able to capture the near-contact anisotropy and the main features of pair microstructure away from contact including the next nearest neighbor peak at $r \approx 4$ and the depleted zones of pair correlation. Figure 3.5 shows $g(\mathbf{r})$ from simulation and theory for $Pe = 10$, again restricted to the shear plane. A clear boundary layer structure with large pair probability is formed at the contact surface in the compressional quadrant, and a region depleted of pair probability (a wake region) is formed near the extensional axis, as found in previous theoretical [27] and simulation [48] studies.

To obtain a clearer picture of the near-contact anisotropy, values of g at the pair contact surface in the shear plane, $g(2;\theta)$, are shown in figure 3.6 at $Pe = 10$ and $\phi =$ 0.20, 0.40, and 0.55. Theoretical predictions are in reasonable quantitative agreement with simulation results. For $\phi = 0.20$, $g(2;\theta)$ shows a maximum near the compressional axis. Increase of volume fraction from $\phi = 0.20$ to $\phi = 0.40$ results in the appearance of a secondary peak in $g(2;\theta)$ and further increase to $\phi = 0.55$ results in a shift of the angle of the secondary peak toward the flow direction. The simulations for $\phi = 0.55$ show that the suspension undergoes a shear-induced ordering transition to strings in the flow direction at $Pe \gg 1$; these strings form hexagonal structures as seen for near hard

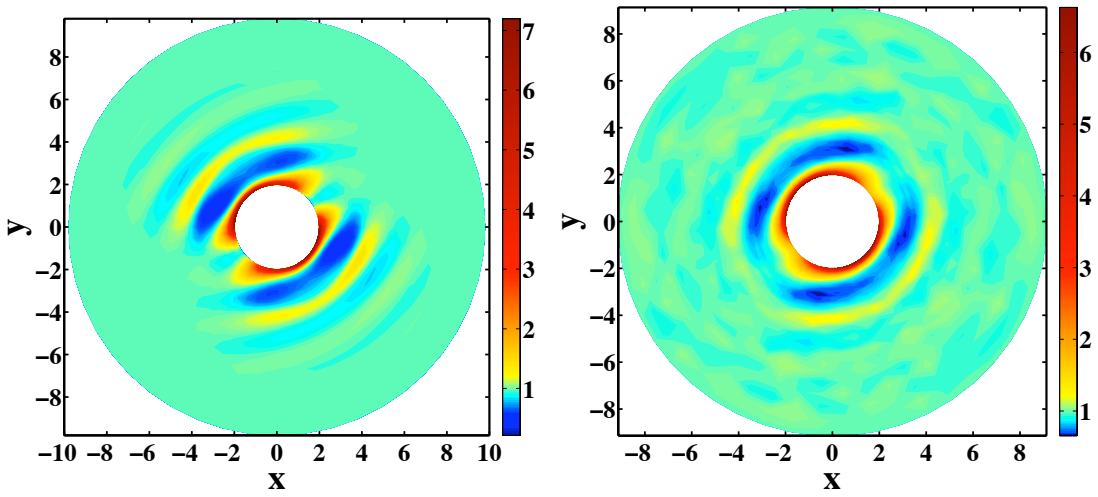

(a) *Theory*, $Pe = 1$ (b) *ASD*, $Pe = 1$

Figure 3.4: The pair distribution function, g, for $\phi = 0.40$, hard-sphere suspensions in the shear plane at $Pe = 1$: (a)Theory prediction (b) results of ASD simulation samplings.

spheres [62]. This is manifested through the strong peak of $g(2;\theta)$ in the flow direction in simulations as seen in figure 3.6(c). In this figure, similar structural development is seen for the theory, although a complete ordering is not observed for reasons discussed below.

Next, the predicted microstructure is used to compute the rheology using relations (3.22b – 3.24). The formulation allows for calculation of normal stress differences, but here we limit our attention to shear viscosity. Normal stress difference results have been described previously for near hard-sphere suspensions [32]. As an example, the simulation results and predicted values for shear viscosity for the $\phi = 0.40$ hard-sphere suspension are presented in figure 3.7. The viscosities are normalized by the pure fluid viscosity; $\hat{\eta}^H$ and $\hat{\eta}^B$ are the increase relative to the pure fluid viscosity due to hydrodynamic and Brownian forces, respectively. Recall that for hard-spheres the interparticle contribution to the stress is negligible. The theory is able to give a reasonable prediction of shear viscosity and the individual contributions from Brownian and hydrodynamic forces agree with the simulation. The shear thinning at low Pe and shear thickening

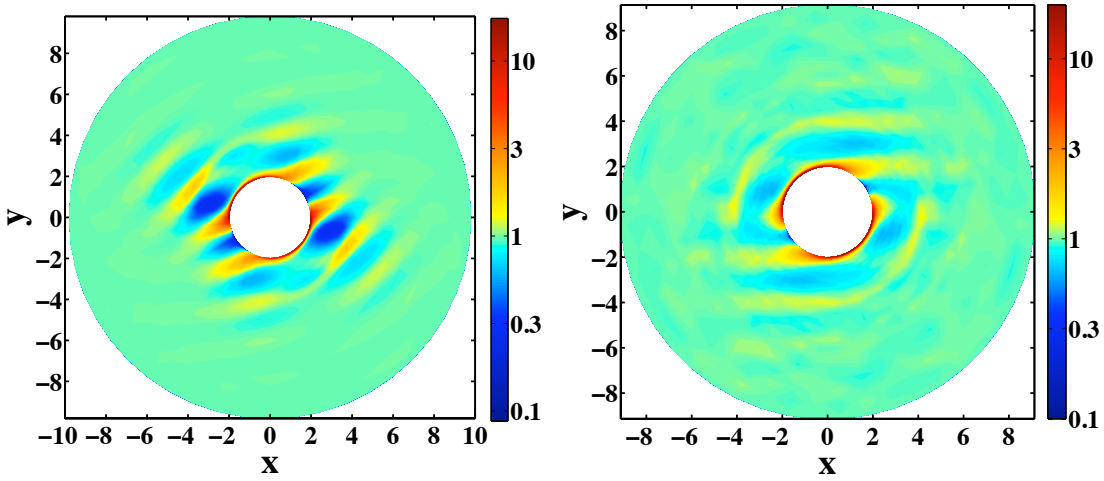

(a) *Theory*, $Pe = 10$ (b) *ASD*, $Pe = 10$

Figure 3.5: The pair distribution function, g, for $\phi = 0.40$, hard-sphere suspensions in the shear plane at $Pe = 10$: (a) Theory prediction (b) results of ASD simulation samplings.

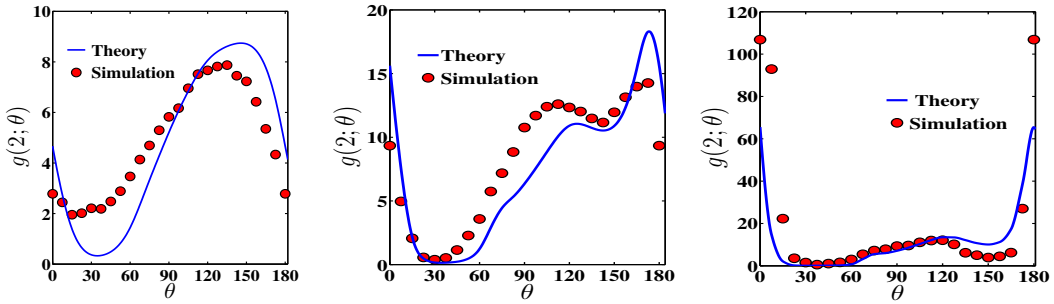

(a) $\phi = 0.20$ (b) $\phi = 0.40$ (c) $\phi = 0.55$

Figure 3.6: The angular variations of pair distribution function at contact in shear plane, $g(2;\theta)$, for $Pe = 10$: (a) $\phi = 0.20$, (b) $\phi = 0.40$, and (c) $\phi = 0.55$.

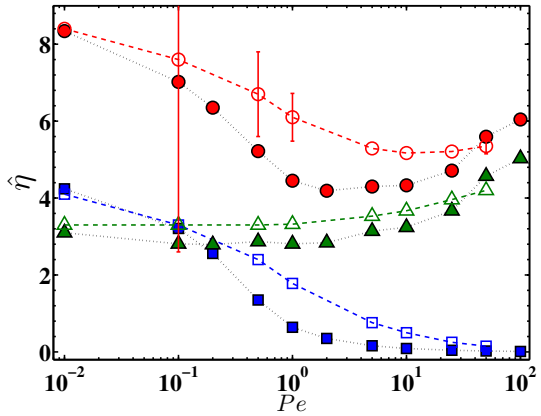

Figure 3.7: Brownian (■, □) and hydrodynamic (▲, △) contributions and total value (○, ●) of relative viscosity as a function of Pe for $\phi = 0.40$. Filled symbols present the predictions and the open symbols are the ASD simulation results.

at high Pe are also observed for other volume fractions, and both behaviors intensify with increasing ϕ, in good agreement with simulation. A more comprehensive study of microstructure predictions for hard-sphere suspensions using the same methodology outlined in this work is given in [32].

3.4.2 Soft repulsive colloids

In soft colloids with repulsive interactions as modeled here, the particles do not approach near contact, and lubrication interactions are consequently not the controlling factor that they represent in hard-sphere systems. Lubrication forces, $\langle \mathbf{F}^{lub} \rangle_2$, are significantly reduced. In addition, the need for diffusion to balance shearing forces to establish a convergent structure is removed, as the shearing is now largely balanced by the interparticle potential force. In fact, for all the predicted results here, $\mathbf{D}^{\dot{\gamma}} = 0$ resulted in a convergent solution. Hence the shear-induced diffusion was not considered for soft colloids. The role of lubrication forces on the final structure is discussed in more detail in §3.5.

Figure 3.8(a) and 3.8(b) compare the predictions and simulation results for the pair

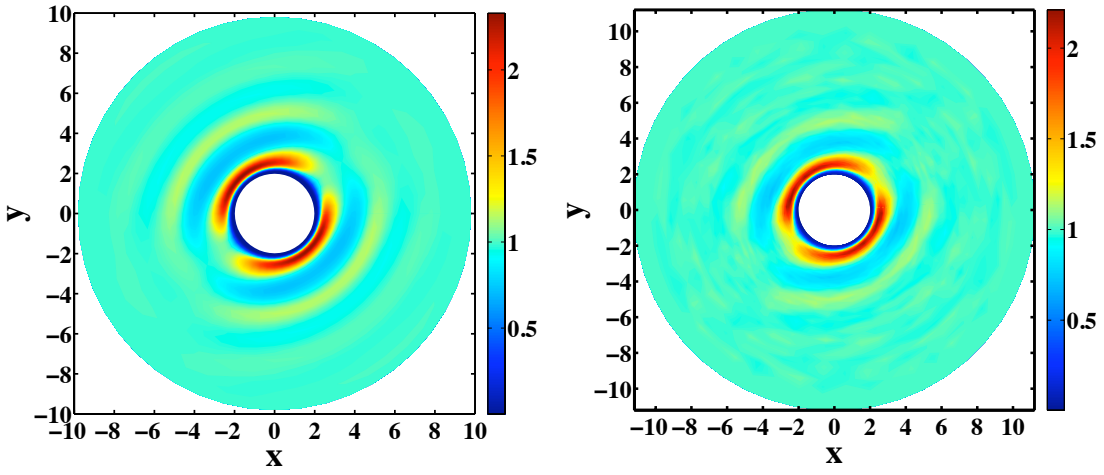

(a) *Theory*, $Pe = 1$ (b) *ASD*, $Pe = 1$

Figure 3.8: The pair distribution function, $g(\mathbf{r})$ in shear plane, for soft repulsive colloids with $\kappa = 6$ at $Pe = 1$: (a) Theory predictions (b) results of ASD simulation samplings.

distribution function in the shear plane for a suspension with $\kappa = 6$ at $Pe = 1$. The predicted microstructure is in good agreement with the simulation results. At $Pe = 1$, for both simulation and theory, the radius of the region near the contact surface where the soft potential causes $g \to 0$ is reduced in the compressional quadrant and increased in the extensional quadrant. Accumulation of pair probability is seen adjacent to the depleted zone, i.e. at the effective contact surface, followed by a low probability region and the next nearest neighbor peak. At $Pe = 10$, a boundary layer structure develops, with a downstream wake; see figures 3.9(a) and 3.9(b). Finally the tendency to form an ordered structure along the flow direction is evident from the high probability regions along the flow direction for both predicted and simulated structures.

For $Pe \geq 15$ the suspension eventually goes through an ordering transition at large strains in our simulations. This is a common structural observation for systems where near-contact lubrication interactions are absent [69, 71], suggesting an important role of lubrication interactions. Since $g(\mathbf{r}) = 1$ is the imposed boundary condition at the outer limit of our computation domain ($r = 10$), the ordering transition cannot be accurately

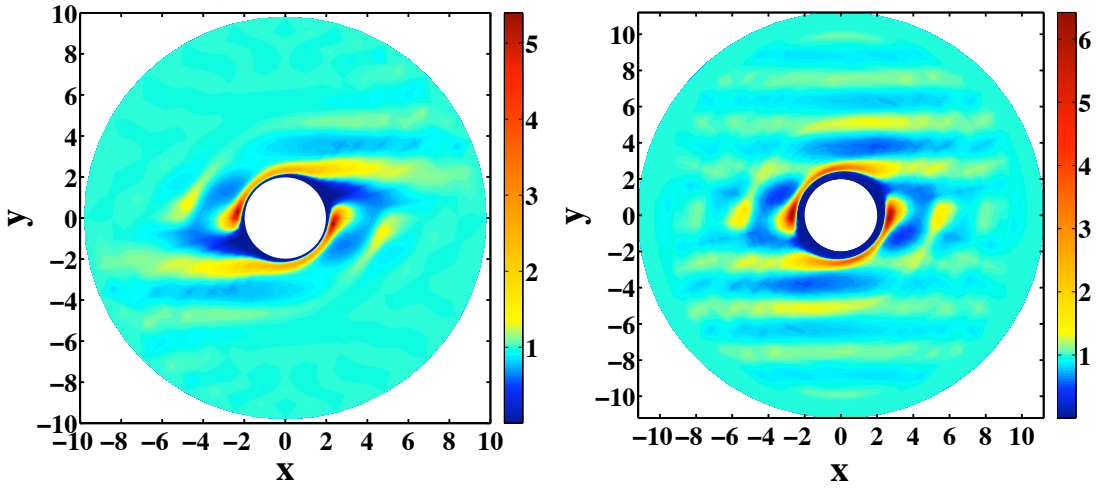

(a) *Theory*, $Pe = 10$ (b) *ASD*, $Pe = 10$

Figure 3.9: The pair distribution function, $g(\mathbf{r})$ in shear plane, for soft repulsive colloids with $\kappa = 6$ at $Pe = 10$: (a) Theory predictions (b) results of ASD simulation samplings.

predicted. Thus the simulated structure at small strain ($\dot{\gamma}t < 8$), when the suspension remains partially disordered, is used here for comparison with the theoretical predictions. The computed $g(\mathbf{r})$ at $Pe = 25$ and $\kappa = 6$ from simulation and theory are presented in figure 3.10. The high probability region in the compressional quadrant, which we have termed a boundary layer, is seen in the predicted $g(\mathbf{r})$ to be convected downstream. In fact, this region extends to the outer boundary of the computational domain where it is truncated due to the noted $g = 1$ B.C. If the outer boundary condition were replaced with a periodic B.C. as in the simulation, this convection of high pair probability is expected to lead to an ordered structure along the flow direction.

It is evident from figures 3.9 and 3.10 that the thickness of the depleted region near the contact surface in compressional zone is smaller for the theory than in the simulation results. In order to explore this aspect in more detail and perform a more thorough quantitative comparison of theory and simulation results, radial variations of pair distribution function along three different θ angles in shear plane ($g(r, \theta, \varphi = 0)$, $\theta = 0$, $\pi/4$, $5\pi/6$) are shown for $\kappa = 6$ and $Pe = 1$, 10 and 25 (prior to ordering transition) in figure 3.11.

For $Pe = 1$, there is very good agreement between the predictions and simulation results at each angle. At $Pe = 10$, general agreement is observed between the predictions and simulated structure. The thickness of the depleted region is, however, under-predicted in compressional zone, $\theta = 5\pi/6$, as well as along the flow direction, $\theta = 0$, while excellent agreement is observed along the extensional axis ($\theta = \pi/4$). In case of $Pe = 25$ the depleted region is significantly smaller than in the simulated structure in the compressional zone and flow direction. This can easily be seen by comparing the r values in which the maximum in g occurs; see figures 3.11(g) and 3.11(i). This difference is propagated toward the outer domain causing, all secondary peaks for $\theta = 0$ and $5\pi/6$ to occur at lower values of r in predictions. Recall that for $Pe = 25$ the system eventually becomes ordered. Thus, the observed discrepancy at $Pe = 25$ is not surprising, considering that the theory is formulated for disordered systems; this makes the theory less accurate as the suspension approaches the ordering transition. We reiterate that applying a periodic boundary condition to the theory might make agreement better but was out of scope for this work.

For a more detailed analysis of the boundary layer structure formed at $Pe \geq 1$, the angular variations of $g(\mathbf{r})$ at the radius for which the pair distribution function is maximized in the shear plane, $g(r_c, \theta, \varphi = 0)$, are shown in figure 3.12. This figure compares simulation and theory for $\kappa = 6$ and $Pe = 1$, 10, and 25. The quantitative agreement between theory and simulation results is satisfactory. The tendency toward shear-induced ordering can be clearly seen in the increase of g along the flow direction with increase of Pe.

The effect of the range of repulsive force is best reflected in shear-induced ordering. The system with softer potential ($\kappa = 3.8$) also undergoes a shear-induced ordering transition, and the transition occurs at lower Péclet numbers ($Pe > 3$) compared to $\kappa = 6$. In the case of $\kappa = 12$, the least soft of the extended range potentials considered in this work, the structure remains disordered over the entire range of Pe studied ($Pe \leq 100$).

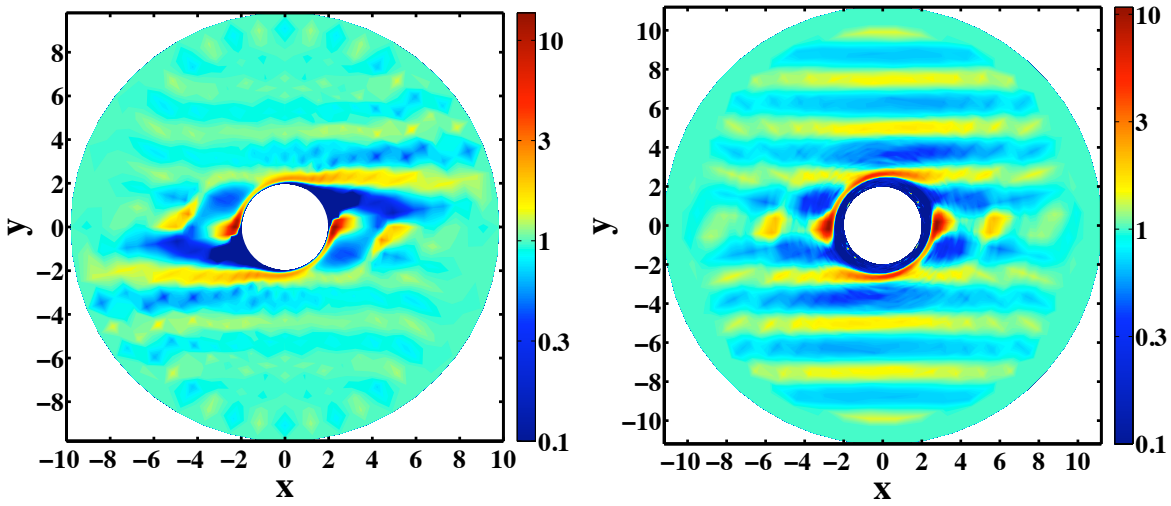

(a) *Theory*, $Pe = 25$ (b) *ASD*, $Pe = 25$, $\dot{\gamma}t < 8$

Figure 3.10: The pair distribution function for $\phi = 0.20$ and $\kappa = 6$ soft colloids in the shear plane at $Pe = 25$: (a) Theory prediction (b) results of ASD simulation samplings before ordering transition (small strain: $\dot{\gamma}t < 8$).

This behavior is illustrated in figure 3.13 which shows $g(r_c, \theta, \varphi = 0)$ as a function of θ at $Pe = 2$ for $\kappa = 3.4$, 6, and 12. As the range of repulsive forces is increased (or alternatively as ϕ_{eff} is increased), $g(r_c, \theta, \varphi = 0)$ along the flow direction increases in the predicted microstructures and simulation results. For $\kappa = 12$, the predictions and simulation were carried out for $\phi = 0.25$. The volume fraction $\phi = 0.25$ was chosen so that the effective equilibrium volume fraction for $\phi = 0.25$ and $\kappa = 12$ equals that of $\phi = 0.20$ and $\kappa = 6$, namely $\phi_{\text{eff}} = 0.34$. Both simulation and theoretical predictions for $\kappa = 12$ and $\phi = 0.25$ show disordered structure over the entire Pe range studied. This is another indication that ordering phenomena are not entirely controlled by ϕ_{eff}; increasing steepness of the repulsive force enabling closer approach of the particle surfaces apparently favors more disordered structures at similar ϕ_{eff}.

Predictions of $g(\mathbf{r})$ are used to calculate the stress due to the particle phase. Figure 3.14 presents the total viscosity non-dimensionalized with fluid viscosity, $\hat{\eta}^T$, for the range of κ and Pe studied in this work. Dimensionless viscosities for hard-sphere suspensions at $\phi = 0.20$ are also presented. Recall that all non-Newtonian behavior in the

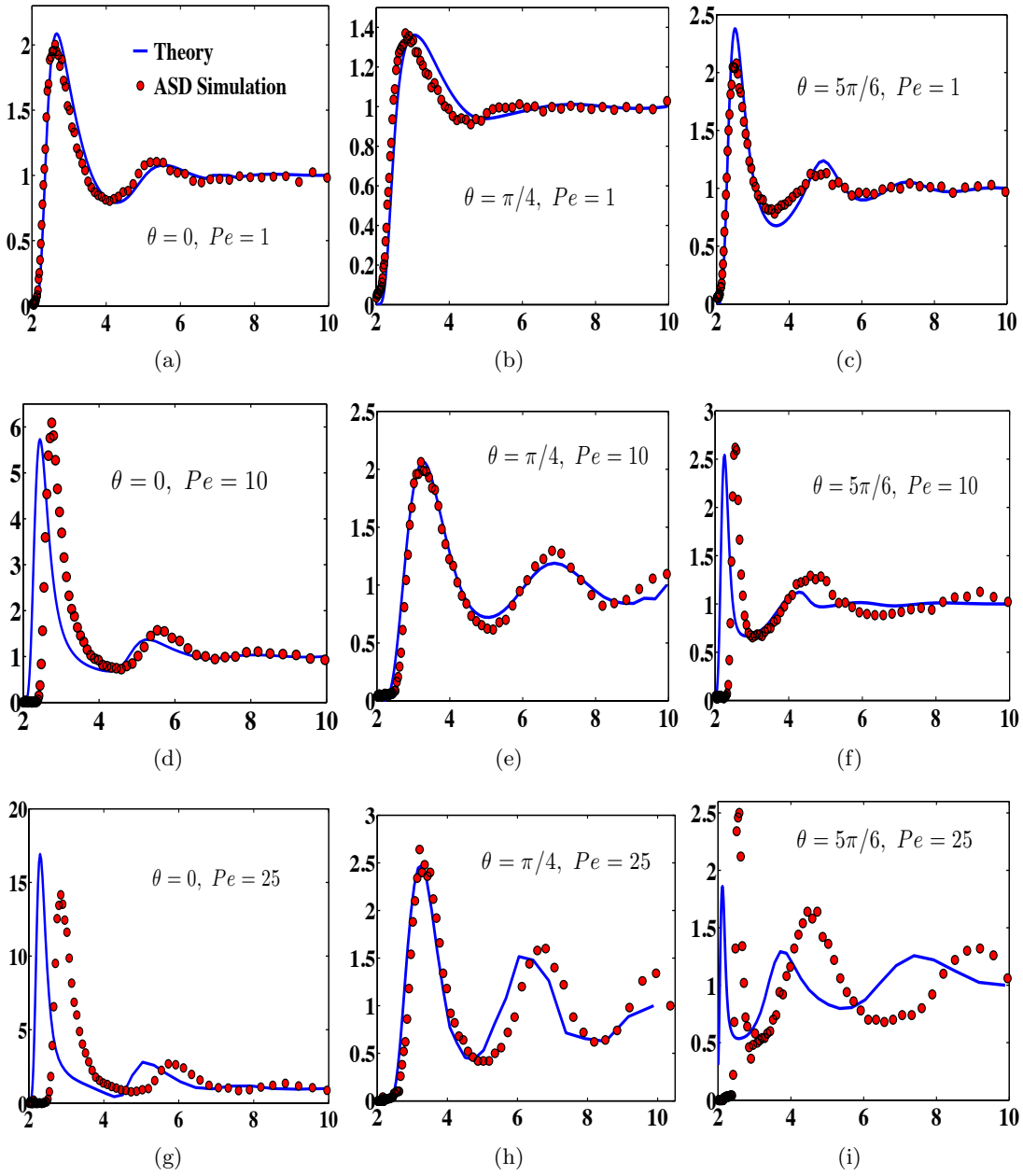

Figure 3.11: Radial variations of pair distribution function at different θ angles in shear plane ($g(r, \theta, \varphi = 0)$, $\theta = 0, \pi/4, 5\pi/6$) for $\kappa = 6$ and $Pe = 1, 10$ and 25: (a) $Pe = 1, \theta = 0$, (b) $Pe = 1, \theta = \pi/4$, (c) $Pe = 1, \theta = 5\pi/6$, (d) $Pe = 10, \theta = 0$, (e) $Pe = 10, \theta = \pi/4$, (f) $Pe = 10, \theta = 5\pi/6$, (g) $Pe = 25, \theta = 0$, (h) $Pe = 25, \theta = \pi/4$, and (i) $Pe = 25, \theta = 5\pi/6$.

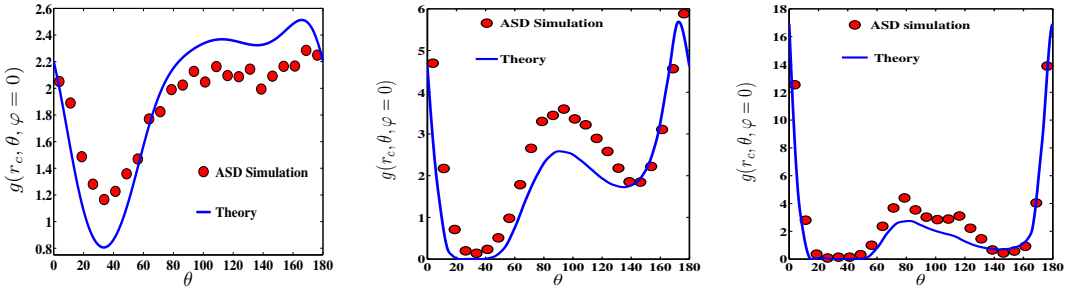

(a) $Pe = 1$ (b) $Pe = 10$ (c) $Pe = 25$, $\gamma < 8$

Figure 3.12: The angular variations of pair distribution function in shear plane at the radius for which g is maximized ($g(r_c, \theta, \varphi = 0)$) for soft colloids with $\kappa = 6$ at: (a) $Pe = 1$, (b) $Pe = 10$, and (c) $Pe = 25$, $\dot{\gamma}t < 8$, before ordering transition. The filled circles are results of simulation samplings and solid lines are our theoretical predictions.

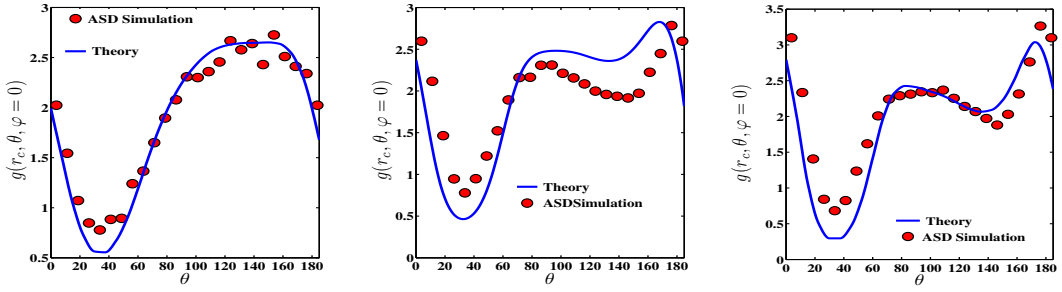

(a) $\kappa = 12$ (b) $\kappa = 6$ (c) $\kappa = 3.8$

Figure 3.13: The angular variations of $g(r_c, \theta, \varphi = 0)$ at $Pe = 2$ for soft colloids with (a) $\kappa = 12$, (b) $\kappa = 6$, and (c) $\kappa = 3.8$.

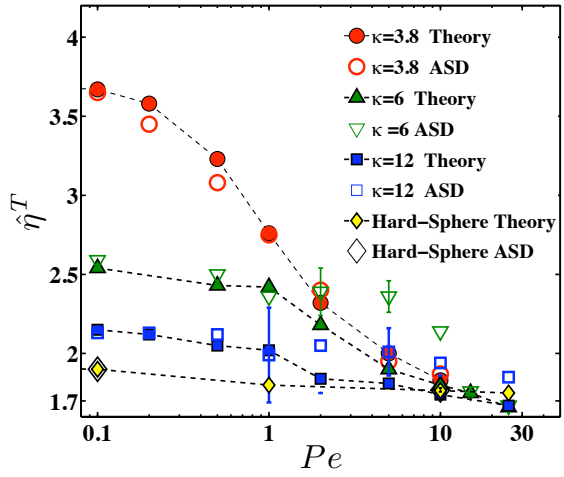

Figure 3.14: Dimensionless total viscosity, $\hat{\eta}^T$, as a function of Pe for $\kappa = 3.8$ (○, ●), $\kappa = 6$ (▽, ▲), and $\kappa = 12$ (■, □). Dimensionless total viscosity of hard-sphere suspensions at $\phi = 0.20$ (◇, ◆) is shown for comparison. Filled symbols are the predictions and open symbols are ASD simulation results.

soft colloids model used here is determined by interparticle stress, $\langle \mathbf{S}^P \rangle$. The error bars are the standard deviation of the shear viscosity from its average value, as determined by simulation. The relative magnitude of the error bar with respect to the average value for each Pe is similar for both $\kappa = 3.8$ and 6, and they are only presented for a few data points at $\kappa = 6$ and 12 to aid visualization. As a general trend the error bars become smaller as Pe is increased.

There is good agreement between predictions and simulation results for $\kappa = 3.8$. For $\kappa = 6$ and 12 the results are in good agreement for $Pe \leq 1$ but shear thinning behavior occurs at lower Pe in the predicted results. Near-equilibrium viscosity increases with ϕ_{eff}. For $\kappa = 3.8$ and $\kappa = 6$, strong shear thinning is seen, and theory agrees with simulation for these conditions. This shear thinning is not as pronounced for $\kappa = 12$. Recall that there is an ordering transition observed for $\kappa = 3.8$ and 6, but not for $\kappa = 12$.

3.5 Concluding remarks

A microstructural theory based on Smoluchowski equation analysis has been developed here for concentrated suspensions of soft repulsive particles. This extends prior work by the authors [32] for concentrated hard-sphere suspensions under shear. Accelerated Stokesian Dynamics (ASD) simulations were also carried out and compared with theoretical predictions. Repulsive forces with different steepness were used in the theory and simulations; examples of hard-sphere suspension results were also presented. The microstructure predictions were presented and compared with simulation for $0.1 \leq Pe \leq 100$. The predictions of $g(\mathbf{r})$ were found to be in good agreement with computed values from simulations. For soft repulsive colloids, good agreement was obtained before the onset of shear-induced ordering in simulations of suspensions with softer potentials.The theory, in its current form, is not able to predict the ordering transition observed in simulations due to the imposed outer boundary condition of no correlation ($g(\mathbf{r}) = 1$). Improved representation of the conditions of simulation could be achieved by applying a periodic boundary condition, but we have not pursued this point.

In hard-sphere suspensions hydrodynamic interactions are dominated by lubrication interaction. In soft colloidal suspensions, however, the repulsive forces prohibit the particles from approaching very near contact and lubrication interactions are reduced significantly compared to a hard-sphere system, and the colloidal forces are thus dominant in setting the structure. We have shown that our theory is able to give reasonable predictions of structure and rheology for both hard-spheres and soft colloids when compared with ASD simulation.

The results of this work provide insight to the balance of forces that establishes structure under a given condition. For hard-sphere dispersions, shear-induced diffusion is essential and the lubrication interactions play a key role. Shear-induced relative diffusion arises from flow-induced fluctuations of forces present in the suspension, and is found from simulation to be significant for all the cases studied here. However, we do not

find it necessary to include this diffusion for the soft repulsive potential suspensions. For hard-sphere suspensions the lubrication forces and diffusion balance to maintain a disordered structure [32]. The flow-induced diffusion is included in the theory through $\left\langle \mathbf{D}^{\dot{\gamma}} \right\rangle_2$. Since lubrication forces and the diffusive flux associated with them scale linearly with $\dot{\gamma}$ the structure maintains its disordered state over the entire range of Pe for $\phi \leq 0.49$. This results in formation of a boundary layer of pair probability where the mean contact values of pair distribution function, $\tilde{g}(2)$, monotonically increase with Pe; see figure 4 in [48]. For soft colloids, lubrication forces are greatly reduced and interparticle repulsive forces balance the external flow to determine the pair microstructure. Our simulations and predictions of $g(\mathbf{r})$ show that mean radial variations of pair distribution function ($g(\mathbf{r})$ averaged over θ and φ, i.e. $\tilde{g}(r)$) is a weak function of shear rate for the range of Péclet numbers studied here. For example the maximum value of $\tilde{g}(r)$ changes from approximately 2 at equilibrium to 2.8 at $Pe = 50$ for $\kappa = 12$ and $\phi = 0.20$. Near-field hydrodynamic interactions may influence the shear-induced ordering behavior observed in soft colloids.

The pair Smoluchowski equation, (3.9a), is intrinsically a transport equation for the pair probability flux; this makes the method presented here appealing for studying sheared systems as shear rate dependent fluxes are introduced naturally. The approximations used in this formalism allow for proper description of two-particle dynamics very near contact and when widely separated. The pair motion is then self-consistently coupled to the bath particles through probabilistic third particle integrals (see (3.11) and (3.15)), an approach which enables the theory to be successfully applied to concentrated suspensions. As a result of this coupling which results in an integro-differential equation for the pair microstructure, the pair near contact are seen to be driven together (or pulled apart) through the mean forces applied by bath particles surrounding them. This correlated structure is then propagated outside the boundary layer through the third-particle integrals. Accordingly the theory gives a reasonable representation of

long-range correlated structures, as demonstrated by secondary maxima in predictions of $g(\mathbf{r})$.

4 Pair-particle dynamics in sheared colloidal dispersions [3]

4.1 Introduction

This work describes a study of the microstructure of sheared Brownian, or colloidal, suspensions. More specifically, the coupled issues of the average pair dynamics and pair microstructure are considered. The pair microstructure is characterized by the pair distribution function, $g(\mathbf{r})$ describing the relative likelihood of finding a pair at any given separation, considering all possible locations of the remaining particles. In a recent theory developed to describe the pair microstructure in concentrated colloidal suspensions, the problem describing the pair microstructure is found to involve coefficients whose form must be determined self-consistently within the theory. In developing these coefficients, we are effectively determining the mean pair dynamics, or the dynamics of a pair immersed in the mean field described by the remaining particles. The dynamics exhibited by the average pair at large particle fraction is found to be remarkably different from its dilute-suspension counterpart, both in the mean motion and in the dispersion around the mean pair trajectory. It is our purpose to present this pair-particle dynamics problem in the context of its direct relevance to the microstructural analysis.

To directly determine certain of the coefficients and test various closures applied in the theory, we have performed Stokesian Dynamics simulations, and we compare the

[3] The contents of this chapter are submitted for publication in *Physics of Fluids* [72].

microstructure and the pair dynamics determined (or assumed) in the theory with the simulation results. The approach is in spirit similar to the use of molecular dynamics simulation to provide detailed "experimental" data for liquid-state theory [73]. Given that simulations are available, some question of the theory's value may be justifiably raised. However, theory provides the ability to determine whether our understanding may be systematized, and when it is successful allows very direct relationships between causes and effects to be developed; examination of the expected behavior of a range of particle interactions may then be done, as we have shown for a theory developed initially for hard-sphere suspensions [32] has been applied to repulsive spheres [63]. More pragmatically, theoretical calculations are typically much more rapidly performed than extended simulations necessary to compute statistically meaningful averages of properties, and system size dependence is more readily eliminated.

We apply the well-accepted Smoluchowski equation theory [5] to describe the microstructure of sheared colloidal suspensions. To introduce the issues of describing the pair dynamics, we consider the governing equation for the steady pair distribution function, derived by reducing the N-particle Smoluchowski equation to the two-particle level by integrating over all possible configurations of $N-2$ particles, as described in §4.2:

$$\nabla_{\mathbf{r}} \cdot \Big(\mathbf{U}(\mathbf{r}) g(\mathbf{r}) - \mathbf{D}(\mathbf{r}) \cdot \nabla_{\mathbf{r}} g(\mathbf{r}) \Big) = 0, \tag{4.1}$$

where $\nabla_{\mathbf{r}}$ is the gradient operator with respect to $\mathbf{r}$, which is the separation vector of the pair of particles (spheres). The coefficients $\mathbf{U}$ and $\mathbf{D}$ are the average pair relative velocity and the relative diffusivity, respectively. It is clear that the pair Smoluchowski equation is inherently a convection-diffusion transport equation in a flowing system, and the ratio of convection to diffusion, a Péclet number where Pe is defined precisely below, represents the distance from equilibrium. In dilute theory for the microstructure [27, 28], when hydrodynamic interactions are accounted, the velocity $\mathbf{U}$ is known (from Batchelor

& Green [45] and later works [74, 30]) and the relative diffusivity is driven by Brownian motion. However, when the suspension becomes concentrated, the pair relative velocity is dependent on the configuration of the surrounding particles, and in average is found to differ quite dramatically from the dilute form. A more fundamental change to the dynamics of a pair is observed in the dispersion about the mean trajectory (i.e., the time integral of $\mathbf{U}$), which for an isolated pair (as encountered in the dilute analysis) becomes negligible relative to the convection at large Pe. Under concentrated conditions, hydrodynamic dispersion of the trajectory is significant, and at elevated Pe is the only dispersion mechanism. We report on the previously-unexplored pair relative dispersion and consider the validity of our own approximation of this quantity as a diffusion.

As indicated in the prior paragraph, the pair microstructure of colloidal hard-sphere suspensions in shear flow (assuming Stokes flow is valid at the particle scale) is defined in terms of two dimensionless parameters, volume fraction of particle phase, ϕ, and Péclet number, $Pe = \dfrac{6\pi\eta\dot{\gamma}a^3}{k_bT}$ which is the ratio of viscous to thermal forces where η is the fluid viscosity, $\dot{\gamma}$ is the shear rate magnitude, a is the particle radius, k_b is the Boltzmann coefficient and T is the absolute temperature. If other interaction forces between particles are present, e.g. electrostatic forces, then further dimensionless parameters will be needed, but we limit consideration here to the simplest case where Pe and ϕ are sufficient. Existing Smoluchowski-equation theoretical approaches, prior to development of our approach described in §4.2 and prior chapters, for the microstructure of flowing suspensions are applicable only in a certain range of Pe and ϕ and can be in general divided to near-equilibrium ($Pe \ll 1$) and dilute ($\phi \ll 1$) theories. Near-equilibrium structure is primarily set by thermal interactions and hydrodynamic interactions play a secondary role, and by perturbing the equilibrium structure known from liquid-state theory, systematic progress has been made [24]. Use of closures from liquid-state theories, such as the hypernetted chain approximation, has resulted in successful prediction of the structure and rheology of weakly sheared suspensions. The dilute theories allow

one to consider the balance of flow and diffusion over a wide range of Péclet [28], and the role of hydrodynamics has been captured in both the relative velocity and relative diffusion. The dilute theory has allowed understanding of the development of extremely distorted microstructure at large Pe, where a boundary layer structure with associated wake develops [27, 75].

The dilute theories have been extended to higher concentration using scaling arguments motivated by simulation results [46, 47, 27]. These theories are successful in predicting the shear viscosity of suspensions for volume fractions prior to the shear-induced ordering transition [37, 7]. However the values of normal stress differences cannot be predicted using the same scalings [7]. Because dilute theories only consider interactions up to two-particle level and neglect many-body interactions, the relative velocity and diffusion applied are actually significantly different from their form in concentrated suspensions, as the present work will show. This change in $\mathbf{U}$ and $\mathbf{D}$ results in formation of new features in the anisotropic pair microstructure, as shown clearly in Morris & Katyal [48], where the near-contact $g(\mathbf{r})$ obtained from Stokesian Dynamics simulation exhibited a qualitatively different form at $\phi > 0.35$ relative to lower particle fractions. As a result, individual components of stress tensor scale differently with ϕ making the use of a single scaling factor for all components of the stress tensor inaccurate. The theory discussed in this work overcomes this difficulty by explicitly coupling the average relative velocity to pair microstructure. In order to elucidate the coupling, we widen the scope beyond the microstructure and rheology to consider in detail the dynamics of two-particle interactions, for various ϕ at $Pe \gg 1$. This is pursued by comparing the average relative velocity and resulting pair trajectories from both theory and sampling the configurations from Accelerated Stokesian Dynamics simulation. As noted, a feature of the pair trajectory is that it shows a remarkable shear-induced dispersion at elevated solid concentrations, and we explore this dispersion, with a focus on demonstrating the form of the relative velocity fluctuations and dispersion around the average pair motion

with time and space.

We begin in the next section by outlining the Smoluchowski equation theory for concentrated suspensions. This is followed in §4.3 with an overview of the predictions of theory of both microstructure and the resulting rheological predictions, with comparison to simulation results. In §4.4 and 4.5, we explore the mean relative motion followed by pairs of particles, and the dispersion characteristics of this trajectory, respectively.

4.2 Theory

The theory presented here follows in most respects directly from our recent work on microstructure and rheology of sheared colloidal suspensions [32, 63], where details of the formulation can be found. Hence the treatment will be brief except in describing, in §4.2.1, a revision of the original theory that improves the predictions of the pair relative velocity.

The probability of configurations of N particles when particle-scale inertial effects are negligible is described by the Smoluchowski equation,

$$\frac{\partial P_N}{\partial t} + \sum_{\alpha=1}^{N} \nabla_\alpha \cdot \mathbf{j}_\alpha = 0, \tag{4.2}$$

where $P_N(\mathbf{x}_1, \mathbf{x}_2, ..., \mathbf{x}_N)$ is the N-particle configurational probability density function, and $\mathbf{j}_\alpha$ is the probability flux associated with particle α, given by

$$\mathbf{j}_\alpha = \left(\mathbf{U}_\alpha^H + \sum_{\beta=1}^{\beta=N} \mathbf{M}_{\alpha\beta}^{UF} \cdot \mathbf{F}_\beta \right) P_N - \sum_{\beta=1}^{\beta=N} \mathbf{D}_{\alpha\beta} \cdot \nabla_\beta P_N. \tag{4.3}$$

Here, $\mathbf{U}_\alpha^H$ is the velocity of particle α induced by bulk flow and hydrodynamic interactions with other particles, $\mathbf{M}_{\alpha\beta}^{UF}$ is the mobility of particle α due to a force on particle β, and $\mathbf{D}_{\alpha\beta} = k_b T \mathbf{M}_{\alpha\beta}^{UF}$ is the Brownian diffusion where k_b is the Boltzmann constant and T is the absolute temperature. The conservative interparticle force on particle β is

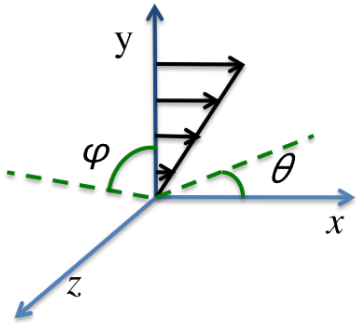

Figure 4.1: Angle definitions defined in a simple-shear flow $u_x(y)$: $0 \leq \theta \leq 2\pi$ is the azimuthal angle measured clockwise from the positive x axis, and $-\pi/2 \leq \varphi \leq \pi/2$ is the polar angle measured from $x-y$ plane.

expressed as $\mathbf{F}_\beta = -\nabla_\beta V$, where V is the interparticle potential and ∇_β is the gradient with respect to the position of particle β. The term $\mathbf{U}_\alpha^P = \sum_{\beta=1}^{\beta=N} \mathbf{M}_{\alpha\beta}^{UF} \cdot \mathbf{F}_\beta$ is the velocity of particle α induced by interparticle forces applied by the rest of the particles.

The equation (4.2) is integrated over all possible configurations of $N-2$ particles keeping two particles fixed which results in a convection-diffusion equation for the pair distribution function $g(\mathbf{r}) = P_2/n^2$. At steady-state, this equation is

$$\nabla_{\mathbf{r}} \cdot \left[\Big(\mathbf{U}^\infty + \langle \mathbf{U}^H \rangle_2(\mathbf{r}) + \langle \mathbf{M} \cdot \mathbf{F}^P \rangle_2(\mathbf{r}) \Big) g(\mathbf{r}) - \langle \mathbf{D} \rangle_2 \cdot \nabla_{\mathbf{r}} g(\mathbf{r}) \right] = 0, \tag{4.4}$$

with

$$\mathbf{U}^H = \mathbf{U}_2^H - \mathbf{U}_1^H, \tag{4.5a}$$

$$\mathbf{F}^P = \mathbf{F}_2^P = -\mathbf{F}_1^P \tag{4.5b}$$

$$\mathbf{M} = 2\big(\mathbf{M}_{11} - \mathbf{M}_{12} \big), \tag{4.5c}$$

$$\mathbf{D} = 2\big(\mathbf{D}_{11} - \mathbf{D}_{12} \big), \tag{4.5d}$$

where $\mathbf{r}$ is the pair separation vector and $\mathbf{U}^\infty$ is the relative velocity of a pair moving with the imposed shear flow. The coordinates are defined in figure 4.1. The quantities $\langle \mathbf{U}^H \rangle_2$

and $\langle \mathbf{U}^P \rangle_2 = \langle \mathbf{M} \cdot \mathbf{F}^P \rangle_2$ are the average relative pair velocity due to hydrodynamic and interparticle interactions, respectively, and $\langle \mathbf{D} \rangle_2(\mathbf{r})$ is the pair relative diffusivity. The relative diffusivity is due to both Brownian and shear-induced velocity fluctuations, and we write this as

$$\langle \mathbf{D} \rangle_2 = k_b T \langle \mathbf{M} \rangle_2 + \mathbf{D}^{\dot{\gamma}}, \tag{4.6}$$

where the first term of the right hand side is the Brownian diffusion with $\langle \mathbf{M} \rangle_2 = 2\big(\mathbf{M}_{11}^{UF} - \mathbf{M}_{12}^{UF}\big)$ and $\mathbf{D}^{\dot{\gamma}}$ is the shear-induced relative diffusion which will be discussed below.

Quantities are made dimensionless as

$$\begin{gathered} \mathbf{r} \sim a; \quad \mathbf{D} \sim D_0; \quad \mathbf{M} \sim \frac{1}{6\pi\eta a}. \\ \mathbf{U}^P \sim D_0/a; \quad \mathbf{U}^H \sim \dot{\gamma} a; \quad \mathbf{U}^\infty \sim \dot{\gamma} a, \end{gathered} \tag{4.7}$$

where $D_0 = k_b T/6\pi\eta a$ is the single particle diffusivity. Note that $F^P \sim k_b T/a$ and $\mathbf{M} \sim \dfrac{1}{6\pi\eta a}$ which makes $\mathbf{U}^P \sim k_b T/6\pi\eta a^2 = D_0/a$. In dimensionless form, (4.4) becomes

$$\nabla \cdot \left[\Big(\mathbf{U}^\infty + \langle\, \mathbf{U}^H \,\rangle_2 + Pe^{-1} \langle\, \mathbf{U}^P \,\rangle_2 \cdot \Big) g - Pe^{-1} \langle\, \mathbf{D} \,\rangle_2 \cdot \nabla g \right] = 0, \tag{4.8}$$

where $\nabla = \nabla_{\mathbf{r}} a$ is the dimensionless gradient operator, and we have defined the Péclet number,

$$Pe = \frac{\dot{\gamma} a^2}{D_0} = \frac{6\pi\eta\dot{\gamma} a^3}{k_b T}. \tag{4.9}$$

The boundary conditions on (4.8) are

$$\mathbf{j}_{\mathbf{r}} = 0 \quad \text{at} \quad r = 2, \tag{4.10a}$$

$$g \sim 1 \quad \text{as} \quad r \to \infty. \tag{4.10b}$$

The first boundary condition implies zero radial flux at contact.

The relative velocity due to interparticle interactions can be written as

$$\langle \mathbf{U}^P \rangle_2 = \langle \mathbf{M} \cdot \mathbf{F}^P \rangle_2 = \langle \mathbf{M} \rangle_2 \cdot \langle \mathbf{F}^P \rangle_2 + \langle \mathbf{M}' \cdot \mathbf{F}' \rangle_2, \tag{4.11}$$

where $\mathbf{M}'$ and $\mathbf{F}'$ are fluctuations of mobility and forces around their average value. To compute $\langle \mathbf{U}^P \rangle_2$ we consider the pair to be immersed in a field that contains the average effect of the bath of the other particles. This mean-field approximation yields a convective flux due to inter particle force determined by the mean forces and mean mobility:

$$\langle \mathbf{U}^P \rangle_2 = \langle \mathbf{M} \rangle_2 \cdot \langle \mathbf{F}^P \rangle_2. \tag{4.12}$$

Dispersion of a pair around the mean trajectory is also a property of the mean field. Thermal fluctuations result in a Brownian diffusivity, $k_b T \langle \mathbf{M} \rangle_2$ in (4.6), but for large Pe the quantity $\langle \mathbf{M}' \cdot \mathbf{F}' \rangle_2$ and its hydrodynamic counterpart generate fluctuations which dominate the Brownian contribution, and we address modeling of this aspect of the mean field in §4.2.2.

In the initial elaboration of the theory[32, 63], the hydrodynamic velocity was modeled as $\langle \mathbf{U}^H \rangle_2 = \langle \mathbf{M} \rangle_2 \cdot \langle \mathbf{F}^{lub} \rangle_2$. The formulation is based on the assumption that particle motions are dominated by their pair-wise lubrication interactions. The equal and opposite lubrication forces for each pair are then modeled using $\mathbf{F}^{lub}(\mathbf{r}) = \mathbf{R}^{FE}_{pair}(\mathbf{r}) : \mathbf{E}^{\infty}$ where $\mathbf{R}^{FE}_{pair}(\mathbf{r})$ is the hydrodynamic resistance tensor for two particles relating the force and strain rate. Lubrication and interparticle forces were assumed to be pairwise additive and were computed using the following integral equation:

$$\langle \mathbf{F}_1 \rangle_2 g(\mathbf{r}) = \mathbf{F}_{21}(\mathbf{r}) g(\mathbf{r}) + n \int \mathbf{F}_{31}(\mathbf{r}_{31})\, g_3(\mathbf{r}, \mathbf{r}_{31}) d\mathbf{r}_{31}, \tag{4.13}$$

where $\mathbf{F}_{21}$ and $\mathbf{F}_{31}$ are forces individual particles 2 and 3 exert on particle 1 respectively

and $g_3(\mathbf{r}, \mathbf{r}_{31})$ is the triplet distribution function and $g_3(\mathbf{r}, \mathbf{r}_{31})d\mathbf{r}d\mathbf{r}_{31}$ is the probability of having particles 1 and 2 in relative distance of $\mathbf{r}$ and $\mathbf{r} + d\mathbf{r}$ and particles 1 and 3 in between $\mathbf{r}_{31}$ and $\mathbf{r}_{31} + d\mathbf{r}_{31}$. In the current formulation $\langle \mathbf{U}^P \rangle_2$ is computed using this formulation. However an alternative formulation is used for hydrodynamic velocity which is given in §4.2.1.

The effect of "bath" particles on relative mobility is described based on a three-body calculation. When the third particle is near contact with one or both particles of the pair of interest, a resistance formulation is used to compute the added resistance due to near-contact interactions:

$$\langle \mathbf{R} \rangle_2(\mathbf{r})g = \mathbf{R}_{pair}(\mathbf{r})g + n \int \Big(\mathbf{R}(\mathbf{r}, \mathbf{r}_{31}, \mathbf{r}_{32}) - \mathbf{R}_{pair}(\mathbf{r}) \Big) g_3 d\mathbf{r}_{31}, \tag{4.14}$$

where $\mathbf{R}(\mathbf{r}, \mathbf{r}_{31}, \mathbf{r}_{32})$ is the resistance for particles 1 and 2 in the presence of a third particle and $\mathbf{R}_{pair}(\mathbf{r})$ is the resistance of the isolated pair 1 and 2. The term in parentheses in the integrand of (4.14) is the increase of the resistance to pair relative motion with respect to the isolated pair, due to the influence of another particle. For particles near contact the resistance is assumed to be pair-wise additive. The average resistance is then inverted to obtain the average mobility.

For configurations of three particles outside the lubrication region, the third particle effect is modeled using a mobility formulation:

$$\langle \mathbf{M} \rangle_2(\mathbf{r})g = \mathbf{M}_{pair}(\mathbf{r})g + n \int \Big(\mathbf{M}(\mathbf{r}, \mathbf{r}_{31}, \mathbf{r}_{32}) - \mathbf{M}_{pair}(\mathbf{r}) \Big) g_3 d\mathbf{r}_{31}, \tag{4.15}$$

where $\mathbf{M}(\mathbf{r}, \mathbf{r}_{31}, \mathbf{r}_{32})$ is the mobility for particles 1 and 2 in the presence of 3 and it is obtained using the method of reflections [53]. The far-field and near-contact effects are then added to give the final value for $\langle \mathbf{M} \rangle_2(\mathbf{r})$.

4.2.1 Hydrodynamic relative velocity $\langle \mathbf{U}^H \rangle_2$

The new formulation is based on the pair-wise summation of the effect of a third particle on pair relative velocity, rather than summation of forces as seen in (4.13)

$$\langle \mathbf{U}^H \rangle_2(\mathbf{r})g = \mathbf{U}^H_{pair}(\mathbf{r})g + n\mathcal{Q} \cdot \int \left(\mathbf{U}^H(\mathbf{r}, \mathbf{r}_{31}, \mathbf{r}_{32}) - \mathbf{U}^H_{pair}(\mathbf{r}) \right) g_3 d\mathbf{r}_{31}, \tag{4.16}$$

where $\mathbf{U}^H(\mathbf{r}, \mathbf{r}_{31}, \mathbf{r}_{32}) - \mathbf{U}^H_{pair}(\mathbf{r})$ is the change in relative pair velocity due to the presence of a third particle. Similar to formulation of the mobility tensor, when the third particle is in a near-contact configuration with one of the pair, a resistance formulation is used and the velocity of particles is obtained by $\left(\mathbf{R}^{FU}\right)^{-1} \cdot \mathbf{R}^{FE} : \mathbf{E}$. Near-contact is defined as regions where r_{13} or $r_{23} < 2.3$. When both $r_{13} > 2.3$ and $r_{23} > 2.3$, the method of refections is used to compute three-particle hydrodynamic interactions up to $O(1/r^6)$. The contributions from the lubrication region and far-field are then added to compute $\langle \mathbf{U}^H \rangle_2(\mathbf{r})$.

To include the many-body effect of the "bath" particles surrounding the triplet at different configurations, the tensor $\mathcal{Q}_{ij}$ is introduced to the formulation. The lubrication interactions of surrounding particles on pair dynamics can be divided into "*discrete*" and "*bath particle*" interactions. When particles 1, 2 and 3 are in near-contact configuration, instead of having a pure fluid around the particles the triplet are surrounded by a sheared suspension. In this case the third particle serves to "transduce" the hydrodynamic force from the surrounding particles to the pair. As a result the driving force is amplified by a factor of $\hat{\eta}$ with respect to having only the pair and a single third particle where $\hat{\eta}$ is the viscosity of the suspension normalized by the viscosity of pure fluid, with this viscosity self-consistently computed as a part of the theory. We refer to this as *bath particle* interactions. Now assume the pair are separated by a third particle between them. In this configuration, the change in relative pair velocity is independent of the

configuration of the rest of the particles and is computed using a three-body calculation which we refer to as *discrete particle* interaction. To incorporate both of these effects $\mathcal{Q}$ is defined as

$$\mathcal{Q} = \mathcal{A}\hat{\mathbf{r}}\hat{\mathbf{r}} + \mathcal{B}\left(\mathbf{I} - \hat{\mathbf{r}}\hat{\mathbf{r}}\right), \tag{4.17}$$

with

$$\mathcal{A} = (\hat{\eta} - 1)\exp\left[-\beta(r-2)\right] + 1 \tag{4.18a}$$

$$\mathcal{B} = 1 \tag{4.18b}$$

In this formulation when the pair of interest is near contact, the pair dynamics is of *bath particle* interactions and as the pair separate the pair dynamics is controlled by discrete interactions of pair particles with a probabilistic third particle. This is modeled through reduction of $\mathcal{A}$ from $\hat{\eta}$ at contact to 1 as r increases. We also take $\mathcal{B} = 1$ i.e. the *bath particle* effect is restricted to $\hat{\mathbf{r}}$ direction and velocities in $\hat{\theta}$ and $\hat{\varphi}$ directions are assumed to be governed by *discrete* interactions. The assumption is based on the observation that the effect of excluded volume causing the increase in viscosity of the suspension is imposed primarily along $\mathbf{r}$. Note that (4.17) is used only in lubrication region and $\mathcal{Q} = \mathbf{I}$ for far-field calculations. A similar approach has been used by other authors [24, 46]; there is no coupling of velocity field and structure, $g(\mathbf{r})$, in these works. The coupling captured in the present theory enables us to predict the complex angular variations and next nearest neighbor peaks in $g(\mathbf{r})$. For all the results presented here, we arbitrarily set $\beta = 4$.

4.2.2 Shear-induced relative diffusion, $\mathbf{D}^{\dot{\gamma}}$

It has been shown by experiments [76, 77], theory [78, 79, 54, 27] and simulation [55, 50] that after a single particle interacts with enough number of particles its movement becomes diffusive with shear-induced self-diffusion scaling as $\mathbf{D}_s \propto \dot{\gamma}a^2$ at large or infinite

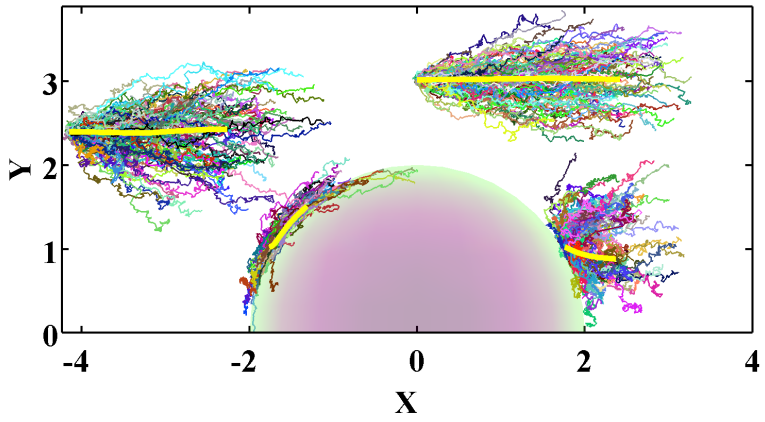

Figure 4.2: Dispersion of pair trajectories for different starting points in shear plane obtained by sampling the configuration from ASD simulation for $\phi = 0.40$ and $Pe = 10$. The thick lines are the average trajectories and the average motion is from left to right along these trajectories.

Péclet numbers. The fluctuating motions driving this random walk process have a similar effect on the relative motion of pairs of particles. We consider the dispersion of the pair trajectories caused by these shear flow-driven fluctuations of velocity.

The dynamics of any pair in a suspension is defined based on the interaction of the pair with the surrounding particles within the specific configuration. Thus for different pairs sampled at the same separation $\mathbf{r}$, the relative velocity will generally differ. This point is illustrated by Figure 4.2, which shows many pair trajectories starting from the same points in shear plane $(x-y)$ obtained from sampling the ASD simulation configurations for $Pe = 10$, $\phi = 0.40$. The average pair trajectory is illustrated with a thick line in each configuration. The spread of trajectories is of the same order of magnitude as the displacement in the flow direction, despite Brownian motion being relatively weak: the dispersion is hydrodynamically driven. Figure 4.2 is a clear indication that the pair dynamics, and presumably the microstructure, depends not only on the average pair velocities at $Pe \gg 1$, but also on the dispersion of pair trajectories. The probability flux associated with flow-induced dispersion of pair trajectories is modeled here by $-\mathbf{D}^{\dot{\gamma}} \cdot \nabla g(\mathbf{r})$ where we define $\mathbf{D}^{\dot{\gamma}}(\mathbf{r})$ as the shear-induced relative diffusivity. The dispersive flux

is a consequence of relative velocity fluctuations and $\mathbf{D}^{\dot{\gamma}}$ is proportional to the strength of these fluctuations. When two particles are near contact their relative velocity and the fluctuations of the relative velocity diminishes along the line of centers. By contrast, particles which are well-separated become decorrelated and $\mathbf{D}^{\dot{\gamma}} = 2\mathbf{D}_s$ where $\mathbf{D}_s$ is the self-diffusion tensor. Based on these two limits, we have proposed the following functional form for shear-induced relative diffusion [32]:

$$\mathbf{D}^{\dot{\gamma}} = D^* \Big[\mathcal{G}(r)\hat{\mathbf{r}}\hat{\mathbf{r}} + \mathcal{H}(r)(\mathbf{I} - \hat{\mathbf{r}}\hat{\mathbf{r}}) \Big], \tag{4.19}$$

where D^* is the magnitude of the far-field shear-induced self-diffusivity. The far-field relative diffusion was approximated with the strongest shear induced self-diffusion component, $D^* = 2D_s^{xx}$, known from prior work [55]. The variation of radial relative diffusivity with r is determined by $\mathcal{G}(r)$ while $\mathcal{H}(r)$ provides variations of relative diffusion along $\hat{\theta}$ and $\hat{\varphi}$ directions with r. The effect of excluded volume primarily restricts the movement along the line of centers and the relative angular motions of particles are less affected. In our initial attempt to model shear-induced diffusion [32] we assumed that $\mathbf{D}^{\dot{\gamma}}$ takes on the far-field value at all separations in $\hat{\theta}$ and $\hat{\varphi}$ directions which gives $\mathcal{H}(r) = 1$. The function $\mathcal{G}(r)$ was approximated as

$$\mathcal{G}(r) = \begin{cases} 1 & r \geqslant 4. \\ \exp\left[-\tilde{n}(\dfrac{4-r}{r-2})\right] & r < 4, \end{cases} \tag{4.20}$$

so that it decays from unity to zero between $r = 4$ and 2. Note that for any value of $\tilde{n}$, $\mathcal{G}(r) \ll r - 2$ as $r \to 2$, which makes the Brownian radial diffusion the dominant dispersion mechanism for separations sufficiently close to contact.

The spatial variation of $\mathbf{D}^{\dot{\gamma}}$ does not allow for evaluation by a Green-Kubo integral, i.e. $\displaystyle\int_0^\infty \langle \mathbf{U}(\mathbf{r}, t=0)\mathbf{U}(\mathbf{r}, t)\rangle dt$, because a particle moves at $t > 0$ to a new environment with different statistical properties from its initial position at $t = 0$. The relative diffu-

sion coefficient is nonetheless proportional to the strength of velocity fluctuations, and we explore these fluctuations here. A measure of velocity fluctuations is given by the variance of relative velocities, $\langle \mathbf{U}'\mathbf{U}' \rangle_2(\mathbf{r}) = \langle \mathbf{U}\mathbf{U} \rangle_2(\mathbf{r}) - \langle \mathbf{U} \rangle_2(\mathbf{r}) \langle \mathbf{U} \rangle_2(\mathbf{r})$. We have computed $\langle \mathbf{U}'\mathbf{U}' \rangle_2$ by sampling configurations from ASD simulations,, with results presented in §4.5. We also incorporate the observations from these samplings to modify the model for shear-induced relative diffusion. The observation used in reformulation of $\mathbf{D}^{\dot{\gamma}}$ is that although fluctuations in $\hat{\theta}$ direction remain finite over all pair separations, the strength of these fluctuations change over pair space, while the angular diffusion was taken as constant in the initial formulation. In the first step of formulating the new model for $\mathbf{D}^{\dot{\gamma}}$, as proposed by Foss and Brady [55] and later amended[50], we divide shear-induced fluctuations to fluctuations due to hydrodynamic and Brownian interactions:

$$\mathbf{D}^{\dot{\gamma}} = \mathbf{D}^{\dot{\gamma}}_{H} + \mathbf{D}^{\dot{\gamma}}_{HB^*}, \tag{4.21}$$

where $\mathbf{D}^{\dot{\gamma}}_{H}$, is the enhanced diffusion as a result of fluctuations of hydrodynamic pair velocity and $\mathbf{D}^{\dot{\gamma}}_{HB^*}$ is the enhanced diffusive motion caused by coupling of Brownian motions to the flow. Each term is modeled using (4.19):

$$\mathbf{D}^{\dot{\gamma}}_{H} = 2D^{xx}_{s,H}\Big[\mathcal{G}_H(r)\hat{\mathbf{r}}\hat{\mathbf{r}} + \mathcal{H}_H(r)(\mathbf{I} - \hat{\mathbf{r}}\hat{\mathbf{r}})\Big], \tag{4.22a}$$

$$\mathbf{D}^{\dot{\gamma}}_{HB^*} = 2D^{xx}_{s,HB^*}\Big[\mathcal{G}_{HB^*}(r)\hat{\mathbf{r}}\hat{\mathbf{r}} + \mathcal{H}_{HB^*}(r)(\mathbf{I} - \hat{\mathbf{r}}\hat{\mathbf{r}})\Big], \tag{4.22b}$$

where

$$\mathbf{D}_{s,H} = \lim_{t\to\infty} \frac{\langle \mathbf{x}^H \mathbf{x}^H \rangle}{dt}, \tag{4.23a}$$

$$\mathbf{D}_{s,HB^*} = \mathbf{D}^{HB}_s + \mathbf{D}^{B}_s - \mathbf{D}^{eq}_s \tag{4.23b}$$

with

$$\mathbf{D}^{HB}_s = \lim_{t\to\infty} \frac{\langle \mathbf{x}^B \mathbf{x}^H \rangle}{dt}, \tag{4.23c}$$

$$\mathbf{D}_s^B = \lim_{t\to\infty} \frac{\langle \mathbf{x}^B \mathbf{x}^B \rangle}{dt}. \tag{4.23d}$$

In the above, $\mathbf{x}^H(t)$ and $\mathbf{x}^B(t)$ are displacements due to Brownian motion and hydrodynamic velocity, respectively [55]. While $\mathbf{D}_{s,H} \propto \dot{\gamma}$, both $\mathbf{D}_s^{HB}$ and $\mathbf{D}_s^B$ are proportional to k_bT; as a result $\mathbf{D}_{s,HB^*}/D_0$ reaches a steady value at $Pe \gg 1$ (see fig. 7 in Foss and Brady [55]). Although $\mathbf{D}_{s,H} \gg \mathbf{D}_{s,HB^*}$ at $Pe \gg 1$, the terms are of comparable magnitude for intermediate Péclet numbers, and including flow-induced Brownian fluctuations in the diffusion formulation improves the agreement of structural predictions with simulation findings. We use the simulation results of angular hydrodynamic fluctuations, $\langle U'_\theta U'_\theta \rangle_2$, at $Pe \gg 1$, which shows that the angular relative velocity fluctuations for suspensions at $\phi > 0.3$ decrease from the far-field value to about one-fourth of this value at contact. We use this ratio of the far-field to contact values of $\mathcal{H}_H$. The angular diffusion caused by coupling of Brownian forces to the flow is assumed to remain unchanged with separation distance. The fluctuations of Brownian velocities also drop to zero near contact in radial direction, and we assumed the same functional form for the decay of radial relative diffusion for the flow-induced hydrodynamic and Brownian fluctuations, for lack of a more detailed understanding. Based on these assumptions, the functions involved in (4.23) are given by

$$\mathcal{G}_H = \mathcal{G}_{HB^*} = 1 - \exp\left[-m(r-2)^2\right], \tag{4.24a}$$

$$\mathcal{H}_H = \alpha + (1-\alpha)\Big[1 - \exp\left(-m(r-2)^2\right)\Big], \tag{4.24b}$$

$$\mathcal{H}_{HB^*} = 1, \tag{4.24c}$$

where $\alpha = 1/4$ and parameter m determines the decay from far-filed diffusion towards contact value for both angular and radial diffusion. The value of m was determined for each volume fraction to give the closest agreement for $g(\mathbf{r})$ from simulation and theory at $Pe = 10$.

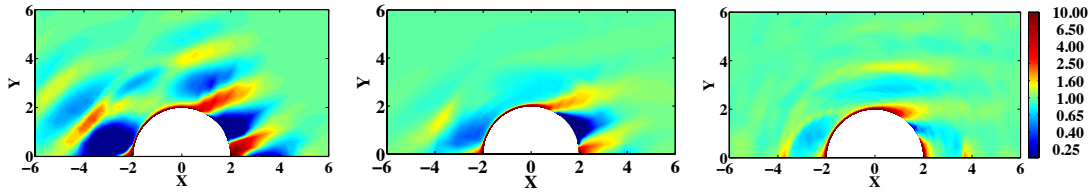

(a) Previous theory (b) Current theory (c) Simulation, $\phi = 0.40$, $Pe = 50$

Figure 4.3: Pair distribution function in shear plane for $\phi = 0.40$ and $Pe = 50$ conditions. (a) Previous theory, (b) Current theory, (c) Simulation results. The color bars are identical for all the figures and are only presented for simulation results. Values of pair distribution function are truncated to $g \leq 10$ to enhance visualization.

The conditionally-averaged values in (4.8) are all expressed in terms of $g(\mathbf{r})$ and $\mathbf{r}$, which yields a closed formulation. The pair microstructure, $g(\mathbf{r})$, is determined by numerically solving the integro-differential equation (4.8) with boundary conditions (4.10a) and (4.10b). An iterative finite element method scheme was used to solve this equation. At $Pe \ll 1$, a regular perturbation expansion of g in terms of powers of Pe was adopted, with the resulting equations were then solved using the same iterative numerical technique. The solution technique for all cases is described further in the original paper [32].

4.3 Structure and rheology

We compare the predictions of $g(\mathbf{r})$ from theory to the structure obtained by sampling of configurations from ASD simulation. The predicted structure is used to compute the nonlinear rheology and the results are also compared against the ASD simulation results. The majority of the results presented are for $Pe \gg 1$ at varying ϕ, with the illustrated structure and pair dynamics primarily in the shear plane $(x - y)$, although theory and simulations are fully three-dimensional.

Figure 4.3 shows $g(\mathbf{r})$ in the shear plane for $\phi = 0.40$ and $Pe = 50$. Results obtained from the previous and current theory are shown alongside simulation results. Although

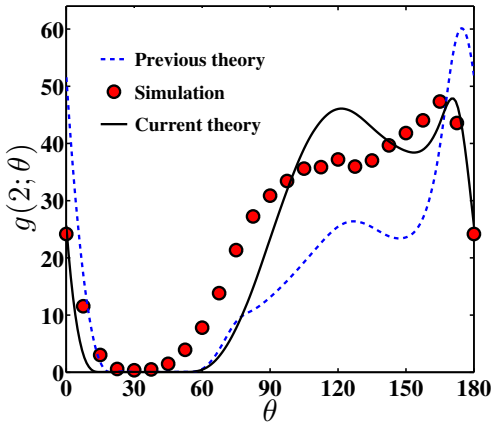

Figure 4.4: Comparison of angular variations of pair distribution in shear plane at contact, $g(r = 2; \theta, 0)$, for $\phi = 0.40$ and $Pe = 50$ suspension from theory and simulation.

some systematic differences from simulation seen in the initial theory persist, the current formulation of the theory gives a considerably closer prediction of structure; the key factor improving agreement is the new form of the hydrodynamic pair velocity as described more thoroughly in §4.4. Figure 4.4 compares theory and simulation results for $\phi = 40$ and $Pe = 50$, with the contact $g(r = 2)$ plotted as a function of the angle from the flow direction, θ, in the shear plane. The agreement between simulation and predictions is significantly improved in the current formulation. Note that the over-prediction of pair probability in the flow direction observed in the previous formulation is now resolved. The theoretical results presented hereafter are the predictions of the current theory unless mentioned otherwise. Angular variation of the pair distribution function for $Pe = 0.1, 1, 10$ and 100, for $\phi = 0.40$ is shown in figure 4.5. For $Pe = 0.1$, only the predicted structure is given due to noisiness in the simulation results. The theory provides a good quantitative prediction of near-contact structure. Figure 4.6 shows predicted and simulation values of $g(2;\theta)$ at $\phi = 20$ and $Pe = 100$, $\phi = 0.30$ and $Pe = 100$, and $\phi = 0.45$ and $Pe = 25$; there is generally good agreement. These results demonstrate that the theory is applicable over a wide range of both ϕ and Pe .

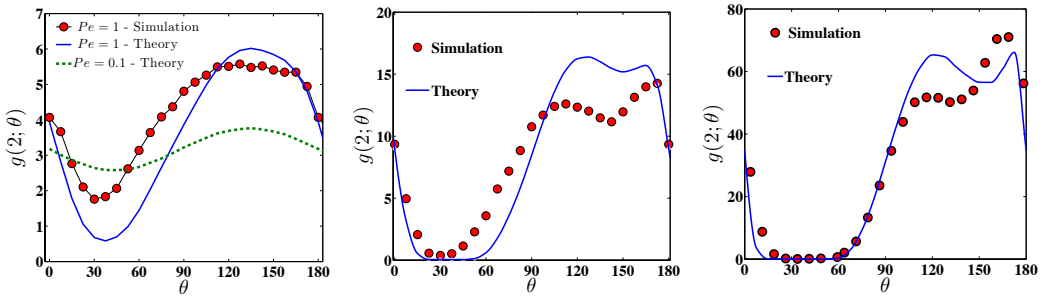

(a) $Pe = 0.1, 1$ (b) $Pe = 10$ (c) $Pe = 100$

Figure 4.5: Angular variations of pair distribution function for $\phi = 0.40$ in shear plane (a) $Pe = 0.1, 1$ (b) $Pe = 10$, (c) $Pe = 100$.

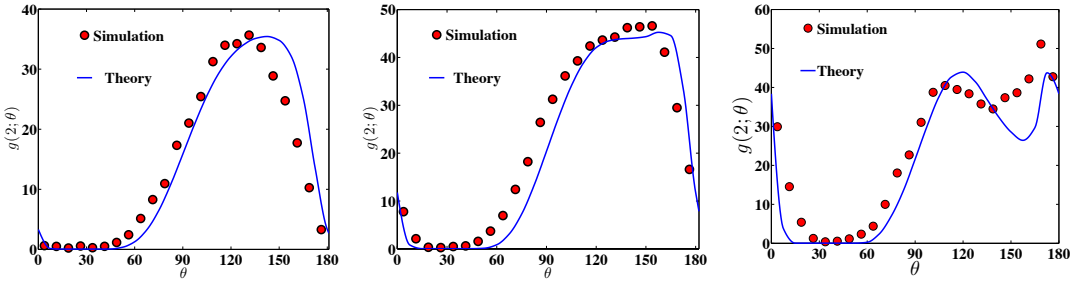

(a) $\phi = 0.20$, $Pe = 100$ (b) $\phi = 0.30$, $Pe = 100$ (c) $\phi = 0.45$, $Pe = 25$

Figure 4.6: Angular variations of pair distribution function in shear plane (a) $\phi = 0.20$ and $Pe = 100$, (b) $\phi = 0.30$ and $Pe = 100$, (c) $\phi = 0.45$ and $Pe = 25$.

The results presented here are all in the range of $Pe\eta'_\infty/\eta \leq 400$. For larger values of Pe, however, a clear discrepancy is observed between predictions and simulation results of $g(\mathbf{r})$; the predicted pair distribution function eventually becomes independent of the Péclet number for $Pe\eta_\infty/\eta > 400$ while the near-contact values of $g(\mathbf{r})$ monotonically increase approximately as $Pe^{0.7}$ for the range of Péclet numbers studied here ($Pe \leq 1000$) and in previous works [48]. The bulk stress of a sheared suspensions is given by

$$\langle \boldsymbol{\Sigma} \rangle = -P\mathbf{I} + 2\eta\mathbf{E}^\infty + n\Big(\langle \mathbf{S}^P \rangle + \langle \mathbf{S}^H \rangle + \langle \mathbf{S}^B \rangle \Big), \tag{4.25}$$

where $-P\mathbf{I} + 2\eta\mathbf{E}^\infty$ is the fluid stress contribution, and the remaining terms are con-

tributed by the particles. The stresslets $\langle \mathbf{S}^B \rangle$, $\langle \mathbf{S}^H \rangle$, and $\langle \mathbf{S}^P \rangle$ give the average single-particle Brownian, hydrodynamic, and interparticle stress contributions, respectively. The detailed relation of the pair microstructure and dynamics to the stress is based on the established formulation [46], with approximations necessary for application to the concentrated suspension case detailed in our previous papers [32, 63]. Only the final expressions for $\langle \mathbf{S}^B \rangle$ and $\langle \mathbf{S}^H \rangle$ are given below. Note that the interparticle stress can be neglected for hard-sphere suspensions in comparison with Brownian and hydrodynamic stress contributions. The Brownian contribution to stress is formulated as

$$n \left\langle \mathbf{S}^B \right\rangle = \mathbf{\Sigma}^{B1} + \mathbf{\Sigma}^{B2}, \tag{4.26a}$$

$$\frac{\left\langle \mathbf{\Sigma}^{B1} \right\rangle}{\eta\dot{\gamma}} = -Pe^{-1}\frac{27}{8\pi}\phi^2 \int \mathbf{nn} g ds, \tag{4.26b}$$

$$\frac{\left\langle \mathbf{\Sigma}^{B2} \right\rangle}{\eta\dot{\gamma}} = Pe^{-1}\frac{27}{8\pi}\phi^2 \int_2^{r^\star} \left(\mathbf{R}^{SU} \cdot (\mathbf{R}^{FU})^{-1}\right)_{pair} \cdot \nabla g d\mathbf{r}, \tag{4.26c}$$

where $\mathbf{n}$ is the unit vector along the line of centers, from particle 1 to 2 and subscript *pair* refers to isolated pair configuration. The first term is a surface integration and the integration in the second term is carried out from contact to $r^\star$. Here $r^\star$ is defined as the radius where the increase in angularly averaged pair distribution function, $\tilde{g}(r)$, from unity drops to 50% of its value at contact, $\tilde{g}(r^\star) - 1 = 0.50\,(\tilde{g}(2) - 1)$. The resistance functions in (4.26c) are the tabulated isolated pair resistance functions.

The hydrodynamic stress is computed as

$$\frac{n\langle \mathbf{S}^H \rangle}{\eta\dot{\gamma}} \approx \eta_\infty(\phi)\mathbf{E} + \frac{27}{16\pi}\phi^2 \int_2^{\tilde{r}} \langle R_{rr}^{FU} \rangle_2 \langle U_r \rangle_2 \hat{\mathbf{r}}\hat{\mathbf{r}} \Big(g(\mathbf{r}) - g^{eq}(r) \Big)\, d\mathbf{r}. \tag{4.27}$$

The integration on the right-hand side is carried out in the volume bounded by contact and $\tilde{r}$ where $\tilde{r}$ is defined as the radius where the increase in $\tilde{g}(r)$ from equilibrium drops to 10 % of increase in g at contact from equilibrium value: $\tilde{g}(\tilde{r}) - g^{eq}(\tilde{r}) = 0.1\,(\tilde{g}(2) - g^{eq}(2))$, in agreement with the definition used by Sierou and Brady [7]. In (4.27), $\langle U_r \rangle_2$ is the

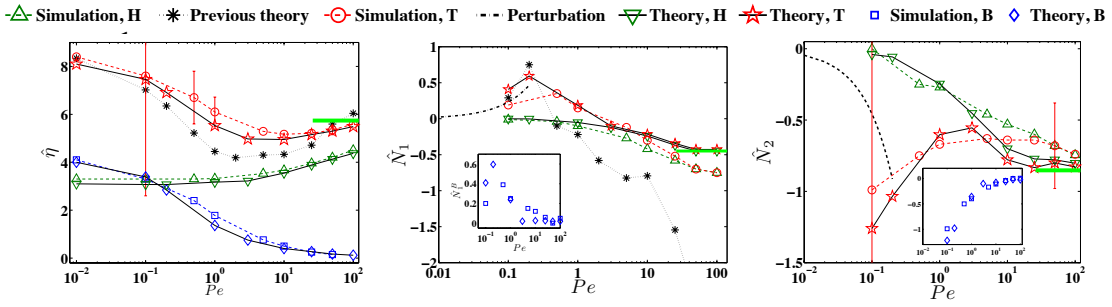

(a) $\phi = 0.40$, $\hat{\eta}$ (b) $\phi = 0.40$, $\hat{N}_1$ (c) $\phi = 0.40$, $\hat{N}_2$

Figure 4.7: Brownian (B) and hydrodynamic (H) contributions and total value (T) of (a) normalized shear viscosity, $\hat{\eta}$, (b) first normal stress difference, $\hat{N}_1$, and (c) second normal stress differences, $\hat{N}_2$, of a $\phi = 0.40$ suspension as a function of Pe. The results of previous theory are shown by symbol "-*-" for comparison. The dotted lines are the results of the perturbation solution at $Pe \ll 1$. The solid straight lines near the axis are the predictions at $Pe \to \infty$.

relative radial hydrodynamic velocity and $\langle R_{rr}^{FU} \rangle_2$ is the relative pair resistance in radial direction, both of which are both computed in solving for $g(\mathbf{r})$ using (4.16) and (4.14). For $Pe \ll 1$, the integral term becomes negligible and the hydrodynamic contribution to the stress is $\eta_\infty \mathbf{E}$.

Figure 4.7 presents predicted and simulated shear viscosity and normal stress differences in the form $\hat{\eta}$, $\hat{N}_1 = \dfrac{\Sigma_{xx} - \Sigma_{yy}}{\eta\dot{\gamma}}$ and $\hat{N}_2 = \dfrac{\Sigma_{yy} - \Sigma_{zz}}{\eta\dot{\gamma}}$. The superscripts "B" and "H" refer to Brownian and hydrodynamic particle stress contributions, respectively, and superscript "T" is the total stress due to particles and fluid. The predictions of the initial version of the present theory are also plotted for comparison. The predicted values of shear viscosity are in good agreement with the simulation results and the current theory improves the agreement relative to the previous theory. Recall that the previous formulation significantly over-predicts the value of near-contact pair probability along the flow direction (see figure 4.4); this results in considerably greater magnitude of N_1, as is clearly observed in figure 4.7(b) by noting that the predicted values of N_1 from the initial formulation continue growing with Pe and go beyond the axis limits of the plot. The current formulation resolves the over-prediction of $g(2;0)$ and as a result a good

quantitative agreement between theory and simulation is obtained for $\hat{N}_1$. Both theories give a good prediction of second normal stress difference. To aid visualization we have only plotted the current formulation results next to simulation results. The dotted lines at $Pe \ll 1$ are the solutions of the perturbation formulation.

Note that the predicted $\hat{N}_1$ and $\hat{N}_2$ approach a constant at $Pe \gg 1$ while the simulation results show a weak growth with Pe. A similar trend is observed for shear viscosity at $Pe > 200$ for $\phi = 0.40$. Recall that the predicted $g(\mathbf{r})$ and pair dynamics do not change with Pe for $Pe\eta_\infty/\eta > 400$ hence, from (4.27), and the predicted rheology thus becomes independent of Pe. In fact, the theory allows for computing the pair microstructure and rheology at infinite Péclet number. This is done by neglecting the Brownian diffusion and interparticle forces in the formulation. The rheological predictions for $Pe \to \infty$ are presented in the figures with a solid horizontal line at the right of the plot. For simulations at $Pe = 1000$ and $\phi = 0.40$, $\hat{\eta} = 6.18$, $\hat{N}_1 = -0.86$ and $\hat{N}_2 = -0.80$ which differ by approximately 10% in magnitude from the values at $Pe = 100$. This indicates that while the near-contact values of g increase, roughly as $Pe^{0.7}$, the rheological properties are a weak function of Pe at high Péclet numbers; this is consistent with the boundary-layer theory predictions of Brady & Morris[27]. Thus, the theory is able to give a fair estimate of nonlinear rheology as $Pe \to \infty$. This has utility for study of non-Brownian suspensions with different interparticle forces.

The effect of volume fraction on nonlinear rheological properties at $Pe \gg 1$ is presented in figure 4.8. The results are given for $Pe\eta'(\phi)/\eta = 270$, where the dimensionless particle pressure, $\hat{\Pi}$, is defined as one-third of the trace of particle stress tensor divided by the fluid shear stress, $\eta\dot{\gamma}$; this quantity is only presented for predicted results as it was not specifically sampled in the present study. In this figure, $\hat{\eta} - \hat{\eta}'_\infty$ is the increase in hydrodynamic viscosity due to shearing motion. We have included simulations at $\phi = 0.53$, where the suspension goes through a shear-induced ordering transition, for comparison. The error bars, based on the standard deviation of the simulation time-series

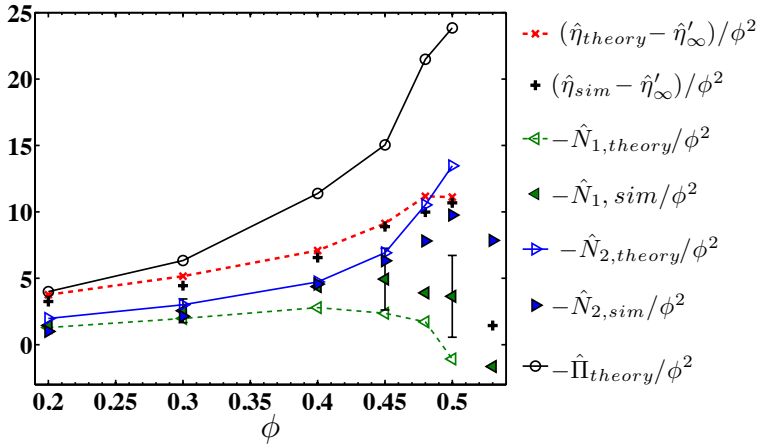

Figure 4.8: Theory predictions and simulation results for nonlinear rheology of sheared suspensions at $Pe\eta'_\infty/\eta = 270$ at different volume fractions. The error bars are approximately the same value for first and second normal stress difference and are only presented for $\hat{N}_1$ at selected ϕ.

results, are approximately the same for the first and second normal stress difference and are only presented for $\hat{N}_1$ at selected ϕ. The error bar generally increases with volume fraction; their values for shear viscosity are much smaller and are not presented here.

The agreement between predictions and simulation results of $\left(\hat{\eta} - \hat{\eta}'_\infty\right)/\phi^2$ is good for the entire range of predicted values. The increase in shear viscosity shows a sudden drop at $\phi = 0.53$ in simulation. This is caused by ordering and has been observed previously [62, 7]. Interestingly, the theory also predicts a maximum at $\phi = 0.48$. For $\hat{N}_2$, the agreement is good for $\phi \leq 0.45$, while at higher volume fraction the theory predicts a larger value than simulation. The theory in general predicts larger values for $\hat{N}_1$. Note that $\hat{N}_1$ is negative for $\phi \leq 0.48$ and $-\hat{N}_1/\phi^2$ is presented in the figure. In both theory and simulation, $\hat{N}_1$ becomes positive at large ϕ. This change in sign of $\hat{N}_1$ is only observed in ordered suspensions in simulation which shows that the theory is capturing an essential features observed in the shear-induced ordering transition. A final point to note is that the increase in magnitude of $\hat{N}_2$ and $\hat{\Pi}$ with ϕ is stronger than the increase in viscosity. For example, the ratio of $-\hat{N}_2/(\hat{\eta} - \hat{\eta}'_\infty)$ increases monotonically

from 0.52 at $\phi = 0.20$ to 1.17 at $\phi = 0.50$ for theory and for simulation the ratio changes from 0.31 at $\phi = 0.20$ to 0.93 at $\phi = 0.50$. Thus we find that different components of the stress tensor scale differently with ϕ, a point which is not readily accounted for in mean-field theories previously proposed for scaling particle stress tensor for concentrated suspensions [27, 37].

4.4 Relative pair velocity and trajectory field

As shown in the prior section, the theory connects microscopic interactions and resulting structure to macroscopic rheological properties. Here, we address the dynamics leading to the microstructural changes. Specifically, we consider the pair interaction in a mean sense. In the present section, we present and analyze average relative hydrodynamic velocity and average pair trajectory fields from theory and simulation, while in the following, §4.5, the results of velocity fluctuations and dispersion of pair trajectories obtained from simulation are presented, and their effects on structure and rheology are discussed. We are unaware of such a consideration of the pair dynamics, which is directly motivated by the analysis of the pair Smoluchowski equation for a concentrated suspension.

The influence of flow on pair dynamics is maximized in the plane of shear $(x - y)$ and the results of average relative velocities and trajectories are presented only in this plane. Figure 4.9 presents the average pair trajectories in a $\phi = 0.20$ suspension at $Pe = 100$ computed from the theory, alongside sampled results (based on integration of sampled pair relative velocities) from simulation. The trajectories for two isolated spheres in Stokes simple shear flow are also presented for comparison. The trajectories from simulations and theory at $\phi = 0.20$ can be divided into three regions. The first region is the reversing trajectories zone, with the final trajectory in this zone shown by a thick solid line. The second zone is that of the compression and wake zone. In this zone the trajectories are bundled in the compressional quadrant near contact and separate

from the contact surface in the extensional quadrant. An example of these trajectories is shown by a thick dotted line. In computing the trajectories, the integration time step was chosen as $\Delta t = 10^{-6}\dot{\gamma}^{-1}$ and the minimum allowed separation distance was set to $r = 2.0002$. For $r < 2.0002$ the radial velocities were set to zero. Based on this method, the trajectories coming from compressional axis do not enter the wake zone, corresponding to the zone with lowest pair probability in $g(\mathbf{r})$ shown in figure 4.3. The point marked as the *stagnation point* separates reversing trajectories from those in the compression and wake zone. The average velocity magnitude is zero at this point. In the absence of fluctuations induced by bath particles, any pair of particles would remain stagnant in this configuration, and $g(\mathbf{r})$ would diverge at this point. Although the presence of fluctuations removes this singularity, the stagnation point is still close to the location of the maximum value of g; see figure 4.6(a). The third trajectory zone contains far-field trajectories which are approximately straight lines following the imposed bulk flow relative velocity. One of these trajectories is also shown by a thick solid line. Note that even at volume fractions as low as $\phi = 0.20$ the pair trajectory is qualitatively different from the isolated pair case. We observe a clear break of fore-aft symmetry in pair trajectories, a structural feature which results in normal stress differences and particle pressure[27]. The main features of pair trajectories change very little up to $\phi \doteq 0.40$ for theory and $\phi \doteq 0.45$ in simulation, and good agreement is found in theory and simulation results.

At higher volume fractions, new regions are formed in addition to the existing features at smaller ϕ. Figure 4.10 shows pair trajectories for $\phi = 0.40$ and 0.50 at elevated Pe alongside $g(\mathbf{r})$ from the same conditions in the shear plane. The trajectory zones appearing at higher solid fraction are illustrated with thick solid lines. We see that the gross features observed in simulation are predicted by the theory. For example, the near-contact trajectories have a strong component along the line of center for both theory and simulation, showing that a pair is pushed strongly towards contact rather

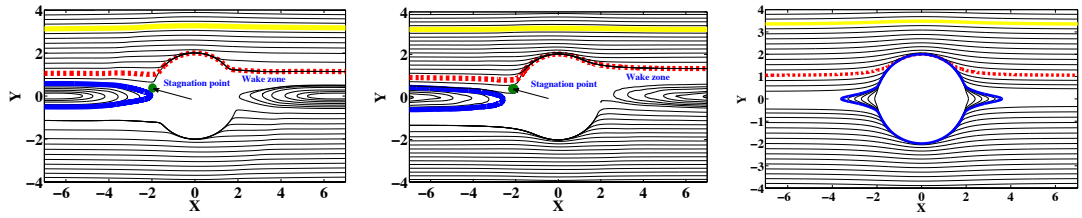

(a) $\phi = 0.2$, $Pe = 100$, theory (b) $\phi = 0.2$, $Pe = 100$, simulation (c) Isolated pair

Figure 4.9: Average pair trajectories in shear plane of a $\phi = 0.20$ suspension at $Pe = 100$ (a) predictions (b) simulation results. (c) Pair trajectories of an isolated pair in simple shear flow.

than tending to rotate more as a double as seen for an isolated pair and at moderate ϕ. The other key predicted feature is the formation of a secondary region of bundled trajectories near contact along the flow direction, a feature also present in the simulation trajectories. This bundled region corresponds to the high probability zone formed along the flow direction. The reasonable prediction of near-contact features enables the theory to give a good prediction of near-contact pair microstructure and rheology.

The predictions, however, are not in agreement with simulation results in the detailed form of the features along the flow direction. It is actually beyond the scope of the theory as envisioned by the authors to capture these features, but it may provide insight to both the dynamics of concentrated suspensions and the means of predicting structure to consider the discrepancies. The theory predicts formation of a "source" along the flow direction at $r \approx 4$ where the term "source" here is used to describe a small volume where trajectories exit but do not enter. As a result, the relative velocity field causes depletion of pair probability around the source point which is observable in the predicted $g(\mathbf{r})$ for these conditions. The trajectories obtained from simulation show a quite different development in this region, appearing to be "sink" points along the flow direction at $r \approx 2, 4$ and 6; sink points are defined as small volumes where a trajectories enter but do not exit. Pairs are pulled to these positions and become stagnant. This is reflected in the simulation results for $g(\mathbf{r})$ shown in figure 4.10(d) through existence of

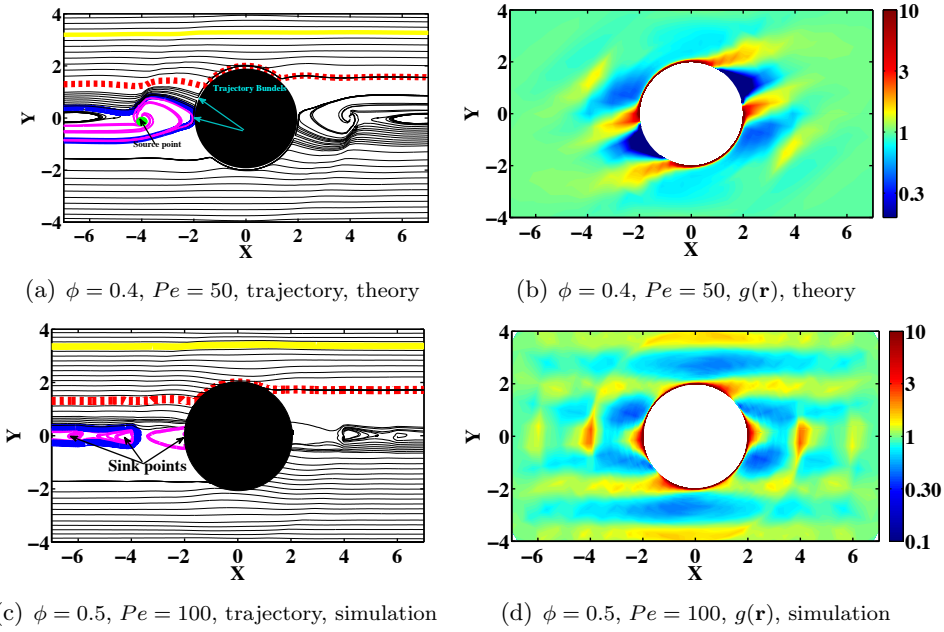

(a) $\phi = 0.4$, $Pe = 50$, trajectory, theory

(b) $\phi = 0.4$, $Pe = 50$, $g(\mathbf{r})$, theory

(c) $\phi = 0.5$, $Pe = 100$, trajectory, simulation

(d) $\phi = 0.5$, $Pe = 100$, $g(\mathbf{r})$, simulation

Figure 4.10: Pair trajectories alongside $g(\mathbf{r})$ in shear plane at $\phi = 0.40$ and 0.50 from theory and simulation respectively.

high probability regions along the flow direction at $r \approx 2$, 4 and 6. These results indicate that the system is close to the flow-induced ordering transition along the flow direction [62].

To gain more insight to the observed discrepancies between the predicted and simulated pair trajectories, we compare the radial and angular relative hydrodynamic velocity components in the shear plane in figure 4.11. The predicted radial velocities are in good qualitative agreement with the simulation results with features generally seen to be "stronger" in the predictions. Near contact, a negative radial velocity is observed near the compressional axis caused by bath particles pushing the pair towards contact. The increase in $g(\mathbf{r})$ and viscosity with Pe and ϕ is caused and controlled by this approaching radial velocity. The positive radial velocity observed at $r \approx 4$ along the compressional axis is due to frequent formation of chain-like structures along the compressional axis where particles 1 and 2 (whose relative velocity is of interest) are separated by an in-

tervening third particle. This configuration effectively stops the approach of particles 1 and 2 along the line of centers and changes the relative radial from the negative value of $r\hat{\mathbf{r}} \cdot \mathbf{E}^{\infty} \cdot \hat{\mathbf{r}}$ to zero. Thus the average effect of bath particles, in this configuration, is to hinder the motion of the pair towards each other which is presented by the positive radial relative velocity at $r \approx 4$ along the compressional axis. The likelihood of formation of chain-like structures near the extensional axis is low, and we do not observe a strong peak at $r = 4$ in that direction.

The qualitative agreement of angular velocities is poorer than the radial velocity. The theory is able to predict the dominant features found in simulation, but with certain clear discrepancies. Most importantly, near-contact variations of U_θ decay quite rapidly away from contact for simulation results while in the predicted U_θ, near-contact features extend farther from contact. As a result the locations of local extrema are shifted roughly about a particle radius to larger r in the predicted results. The cause of this systematic error remains unknown.

4.5 Velocity fluctuations, and $\mathbf{D}^{\dot{\gamma}}$

The probability flux associated with shear-induced fluctuations around the average pair motion is approximated with $-\mathbf{D}^{\dot{\gamma}} \cdot \nabla g$. There is no explicit microstructural relationship for computing $\mathbf{D}^{\dot{\gamma}}$ and this variable has been modeled based on observations from simulation and use of limits for its near-contact and widely separated values. The physical arguments and the final forms of shear-induced relative diffusion were given in §4.2.2. Although the need of including this influence of hydrodynamic fluctuations in sheared suspension theory appears to be validated by the work done to date, understanding of the functional form of the "dispersion flux" and its connection to pair microstructure is in the preliminary stages. We use results, strictly from ASD simulation, to shed some light on relative velocity fluctuations and their relation to dispersion flux and steady microstructure.

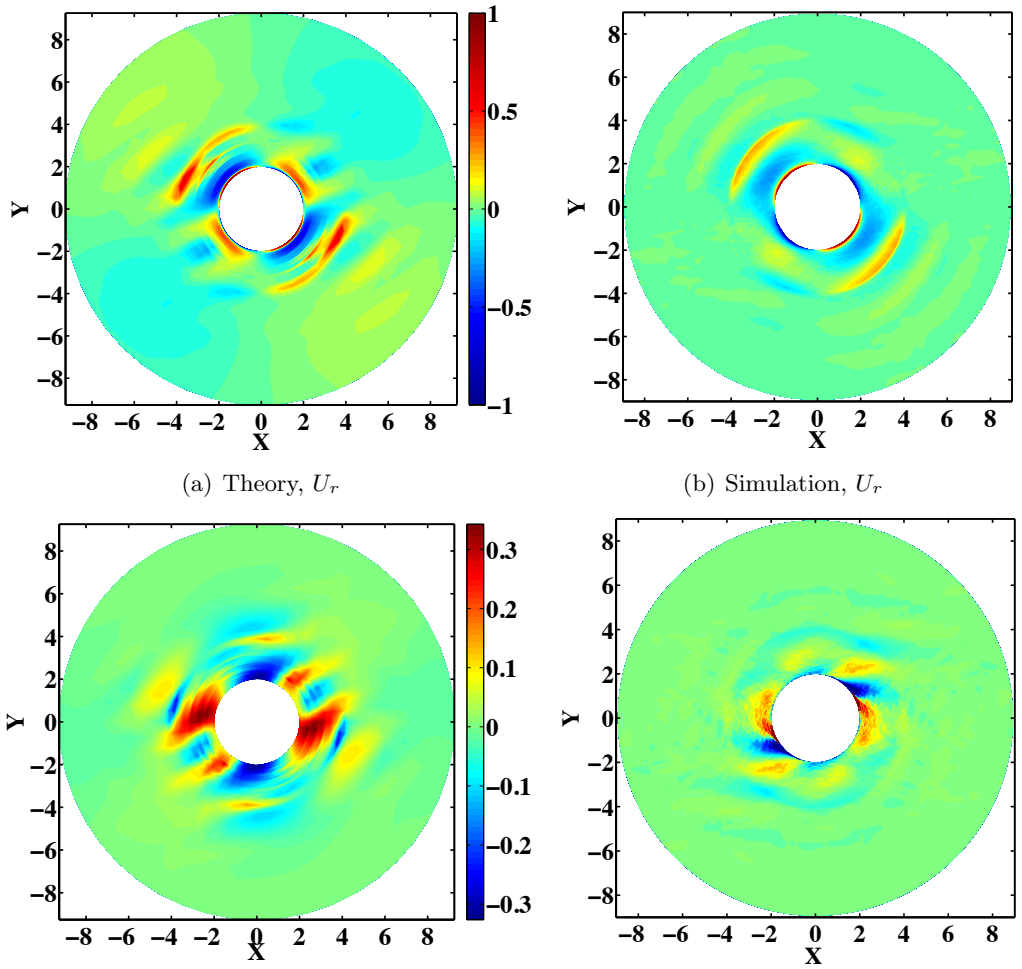

(a) Theory, U_r

(b) Simulation, U_r

(c) Theory, U_θ

(d) Simulation, U_θ

Figure 4.11: Average pair relative velocities in shear plane at $Pe \gg 1.0$. The left hand side figures are theoretical predictions and right hand side is the results of simulation samplings of radial and angular velocities respectively . (a) Theory, radial velocity, $\phi = 0.40$, $Pe = 50$, (b)Simulation, radial velocity, $\phi = 0.40$, $Pe = 1000$, (c) Theory, angular velocity, $\phi = 0.40$, $Pe = 50$, (d) Simulation, angular velocity, $\phi = 0.40$, $Pe = 1000$. The colorbars for theory and simulation results are identical and they are shown next to the theoretical results.

To begin, we study the fluctuations of relative velocity by computing the variance of sampled relative velocities at each pair separation: $\langle \mathbf{U}'\mathbf{U}' \rangle_2 = \langle \mathbf{U}\mathbf{U} \rangle_2 - \langle \mathbf{U} \rangle_2^2$. Figure 4.12 (a-c) shows the variance of relative radial velocity in the shear plane, $\langle U_r' U_r' \rangle_2 = \langle U_r U_r \rangle_2 - \langle U_r \rangle_2 \langle U_r \rangle_2$. Results are presented for $Pe = 1000$, at solid fractions of $\phi =$ 0.20, 0.40 and 0.50. Figure 4.12(d) plots variations of $\langle U_r' U_r' \rangle_2$ with r at the fixed angle $\theta = 3\pi/4$ for the same volume fractions with the values normalized by the far-field values. The radial fluctuations approach zero near contact in all directions. This is a simple consequence of excluded volume although the form of decay to zero is determined by many-body interactions. This has been accounted for modeling the radial component of shear-induced relative diffusivity in (4.24a). Figure 4.12(d) shows that the decay towards zero starts at larger separations as ϕ decreases. The decay of radial shear-induced diffusion in the theory is controlled by parameter m in (4.24a). The values of m (obtained based on the best matching between the predictions and simulation results) increase monotonically from $m = 8.0$ at $\phi = 0.20$ to $m = 20.0$ for $\phi = 0.50$, in agreement with the trend observed in figure 4.12(d). Note that the far-field radial velocity fluctuations are anisotropic with the maximum and minimum values being along the compressional and extensional axis respectively. The largest fluctuations occur when bath particles and one of particles 1 or 2 are in a near-contact configuration along the compressional axis of the flow. The projection of this fluctuation is maximized in $\hat{\mathbf{r}}$ direction when $\hat{\mathbf{r}}$ is along the compressional axis ($\theta = 3\pi/4$) and minimized when $\hat{\mathbf{r}}$ is along the extensional axis ($\theta = \pi/4$) .

The other key feature observed is the existence of next-nearest-neighbor fluctuation zones near the compressional axis. These regions are induced by configurations where bath particles intervene between the pair of interest, i.e. due to formation of a chain-like clustered structure. For $\phi = 0.20$, we see a strong peak at $r \approx 4$ and weaker peaks at $r \approx 6$ and $r \approx 8$. This shows that chain-like structures consisting of three particles are frequently formed in compressional axis while formation of longer chains is less probable

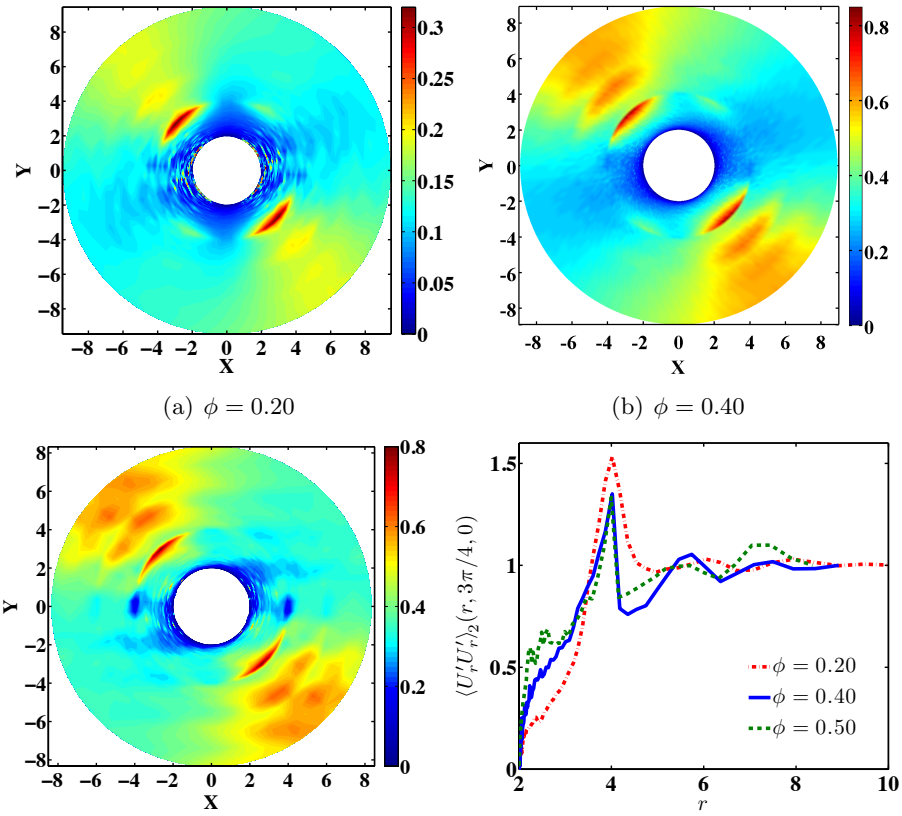

(a) $\phi = 0.20$ (b) $\phi = 0.40$

(c) $\phi = 0.50$ (d)

Figure 4.12: Average relative radial velocity fluctuations, $\langle U_r' U_r' \rangle_2$, in the shear plane from simulation: (a) $\phi = 0.20$, (b) $\phi = 0.40$ (c) $\phi = 0.50$ (d) variations of radial velocity fluctuations with separation distance, r, in shear plane along compressional axis, $\theta = 3\pi/4$ for $\phi = 0.20$, 0.40 and $\phi = 0.50$.

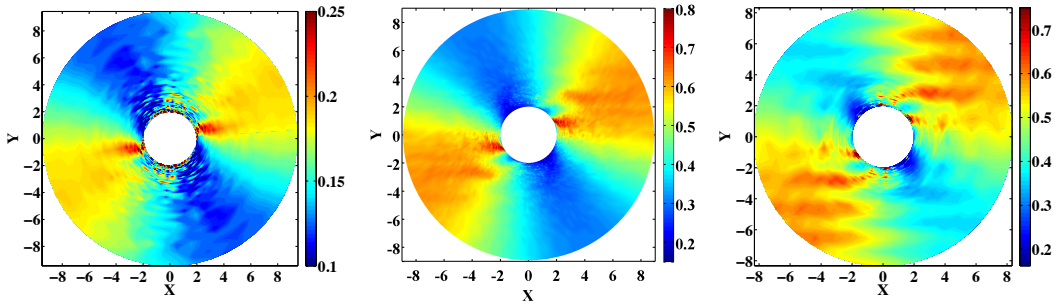

(a) $\phi = 0.20$ (b) $\phi = 0.40$ (c) $\phi = 0.50$

Figure 4.13: Average angular velocity fluctuations, $\langle U'_\theta U'_\theta \rangle_2$ in the shear plane from simulation: (a) $\phi = 0.20$, (b) $\phi = 0.40$, and (c) $\phi = 0.50$.

but still weakly apparent. At $\phi = 0.40$, the second peak is more pronounced than the peak observed at $\phi = 0.20$, suggesting regular formation of chain-like structures with four and more particles. Finally, for $\phi = 0.50$ the peaks extend to $r = 8$. The size of the chain-like clusters at $\phi = 0.50$ is likely affected by the size of the computational box.

Note that there is a reduction of fluctuation strength along the flow direction at $r = 4$. This is related to formation of chains along the flow directions. These structures are stable with time which results in reduction of fluctuations of velocity while chain-like clusters along the compressional axis have a "lifetime" of $O(1)$ in dimensionless time $\dot{\gamma}t$ (strain), and their rotational motion demands large fluctuation of velocity. Recall that the pair trajectory results showed that the pair are attracted to these stagnation points along the flow direction at $\phi = 0.50$ (see figure 4.10(d)). Since the fluctuations imposed by bath particles are weakened in these locations, the particles can retain their ordered structure without fluctuations driving them away, again an indication that the suspension is near the ordering transition.

The fluctuations of angular velocities, $\langle U'_\theta U'_\theta \rangle_2$ for the same conditions are presented in figures 4.13 (a-c). We note that fluctuations remain nonzero everywhere, as discussed in the modeling for shear-induced relative diffusion. The largest angular velocity fluctuations are observed near contact along the extensional axis, while the smallest are near

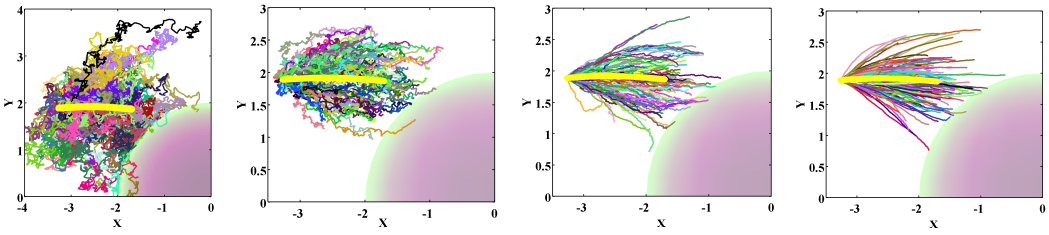

(a) $Pe = 1$ (b) $Pe = 10$ (c) $Pe = 100$ (d) $Pe = 1000$

Figure 4.14: Dispersion of trajectories starting from $r = 3.5$, $\theta = 5\pi/6$ and $\varphi = 0$ for a $\phi = 0.40$ suspension from samplings of simulation configurations projected to shear plane: (a) $Pe = 1$, (b) $Pe = 10$, (c) $Pe = 100$, (d) $Pe = 1000$. The solid line represents the mean trajectory and motion is from left to right along this trajectory.

the compressional axis adjacent to contact. The far-field fluctuations are anisotropic with the maximum and minimum values being in the extensional and compressional quadrants, respectively. The fluctuation strength near the compressional axis at contact is approximately 1/4 of the far-field value along the extensional axis for both $\phi = 0.20$ and $\phi = 0.40$. This was the general trend observed for $Pe \gg 1$ and $\phi \leq 0.45$. We applied this observation in our simplified model for variations of angular shear-induced relative diffusion by setting $\alpha = 1/4$ in (4.24b).

We now consider the dispersion around the pair average motion by following the pair trajectories at different initial pair separations, $\mathbf{r}_0$, forward in time. As an example, figure 4.14 shows the dispersion of pair trajectories starting at $r = 3.5$ and $\theta = 5\pi/6$ for a $\phi = 0.40$ suspension at $Pe = 1$, 10, 100 and 1000. The trajectories are followed to strain of $\dot{\gamma}t = 0.80$, and the average pair trajectory is shown with a thick solid line. At $Pe = 1$ a considerable number of trajectories move in the opposite direction of the average motion, which shows that Brownian motion has a significant role at this Péclet number. Due to the existence of significant Brownian and flow-induced dispersion, $Pe = 1$ has the largest dispersion of trajectories among the results presented here. For $Pe = 10$, 100 and 1000 the trajectories show an average motion in the flow direction (x) and the dispersion around the average trajectory remains qualitatively the same for

this range of Pe. This shows that the dispersion is primarily governed by hydrodynamic fluctuations in the limit of $Pe \geq 100$ and the effect of Brownian motion is very weak. At $Pe = 100$ and 1000, the radius of dispersion around the average trajectory shows a linear increase with average distance traveled by the pair (or equivalently with time). This is characteristic of a super-diffusive motion, and we find that the dispersion is changing from diffusive at $Pe = 1$ to super-diffusive at $Pe \geq 100$.

We can quantify the dispersion around the average trajectory at each pair separation as function of time by subtracting the average pair motion from all the the trajectories starting at the same point: $\langle \mathbf{r}'\mathbf{r}' \rangle_2(t) = \langle \mathbf{r}\mathbf{r} \rangle_2(t) - \langle \mathbf{r} \rangle_2(t) \langle \mathbf{r} \rangle_2(t)$. The results are only presented for pairs located in the shear plane at $t = 0$, and only the dispersion in this plane is displayed, with the focus being on the dispersion of trajectories along the line of centers. In order to pursue this, we define a time-dependent coordinate, $\hat{\mathbf{r}}(t)$, $\hat{\theta}(t)$ and $\hat{\varphi}(t)$ based on the average relative distance of the pair of interest with time, $\langle \mathbf{r} \rangle_2(t)$ and project, $\langle \mathbf{r}'\mathbf{r}' \rangle_2(t)$ along $\hat{\mathbf{r}}(t)\hat{\mathbf{r}}(t)$.

Figures 4.15(a-h) show the spatial variations of dispersion of pair trajectories along the line of centers, $\langle r'r' \rangle_2(t)$, in shear plane for $\phi = 0.40$ and $Pe = 1$, 10 and $Pe = 100$. For $Pe = 1$, the results are presented at strains of $\dot{\gamma} = 0.1$, 0.2, 0.4 and 0.6 while for brevity, at $Pe = 10$ and $Pe = 100$ we only present the results at $\dot{\gamma} = 0.1$ and $\dot{\gamma} = 0.6$. For $Pe = 1$, at small strain $\dot{\gamma}t = 0.1$, a minimum in fluctuation strength is observed at $r \approx 4$ along the compressional axis. This feature is extended with time along the compressional axis. As a result the far-field becomes anisotropic at longer times with the dispersion being larger in the extensional zone. A striking finding is that the results are quite the opposite at $Pe = 100$, for which condition we see that the spatial variations of dispersion are similar in form to the velocity fluctuations shown in figure 4.12; the maximum dispersion occurs at $r \approx 4$ along the compressional axis. The transition between the form of $\langle \mathbf{r}'\mathbf{r}' \rangle_2(t)$ at $Pe = 1$ to $Pe = 100$ is observed in the spatial variations of dispersion at $Pe = 10$ shown in figures 4.15(e) and 4.15(f). For all three Pe, the near-contact small fluctuation region

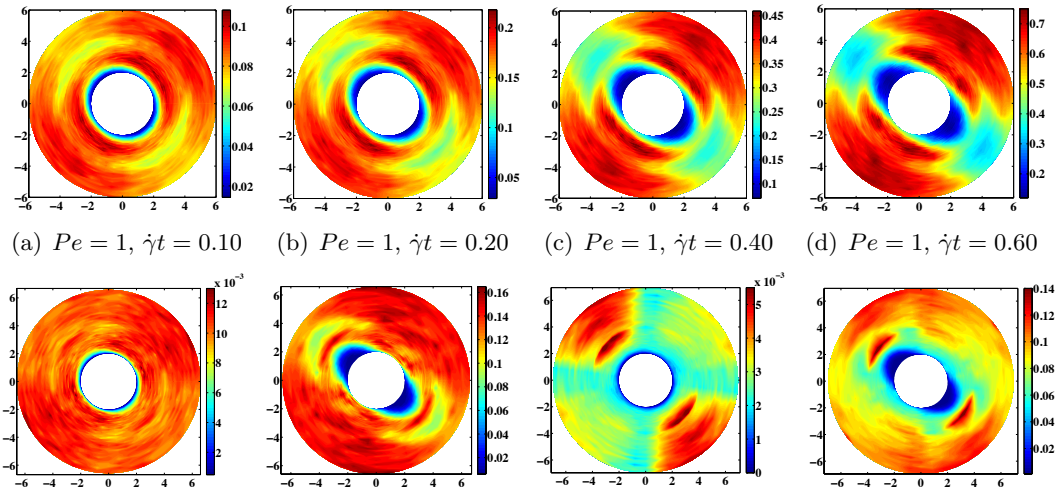

(a) $Pe = 1$, $\dot{\gamma}t = 0.10$ (b) $Pe = 1$, $\dot{\gamma}t = 0.20$ (c) $Pe = 1$, $\dot{\gamma}t = 0.40$ (d) $Pe = 1$, $\dot{\gamma}t = 0.60$

(e) $Pe = 10$, $\dot{\gamma}t = 0.10$ (f) $Pe = 10$, $\dot{\gamma}t = 0.60$ (g) $Pe = 100$, $\dot{\gamma}t = 0.10$ (h) $Pe = 100$, $\dot{\gamma}t = 0.60$

Figure 4.15: Spatial variations of radial dispersion of pair trajectories with time, $\langle r'r' \rangle_2(t)$. Figures (a) to (d) are variations at different strains related to $Pe = 1$ and $\phi = 0.40$: (a) $\dot{\gamma}t = 0.1$, (b) $\dot{\gamma}t = 0.2$, (c)$\dot{\gamma}t$=0.4 and (d)$\dot{\gamma}t = 0.6$. Figures (e) to (h) show the spatial variations for $Pe = 10$ and 100 at $\phi = 0.40$: (e) $Pe = 10$, $\dot{\gamma}t = 0.1$, (f) $Pe = 10$, $\dot{\gamma}t = 0.6$, (g)$Pe = 100$, $\dot{\gamma}t = 0.1$ and (h) $Pe = 100$, $\dot{\gamma}t = 0.6$.

extends to larger r with time.

At $Pe = 1$, the dispersion is primarily controlled by Brownian motion and therefore $\langle \mathbf{r}'\mathbf{r}' \rangle_2(t) \approx 2k_bT\langle \mathbf{M} \rangle_2$ where $\langle \mathbf{M} \rangle_2$ is the average pair relative mobility. However, the flow-induced structure is important, as it generates the strong likelihood of having chain-like structures along the compressional axis, and a consequence is that $\langle \mathbf{M} \rangle_2$ is reduced at $r \approx 4$. This results in a reduction of Brownian contribution to the radial dispersion in this region. At $Pe = 100$, the dispersion is controlled by fluctuations of hydrodynamic relative velocities, which induces a large dispersion at $r \approx 4$ due to frequent formation of chain-like structures in compressional axis. At $Pe = 10$, we see a transition between these behaviors.

The near-contact dispersion at $Pe = 100$ remains $O(10^{-4})$ up to $\dot{\gamma}t = 0.8$. By contrast for $Pe = 1$, while the values remain small they are significantly larger than the values at $Pe = 100$, indicating the near-contact radial dispersion is dominated by Brownian

diffusion. This is in agreement with the assumption made in formulating the radial relative diffusion. From (4.24a), shear-induced radial diffusivity scales as $\dot{\gamma}a^2(r-2)^2$ near contact, while Brownian diffusion is proportional to $k_bT(r-2)$ which makes Brownian diffusion larger than shear-induced relative diffusion at fixed Pe as $r \to 2$.

With increase of time, the average position of the pair changes with respect to the initial position. For example, pairs in the compressional zone approach the near-contact configuration with time and pairs in near-contact configuration along the extensional axis recede from one another. As a result, the low dispersion region is extended to larger separations along the compressional axis and it is compressed along the extensional axis for both Péclet numbers.

A further observation is that the magnitude of the radial dispersion defined by the colorbar next to each figure shows an almost linear increase with time (strain) at $Pe = 1$ which is an indication that the dispersion is diffusive. On the other hand, at $Pe = 10$ and $Pe = 100$, the increase in values is approximately $t^{1.4}$ and $t^{1.8}$, respectively, indicating the dispersion becomes super-diffusive with increase of Pe. A final point is that at long time, or large strain, pairs all become decorrelated, so that the dispersion becomes uniform and independent of initial pair separation. For the range of strains studied here, however, the dispersion remains a strong function of initial position, indicating that the configurations controlling the pair dynamics remain highly correlated up to $\dot{\gamma}t = 0.80$.

4.6 Conclusion

This work takes a novel approach to the use of the pair Smoluchowski equation (SE) in sheared colloidal suspensions. The pair SE is a convection-diffusion equation for transport of pair distribution function, $g(\mathbf{r})$. The convective flux is a result of average motion of two particles in the presence of the remaining, or bath, particles and is given by $\mathbf{j} = \langle \mathbf{U} \rangle_2 g(\mathbf{r})$ where $\langle \mathbf{U} \rangle_2$ is the average relative pair velocity. The dispersive flux is the flux associated with dispersion of two particle around the average trajectory (see figure

4.2). In this work, we have described the pair SE-based predictions of pair microstructure and rheology for concentrated suspensions developed in prior work, and proceeded to describe a study of the the dynamical variables which appear as coefficients in the pair SE. These variables, $\langle \mathbf{U} \rangle_2$ and $\langle \mathbf{D} \rangle_2$, control the form of $g(\mathbf{r})$. In pursuing this pair dynamics information, we have considered both the predictions of our microstructural theory (for the velocity only) and Accelerated Stokesian Dynamics simulation results. The fluxes associated with Brownian and interparticle interactions are well-defined and pose little difficulty. Thus we have focused on strongly sheared suspensions where hydrodynamic interactions control the microstructure.

The microstructural theory based on the pair SE presented here follows directly from our recently proposed theory for sheared suspensions [32]. The current theory modifies the original formulation in the manner of handling the hydrodynamic contribution to the pair relative velocity. Also we make use of simulation results and propose a more detailed description of shear-induced diffusion. These modifications significantly improve the predictions, eliminating or reducing discrepancies of predictions of microstructure and rheology from those determined in simulation. One clear discrepancy between simulation and predictions is that the predictions of pair microstructure tend to become independent of Pe at large Péclet numbers while the simulated values of g continue growing as $Pe^{0.7}$. The comparison of rheological results at $Pe = 1000$ from simulations and predicted rheology as $Pe \to \infty$ shows that the current theory provides reasonable predictions of nonlinear rheology in the limit of $Pe \to \infty$ and may be used to study non-Brownian dispersions with interparticle interactions.

The average pair trajectories from the theory and simulation were presented for a selection of volume fractions at $Pe \gg 1$. The trajectories at volume fractions as low as $\phi = 0.20$ were strikingly different from the case of isolated pair of spheres for both theory and simulations. Many-body hydrodynamic interactions become stronger with increase of ϕ and induce changes in the anisotropic form of $g(\mathbf{r})$. The origin of these

structural developments is clearly reflected in pair trajectories. The theory gives a very good prediction of trajectories up to intermediate concentrations, ($\phi = 0.35$) and is able to predict the main near-contact features of pair trajectories at higher volume fractions. However, the predictions were not in agreement with simulation for the features observed along the flow direction at elevated ϕ, and a more detailed inquiry shows that the disagreement is largely due to the predicted angular relative velocities differing from simulations.

One of the most challenging parts in theoretical development of pair Smoluchowski equation for sheared suspensions is formulation of the flow-induced dispersion flux. This flux was modeled in this work with a diffusion, i.e. $\mathbf{j}^D = -\mathbf{D}^{\dot{\gamma}}(\mathbf{r}) \cdot \nabla g(\mathbf{r})$. We have utilized simulation to gain more insight to the rational development of a model for $\mathbf{D}^{\dot{\gamma}}$. It is important to realize that the diffusive form considered for dispersive flux is an approximation which is exact only when pair trajectories go through an instantaneous diffusive motion with respect to the flow time [80], $\langle \mathbf{r}'\mathbf{r}' \rangle_2 = \mathbf{D}^{\dot{\gamma}} t$. The results presented in this work show this is clearly not the case for $Pe > 1$. The dispersion at $Pe \gg 1$ is super-diffusive i.e. $\langle \mathbf{r}'\mathbf{r}' \rangle_2(t) = t^\alpha$ with $\alpha > 1$ in short times; see figure 4.15. At large strains, the pair particle motions eventually become uncorrelated, and the dispersion becomes diffusive with the diffusion being determined by the shear-induced self diffusion. One expects that the approximation of the dispersion as an instantaneous diffusion would grow less accurate as $Pe \to \infty$. This can be observed in the predicted microstructure, where $g(\mathbf{r})$ is saturated at $Pe\eta'_\infty/\eta > 270$ while near-contact $g(\mathbf{r})$ in simulation results continues to grow as $Pe^{0.7}$. However the nonlinear rheology is a weak function of Péclet number as $Pe \to \infty$; hence the theory is able to give a reasonable prediction of nonlinear rheology in the limit of infinite Péclet number.

The flow-induced dispersion of pair trajectories observed in sheared suspensions may, in a wider scope, be categorized as anomalous diffusion [81], which is defined as any dispersive process where the mean-square displacement behaves nonlinearly with time

($\alpha \neq 1$). One may view the diffusion approximation made here in terms of Fokker-Planck equation theory [82]. It is known that systems with anomalous diffusion are not described by the classical Fokker-Planck equation, and one must use the *fractional* [81, 83] or *nonlinear*[84] Fokker-Planck equation. While it remains unclear how to formulate the present theory in such terms, this may prove to be a valuable direction of study.

5 Active microrheology

5.1 Introduction

In the previous chapters, a theory for microstructure and rheology of colloidal dispersions was developed based on the Smoluchowski theory for the configurational probability. The structural and rheological predictions of the theory were compared against Stokesian Dynamics simulations to test it and recognize its limitations. The theory offers a general framework for considering many-body thermal and hydrodynamic interactions of particles in flow-driven suspensions and it is not limited only to studying the shear flow conditions.

Here, we study active microrheology of colloidal suspension within the developed framework. In active microrheology, a probe particle is pulled through the fluid sample with an external force or a fixed velocity and a measure of the viscosity of the fluid is obtained by taking the average velocity of the probe in case of applying an external force (or measuring the average force on the probe when the velocity is imposed on the probe) and using Stokes drag law, $\eta_{micro} = \dfrac{F^{ext}}{6\pi U a}$ for a spherical probe particle. The problem has significant practical and fundamental relevance [85] and it is an ideal ground for examining and extending the theory. Over the last two decades microrheology has emerged as a rapidly growing field of research in rheology and soft matter physics [85]. A general review of the field would demand a separate chapter. Here we only give a very brief review of the literature focusing on active microrheology in colloidal dispersions. The interested reader is referred to the review papers by MacKintosh & Schmidt [86],

Waigh [87] and Squires & Mason [85].

In traditional rheological measurements (hereafter, macrorheology), a macroscopic sample of fluid is subjected to a controlled rate of strain (such as oscillatory and simple shear) or controlled shear stress in rheometers with different geometries of flow zone defined by various fixtures, including cone-and-plate or parallel-plate, and the bulk rheological properties of the material including shear viscosity, normal stress differences as well as elastic and loss moduli are measured from the response of the material [88, 89, 90]. Macrorheology has a number of limitations. For example, it measures the bulk response of material averaged over large length scales compared to the characteristic size of the microscopic constituents of the fluid, i.e. polymer chain length in polymer melts and the size of particles in colloidal dispersions. Macrorheology also requires milliliter-scale volumes of the complex fluid to be able to run the experiments, which makes it problematic for characterization of samples which are rare or expensive to produce in such volumes. In microrheology, rheology is measured by studying the dynamics of a probe particle inside the sample. Since the probe is usually of micrometers in size, it allows study of the microstructural heterogeneity at length scales significantly smaller than macrorheology. Also the dynamical characterization is carried out in microliter samples which enables rheological measurements on samples available in limited volumes.

In what is known as passive microrheology, the probe wanders around the fluid through thermal fluctuations. The probe's motion is monitored and from statistical measures such as mean-square displacement and velocity autocorrelation function of the probe, the linear viscoelastic response of the material is computed using an extended form of Stokes-Einstein relation in linear viscoelastic regime known as generalized Stokes-Einstein relation (GSER) [91]. This method has been applied to a variety of complex fluids and has shown promising agreement with linear viscoelastic measurements. However, the validity of GSER becomes questionable in certain situations discussed by Squires & Mason [85]. The main limitation of passive microrheology is that it only pro-

vides information on the linear response of the material. However in many applications it is desired to know the behavior of the fluid under conditions where the fluid is strongly deformed and hence is away from its linear response regime.

In an active microrheology experiment, the probe is actively moved through the fluid by means, for example, of magnetic forces [92] or optical tweezers [93]. As a result the fluid is driven away from the equilibrium state around the probe. This provides a way to study the nonlinear response of the material. Unlike the passive microrheology where a solid theoretical foundation is available through equilibrium statistical mechanics and linear response theory, the theoretical foundations of active microrheology are still very undeveloped due to the inherent complexity associated with non-equilibrium statistical mechanics. One of most important questions here is perhaps to what degree the results of active microrheology can be compared against the macrorheology; what are the main differences between the two methods, and do those differences offer a new insight about the material?

It is the aim of this chapter to shed some light on some aspects of these questions. For this purpose, it is more appropriate to study a system for which a microscopic theory of some completeness in macroscopic level is already developed and can be envisioned for microrheology as well. Here, we use the framework of the microstructural theory developed for sheared suspension to study structure and rheology in active microrheology. To measure the success of the theory and realize its shortcomings, we perform Accelerated Stokesian Dynamics simulations of colloidal dispersions active microrheology by setting the shear rate equal to zero and applying an external force, F^{ext}, on one of the colloidal particles, the probe particle, while no net force/torque is applied on the remaining particles. This is an exact replica of constant force active microrheology. The microstructure from sampling the configurations from ASD simulation are compared against the predictions at $Pe_f = \dfrac{F^{ext}a}{k_bT} = 1, 10$ and 100 for $\phi = 0.40$ where Pe_f is the ratio of external force to Brownian force. To study the differences and similarities between micro and

macro rheology, the predictions of micro-viscosity are compared the against the ASD shear viscosity as a presentation of macrorheological measurements.

The motion of the probe can be regulated by either controlling the external force, F^{ext}, on the probe which is typically achieved using magnetic beads as the probe [92] or by setting the velocity, U, of the probe normally done by optical tweezers [93]. This may be regarded as the equivalent of controlled stress vs rate of strain rheometry in macrorheology. While in macrorheology, the two methods typically yield similar results, in active microrheology it is not certain that the two methods are equivalent. Squires & Brady [94] theoretically studied the problem for a spherical probe in a dilute colloidal dispersion with no hydrodynamic interactions amongst the particles. They considered both cases of fixed external force and velocity on the probe as well as the effect of ratio of the size of the probe to suspended particles. Khair & Brady later extended this work by taking into account the pair hydrodynamic interactions [95] when the external force is fixed on the probe. In a separate work, they also studied the role of shape of the probe particle on the predicted micro-viscosity [96]. Results of Brownian dynamics simulations performed over a wide range of volume fractions for hard-sphere colloidal suspensions are in qualitative agreement with the dilute theories but quantitative agreement is not obtained [97].

Our theory extends on the previous ones by explicitly taking into account the effect of many-body interactions on microstructure and rheology. As a result it enables investigating colloidal dispersions at high volume fractions. We know of only one work by Gnann et al. [98] who studied dense colloidal suspensions in active microrheology. The noted work used mode-coupling theory to predict the micro-viscosity of a probe in colloidal suspension under a constant external force near the jamming transition. Hydrodynamic interactions are neglected in their work, with fitting parameters introduced at each volume fraction to enable close predictions of theory and experimental results. Our theory on the other hand considers full near-field and far-field hydrodynamic inter-

actions and has essentially no adjustable parameters. We consider both conditions of fixed external force and velocity of the probe. The main difference between these two methods of probing a material lies in the existence of force-induced fluctuating motion of the probe in case of applying an external force; in constant velocity forcing, the trajectory of the probe remains a straight line. This points to the other novel aspect of this theory, which is the inclusion of this additional dispersion induced by the probe's motion in the pair Smoluchowski equation through a diffusion flux. As a result, the microstructural and microrheological differences between the two methods can be studied systematically.

5.2 Microstructure formulation

5.2.1 Constant velocity probe

Consider N identical spherical particles dispersed in an incompressible Newtonian fluid. We are interested in the case where one of these particles, i.e. the probe particle tagged here as particle 1, is pulled through the bath of particles with a constant velocity (CV), $\mathbf{U}_1$. The goal is to compute the force exerted on the probe from the bath particles and the fluid. The motion of the probe particle through the suspension changes the distribution of force/torque free bath particles around it . The resistance to motion of the probe depends on this distribution, as the exerted force and suspension microstructure are coupled. We assume the coupling of microstructure and probe particle motion is governed by the Smoluchowski equation (SE) which for N-particle configurational space is written

$$\frac{\partial P_N}{\partial t} + \sum_{\alpha=1}^{N} \nabla_\alpha \cdot \mathbf{j}_\alpha = 0, \tag{5.1}$$

where $P_N(\mathbf{x}_1, \mathbf{x}_2, ..., \mathbf{x}_N)$ is the N-particle configurational probability distribution, and $\mathbf{j}_\alpha$ is the probability flux associated with particle α. In case of pulling the probe with a fixed velocity, the probability flux associated with the probe is purely convective and

expressed as $\mathbf{j}_1 = \mathbf{U}_1 P_N$. The rest of the particles, however, can move freely in response to Brownian, interparticle and hydrodynamic forces; the flux for $\alpha \neq 1$ is expressed as

$$\mathbf{j}_\alpha = \mathbf{U}_\alpha^H P_N + \left(\sum_{\beta=1}^{\beta=N} \mathbf{M}_{\alpha\beta}^{UF} \cdot \mathbf{F}_\beta^P \right) P_N - \sum_{\beta=1}^{\beta=N} \mathbf{D}_{\alpha\beta} \cdot \nabla_\beta P_N, \tag{5.2}$$

where $\mathbf{U}_\alpha^H$ is the hydrodynamic velocity of particle α induced by motion of the probe particle and its hydrodynamic interaction with bath particles, $\mathbf{M}_{\alpha\beta}^{UF}$ is the mobility of particle α due to a force on particle β, and $\mathbf{D}_{\alpha\beta} = k_b T \mathbf{M}_{\alpha\beta}^{UF}$ is the diffusion tensor. The term $\mathbf{U}_\alpha^P = \sum_{\beta=1}^{\beta=N} \mathbf{M}_{\alpha\beta}^{UF} \cdot \mathbf{F}_\beta^P$ is, therefore, the velocity of particle α induced by interparticle forces applied on the rest of the particles and $\mathbf{U}_\alpha^B = -\sum_{\beta=1}^{\beta=N} \mathbf{D}_{\alpha\beta} \cdot \nabla_\beta P_N / P_N$ is the velocity of particle α induced by Brownian forces from bath particles. The interparticle force exerted on particle β is expressed in terms of an interparticle potential V as $\mathbf{F}_\beta^P = -\nabla_\beta V$, where ∇_β is the gradient with respect to the position of particle β.

The minimum level of description of the distribution of bath particles around the probe (where still some theoretical progress is possible) is the distribution of number density of bath particles around the probe, $P(\mathbf{r}) = ng(\mathbf{r})$ where $n = N/V$ is the average number density and $g(\mathbf{r})d\mathbf{r}$ is the likelihood of observing a bath particle between $\mathbf{r}$ and $\mathbf{r} + d\mathbf{r}$. To reduce to an equation for $g(\mathbf{r})$, (5.1) is integrated over all possible configurations of $N-2$ particles keeping particle 1 and one bath particle (which we refer to as particle 2) fixed (meaning of known position, but mobile), yielding

$$\frac{\partial g}{\partial t} + \nabla \cdot \left\langle \mathbf{j}_2 - \mathbf{j}_1 \right\rangle_2 = 0. \tag{5.3}$$

The average of a function $A(\mathbf{r})$ at a fixed separation is denoted $\langle A \rangle_2(\mathbf{r})$, with the averaging performed over all possible configurations of the other $N-2$ "bath" particles. We make a mean-field approximation, assuming that the particle pair of interest is immersed in a field that contains the average effect of the bath of other particles. As a result of

this, we neglect the convective flux associated with fluctuations of force and mobility:

$$\langle\, \mathbf{M} \cdot \mathbf{F} \,\rangle_2 = \langle\, \mathbf{M} \,\rangle_2 \cdot \langle\, \mathbf{F} \,\rangle_2. \tag{5.4}$$

Applying the mean-field approximation to (5.3), the average velocities of particles 1 and 2 are related to the average hydrodynamic forces on each particle as follows:

$$\begin{bmatrix} \langle \mathbf{F}_1^H \rangle_2 \\ \\ \langle \mathbf{F}_2^H \rangle_2 \end{bmatrix} = \begin{bmatrix} \mathbf{R}_{11} & \mathbf{R}_{12} \\ \\ \mathbf{R}_{21} & \mathbf{R}_{22} \end{bmatrix} \cdot \begin{bmatrix} -\mathbf{U}_1 \\ \\ -\langle \mathbf{U}_2 \rangle_2 \end{bmatrix} \tag{5.5}$$

where

$$\begin{bmatrix} \mathbf{R}_{11} & \mathbf{R}_{12} \\ \\ \mathbf{R}_{21} & \mathbf{R}_{22} \end{bmatrix} = \begin{bmatrix} \langle \mathbf{M}_{11}^{UF} \rangle_2 & \langle \mathbf{M}_{12}^{UF} \rangle_2 \\ \\ \langle \mathbf{M}_{21}^{UF} \rangle_2 & \langle \mathbf{M}_{22}^{UF} \rangle_2 \end{bmatrix}^{-1} . \tag{5.6}$$

Note that the formulation is written for hydrodynamic forces applied from the fluid to the particles, resulting in a negative sign factor for velocities in (5.5). Since the probe velocity is fixed and does not fluctuate, no Brownian force is applied from the probe on any of the bath particles and the Brownian force on particle 2 from the bath particles is

$$\langle \mathbf{F}_2^B \rangle_2 = -k_b T \nabla g(\mathbf{r}) / g(\mathbf{r}). \tag{5.7}$$

Recall that the bath particles are force/torque free, $\langle \mathbf{F}_2 \rangle_2 = \langle \mathbf{F}_2^H \rangle_2 + \langle \mathbf{F}_2^B \rangle_2 + \langle \mathbf{F}_2^P \rangle_2 = 0$. Incorporating (5.5) and (5.7) to the force/torque free condition of bath particles, $\langle \mathbf{U}_2 \rangle_2$ is written as

$$\langle \mathbf{U}_2 \rangle_2 = (\mathbf{R}_{22})^{-1} \cdot \Big[-\mathbf{R}^{21} \cdot \mathbf{U}_1 + \langle \mathbf{F}_2^P \rangle_2 - k_b T \nabla g(\mathbf{r}) / g(\mathbf{r}) \Big]. \tag{5.8}$$

Taking $\langle\, \mathbf{j}_2 - \mathbf{j}_1 \,\rangle_2 = (\langle \mathbf{U}_2 \rangle_2 - \mathbf{U}_1)\, g(\mathbf{r})$, (5.3) in steady state is modified to pair SE for

CV

$$\nabla_{\mathbf{r}} \cdot \left[\mathcal{C} \cdot \mathbf{U}_1 g(\mathbf{r}) + \mathbf{M} \cdot \langle \mathbf{F}_2^P \rangle_2 g(\mathbf{r}) - k_b T \mathbf{M} \cdot \nabla_{\mathbf{r}} g(\mathbf{r}) \right] = 0, \tag{5.9}$$

where $\mathcal{C} = -\left(\mathbf{R}_{22}\right)^{-1} \cdot \mathbf{R}_{21} - \mathbf{I}$ and $\mathbf{M} = \left(\mathbf{R}_{22}\right)^{-1}$.

It is convenient to write the pair SE in dimensionless form. The quantities are non-dimensionalized as follows

$$\mathbf{r} \sim a, \quad \langle \mathbf{M}_{\alpha\beta} \rangle_2 \sim M_0, \quad \mathbf{R}_{\alpha\beta} \sim M_0^{-1}, \quad \mathbf{U}_1 \sim U_a, \quad \langle \mathbf{F}^P \rangle_2 \sim k_b T/a,$$

and $M_0 = \dfrac{1}{6\pi\eta a}$ is the single particle mobility. The pair SE in dimensionless form is

$$\nabla \cdot \left[\mathcal{C} \cdot \mathbf{U}_1 g(\mathbf{r}) + Pe_U^{-1} \cdot \Big(\mathbf{M} \cdot \langle \mathbf{F}_2^P \rangle_2 g(\mathbf{r}) - \nabla g(\mathbf{r}) \Big) \right] = 0, \tag{5.10}$$

where

$$Pe_U = \frac{U_a a}{k_b T M_0} = \frac{6\pi\eta U_a a^2}{k_b T}. \tag{5.11}$$

The boundary conditions for (5.10) are

$$\mathbf{j}_{\mathbf{r}} = 0 \quad \text{at} \quad r = 2, \tag{5.12a}$$

$$g \to 1 \quad \text{as} \quad r \to \infty. \tag{5.12b}$$

The first boundary condition imposes zero radial flux at contact due to excluded volume. In order to solve (5.10), the conditional averages in the equation including average pair mobility and interparticle force should be formulated in terms of $\mathbf{r}$ and $g(\mathbf{r})$. The formulations are given in §5.2.3.

5.2.2 Constant force probe

We now consider the case where the probe particle is pulled through the bath with a constant force (CF), $\mathbf{F}^{ext}$, and take the force direction to be along $\mathbf{z}$ axis. The dispersive

flux induced by velocity fluctuations of the probe and bath particles is the fundamental difference of CF and CV active microrheology. In a CF experiment, unlike when the probe is dragged with a constant velocity, the probe can change its direction and speed. As a result, the probe trajectory is not always in the direction of the applied force, and there is also a dispersion around the average motion. In the limit of the probe being pulled with a force significantly greater than the thermal forces in the system, $Pe_f = \dfrac{F^{ext}a}{k_bT} \gg 1$, the thermal fluctuations become negligible with respect to the force-induced fluctuations; thus it is essential to include this term for formulating the active mirorheology with CF at $Pe_f \gg 1$. Note that, in defining Pe_f, $F^{ext} = |\mathbf{F}^{ext}| = F_z^{ext}$.

The CF formulation follows the CV formulation until the relation (5.3). The probability fluxes are calculated, however, based on a mobility formulation here. The hydrodynamic velocities of the probe and particle 2 are expressed as

$$\begin{bmatrix} \langle \mathbf{U}_1^H \rangle_2 \\ \\ \langle \mathbf{U}_2^H \rangle_2 \end{bmatrix} = \begin{bmatrix} \langle \mathbf{M}_{11}^{UF} \rangle_2 & \langle \mathbf{M}_{12}^{UF} \rangle_2 \\ \\ \langle \mathbf{M}_{21}^{UF} \rangle_2 & \langle \mathbf{M}_{22}^{UF} \rangle_2 \end{bmatrix} \cdot \begin{bmatrix} \mathbf{F}^{ext} \\ \\ 0, \end{bmatrix}, \tag{5.13}$$

which gives

$$\mathbf{U}^H = \langle \mathbf{U}_2^H \rangle_2 - \langle \mathbf{U}_1^H \rangle_2 = -\left(\langle \mathbf{M}_{11}^{UF} \rangle_2 - \langle \mathbf{M}_{21}^{UF} \rangle_2 \right) \cdot \mathbf{F}^{ext}. \tag{5.14}$$

Note that the bath particles are force free, i.e. $\mathbf{F}_2^{ext} = 0$ and F^{ext} in (5.13) is applied externally; as a result the hydrodynamic force applied on particles from the fluid to balance the external force is $-F^{ext}$ and in (5.13), unlike (5.5), there is no negative sign factor in the velocity components. The relative velocity associated with interparticle forces can be computed using a relation similar to (5.13), and is equal to

$$\mathbf{U}^P = \langle \mathbf{U}_2^P \rangle_2 - \langle \mathbf{U}_1^P \rangle_2 = (\langle \mathbf{M}_{22} \rangle_2 - \langle \mathbf{M}_{12} \rangle_2) \cdot \langle \mathbf{F}_2^P \rangle_2 + (\langle \mathbf{M}_{21} \rangle_2 - \langle \mathbf{M}_{11} \rangle_2) \cdot \langle \mathbf{F}_1^P \rangle_2, \tag{5.15}$$

where the UF superscript of the mobility tensor $\mathbf{M}$ is dropped for convenience.

We model the flux associated with the flow-induced dispersion as a diffusion. The relative flux due to velocity fluctuations is therefore written as

$$\mathbf{j}_2^D - \mathbf{j}_1^D = -\left(\mathbf{D}_{22} - \mathbf{D}_{12} + \mathbf{D}_{11} - \mathbf{D}_{21}\right) \cdot \nabla g(\mathbf{r}), \tag{5.16}$$

where

$$\mathbf{D}_{22} = k_b T \langle \mathbf{M}_{22} \rangle_2, \tag{5.17a}$$

$$\mathbf{D}_{12} = k_b T \langle \mathbf{M}_{12} \rangle_2, \tag{5.17b}$$

$$\mathbf{D}_{11} = k_b T \langle \mathbf{M}_{11} \rangle_2 + \mathbf{D}_{11}^f, \tag{5.17c}$$

$$\mathbf{D}_{21} = k_b T \langle \mathbf{M}_{21} \rangle_2 + \mathbf{D}_{21}^f, \tag{5.17d}$$

where D superscript on $\mathbf{j}$ in (**??**) is indicative of the dispersion flux. The force-induced dispersion only appears on $\mathbf{D}_{21}$ and $\mathbf{D}_{11}$, since only interparticle and thermal forces act on particle 2 ($\mathbf{D}_{22}^f$ and $\mathbf{D}_{12}^f$ are zero); recall that $\mathbf{D}_{\alpha\beta}$ is the diffusion of particle α induced by the force on particle β. The diffusion induced by Brownian forces scales as $k_b T M_0$ where $k_b T/a$ is the thermal force, and M_0 is the single particle mobility. When $Pe_f = \dfrac{F^{ext} a}{k_b T} \gg 1$, the diffusion of the probe is expected to scale with F^{ext} instead of $k_b T/a$, i.e. $\mathbf{D}^f \sim M_0 F^{ext} a$. Based on the given relations, the CF pair SE reduces to

$$\nabla_{\mathbf{r}} \cdot \left[\Big(\mathbf{U}^H(\mathbf{r}) + \mathbf{U}^P(\mathbf{r}) \Big) g(\mathbf{r}) - \Big(\mathbf{D}^B(\mathbf{r}) + \mathbf{D}^f(\mathbf{r}) \Big) \cdot \nabla_{\mathbf{r}} g(\mathbf{r}) \right] = 0, \tag{5.18}$$

with

$$\mathbf{D}^B = k_b T \Big(\langle \mathbf{M}_{11} \rangle_2 - \langle \mathbf{M}_{21} \rangle_2 + \langle \mathbf{M}_{22} \rangle_2 - \langle \mathbf{M}_{12} \rangle_2 \Big), \tag{5.19a}$$

$$\mathbf{D}^f(\mathbf{r}) = \mathbf{D}_{11}^f(\mathbf{r}) - \mathbf{D}_{21}^f(\mathbf{r}), \tag{5.19b}$$

where $\mathbf{D}^B(\mathbf{r})$ and $\mathbf{D}^f(\mathbf{r})$ are relative diffusivities induced by Brownian and external forces. The quantities are made dimensionless using the scaling below

$$\mathbf{r} \sim a, \quad \mathbf{U}^H \sim M_0 F^{ext}, \quad \mathbf{U}^P \sim k_b T\, M_0/a, \quad \mathbf{D}^B \sim k_b T\, M_0, \quad \mathbf{D}^f \sim M_0 F^{ext} a.$$

The dimensionless form of the pair SE is

$$\nabla \cdot \left[\Big(\mathbf{U}^H(\mathbf{r}) + Pe_f^{-1} \mathbf{U}^P(\mathbf{r}) \Big) g(\mathbf{r}) - \Big(Pe_f^{-1} \mathbf{D}^B(\mathbf{r}) + \mathbf{D}^f(\mathbf{r}) \Big) \cdot \nabla g(\mathbf{r}) \right] = 0, \qquad (5.20)$$

where $Pe_f = \dfrac{F^{ext} a}{k_b T}$. The boundary conditions are the same as the CV case, given by (5.12). Similar to the CV the average mobility and interparticle force for the probe and particle 2 should be formulated in terms of $\mathbf{r}$ and $g(\mathbf{r})$. In addition $\mathbf{D}^f$ also needs to be defined.

5.2.3 Average mobility and interparticle forces

The formulation of average mobility and interparticles forces is identical to the shear flow problem which is explained in detail in our earlier work [32], and in Chapters 2 and 4. Here we will only give the final equations. There is, however, one key difference between conditional averages in active microrheology and shear flow. In the shear flow, the external straining flow is imposed on each individual particle while in microrheology only the probe particle is subjected to an external force/velocity. As a result, when the Smoluchowski equation is integrated to pair particle level in shear flow, particles 1 and 2 are statistically identical, resulting in certain important symmetries. As a result $\langle \mathbf{M}_{11} \rangle_2 = \langle \mathbf{M}_{22} \rangle_2$, $\langle \mathbf{M}_{12} \rangle_2 = \langle \mathbf{M}_{21} \rangle_2$, and $\langle \mathbf{F}_2 \rangle_2 = -\langle \mathbf{F}_1 \rangle_2$. On the other hand, in the pair SE for active microrheology (whether for CF or CV), the distribution of bath particles around the probe is intrinsically different from that around particle 2 since the force/velocity is only imposed on the probe. A clear example would be the case

where particle 2 and the probe are well-separated. In this configuration, particle 2 is decorrelated from the probe; hence particle 2 and the bath particles around it are in the equilibrium distribution, $g(\mathbf{r_{32}}) = g^{eq}(r_{32})$ where $\mathbf{r}_{32}$ is the separation vector of particle 2 and a third bath particle. On the other hand, as it is shown in previous works and will be shown here, the distribution of bath particles around the probe is anisotropic with more particles accumulating in the direction of probe motion and a depleted zone of particles behind the probe. As a result the symmetry properties in shear flow do not hold here, and in general

$$\langle \mathbf{M}_{11} \rangle_2 \neq \langle \mathbf{M}_{22} \rangle_2, \quad \langle \mathbf{F}_2^P \rangle_2 \neq -\langle \mathbf{F}_1^P \rangle_2.$$

This effect of heterogeneity becomes negligible for dilute suspensions, since the interactions are limited to the pair level (particle 1 and 2) while for concentrated suspensions it must be included in the formulation. This is taken into account through modification of the triplet distribution function, $g_3(\mathbf{r}, \mathbf{r}_{13})$, where $g_3(\mathbf{r}, \mathbf{r}_{31}) d\mathbf{r} d\mathbf{r}_{32}$ is the likelihood of having the probe and a third particle between $\mathbf{r}_{31} + d\mathbf{r}_{31}$ and the probe and particle 2 at $\mathbf{r} + d\mathbf{r}$ and $\mathbf{r}$ described below.

Interparticle forces are assumed to be pair-wise additive and the conditional average forces are formulated as

$$\langle \mathbf{F}_1 \rangle_2 g(\mathbf{r}) = \mathbf{F}_{21}(\mathbf{r}) g(\mathbf{r}) + n \int \mathbf{F}_{31}(\mathbf{r}_{31})\, g_3(\mathbf{r}, \mathbf{r}_{31}) d\mathbf{r}_{31}. \tag{5.21}$$

where the forces $\mathbf{F}_{21}$ and $\mathbf{F}_{31}$ are exerted on particle 1 by particles 2 and 3, respectively. The hard-sphere interparticle force is modeled here through a steep repulsive force written as

$$\mathbf{F}_1^P = -(k_b T/a) \frac{\tau \exp(-\tau\epsilon)}{1 - \exp(-\tau\epsilon)} \hat{\mathbf{r}} \tag{5.22}$$

where $\epsilon = r/a - 2$ is the dimensionless gap size between the pair. The parameter τ

determines the steepness of the repulsive force; larger τ results in a steeper decay of the repulsion, and we have used $\tau = 400$ for all the calculations of active microrheology. It is necessary to express the triplet distribution, g_3, in terms of the pair distribution function to obtain a relationship which is only a function of $g(\mathbf{r})$ and $\mathbf{r}$. This is pursued through a modified Kirkwood superposition closure approximation [51] given by

$$g_3(\mathbf{r}, \mathbf{r}_{31}) = g(\mathbf{r})g(\mathbf{r}_{31})g(\mathbf{r}_{32}) \exp(\tau^\star(\mathbf{r}, \mathbf{r}_{31}, \phi)). \tag{5.23}$$

This modifies the Kirkwood superposition through the exponential term which is tabulated based on separation distance (r_{31} here) and various values of ϕ. The reader is referred to the original paper by Rice & Lekner [51] for details. To take into account the fact that configurations of bath particles around particle 2 and the probe are generally different from one another this closure is modified to

$$g_3(\mathbf{r}, \mathbf{r}_{31}, \mathbf{r}_{32}) = g(\mathbf{r})g(\mathbf{r}_{31})\big(\lambda g^*(\mathbf{r}_{32}) + (1-\lambda)g^{eq}(r_{32})\big) \exp(-\tau^*), \tag{5.24}$$

where λ is a measure of connectivity of particles 2 and 3 with the probe (particle 1) and is approximated as

$$\lambda(\mathbf{r}, \mathbf{r}_{31}, \mathbf{r}_{32}) = \frac{\max\left(|\mathbf{U}_2|, |\mathbf{U}_3|\right)}{|\mathbf{U}_1|}, \tag{5.25}$$

where $\mathbf{U}_1$ to $\mathbf{U}_3$ are velocities of particles 1 to 3 at each triplet configuration based on CF and CV on the probe (particle 1). Here $|\mathbf{U}|$ is the absolute magnitude of vector $\mathbf{U}$ and $\max\left(|\mathbf{U}_2|, |\mathbf{U}_3|\right)$ is the maximum value of the velocity magnitudes of particles 2 and 3. This expression gives a correct description of the limits where particles are touching or well-separated. For example, if both 2 and 3 are well separated from the probe particle, $\lambda \to 0$ and the distribution of bath particles around particle 2 is the equilibrium distribution, $g^{eq}(r_{32})$. Also when all three particles are connected in the

direction of the applied force $\lambda \to 1$ since three particles move as a single body along the force direction. Unlike the shear flow, $g(\mathbf{r}_{23}) \neq g(\mathbf{r}_{32})$. To correctly take this into account, in (5.25) the separation vector of particles 2 and 3 is measured from the particle closer to 1 to the one further away. For example, in the case of having particle 3 in between particles 1 and 2, $g^*(\mathbf{r}_{32}) = g(\mathbf{r}_{32})$, while when particle 2 is between 1 and 3, $g^*(\mathbf{r}_{32}) = g(-\mathbf{r}_{32})$. In other words, between particles 2 and 3, the one closer to the probe carries the information on the motion of the probe to the particle at a greater distance.

Calculation of the average mobility depends on the pair separation. For nearly touching configurations of particle 1 and 2 with bath particles, a resistance formulation is used. For configurations of the bath particles outside the lubrication zone of 1 and 2, the bath particle effect is computed using a mobility formulation. For nearly-touching configurations, $\langle \mathbf{R} \rangle_2$ is formulated as

$$\langle \mathbf{R}_{\alpha\beta} \rangle_2(\mathbf{r}) g = \mathbf{R}^{pair}_{\alpha\beta}(\mathbf{r}) g + n \int \Big(\mathbf{R}_{\alpha\beta}(\mathbf{r}, \mathbf{r}_{31}, \mathbf{r}_{32}) - \mathbf{R}^{pair}_{\alpha\beta}(\mathbf{r}) \Big) \, g_3 d\mathbf{r}_{31}, \tag{5.26}$$

where $\alpha = 1, 2$, $\beta = 1, 2$ and $\mathbf{R}(\mathbf{r}, \mathbf{r}_{31}, \mathbf{r}_{32})$ is the resistance to motion in the presence of a third particle and $\mathbf{R}^{pair}(\mathbf{r})$ is the equivalent resistance of the isolated pair 1 and 2. The term $\mathbf{R}_{\alpha\beta}(\mathbf{r}, \mathbf{r}_{31}, \mathbf{r}_{32}) - \mathbf{R}^{pair}_{\alpha\beta}(\mathbf{r})$ in the integrand (5.26) is thus the change (increase quite generally) of the resistance with respect to the isolated pair due to the other particles, as captured through the third-particle integral. To calculate the resistance components in triplet configurations for particles near contact, the resistance is assumed to be pair-wise additive. The resistance determined in this way is then inverted to obtain the modified mobility due to lubrication interactions. When the particles are outside the lubrication zone, the bath particle effect is computed using a mobility formulation

$$\langle \mathbf{M} \rangle_2(\mathbf{r}) g = \mathbf{M}_{pair}(\mathbf{r}) g + n \int \Big(\mathbf{M}(\mathbf{r}, \mathbf{r}_{31}, \mathbf{r}_{32}) - \mathbf{M}_{pair}(\mathbf{r}) \Big) g_3 d\mathbf{r}_{31}, \tag{5.27}$$

where we have dropped the 1 and 2 indices for convenience and $\mathbf{M}(\mathbf{r}, \mathbf{r}_{31}, \mathbf{r}_{32})$ is the mobility for particles 1 and 2 in the presence of a third particle obtained using the method of reflections [53]. The far-field and near-contact contributions are summed to give the final form of mobility.

5.2.4 Force-induced diffusion

Variations of $\mathbf{D}^f_{11} - \mathbf{D}^f_{21}$ with separation are modeled in a similar fashion to that used in shear flow [32], as shown in Chapters 2 & 4:

$$\mathbf{D}^f_{11} - \mathbf{D}^f_{21} = \mathbf{D}^f(\mathbf{r}) = M_0 F^{ext} a D^* \Big(\mathcal{G}(r) \hat{\mathbf{r}}\hat{\mathbf{r}} + \mathcal{H}(r) \left(\mathbf{I} - \hat{\mathbf{r}}\hat{\mathbf{r}} \right) \Big), \tag{5.28}$$

where $D^* = \dfrac{D_s^\infty(\phi, Pe)}{M_0 F^{ext} a}$ is the dimensionless probe long-time self-diffusion and $\mathcal{G}(r)$ and $\mathcal{H}(r)$ determine the variations of force-induced relative diffusivity, $\mathbf{D}^f$, along the line of centers and the plane perpendicular to radial direction, i.e. the local $(\hat{\theta} - \hat{\varphi})$ plane. As was done for sheared suspensions, we model the relative dispersion based on the behavior of $\mathbf{D}^f$ in the limits of the probe and particle 2 being well-separated, $r/2a \gg 1$, and very near contact, $r \to 2a$. When the pair are well-separated, the particles become decorrelated and the induced dispersion on particle 2 due to motion of the probe vanishes, $\mathbf{D}^f_{21}(\mathbf{r}) = 0$, and $\mathbf{D}^f_{11}(\mathbf{r}) \to \mathbf{D}^f_s$ where $\mathbf{D}^f_s$ is the long time average self-diffusivity of the probe. The relative dispersion is driven by fluctuations of relative velocity around the average value; the relative diffusivity is thus proportional to relative velocity fluctuations i.e. $\mathbf{D}^f(\mathbf{r}) \propto \tilde{\tau} \langle \mathbf{U}'(\mathbf{r}) \mathbf{U}'(\mathbf{r}) \rangle_2$, where $\mathbf{U}'$ is the difference of the local relative velocity with respect to the average value and τ is the characteristic time scale over which relative motion becomes decorrelated. When the probe and particle 2 are in near-contact configurations, the relative radial velocity and its fluctuations approach zero due to the excluded volume effect, $\mathbf{U} \propto r - 2a$ and $\mathbf{U}' \propto r - 2a$. Thus the relative diffusivity in the radial direction is expected to approach zero as $(r - 2a)^2$. The excluded

volume restriction is primarily imposed along the line of centers and the fluctuations of relative relative velocity in the angular direction remain on the order of the probe velocity. As a result, $\mathbf{D}^f \propto M_0 F^{ext} a$ in $\hat{\theta}$ and $\hat{\varphi}$ directions.

When the suspension is in equilibrium, a relationship between the collective diffusivity and osmotic pressure can be deduced in colloidal suspensions [5], $D_c^{eq} = M_c^{eq} \dfrac{\partial \Pi^{eq}}{\partial n}$ where subscript c refers to collective diffusion and mobility. Since mobility and pressure are still well-defined outside equilibrium, one may extend the equilibrium relationship to non-equilibrium systems by analogy and write $\mathbf{D} = \mathbf{M} \cdot \dfrac{\partial \Sigma}{\partial n}$ where Σ is the stress induced by the particle phase. The microstructural theories for predicting single particle and collective diffusion of sheared suspension also find a general linear correspondence between the shear induced stress and diffusion [27, 99, 100].

In a recent work, Zia & Brady [101] extended this idea to active microrheology to relate probe diffusivity to the force-induced stress on the probe. They consider a phase composed of suspension of probe particles where the suspension is so dilute that the probes have no interaction among themselves. The momentum balance is written for this phase and an extract relationship between the force-induced stress and diffusion for dilute suspension is derived. Their analysis, however, neglects hydrodynamic interactions between the probe and the bath particles which makes a direct extension of their theory to the problem under study here difficult. Instead of their detailed formulation, we use the analogy in the simplest form to compute the limiting value of $\mathbf{D}^f(\mathbf{r})$ when the probe and particle 2 are well-separated, $\mathbf{D}_s^f$ and write

$$\mathbf{D}_c^f = \mathbf{D}_s^f = \mathbf{M} \cdot \frac{\partial \Sigma}{\partial n_a}, \tag{5.29}$$

where n_a is the number density of the probe phase ($n_a \ll 1$) and Σ is the average stress on the probe phase per unit volume. Note that since the probe phase is considered very dilute (no interactions between the probes), the collective diffusivity and mobility

become identical to their single particle values as shown by superscript s in (5.29).

In the next step, we take the enhanced diffusion to be dominated by hydrodynamic velocity fluctuations (at $Pe_f \gg 1$ where the effect is pronounced) and hence only consider the hydrodynamic contribution to the stress in (5.29). If we assume the hydrodynamic stress is dominated by near-contact lubrication stress, Σ can be written in terms of the moment of external force in the radial direction:

$$\Sigma = n_a n \int_{2a}^{r^*} \left(\mathbf{F}^{ext} \cdot \mathbf{r}\right) \hat{\mathbf{r}}\hat{\mathbf{r}} \left(g(\mathbf{r}) - g^{eq}(r)\right) d\mathbf{r}. \tag{5.30}$$

The integration is carried out from contact to $r = r^*$ where r^* is the radius at which the increase in angularly averaged pair correlation function, $\tilde{g}(r)$, from the equilibrium distribution drops to 10% of the contact values i.e. $\tilde{g}(r^*) = 0.1\left[\tilde{g}(2a) - g^{eq}(2a)\right] + g^{eq}(r^*)$. To be able to present $\mathbf{D}^f$ in the form given in (5.28), the far-field relative diffusion is considered isotropic and is approximated with $tr(\mathbf{D}_s^f)/3$ of the computed values from (5.29). Note that $\mathbf{D}^f$ has no dependence on n_a after taking the derivative with respect to n_a in (5.29).

As mentioned, the relative radial diffusion caused by the force on the probe diminishes near contact in radial direction as $(r - 2a)^2$. We would like to know how this decay is changed with volume fraction. To study this, we consider configurations of chains of bath particles aligned with the probe in the direction of the applied force. This configuration was chosen since the fluctuation in pair motion near contact, in the radial direction, is most pronounced here. Consider the configuration of the probe and particle 2 aligned in the force direction and separated by $\epsilon = (r/a - 2) \ll 1$ with no bath particles in the vicinity. The relative mobility from lubrication solution is $2.0\epsilon M_0$ which makes relative velocity $\mathbf{U} = 2.0 M_0 \epsilon \mathbf{F}^{ext}$. Now if a third particle is added in force direction with ϵ separation from particle 2, forming a triplet chain, the relative velocity can be obtained by forming the resistance matrix based on pair-wise additive lubrication interactions for

this configuration; we then solve the linear set of equations $\mathbf{R} \cdot \mathbf{U} = \mathbf{F}$. We find that for the triplet chains $\mathbf{U}(\mathbf{r})/U_0$ modifies to 2.40ϵ and thus $\mathbf{U}' \approx 0.40\epsilon U_0$ with respect to the isolated pair configuration. Adding the fourth and fifth particles to the chain changes the relative velocity only by a small amount with respect to the triplet configuration, $\mathbf{U}' = 0.60\epsilon U_0$ to $0.80\epsilon U_0$. If we take the fluctuations associated with formation of chain-like structures as a scale for the average fluctuations, in case of having interactions only to three-particle level, we expect $\mathbf{U}' \propto 0.4\epsilon\phi U_0$. Additional fluctuations due to interactions of four and five particles would roughly scale as $0.20\epsilon\phi^2 U_0$ and $0.2\epsilon\phi^3 U_0$. The prefactors 0.2 result from the increase in fluctuation magnitude as a result of increasing the chain length from 3 to 4 particles ($0.6\epsilon U_0 - 0.4\epsilon U_0$) and from 4 to 5 particles ($0.8\epsilon U_0 - 0.6\epsilon U_0$).

This analysis does not take into account the effect of dispersed bath particles around these formed chainlike structures. We make a mean-field assumption and take the relative velocity fluctuations to scale with the average probe velocity. As a result the fluctuations are reduced by a factor of $\langle \hat{M} \rangle = \langle M_{11}^{zz} \rangle / M_0$ compared to having the isolated chain-like structures where $\langle M_{11}^{zz} \rangle$ is the average mobility of the probe particle in the motion direction. Thus the relative velocity fluctuation near contact should scale as, $\mathbf{U}' \propto U_0 \epsilon \langle \hat{M} \rangle \left(0.40\phi + 0.20\phi^2 + 0.20\phi^3 + O(\phi^4)\right)$. We see that, for $\phi \leq 0.50$, the radial velocity fluctuations are mostly controlled by the first term, $0.4\epsilon\phi$, which is induced by near-contact interactions of particles 1 and 2 with the third particle. We neglect ϕ^n terms with $n > 1$ and assume $\mathbf{U}' \propto \phi \langle \hat{M} \rangle \epsilon$.

The time required for the probe to become decorrelated with particle 2 scales inversely with the rate of the close interactions with bath particles, $\tilde{\tau}^{-1} \propto |\langle \mathbf{U}_1 \rangle| \phi / a$ where $\langle \mathbf{U}_1 \rangle = \langle \mathbf{M}_{11} \rangle \cdot \mathbf{F}^{ext}$ is the average probe velocity. Combining the scalings of $\mathbf{U}'$ and $\tilde{\tau}$ with $\mathbf{D}^f \propto \tilde{\tau} \langle \mathbf{U}' \mathbf{U}' \rangle_2$, the radial relative diffusion near-contact scales as $\mathbf{D}_{rr}^f \propto \epsilon^2 \phi \langle \hat{M} \rangle$.

Since there is little simulation data on active microrheology to provide meaningful averages of the probe and bath dynamics, we use the insight from shear flow Accelerated Stokesian Dynamics simulations for modeling the variations of angular diffusivity. The

results of simulation sampling at $Pe \gg 1$ show the magnitude of shear-induced angular relative velocity fluctuations remains finite and is reduced to approximately 1/4 of the maximum far-field value. We use the observations from shear flow simulations and assume the angular diffusivity remains finite over all separations and is reduced to 1/2 of the far-field value. Note that the decaying to 1/2 of the far-field in active microrheology in comparison to 1/4 is shear flow is due to the fact that in active microrheology, when the probe is separated from particle 2, only the probe goes through an enhanced diffusion due to the applied force while in shear flow the shearing motion is imposed on all particles and therefore $\mathbf{D}^{\dot{\gamma}}(\mathbf{r}) = 2\mathbf{D}_s^{\dot{\gamma}}$ where $\mathbf{D}^{\dot{\gamma}}(\mathbf{r})$ is the shear-induced relative diffusion and $\mathbf{D}_s^{\dot{\gamma}}$ is the shear-induced self diffusion. For simplicity and lack of a better understanding we take the same decaying function for radial and angular components of $\mathbf{D}^f(\mathbf{r})$ which gives

$$\mathcal{G}(r) = 1 - \exp\left[\frac{-\tilde{m}\epsilon^2\langle\hat{M}\rangle\phi}{D^*}\right], \tag{5.31a}$$

$$\mathcal{H}(r) = (1/2)\left(1 - \exp\left[\frac{-\tilde{m}\epsilon^2\langle\hat{M}\rangle\phi}{D^*}\right]\right) + 1/2, \tag{5.31b}$$

where $\tilde{m}$ is a constant arbitrarily set as 0.20 for all conditions of ϕ and Pe_f.

5.2.5 Solution technique

The conditional averages appearing in (5.10) and (5.20) are all expressed in terms of integrals of $g(\mathbf{r})$. The resulting balance equations for both CF and CV are nonlinear integro-differential equations which we solve using a finite element iterative scheme with the boundary conditions given in (5.12). The details of the solution technique are given in [32] and Chapter 2 of this thesis. There is, however, one difference in computation domain of the active microrheology and shear flow. In shear flow, the structure changes in all three directions in space while the active microrheology is an axisymmetric problem with symmetry about the direction of external force/velocity on the probe. As

a result the computation of structure in active microrheology is 2D axisymmetric and significantly faster than shear flow.

5.3 Micro-viscosity

In this section, we develop the relationship between $g(\mathbf{r})$ and the micro-viscosity which is calculated using the Stokes relationship, $\eta_{micro} = \dfrac{F^{ext}}{6\pi U_a a}$. In a CF experiment, F^{ext} is known and the goal is to compute U_a as a function of $g(\mathbf{r})$ for which average probe mobility, $\langle \mathbf{M}_{11} \rangle_2$, is needed. For CV, the problem is reversed; the velocity is fixed and the external force should be calculated which requires computation of the probe average resistance. We first present the CV micro-viscosity formulation, and then proceed to CF.

5.3.1 Constant velocity micro-viscosity, η_U

As mentioned, the forces acting on the probe in a colloidal suspension are hydrodynamic, Brownian, and interparticle forces represented with H, B and P superscripts, respectively. These forces are formulated as

$$F_z^B = n\, k_b T \int \nabla g(\mathbf{r}) \cdot \hat{\mathbf{z}} d\mathbf{r} = -n\, k_b T \oint \hat{\mathbf{n}} \cdot \hat{\mathbf{z}} g(2,\varphi) ds, \tag{5.32a}$$

$$F_z^P = n\, k_b T \int \left(\mathbf{F}^P(\mathbf{r}) \cdot \hat{\mathbf{z}} \right) g(\mathbf{r}) d\mathbf{r}, \tag{5.32b}$$

$$F_z^H = -\langle R_{11}^{zz} \rangle U_a, \tag{5.32c}$$

where subscript z implies the component of the force along the direction of probe motion and $\langle R_{11}^{zz} \rangle$ is the average probe resistance tensor when the probe is well-separated from the particle 2. The divergence theorem was used in (5.32a) to convert the volume integral to a surface integral where $g(2,\varphi)$ is the variation of the pair distribution function at contact with azimuthal angle, φ. Recall that $\mathbf{z}$ is the axis of symmetry in this

problem and there is no variations with polar angle θ. The summation of the forces in (5.32) gives the force applied on the probe from the fluid and bath particles. Thus $F_U^{ext} = -\left(F_z^B + F_z^P + F_z^H\right)$ needs to be externally applied to the probe to maintain its constant velocity of U_a. The integrals in (5.32) are easily computable once $g(\mathbf{r})$ is known from the theory. The micro-viscosity is calculated as

$$\frac{\eta_U}{\eta} = \hat{\eta}_U = \frac{-\left(F_z^B + F_z^P + F_z^H\right)}{6\pi\eta U_a a}, \tag{5.33}$$

As mentioned, we only consider hard-sphere interparticle interactions. Thus, $\mathbf{F}^P$ is only non-zero at contact. The hard-sphere force is modeled using a steep repulsive radial force, (5.22). Using simple scaling arguments, it is straightforward to show that $F_z^P \propto F_z^B \tau^{-1}$. Hence the interparticle force is neglected here in comparison with Brownian forces. This is not an accurate assumption for particles interacting through long-ranged soft potentials which was shown explicitly for sheared suspensions in Chapter 3 [63]. The hydrodynamic dimensionless viscosity is thus computed as

$$\hat{\eta}_U^H = \langle R_{11}^{zz} \rangle / R_0, \tag{5.34}$$

where $R_0 = 6\pi\eta a$ is the single particle resistance. The Brownian micro-viscosity is $\hat{\eta}_U^B = \hat{\eta}_U - \hat{\eta}_U^H$.

5.3.2 Constant force micro-viscosity, η_f

The CF micro-viscosity is defined as

$$\eta_f = \frac{F^{ext}}{6\pi\langle U_a \rangle a}, \tag{5.35}$$

where $\langle U_a \rangle$ is the average velocity of the probe particle in the direction of the applied force. The average probe velocity is composed of contributions from hydrodynamic,

interparticle and Brownian interactions:

$$\langle \mathbf{U}_a \rangle = \mathbf{U}_0 + \mathbf{U}^H + \mathbf{U}^P + \mathbf{U}^B. \tag{5.36}$$

These velocities are related to $g(\mathbf{r})$ through the following relations:

$$\mathbf{U}^H = (\langle \mathbf{M}_{11} \rangle - \mathbf{I}) \cdot \mathbf{F}_1^{ext}, \tag{5.37a}$$

$$\mathbf{U}^P = n \int \left(\langle \mathbf{M}_{11} \rangle_2 \cdot \mathbf{F}_1^P(\mathbf{r}) + \langle \mathbf{M}_{12} \rangle_2 \cdot \mathbf{F}_2^P(\mathbf{r}) \right) g(\mathbf{r}) d\mathbf{r}, \tag{5.37b}$$

$$\mathbf{U}^B = n \int \nabla \cdot \langle \mathbf{M}_{11} - \mathbf{M}_{12} \rangle_2 g(\mathbf{r})\, d\mathbf{r}, \tag{5.37c}$$

where $\mathbf{U}_0$ is the velocity of the isolated probe in the pure fluid in the absence of all bath particles. The other velocities in (5.36) are velocities induced by the bath particles and as a general trend act in the opposite direction of the applied force reducing the average velocity. Specifically, $\mathbf{U}^H$ is the hydrodynamic velocity due to external force, $\mathbf{U}^P$ is the velocity induced by interparticle forces applied by bath particles, and $\mathbf{U}^B$ presents the velocity caused by Brownian forces applied by bath particles. All the coefficients appearing in (5.37a - 5.37c) are known through solving for $g(\mathbf{r})$.Note that, since z is the axis of symmetry of $g(\mathbf{r})$, all the velocity terms in (5.36) are along z axis with no components along $\hat{\theta}$ and $\hat{\mathbf{r}}$ directions in cylindrical coordinates.

For near hard-sphere dispersions, the contribution of bath particles to viscosity is taken to be a summation of contributions from pure fluid, Brownian, and hydrodynamic interactions. The hydrodynamic contribution to viscosity is defined as

$$\frac{\eta_f^H}{\eta} = \hat{\eta}_f^H = \frac{M_0}{\langle M_{11}^{zz} \rangle} \tag{5.38}$$

where $\langle M_{11}^{zz} \rangle$ is the average probe mobility in the force direction. Brownian viscosity is obtained by subtracting hydrodynamic viscosity from the total viscosity: $\hat{\eta}^B = \hat{\eta}_f - \hat{\eta}_f^H$.

5.4 Microstructure

We start by presenting the results of near-equilibrium microstructure at Pe_U and $Pe_f \ll 1$. The number of configurations required to obtain statistically meaningful values for $g - g^{eq}$ at $Pe \ll 1$, is very large compared with $Pe \geq 1$. Thus the microstructure at low Péclet numbers is studied only using the predictions of the theory. At $Pe \ll 1$, the distortion of structure from equilibrium can be expressed using a regular perturbation expansion in terms of Pe as

$$g_U(\mathbf{r}) = g^{eq}(r) + Pe_U f_1^U(r)\mathbf{U}_1 \cdot \hat{\mathbf{r}} + Pe^2 f_2^U(r)\mathbf{U}_1\mathbf{U}_1 : \hat{\mathbf{r}}\hat{\mathbf{r}}, \tag{5.39a}$$

$$g_f(\mathbf{r}) = g^{eq}(r) + Pe_f f_1^f(r)\mathbf{F}^{ext} \cdot \hat{\mathbf{r}} + Pe^2 f_2^f(r)\mathbf{F}^{ext}\mathbf{F}^{ext} : \hat{\mathbf{r}}\hat{\mathbf{r}}, \tag{5.39b}$$

where subscripts U and f present the constant velocity and force conditions. When $Pe \to 0$, the Pe^2 contribution to the structure becomes negligible, and the zero-force/velocity micro-viscosity is determined based on f_U^1 and f_f^1. To calculate these functions, we compute $g(\mathbf{r})$ for $\phi \leq 0.40$ at Pe_f and $Pe_U = 0.01$, for which Pe^2 and higher order terms can be neglected. Note that $\phi = 0.40$ is the largest possible volume fraction for which the modified Kirkwood superposition gives a convergent solution for $g(\mathbf{r})$. The expressions (5.39a) and (5.39b) are then fitted (with excellent agreement) to the predicted microstructures at $Pe_{f,U} = 0.01$ to give $f_1^U(r)$ and $f_1^f(r)$. The predictions at $Pe_f = 0.01$ at different ϕ should be re-scaled so that the structures at CF and CV are compared against each other at equal average probe velocities $\langle U_a \rangle = U_a$. For this purpose it is more appropriate to write (5.39b) in terms of $Pe_{\langle U \rangle} = \dfrac{6\pi\eta a^2 \langle U_a \rangle a}{k_b T} = \dfrac{Pe_f}{\hat{\eta}_f}$. In other words, to make a comparison of the distortion of microstructure near equilibrium, $f_1^U(r)$ should be compared against $f_1^f(r)\hat{\eta}_f$.

Figure 5.1 shows the variations of $f_U^1(2)$ and $f_f^1(2)\hat{\eta}_f$ with ϕ. The distorted microstructure increases strongly with volume fraction and the values are roughly similar for CF

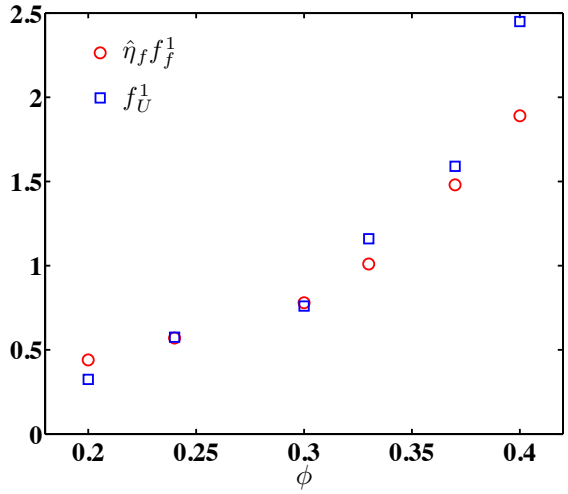

Figure 5.1: The contact values of $O(Pe)$ structural deformation functions for CF and CV, $\hat{\eta}_f f_f^1(2)$ and $f_U^1(2)$ in (5.39a,b) , vs ϕ.

and CV. Note that the formulations relating distorted microstructure to micro-viscosity are different for CF and CV and in general similar distorted microstructure does not necessarily result in similar values for micro-viscosity.

We now consider $g(\mathbf{r})$ away from linear response regime. Figures 5.2 (a-i) compare CF and CV predictions of spatial variations of $g(\mathbf{r})$ in the plane of symmetry with the results obtained from sampling the configurations from ASD simulations at $Pe_{\langle U\rangle} = Pe_U = 0.33, 3.15$ and 27. Recall that the current implementation of the simulation (applying an external force on the probe while the rest of the particles are force-free) is a representation of CF conditions and not applicable to CV case. Only the predictions of theory are provided for CV. Identical color bars are considered for the predictions and simulation results. The maximum value in each color bar indicates the scale of the near-contact pair probability. The lower limit of the color bars and colors presenting $O(1)$ features of $g(\mathbf{r})$ are similar for all Péclet numbers to enable direct comparison.

At $Pe_U = 0.33$ the predicted and simulated $g(\mathbf{r})$ shows small disturbance with respect to the equilibrium conditions and the structure remains almost isotropic. At $Pe_U = 3.15$ a clear distortion of equilibrium structure is observed. The anisotropic features

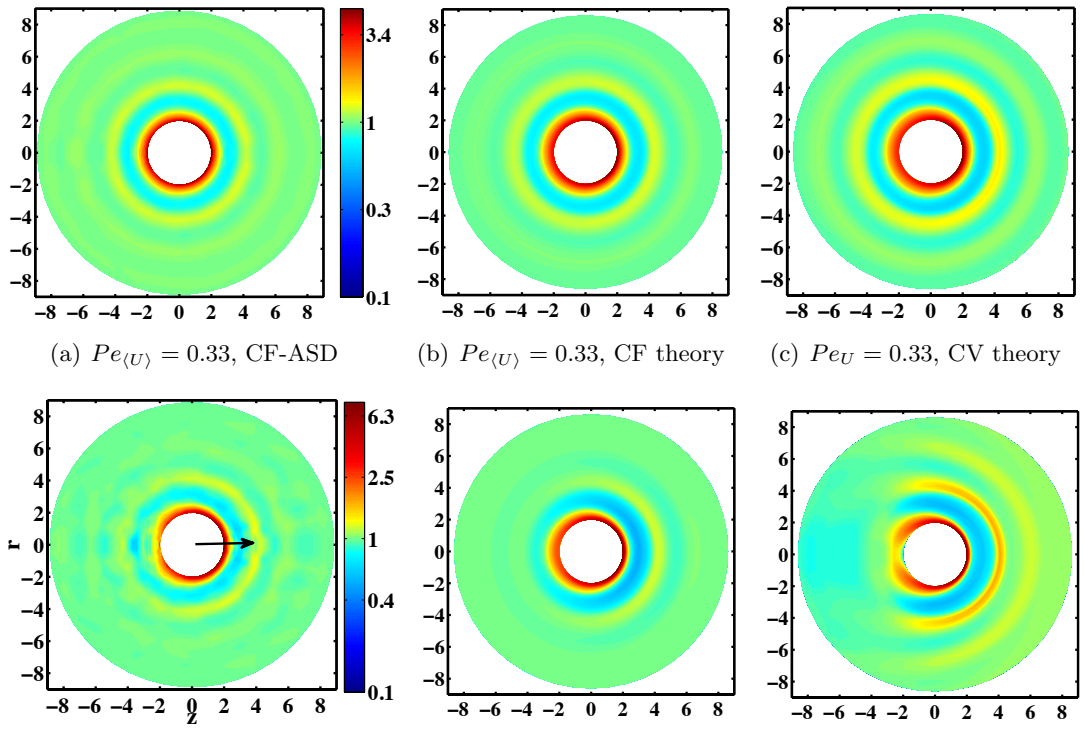

(a) $Pe_{\langle U\rangle} = 0.33$, CF-ASD (b) $Pe_{\langle U\rangle} = 0.33$, CF theory (c) $Pe_U = 0.33$, CV theory

(d) $Pe_{\langle U\rangle} = 3.15$, CF-ASD (e) $Pe_{\langle U\rangle} = 3.15$, Theory (f) $Pe_U = 3.15$, CV theory

(g) $Pe_{\langle U\rangle} = 27$, CF-ASD (h) $Pe_{\langle U\rangle} = 27$, CF theory (i) $Pe_U = 27$, CV theory

Figure 5.2: The variations of $g(\mathbf{r})$ in $(r-z)$ symmetry plane from fixed force simulation results (CF-ASD), and predictions of the theory at fixed force (CF theory) and velocity (CV theory) at $\phi = 0.40$. (a) CF-ASD and $Pe_{\langle U\rangle} = 0.33$, (b) CF theory and $Pe_{\langle U\rangle} = 0.33$, (c) CV theory and $Pe_U = 0.33$, (d) CF-ASD and $Pe_{\langle U\rangle} = 3.15$, (e) CF theory and $Pe_{\langle U\rangle} = 3.15$, (f) CV theory and $Pe_U = 3.15$, (g) CF-ASD and $Pe_{\langle U\rangle} = 27$, (g) CF theory and $Pe_{\langle U\rangle} = 27$, and (i) CV theory and $Pe_U = 27$.

are qualitatively similar in all three cases and are most pronounced in the predictions of CV due to the absence of force-induced diffusion. Number of observations can be made: A region of large probability is formed in the front of the probe and the near-contact probability is smallest behind the probe. The second nearest neighbor peaks are also distorted in a similar fashion as near-contact i.e. the values are largest in the flow direction and smallest behind the probe. There is a good agreement between CF prediction and simulation results.

As the Péclet number is increased to $Pe_U = 27$, the near contact values of $g(\mathbf{r})$ are increased in motion direction (note the color bar scales) and the high probability region separates from the contact surface behind the probe resulting in formation of a boundary layer with a zone of large $g(\mathbf{r})$ in the direction of motion and a zone depleted of bath particles (wake zone) behind the probe. A similar trend is observed for second nearest neighbor peaks. The force-induced fluctuations become the dominant mechanism of dispersion at $Pe_f \gg 1$ and play a key role in setting the CF microstructure in this limit. This is clearly seen by comparing the predicted and sampled CF $g(\mathbf{r})$ (figures 5.2(g) and 5.2(h)) with the predictions of CV (figure 5.2(i)). The boundary layer features are considerably stronger in CV pair microstructure. The streak of high probability region persists up to 7 particle radii behind the probe while for both ASD and predicted CF $g(\mathbf{r})$ the boundary layer diffuses away after approximately 3 particles radii. Also the next nearest neighbor peaks along the motion direction are dramatically stronger in CV and indicate formation of an ordered structure along the probe motion direction.

The predictions of CF pair distribution function are in good agreement with the simulation results at $Pe_{\langle U \rangle} = 27$ (corresponding to $Pe_f = 100$). However few differences can be noted: The low probability region formed adjutant to near-contact high probability zone is stronger in the predictions and extends (and merges with the wake zone) behind the probe. This region is diffused away at smaller pair separations in the ASD results. Also the strength of second nearest neighbor peak is over predicted by the theory. The

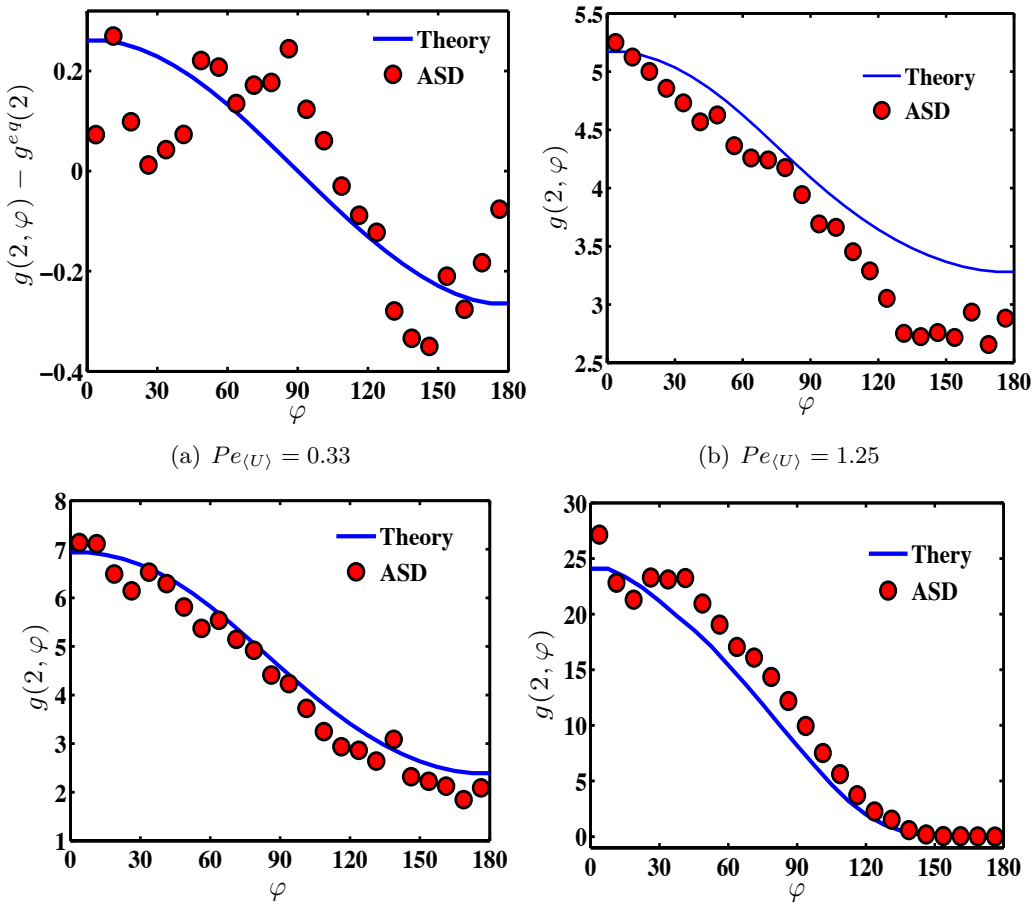

(a) $Pe_{\langle U\rangle} = 0.33$

(b) $Pe_{\langle U\rangle} = 1.25$

(c) $Pe_{\langle U\rangle} = 3.15$

(d) $Pe_{\langle U\rangle} = 27$

Figure 5.3: The predictions and simulation results of pair distribution function at contact as a function of azimuthal angel, $g(2,\varphi)$, (a) $Pe_{\langle U\rangle} = 0.33$, (b) $Pe_{\langle U\rangle} = 1.25$, (c) $Pe_{\langle U\rangle} = 3.15$, (d) $Pe_{\langle U\rangle} = 27$.

influence of probe's motion on average resistance (i.e, micro-viscosity) is primarily controlled by near-contact interactions of the probe with bath particles. This is determined by the near-contact magnitude and variations of $g(\mathbf{r})$. For this reason and to have a more quantitative evaluation of the theory, the values of pair microstructure at contact, $g(2,\varphi)$, from theory and simulation are compared against each other in figure 5.3 at $Pe_{\langle U\rangle} = 0.33, 1.25, 3.15$ and 27 (corresponding to $Pe_f = 1, 4, 10$ and 100) and $\phi = 0.40$. The theory gives a good quantitative prediction of simulation results in the range of Pe studied. We reiterate that including force-induced diffusion changes the predictions both qualitatively and quantitatively and it is a key parameter to the success of this theory.

Obtaining statistical measures of pair microstructure and dynamics in active microrheology requires a considerably larger number of configuration compared to shear flow because the dynamics is sampled only with respect to the probe. In the given time, we have been able to get reliable sampled $g(\mathbf{r})$ for a single volume fraction of $\phi = 0.40$ (while simulations of other volume factions are currently being carried out). For the moment, the effect of volume fraction on microstructure and micro-viscosity is studied only using the predictions of the theory. The variations of $g(\mathbf{r})$ with Pe at lower volume fractions are similar to what is seen at $\phi = 0.40$, with the second nearest neighbor high probability zones getting less pronounced with decrease of ϕ. Figures 5.4(a) and 5.4(b) show variations of CV and CF pair distribution function at contact, $g(2,\varphi)$ at $\phi = 0.20$, 0.30 and 0.40 and $Pe_U = Pe_{\langle U\rangle} = 100$ respectively. Recall that force-induced diffusion is a result of many-body hydrodynamic interactions and it reduces in magnitude with decrease of ϕ. As a result, contact values for $\phi = 0.20$ and $\phi = 30$ are in the same range for CF and CV. The difference between CF and CV predictions is most apparent at $\phi = 0.40$ where force-induced diffusion is a determining factor in setting the microstructure.

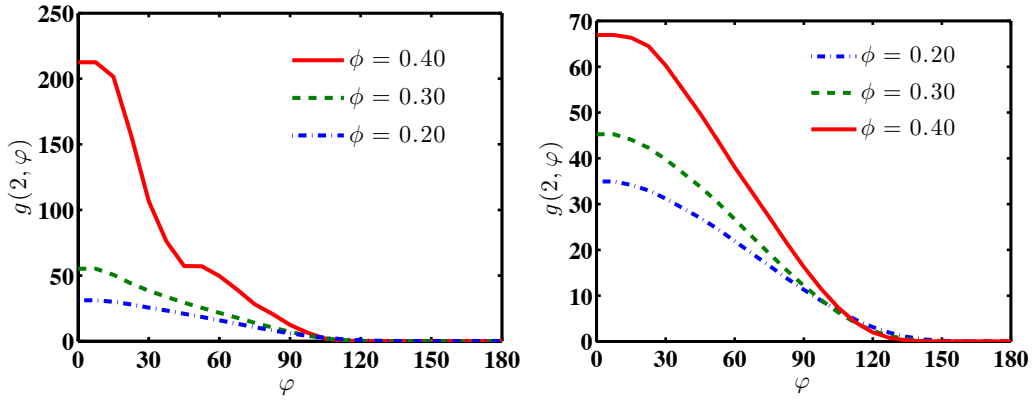

(a) CV, $Pe_U = 100$ (b) CF, $Pe_{\langle U \rangle} = 100$

Figure 5.4: Pair distribution function at contact as a function of azimuthal angel, $g(2,\varphi)$, at volume fractions $\phi = 0.20$, 0.30 and 0.40, and $Pe_U = Pe\langle U \rangle = 100$, (a) fixed velocity (CV) and (b) fixed force (CF).

5.5 Microrheology

Figure 5.5 shows the predicted dimensionless hydrodynamic, Brownian, and total zero-force/velocity micro-viscosity as a function of ϕ for CF and CV. The Accelerated Stokesian Dynamics simulation values (obtained using a Green-Kubo relation) are also presented for comparison. The predicted values for zero-force/velocity hydrodynamic micro-viscosity are identical for both CF and CV since the average mobility near equilibrium is independent of Pe and is defined by $g^{eq}(r)$ (recall that the hydrodynamic viscosity is the inverse of the average probe mobility). Hence the results are presented only for CV predictions. The CF predictions of Brownian micro-viscosity are considerably smaller than CV. This difference can be best understood by comparing the predictions at $\phi \ll 1$. Khair & Brady computed $f_f^1(r)$ using regular perturbation expansion for fixed force and dilute suspensions [95] and found $f_f^1(2) = 0.254$. Using the disturbance field, $f_f^1(r)$, and (5.37c) they compute the contribution of Brownian forces to micro-viscosity as $\hat{\eta}^B_{f,dilute} = 0.25\phi$. It is straightforward to show that using (5.39a), $\hat{\eta}^B_U = 4\phi f_U^1(2)$. If we take $f_f^1 \approx f_U^1$, for $\phi \ll 1$, we have $\hat{\eta}^B_U \approx 1.09\phi$. This is about 1/4 of the value predicted

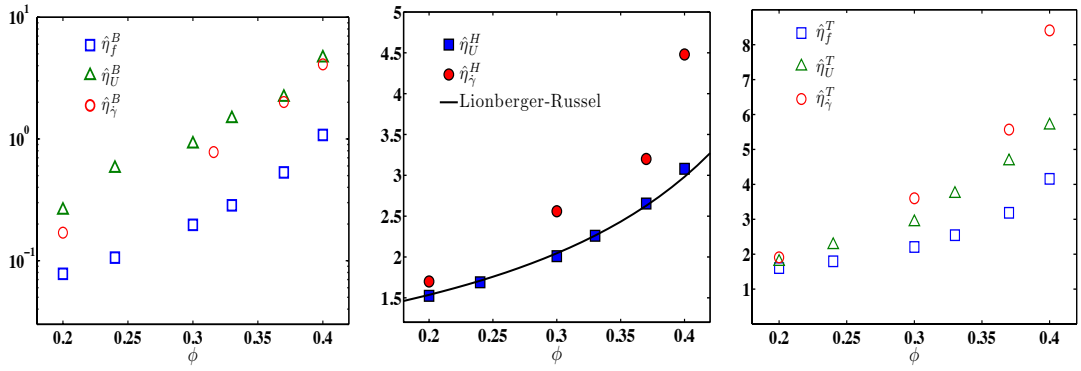

(a) $\hat{\eta}^B$ (b) $\hat{\eta}^H$ (c) $\hat{\eta}^T$

Figure 5.5: The predicted near-equilibrium CF and CV micro-viscosities as a function of ϕ compared against Accelerated Stokesian Dynamics (ASD) simulation results, (a) contributions from Brownian forces, (b) contributions from hydrodynamic interactions and (c) the summation of Brownian and hydrodynamic effects.

by Squires & Brady [94] for this limit ignoring hydrodynamic interactions and a factor of 4.36 larger than the predictions of Khair & Brady for dilute fixed force Brownian micro-viscosity. Our predicted values show a ratio of $\dfrac{\eta_U^{B,eq}}{\eta_f^{B,eq}} = 3.35$ and 4 for $\phi = 0.20$ and 0.40 respectively.

The predicted near equilibrium hydrodynamic micro-viscosity is smaller than the values obtained in shear flow for all volume fractions. There is a very good agreement between $\hat{\eta}^H$ and the solid line in Figure 5.5(b), which presents the empirical relationship for inverse of dimensionless short time self-diffusion coefficient in equilibrium, $D_0/D_s^s(\phi) = \dfrac{1}{(1-1.56\phi)(1-0.27\phi)}$, given by Lionberger & Russel [24] based on fitting to experimental measurements of Pearson & Shikata on hard-sphere suspensions near equilibrium [102] where $D_0 = k_bTM_0$ is the isolated particle short-time self-diffusion; recall that $\hat{\eta}^H = \dfrac{M_0}{\langle M \rangle} = \dfrac{D_0}{D_s^s(\phi, Pe)}$. This indicates that zero force/velocity mobility of the probe is predicted accurately for $\phi \leq 0.40$.

Figure 5.6 shows variations of predicted values of CF and CV micro-viscosities as a function of the relevant Péclet number for a $\phi = 0.40$ hard-sphere suspension. The results are compared against the simulation results for shear flow at different $Pe_{\dot{\gamma}} = \dfrac{6\pi\eta\dot{\gamma}a^3}{k_bT}$.

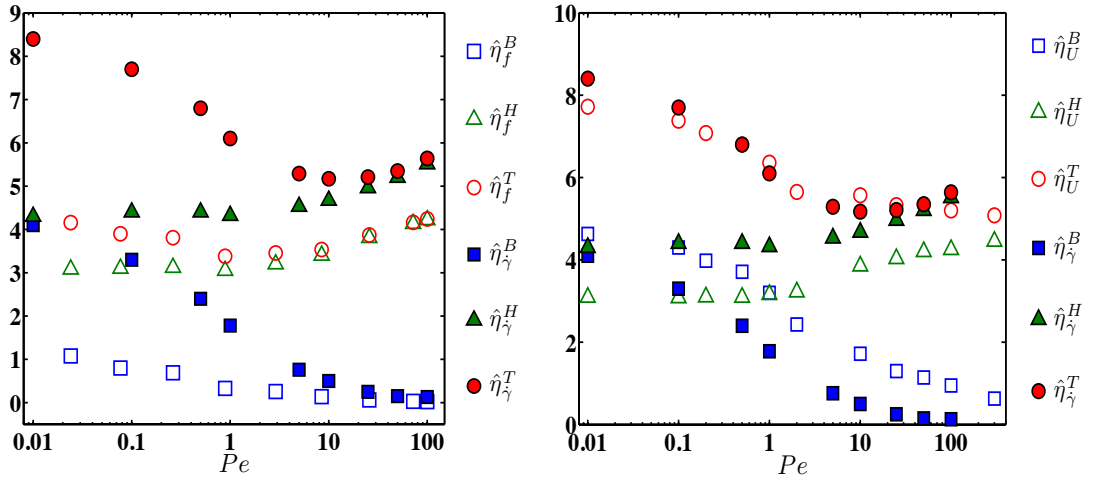

(a) Constant force (b) Constant velocity

Figure 5.6: Micro-viscosity as a function of Pe for $\phi = 0.40$ at (a) constant force and (b) constant velocity. The open symbols are the predicted values and filled symbols are the results of ASD for the equivalent $Pe_{\dot{\gamma}}$.

The hydrodynamic contributions to micro-viscosity in both CF and CV predictions follow the trend observed in the shear flow results and show very little change with Péclet number until $Pe = 1$ and afterwards they mildly increase with Pe in the range of Pe studied here. Brownian contributions in all cases are reduced with increase of Pe. Similar to the equilibrium results given in fig 5.5(a), the Brownian micro-viscosity is significantly smaller in CF compared with shear flow and CV results in all Pe. Also $\hat{\eta}_U^B$ decays more slowly than the Brownian shear viscosity, $\hat{\eta}_{\dot{\gamma}}^B$, and remains of $O(1)$ even at $Pe = 50$. As a result, the decrease in $\hat{\eta}_U^B$ remains of the same order of the increase in $\hat{\eta}_U^H$ and consequently the shear and force thickening shown in shear flow and CF predictions are not observed in CV results in the range of Pe studied; the micro-viscosity appears to approach a constant.

Figure 5.7 presents the increase in micro-viscosity from the equilibrium hydrodynamic value, $\hat{\eta}^{H,eq}$, for CF, CV and shear flow at $Pe = 100$. The Brownian contributions to viscosity are very small for shear flow and CF at $Pe = 100$ and the results would

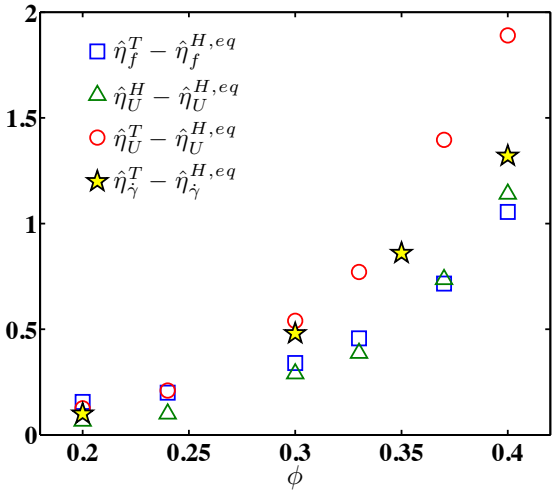

Figure 5.7: The increase in the computed micro-viscosity from the near-equilibrium hydrodynamic micro-viscosity, $\hat{\eta}^{H,eq}$, induced by external force and velocity on the probe particle at $Pe = 100$ and different volume fractions.

remain practically unchanged if only the hydrodynamic viscosities were presented for these conditions (this is not the case in CV conditions). Thus the increase with respect to the equilibrium value is only due to force/shear thickening of hydrodynamic viscosity. To facilitate visualizing the effect of Brownian stresses in CV relative to shear flow and CF conditions, the increase in hydrodynamic viscosity, $\hat{\eta}_U^H - \hat{\eta}_U^{H,eq}$, is presented separately. The values of $\hat{\eta}_U^H - \hat{\eta}_U^{H,eq}$ are very close to $\hat{\eta}_f^T - \hat{\eta}_f^{H,eq}$ predictions and are less than the shear flow viscosity increase. This shows that the increase in hydrodynamic micro-viscosity with Pe is very similar for CV and CF conditions. However, the Brownian forces have a noticeable effect on viscosity in CV mircrheology, a factor which makes the total viscosity increase in CV larger than in shear flow at $Pe = 100$.

As shown in figure 5.4, the contact values of pair distribution function at $Pe \gg 1$ and $\phi = 0.40$ are significantly larger in CV than in CF microrheology. This may suggest a smaller mobility and larger hydrodynamic viscosity for CV and thus may appear inconsistent with the rheological predictions presented in figure 5.7. However, we should note that it is not only the contact value of g which determines the bath particle effect on

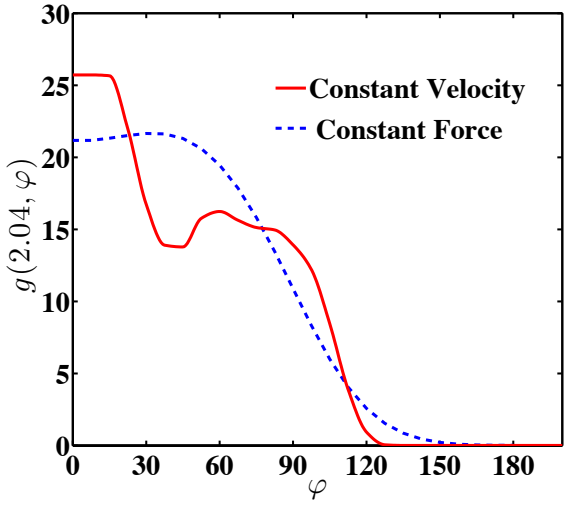

Figure 5.8: The comparison between CF and CV predictions of pair distribution function averaged from $r/a = 2.001$ to $r/a = 2.04$.

the probe mobility; the reduced mobility due to close contact interactions is controlled by the average value of g in the region where $\epsilon = (r/a - 2) \ll 1$. As an example, in figure 5.8 the values of pair distribution function averaged from $r/a = 2.001$ to $r/a = 2.04$, $g(2.04, \varphi)$ are compared against each other for $\phi = 0.40$ at $Pe_U = Pe_{\langle U \rangle} = 100$. We see that the average pair distribution function at separations as small as $\epsilon = 0.04$ are of the same order of magnitude. As a result, the predicted hydrodynamic micro-viscosities at $Pe \gg 1$ are quantitatively close for both fixed force and velocity conditions.

5.6 Summary

We have developed a theoretical framework based on the pair Smoluchowski equation for studying structure and rheology of colloidal dispersions in active microrheology. In this situation, a probe particle is pulled through the bath of suspension with a fixed force or velocity. This work extends the previous related theories by explicitly taking into account the many-body thermal and hydrodynamic effects. This results in an integro-differential equation in terms of $g(\mathbf{r})$ which is the likelihood of observing the colloidal

bath particles at a distance $\mathbf{r}$ from the probe. The equation is solved numerically using an iterative finite element technique. As a result the theory is applicable to suspensions with $\phi \leq 0.40$ over the entire range of Pe. The predicted $g(\mathbf{r})$ is then used to compute the average mobility of the probe and hence the apparent micro-viscosity as a function of ϕ and Pe.

We have considered both conditions of pulling a probe particle with fixed external force and velocity. One major difference between these two methods is the dispersive motion of the probe induced by external force in addition to the thermal fluctuations whereas in moving the probe with a fixed velocity the trajectory is fixed and the probe has no dispersive motion. This effect has not been considered in the previous theories since they assume $\phi \ll 1$ and limit the interactions to two particle level. We followed the guidelines established in our work studying sheared suspensions [32] (also see Chapters 2 & 3) and modeled the force-induced relative dispersion flux with a diffusion flux in the pair Smoluchowski equation; the force-induced relative diffusion coefficient (relative meaning the relative motion of the probe and bath particle of interest) was modeled based on the two limits of the probe and a bath particle touching and when they are well-separated and hence decorrelated. In case of the particles being well-separated, the relative diffusivity equals the probe long-time self-diffusion which was modeled, by analogy to the equilibrium theory relating the diffusion coefficient to an osmotic pressure variation, i.e. $D_s^{eq} = M^{eq} \cdot \dfrac{\partial \Pi^{eq}}{\partial \phi}$, as $\mathbf{D}_s^f = \mathbf{M} \cdot \Sigma / n_a$ where $\mathbf{M}$ is the probe average mobility, Σ is the force-induced hydrodynamic stress and n_a is the density of the probe phase. In the limit of the probe and bath particles in a near-contact configuration, the relative velocity and its fluctuations along the line of centers goes to zero. A form based on scaling arguments was proposed to consider the rate by which the radial diffusivity decays to zero at contact. The variations of relative diffusion in the angular direction were modeled using insights from shear flow simulation results. The key aspect of the angular diffusivity is that it remains finite at all pair separations including near contact.

The predictions of the near-equilibrium, $Pe \ll 1$, distorted microstructure are quite similar for both fixed force and velocity conditions. This is not in agreement with the predictions of Squires & Brady for dilute Brownian suspensions with no hydrodynamic interactions who predicted a distortion twice as large for constant velocity compared to constant force. This difference can be explained in terms of the magnitude of relative radial diffusivity at $Pe \ll 1$. In case of the probe motion with an external force and no hydrodynamic interactions, the relative diffusion in pair SE is $D_{rr} = 2k_bTM_0$, while for the case of pulling with fixed velocity $D_{rr} = k_bTM_0$ which results in a distortion of microstructure twice as large as the fixed force setup. When hydrodynamic interactions are considered, for constant velocity, the relative diffusivity is given by $\mathbf{D} = k_bT\mathbf{R}_{21} \cdot (\mathbf{R}_{22})^{-1}$. Using the lubrication expressions for the resistance tensors involved in this expression, it is straightforward to show that the relative diffusivity goes as $4(r-2)$ in the radial direction, which is the same value as relative diffusion in a constant force scenario with hydrodynamic interactions. As a result, similar microstructural distortions are predicted for near-equilibrium conditions.

Accelerated Stokesian Dynamics simulations of CF active microrheology were carried out for $\phi = 0.40$ and $Pe_f = 1, 4, 10$ and 100. The microstructure for fixed velocity condition was studied via predictions of the theory and $g(\mathbf{r})$ obtained from sampling the configurations of simulations was compared against the predictions of fixed force (CF) and velocity (CV). The theory was able to give a good prediction of the spatial variations of $g(\mathbf{r})$ in the fixed force condition in the range of Pe studied. The discrepancies were also noted and discussed. Also, in a more quantitative evaluation of the theory, the predicted variations of pair distribution function at contact were compared against ASD results and the results were in quite good agreement. At $Pe \gg 1$, a boundary layer structure of high bath particle probability is formed in constant force and velocity predictions and simulation results, with large values of $g(\mathbf{r})$ in front of the probe and a depleted zone of bath particles ($g(\mathbf{r}) \ll 1$) behind the probe. In addition, at high Péclet

number the effect of force-induced dispersion becomes significant, a factor which results in apparent differences between the predictions and simulated results of $g(\mathbf{r})$ under conditions of fixed force and prediction of fixed velocity. As a general trend, the depleted and high probability regions become more pronounced in constant velocity. Many-body interactions result in existence of local regions of high and low probability away from contact (secondary peaks in $g(\mathbf{r})$). When the probe is moved with a constant velocity at $Pe_U \gg 1$, these high probability zones are formed along the motion direction. The presence of force-induced dispersion in fixed force conditions results in a more uniform variations of pair distribution function with relative separation vector, $\mathbf{r}$, and reduces the magnitude of secondary peaks in $g(\mathbf{r})$. The near-contact anisotropy and local regions with high probability become more pronounced with increase of ϕ and the variations are considerably stronger in the case of constant velocity.

The predictions of Brownian contribution to CV micro-viscosity near-equilibrium is about a factor of four larger than CF and very close to the shear flow simulation results. The hydrodynamic contribution to micro-viscosity as a function of Pe is predicted to show little difference between constant force and velocity conditions. Our explanation is that the average value of the pair distribution function in a region near contact (not the actual contact value) is quantitatively close in the two cases.

We have limited our study here to the case of equal size of probe and bath particles. Previous studies have shown a strong influence of probe to bath particles size ratio on microstructure and microrheology [103]. This theory can be extended to consider different size ratios through modification of the pair resistance and mobility functions. Also, in this study of active microrheology only hard-sphere suspensions were considered whereas the theory can be easily extended to colloidal suspensions with other types of interactions. Finally simulation of a wider range of Pe and ϕ as well as implementation of ASD for simulation of CV active microrheology are two the important directions for future studies. Having access to pair microstructure and dynamics from simulations

would tremendously help gaining a clearer theoretical understanding of this problem.

6 Topics for future explorations

This chapter presents two extensions of the developed theory for colloidal dispersion: 1- microstructure and rheology of non-Brownian suspensions ($Pe \to \infty$) and 2- study of microstructure and rheology of colloidal dispersions in general linear flow kinematics. The results presented for the mentioned topics are not conclusive but are indicative of the utility of this theoretical approach in tackling such problems.

6.1 Rheology of non-Brownian dispersions

As was discussed in Chapter 3, the predictions of $g(\mathbf{r})$ and rheology become essentially independent of Péclet number at $Pe \gg 1$. Thus the theory gives a prediction of structure and rheology at the limit of $Pe \to \infty$. This opens the possibility of studying non-Brownian dispersions with typical particle size of $O(100\ \mu\text{m})$ with different types of interparticle interactions. As an example we present the predictions of the dimensionless shear viscosity, and normal stress differences at $Pe \to \infty$ for hard-sphere suspension next to the ASD simulation results at $Pe = 1000$ in figure 6.1. The agreement of predictions with simulation results is reasonable. Application of this theory to dispersions with interparticle interactions other than hard-spheres appears to be a good avenue of research. One example of significant practical relevance is concentrated suspensions where particles make contact due to their rough surfaces. The theory can be modified to study this system through incorporating an appropriate contact model as the interparticle force.

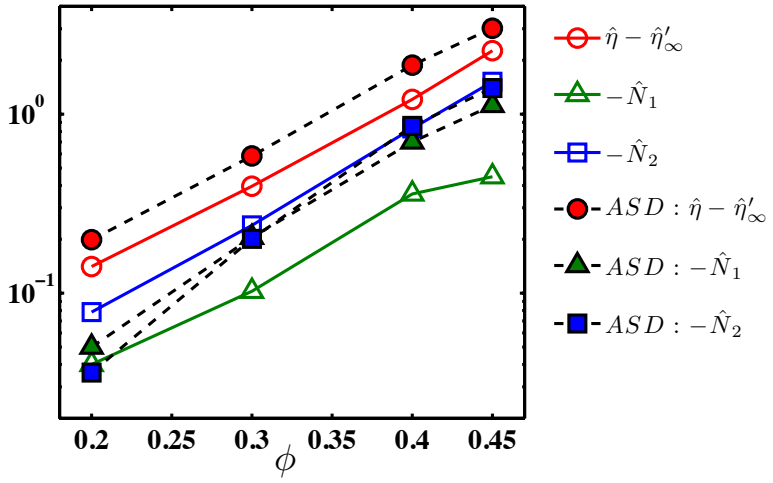

Figure 6.1: Predictions of non-Newtonian rheology at $Pe \to \infty$ at different volume fractions compared against ASD simulations at $Pe = 1000$.

6.2 General linear flow kinematics

The results presented so far in this thesis considered the shear flow kinematics and active microrheology. The transport of dispersions, however, involves more complex flow fields. The examples include flow in channels (or microchannels) and pipes [61], expansion and contraction of flow cross-section in channels [104], and free surface flows [105]. Variations of the flow kinematics across the geometry (i.e. the velocity gradient changes across the geometry) induces macroscopic structural changes. For example in the flow of the suspension in a cylindrical pipe (or rectangular duct), the particles migrate towards regions with lower local shear rate (the center of the pipe) and a concentration gradient is formed across channel which is known as shear-induced migration [61]. It is not clear how to extend the current microstructural theories based on probability distribution functions to ensembles with gradient in volume fraction and spatial correlation, $g(\mathbf{r})$. Instead, a typical practice is to assume the complex fluid as a continuum and "pass on" the microscopic information in the form of a constitutive equation relating the stress, Σ, to the rate of strain, $\mathbf{E} = \left[\nabla \mathbf{U}^\infty + (\nabla \mathbf{U}^\infty)^T\right]/2$ tensor in the momentum equation.

This method has been widely used to study polymer flow and processing [90, 89] and its foundations serve as the guiding principles for studying other classes of complex fluids including suspensions [39, 106]. The goal of this section is to take the first step towards obtaining a constitutive equation for suspensions, i.e. to study the rheology in general linfear flow kinematics.

The velocity field in a general linear flow kinematics is expressed as

$$\mathbf{U}^{\infty}(\mathbf{x}) = \boldsymbol{\Omega} \times (\mathbf{x} - \mathbf{x}_0) + \mathbf{E} \cdot (\mathbf{x} - \mathbf{x}_0), \tag{6.1}$$

where $\Omega = \nabla \times \mathbf{U}^{\infty}$ is the vorticity vector. Since the velocity field is linear with respect to position, $|\boldsymbol{\Omega}| = \sqrt{\boldsymbol{\Omega} \cdot \boldsymbol{\Omega}}$ and $|\mathbf{E}| = \sqrt{\mathbf{E} : \mathbf{E}}$ remain constant in space. We refer to the first term of the right hand side of (6.1) as the rotation piece of the velocity field since there is no component of the velocity in the direction of $\mathbf{x} - \mathbf{x}_0$ and to the second term as the straining piece. The simple shear flow relative velocity field can be decomposed into these two pieces as

$$\mathbf{U}^{\infty}(\mathbf{r}) = \dot{\gamma} y \hat{\mathbf{i}} = |\boldsymbol{\Omega}| \left(y\hat{\mathbf{i}} - x\hat{\mathbf{j}} \right) + |\mathbf{E}| \left(y\hat{\mathbf{i}} + x\hat{\mathbf{j}} \right), \tag{6.2}$$

where $\mathbf{r} = x\hat{\mathbf{i}} + y\hat{\mathbf{j}} + z\hat{\mathbf{k}}$, and the first and second term on the right hand side of (6.2) are the rotational and straining parts of the motion with $|\boldsymbol{\Omega}| = |\mathbf{E}| = \dot{\gamma}/2$. Here, we extend the shear flow results by considering different values for $\chi = \dfrac{|\boldsymbol{\Omega}|}{|\mathbf{E}|}$ by keep the straining part constant and varying the strength of rotation. As a result we can model flow fields ranging from pure straining, $\chi = 0$, to flows dominated by vorticity, here taking values as large as $\chi = 4$. All the variables in the pair SE remain identical to the shear flow condition except for $\mathbf{U}^{\infty}$ which is modified according to (6.2). The analysis is carried out at $\phi = 0.40$ and $Pe \to \infty$. Note that to ensure a frame-invariant measure of rotation, the relative rotation should be defined as the difference between the local angular velocity and the local rotation velocity of axes of rate of strain which are defined

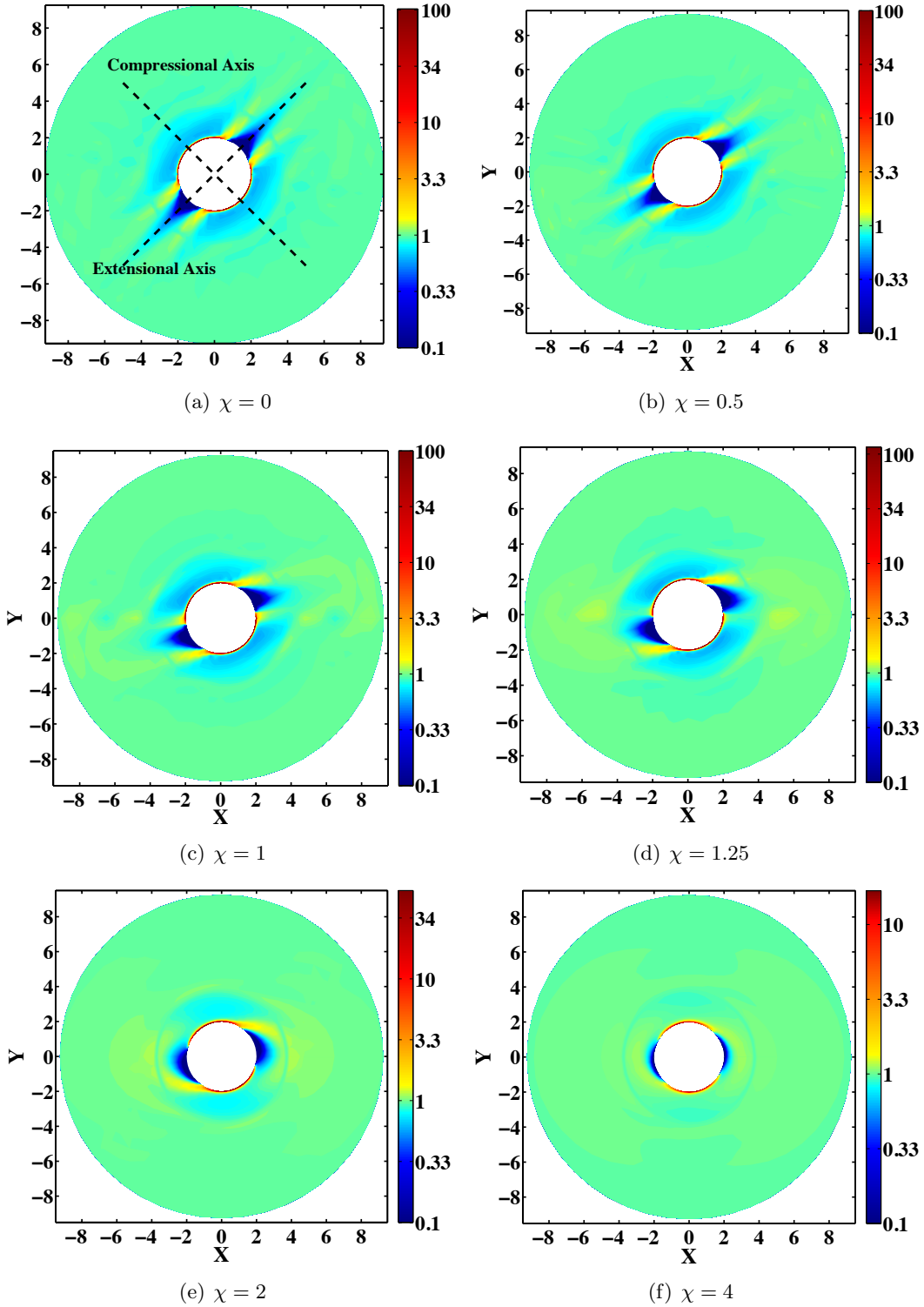

(a) $\chi = 0$ (b) $\chi = 0.5$

(c) $\chi = 1$ (d) $\chi = 1.25$

(e) $\chi = 2$ (f) $\chi = 4$

Figure 6.2: Pair distribution function is straining plane $(x - y)$ at different ratios of vorticity to strain rate magnitudes, $\chi = \frac{|\mathbf{\Omega}|}{|\mathbf{E}|}$, (a) $\chi = 0$, (b) $\chi = 0.5$, (c)=$\chi = 1$, (d) $\chi = 1.25$, (e) $\chi = 2$, (f) $\chi = 4$. The extensional and compressional axes of the straining flow ($\theta = \pi/4$, and $\theta = 3\pi/4$ respectively) are shown as dotted lines in figure 6.2(a).

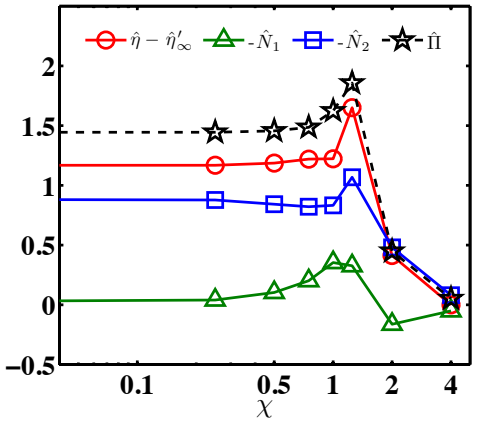

Figure 6.3: Non-Newtonian rheology of a non-Brownian suspension as a function of χ.

as the eigenvectors of the rate of strain tensor [106]. In case of linear flows, the strain rate tensor is uniform in space and the axes of rate of strain do not rotate. Hence $|\mathbf{\Omega}|$ is equal to the magnitude of fluid angular velocity. However in nonlinear flows with large gradients of strain rate (such as sharp corners), the rotation of the strain rate axes may become of the same order of magnitude as the local fluid vorticity and the frame-invariant form of measuring the relative rotation should be used.

Figure 6.2 presents the variations of $g(\mathbf{r})$ in the plane of biaxial straining flow, $(x-y)$, as a function of χ. At $\chi = 0$, the microstructure is symmetric along the compressional and extensional axes ($\theta = \pi/4$ and $3\pi/4$) and for $\chi < 1$, the boundary layer separation occurs at larger θ compared with the shear flow, $\chi = 1$. The contact values of $g(\mathbf{r})$ remain similar for $\chi \leq 1.25$ and show a dramatic decrease for $\chi = 2$ and 4.

The computed nonlinear rheology based on the predictions of microstructure as a function of χ is presented in figure 6.3. The increase in viscosity due to straining motion (shear-thickening), particle pressure and second normal stress difference remain unchanged for $\chi \leq 1$. The first normal stress difference is identically zero at pure straining flow due to the symmetry of the microstructure around $\theta = \pi/4$ and $3\pi/4$ and starts to increase in magnitude with χ for $\chi \leq 1$. The non-Newtonian rheology shows a max-

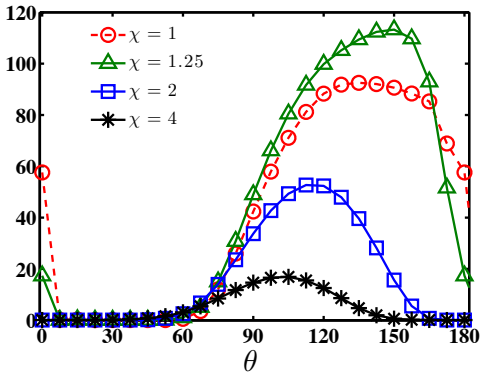

Figure 6.4: Variations of $g(2;\theta)$ for different values of $\chi \geq 1$.

imum at $\chi = 1.25$ and the values of $\hat{\eta} - \hat{\eta}'_{\infty}$, $\hat{\Pi}$ and $\hat{N}_2$ show a sudden drop towards zero at $\chi = 2$ and 4. The first normal stress difference also shows a significant drop in magnitude and becomes positive going from $\chi = 1.25$ to $\chi = 2$ and is reduced to nearly zero at $\chi = 4$, similar to the other functions. The sign change observed in $\hat{N}_1$ at $\alpha = 2$ can be explained in terms of variations of $g(2;\theta)$ with χ as presented in figure 6.4. The values of pair distribution function in flow direction are reduced with increase of χ and the maximum peak is shifted to lower θ near $\theta = \pi/2$ when χ is increased to 2 and 4. As a result Σ_{xx} is significantly reduced at $\chi = 2$ while, since the values of g are still large and asymmetric around $\theta = \pi/2$, Σ_{yy} remains large and negative. As a result $\hat{N}_1 = \dfrac{\Sigma_{xx} - \Sigma_{yy}}{\eta\dot{\gamma}}$ changes sign and becomes positive. At $\chi = 4$, the contact values are decreased further which results in drop in all components of particle stress including $\hat{N}_1$. Finally note that the maximum value of g takes its largest value at $\chi = 1.25$ and the maximum occurs near the compressional axis. This may explain why the nonlinear rheology exhibits a maximum at this χ at illustrated in figure 6.3.

The presented results suggest that the nonlinear rheology remains independent of χ for $\chi \leq 1$ and shows a slight maximum in viscosity, particle pressure and second normal stress difference at $\chi = 1.25$ and the rheology quickly become Newtonian with further increase of the strength of rotational flow. The predictions are only presented for a single

volume fraction, $\phi = 0.40$, and a few χ. Exploration of parameter space in terms of ϕ, χ and perhaps Pe is needed for reaching a clearer understanding of this problem. The main unresolved issue in understanding the effects of flow kinematics on rheology is, however, the lack of simulation and experimental results to compare against the theoretical predictions; we know of no experiments on any linear flow besides shear flow and only one set of simulation results by Sami & Brady [107] where Stokesian Dynamics simulation runs were performed on pure straining flows. Their results are in agreement with our predictions and show no difference between the rheological predictions of pure straining flow and simple shear flow. Access to experimental results and more simulational data would greatly facilitate our evaluation of the theory for general kinematics.

7 Bibliography

[1] E. Guazzelli and J. F. Morris. *A Physical Introduction to Suspension Dynamics.* Cambridge University Press, January 2012.

[2] X. Huang and M. H. Garciá. A Herschel–Bulkley model for mud flow down a slope. *J. Fluid Mech.*, 374:305–333, 1998.

[3] S. C. Glotzer and M. J. Solomon. Anisotropy of building blocks and their assembly into complex structures. *Nature Materials*, 6:557–562, 2007.

[4] W. B. Russel, D. A. Saville, and W. R. Schowalter. *Colloidal Dispersions.* Cambridge University Press, 1995.

[5] J. K. G. Dhont. *An Introduction to Dynamics of Colloids.* Elsevier, January 1996.

[6] F. Gadala-Maria and A. Acrivos. Shearinduced structure in a concentrated suspension of solid spheres. *J. Rheol.*, 24:799–814, 1980.

[7] A. Sierou and J. F. Brady. Rheology and microstructure in concentrated noncolloidal suspensions. *J. Rheol.*, 46:1031–1056, 2002.

[8] C. Aidun, Y. Lu, and E. J. Ding. Direct analysis of particulate suspensions with inertia using the discrete Boltzmann equation. *J. Fluid Mech.*, 373:287–311, 1998.

[9] P. M. Kulkarni and J. F. Morris. Suspension properties at finite Reynolds number from simulated shear flow. *Phys. Fluids*, 20:040602, 2008.

[10] N. Huang, G. Ovarlez, F. Bertrand, P. Coussot, and D. Bonn. Flow of wet granular materials. *Phys. Rev. Lett.*, 94:028301, 2005.

[11] P. C. Hienmenz and R. Rajagopalan. *Principles of colloid and surface chemistry.* Marcel Dekker Inc., 3rd edition, 1997.

[12] Grzelczak M., J. Vermant, E. M. Furst, and L. M. Liz-Marza'n. Directed self-assembly of nanoparticles. *ACS Nano*, 4:3591–3605, 2010.

[13] A. Van Blaaderen. Materials science: Colloids get complex. *Nature Materials*, 439:545–546, 2006.

[14] G. M. Gratson, M. Xu, and J. A. Lewis. Microperiodic structures: Direct writing of three-dimensional webs. *Nature*, 428:386, 2004.

[15] J. A. Lewis. Colloidal processing of ceramics. *J Am. Ceram. Soc.*, 83:2341–59, 2000.

[16] A. Terray, J. Oakey, and D. W. M. Marr. Microfluidic control using colloidal devices. *Nature*, 296:1941–44, 2002.

[17] J-P Hansen and R. I. McDonald. *Theory of simple liquids.* Elsevier, 3rd edition, May 1986.

[18] M. K. Lyon, Mead D. W., R. E. Elliot, and L. G. Leal. Structure formation in moderately concentrated viscoelastic suspensions in simple shear flow. *J. Rheol.*, 45:881–90, 2001.

[19] D. Saintillan. *Collective dynamics in dispersions of anisotropic and deformable particles.* PhD thesis, Stanford University, August 2006.

[20] G. M. H. Wikins, P. T. Spicer, and M. J. Solomon. Nanocolloidal system to explore structural and dynamical transitions in rod networks, gels and glasses. *Langmuir*, 25:8951–8959, 2008.

[21] A. Van Blaaderen and A. Yethiraj. A colloidal model system with an interaction tunable from hard sphere to soft and dipolar. *Nature*, 421:513–517, 2003.

[22] J. Vermant and M. J. Solomon. Flow induced structure in colloidal suspensions. *J. Phys: Cond. Matt. Phys.*, 17:R187–R216, 2005.

[23] W. B. Russel and A. P. Gast. Nonequilibrium statistical mechanics of concentrated colloidal dispersions: Hard spheres in weak flows. *J. Chem. Phys.*, 84:1815–1826, 1986.

[24] R. A. Lionberger and W. B. Russel. A Smoluchowski theory with simple approximations for hydrodynamic interactions in concentrated dispersions. *J. Rheol.*, 41:399–425, 1997.

[25] G. Szamel. Nonequilibrium structure and rheology of concentrated colloidal suspensions: Linear response. *J. Chem. Phys.*, 114, 2001.

[26] M. Fuchs and M. E. Cates. A mode coupling theory for Brownian particles in homogeneous steady shear flow. *J. Rheol.*, 53:957–1000, 2009.

[27] J. F. Brady and J. F. Morris. Microstructure of strongly sheared suspensions and its impact on rheology and diffusion. *J. Fluid Mech.*, 348:103–139, 1997.

[28] J. Bergenholtz, J. F. Brady, and M. Vicic. The non-Newtonian rheology of dilute colloidal suspensions. *J. Fluid Mech.*, 456:239–275, 2002.

[29] J. F. Brady and G. Bossis. Stokesian Dynamics. *Ann. Rev. Fluid Mech.*, 20:111–157, 1988.

[30] S. Kim and S. Karrila. *Microhydrodynamics: Principles and Selected Applications*. Dover, 1st edition, 2005.

[31] A. J. Banchio and J. F. Brady. Accelerated Stokesian Dynamics: Brownian motion. *J. Chem. Phys.*, 118:10323–10332, 2003.

[32] E. Nazockdast and J. F. Morris. Microstructural theory and the rheology of concentrated colloidal suspensions. *J. Fluid Mech.*, 713:420–452, 2012.

[33] J. Vermant and M. J. Solomon. Flow-induced structure in colloidal suspensions. *Journal of Physics: Condensed Matter*, 17:R187–R216, 2005.

[34] R. C. Ball and J. R. Melrose. Lubrication breakdown in hydrodynamic simulations of concentrated colloids. *Advances in Colloid and Interface Science*, 59:19–30, 1995.

[35] J. C. van der Werff and C. G. de Kruif. Hard-sphere colloidal dispersions: the scaling of rheological properties with particle size, volume fraction, and shear rate. *J. Rheol.*, 33:421–454, 1989.

[36] I. E. Zarraga, D. A. Hill, and D. T. Leighton. The characterization of the total stress of concentrated suspensions of noncolloidal spheres in Newtonian fluids. *J. Rheol.*, 44:185–220, 2000.

[37] D. R. Foss and J. F. Brady. Structure, diffusion and rheology of Brownian suspensions by Stokesian Dynamics simulation. *J. Fluid Mech.*, 407:167–200, 2000.

[38] D. T. Leighton and A. Acrivos. The shear-induced migration of particles in concentrated suspensions. *J. Fluid Mech.*, 181:415–439, 1987.

[39] J. F. Morris and F. Boulay. Curvilinear flows of noncolloidal suspensions: The role of normal stresses. *J. Rheol.*, 43:1213–1237, 1999.

[40] H. A. Barnes. Shear-thickening ("Dilatancy") in suspensions of nonaggregating solid particles dispersed in Newtonian liquids. *J. Rheol.*, 33:329–366, 1989.

[41] A. Sierou and J. F. Brady. Accelerated Stokesian Dynamics simulations. *J. Fluid Mech.*, 448:115–146, 2001.

[42] C. Gao, S. D. Kulkarni, J. F. Morris, and J. F. Gilchrist. Direct investigation of anisotropic suspension structure in pressure-driven flow. *Phys. Rev. E*, 81:041403–041407, 2010.

[43] L. B. Chen, C. F. Zukoski, and B. J. Ackerson. Rheological consequences of microstructural transitions in colloidal crystals. *J. Rheol.*, 38:193–216, 1994.

[44] G. K. Batchelor and J. T. Green. The determination of the bulk stress in a suspension of spherical particles to order c^2. *J. Fluid Mech.*, 56:401–427, 1972.

[45] G. K. Batchelor and J. T. Green. The hydrodynamic interaction of two small freely-moving spheres in a linear flow field. *J. Fluid Mech.*, 56:375–400, 1972.

[46] J. F. Brady. The rheological behavior of concentrated colloidal dispersions. *J. Chem. Phys.*, 99:567–581, 1993.

[47] J. F. Brady and M. Vicic. Normal stresses in colloidal dispersions. *J. Rheol.*, 39:545–566, 1995.

[48] J. F. Morris and B. Katyal. Microstructure from simulated Brownian suspension flows at large shear rate. *Phys. Fluids*, 14:1920, March 2002.

[49] D. T. Leighton and A. Acrivos. Measurement of shear-induced self-diffusion in concentrated suspensions of spheres. *J. Fluid Mech.*, 177:109–131, 1987.

[50] A. Sierou and J. F. Brady. Shear-induced self-diffusion in non-colloidal suspensions. *J. Fluid Mech.*, 506:285–314, 2004.

[51] A. S. Rice and J. Lekner. On the equation of state of the rigid-sphere fluid. *J. Chem. Phys.*, 42:3559–3565, 1965.

[52] Y. Yurkovetsky and J. F. Morris. Triplet correlation in sheared suspensions of Brownian particles. *J. Chem. Phys.*, 124:204908–204919, 2006.

[53] P. Mazur and W. Van Saarloos. Many-sphere hydrodynamic interactions and mobilities in a suspension. *Physica A: Statistical and Theoretical Physics*, 115:21–57, 1982.

[54] J. F. Morris and J. F. Brady. Self-diffusion in sheared suspensions. *J. Fluid Mech.*, 312:223–252, 1996.

[55] D. R. Foss and J. F. Brady. Self-diffusion in sheared suspensions by dynamic simulation. *J. Fluid Mech.*, 401:243–274, 1999.

[56] G. K. Batchelor. The effect of Brownian motion on the bulk stress in a suspension of spherical particles. *J. Fluid Mech.*, 83:97–117, 1977.

[57] G. Throop and R. Bearman. Numerical solutions of the Percus-Yevick equation for the hard-sphere potential. *J. Chem. Phys.*, 42:2408–2411, 1965.

[58] Y. Yurkovetsky and J. F. Morris. Particle pressure in sheared Brownian suspensions. *J. Rheol.*, 52:141–164, 2008.

[59] M. J. Allen and D. J. Tildesley. *Computer simulation of liquids*. Oxford University Press, 1989.

[60] N. J. Wagner and B. J. Ackerson. Analysis of nonequilibrium structures of shearing colloidal suspensions. *J. Chem. Phys.*, 97:1473–1484, 1992.

[61] M. Frank, D. Anderson, E. A. Weeks, and J. F. Morris. Particle migration in pressure-driven flow of a Brownian suspension. *J. Fluid Mech.*, 493:363–378, 2003.

[62] S. D. Kulkarni and J. F. Morris. Ordering transition and structural evolution under shear in Brownian suspensions. *J. Rheol.*, 53:417–439, 2009.

[63] E. Nazockdast and J. F. Morris. Effect of repulsive interactions on structure and rheology of sheared colloidal dispersions. *Soft Matter*, 8:4223–4234, March 2012.

[64] J. F. Morris. A review of microstructure in concentrated suspensions and its implications for rheology and bulk flow. *Rheol. Acta*, 48:909–923, 2009.

[65] J. M. Brader. Nonlinear rheology of colloidal dispersions. *Journal of physics: Condensed Matter*, 22:363, 2010.

[66] A. J. C. Ladd and R. Verberg. Lattice-Boltzmann simulations of particle-fluid suspensions. *Journal of Statistical Physics*, 104:1192–1250, 2001.

[67] M. Fuchs and M. E. Cates. Theory of nonlinear rheology and yielding of dense colloidal suspensions. *Phys. Rev. Lett.*, 89:248304–248307, November 2002.

[68] W. Xue and G. S. Grest. Shear-induced alignment of colloidal particles in the presence of a shear flow. *Phys. Rev. Lett.*, 64:419–422, 1990.

[69] S. R. Rastogi, N. J. Wagner, and S. R. Lustig. Rheology, selfdiffusion, and microstructure of charged colloids under simple shear by massively parallel nonequilibrium brownian dynamics. *J. Chem. Phys.*, 104:9234–9248, 1996.

[70] E. E. Salpeter. On mayer's theory of cluster expansions. *Ann. Phys.*, 5:183–223, 1958.

[71] D. R. Foss and J. F. Brady. Brownian dynamics simulation of hard-sphere colloidal dispersions. *J. Rheol.*, 44:629–651, 2000.

[72] E. Nazockdast and J. F. Morris. Pair-particle dynamics and microstructure in sheared colloidal suspensions: simulation and smoluchowski theory. Submitted for publication in Physics of Fluids, September 2012.

[73] U. Balucani and M. Zoppi. *Dynamics of the Liquid State*. Oxford University Press, 1995.

[74] D. J. Jeffrey and Y. Onishi. Calculation of the resistance and mobility functions for two unequal rigid spheres in low-reynolds-number flow. *J. Fluid Mech.*, 139:261–290, 1984.

[75] H. J. Wilson. An analytic form for the pair distribution function and rheology of a dilute suspension of rough spheres in plane strain flow. *J. Fluid Mech.*, 534:97–114, 2005.

[76] E. C. Eckstein, D. C. Bailey, and A. H. Shapiro. Self-diffusion of particles in shear-flow of a suspension. *J. Fluid Mech.*, 79:211–223, 1977.

[77] V. Breedveld, D. van den Ende, A. Triphati, and A. Acrivos. The measurement of the shear-induced particle and fluid tracer diffusivities by a novel method. *J. Fluid Mech.*, 375:297–318, 1998.

[78] A. Acrivos, G. K. Batchelor, E. J. Hinch, D. L. Koch, and R. Mauri. The longitudinal shear-induced diffusion of spheres in a dilute suspension. *J. Fluid Mech.*, 240:651–657, 1992.

[79] F. R. Da Cunha and E. J. Hinch. Shear-induced dispersion in a dilute suspension of rough spheres. *J. Fluid Mech.*, 309:211–223, 1996.

[80] N. G. Van Kampen. *Stochastic Processes in Physics and Chemistry.* North-Holland, 1981.

[81] R. Metzler and J. Klafter. The random walk's guide to anomalous diffusion: a fractional dynamics approach. *Physics Reports*, 339:1–77, 2000.

[82] H. Risken. *The Fokker-Planck Equation: Methods of Solutions and Applications.* Springer, 1996.

[83] R. Metzler and J. Klafter. The restaurant at the end of the random walk: recent

developments in the description of anomalous transport by fractional dynamics. *Journal of Physics A: Mathematical and General*, pages R161–R208, 2004.

[84] L. Borland. Microscopic dynamics of the nonlinear Fokker-Planck equation: A phenomenological model. *Phys. Rev. E*, 57:6634–6642, 1998.

[85] T. M. Squires and T. G. Mason. Fluid mechanics of microrheology. *Ann. Rev. Fluid Mech.*, 42:413–438, January 2010.

[86] F. C. MacKintosh and C. F. Schmidt. Microrheology. *Curr. Opin. Colloid Interface Sci.*, 4:300–307, 1999.

[87] T. A. Waigh. Microrheology of complex fluids. *Reports on Progress in Physics*, 68:685–742, 2005.

[88] C. Macosko. *Rheology: Principles, Measurements, and Applications.* Wiley-VCH, 1994.

[89] M. M. Denn. *Polymer Melt Processing: Foundations in Fluid Mechanics and Heat Transfer.* Cambridge University Press, 2008.

[90] R. G. Larson. *The Structure and Rheology of Complex Fluids.* Oxford University Press, 1998.

[91] T. G. Mason and D. A. Weitz. Optical measurements of frequency-dependent linear viscoelastic moduli of complex fluids. *Phys. Rev. Lett.*, 74:1250–1253, 1995.

[92] P. Habdaas, D. Schaar, A. C. Levitt, and E. A. Weeks. Forced motion of a probe particle near the colloidal glass forced motion of a probe particle near the colloidal glass transition. *Europhys. Lett.*, 67:477–483, 2004.

[93] I. Sriram, A. Meyer, and E. M. Furst. Active microrheology of a colloidal suspension in the direct collision limit. *Phys. Fluids*, 22:062003, 2010.

[94] T. M. Squires and J. F. Brady. A simple paradigm for active and nonlinear microrheology. *Phys. Fluids*, 17:073101, July 2005.

[95] A. Khair and J. F. Brady. Single particle motion in colloidal dispersions: a simple model for active and nonlinear microrheology. *J. Fluid Mech.*, 557:73–117, 2006.

[96] A. Khair and J. F. Brady. Microrheology of colloidal dispersions: Shape matters. *J. Rheol.*, 52:165–196, 2008.

[97] I. C. Carpen and J. F. Brady. Microrheology of colloidal dispersions by Brownian dynamics simulations. *J. Rheol.*, 49:1483–1502, 2005.

[98] M. V. Gnann, I. Gazuz, A. M. Puertas, M. Fuchs, and Th. Voigtmann. Schematic models for active nonlinear microrheology. *Soft Matter*, 7:1390–1396, 2011.

[99] A. M. Leshansky and J. F. Brady. Dynamic structure factor study of diffusion in strongly sheared suspensions. *J. Fluid Mech.*, 527:141–169, 2005.

[100] A. M. Leshansky, J. F. Morris, and J. F. Brady. Collective diffusion in sheared colloidal suspensions. *J. Fluid Mech.*, 597:305–341, 2008.

[101] R. N. Zia and J. F. Brady. Microviscosity, microdiffusivity, and normal stresses in colloidal dispersions. *J. Rheol.*, 56:1175–1208, June 2012.

[102] D. S. Pearson and T. Shikata. Viscoelastic behavior of concentrated spherical suspensions. *J. Rheol.*, 38:601–616, 1994.

[103] Y. Almog and H. Brenner. Non-continuum anomalies in the apparent viscosity experienced by a test sphere moving through an otherwise quiescent suspension. *Phys. Fluids*, 9:16–22, 1997.

[104] S. A. Altobeli, E. Fukushima, and L. A. Mondy. Nuclear magnetic resonance imaging of particle migration in suspensions undergoing extrusion. *J. Rheol.*, 41:1105–1115, 1997.

[105] M. Tirumkudulu and A. Acrivos. Particle segregation in monodisperse sheared suspensions. *Phys. Fluids*, 11:507, 1999.

[106] R. M. Miller, J. P. Singh, and J. F. Morris. Suspension flow modeling for general geometries. *Chem. Eng. Sci.*, 64:4597–4610, 2009.

[107] S. Sami. Stokesian dynamics simulation of extensional flow of Brownian suspensions. Master's thesis, California Institute of Technology, 1997.